



DISSERTATION

Two-photon double ionization of helium

ausgeführt zum Zwecke der Erlangung des akademischen Grades eines
Doktors der technischen Wissenschaften unter der Leitung von

O.Univ.-Prof. Dipl.-Phys. Dr.rer.nat. Joachim Burgdörfer
Institut für Theoretische Physik (136)

eingereicht an der Technischen Universität Wien
Fakultät für Physik

von

Dipl.-Ing. Johannes Feist

Matrikelnummer: 002595

Leitermayergasse 35/9

A-1180 Wien

johannes.feist@tuwien.ac.at

Wien, am _____

Contents

1	Introduction	1
2	The helium atom	3
2.1	The non-relativistic Hamiltonian	3
2.2	Spin and symmetry	5
2.3	Classification of levels	6
2.4	Spectral properties	7
2.5	Interaction with electromagnetic radiation	8
2.5.1	Semi-classical approximation	9
2.5.2	Dipole approximation	9
2.6	Resulting Hamiltonian	11
2.7	Atomic units	11
I	Method	13
3	Time-dependent close coupling method	15
3.1	Kinetic energy and electron-nucleus interaction	17
3.2	Electron-electron interaction	17
3.3	Electron-laser interaction	18
3.3.1	Length gauge	18
3.3.2	Velocity gauge	20
3.4	Close-coupling equations	21
3.4.1	Symmetry considerations	22
3.4.2	Selection rules	23
4	Numerical methods	25
4.1	Radial discretization	25
4.1.1	Finite elements	26
4.1.2	Discrete variable representation	26
4.1.3	Finite element discrete variable representation	30
4.2	Temporal discretization	34
4.2.1	Lanczos propagation	35

5	Computational implementation	39
5.1	Representation of the wave function	39
5.1.1	Partial waves	39
5.1.2	FEDVR basis	41
5.2	Implementation of the electron-electron interaction	43
5.3	Temporal propagation	45
5.3.1	Calculation of the ground state	45
5.4	Absorbing boundaries	45
5.5	Parallelization	46
5.5.1	Splitting the grid	46
5.5.2	Communication pattern	48
5.5.3	L-shaped grid	49
5.6	Benchmarks	49
5.6.1	Available machines	50
5.6.2	Total runtime	50
6	Observables	53
6.1	Continuum wave functions	53
6.2	Ionization probability distributions	57
6.2.1	Fully differential probability distributions	57
6.2.2	Energy probability distributions	58
6.2.3	Angular probability distributions	59
6.2.4	Angular distribution for single ionization	60
6.3	Recoil ion momentum distribution	61
6.3.1	Generation of randomly distributed electron configurations	62
7	Eigenstates	65
7.1	Doubly excited resonances	66
II	Two-photon double ionization	69
8	Introduction	71
8.1	Sequential and nonsequential regimes of TPDI	72
8.2	Second-order perturbation theory	74
9	Convergence issues	81
9.1	Dependence on pulse parameters	81
9.2	Differential distributions and cross sections	85
9.3	Influence of final-state correlations	87
9.4	Numerical convergence tests	94
9.5	Conclusions	95

10 Cross sections for nonsequential TPDI	99
11 Differential distributions: Photon energy dependence	107
11.1 Angular correlations	110
11.2 Nuclear recoil and one-electron angular distributions	118
12 Differential distributions: Pulse duration dependence	125
12.1 Energy spectrum	126
12.2 Shake-up interferences	131
12.3 Angular correlations	134
12.4 Nuclear recoil	144
13 Summary	149
13.1 Outlook	151
III Appendix	155
A Orthogonal polynomials and quadratures	157
A.1 Orthogonal polynomials	157
A.2 Gauss quadratures	158
A.3 Gauss-Legendre quadrature	159
A.4 Gauss-Lobatto quadrature	160
B Angular momentum algebra	161
B.1 Clebsch-Gordan coefficients	161
B.2 The Wigner 3j-symbol	162
B.3 The Wigner 6j-symbol	163
B.4 The Wigner-Eckart theorem	165
C Derivation of angular asymmetry parameters	167
D Stability of computational speed on different machines	171
D.1 Summary	172
List of Figures	177
Bibliography	181
Acknowledgments	199

1 Introduction

Double ionization of helium has long been of great interest in atomic physics since it provides fundamental insights into the role of electronic correlation in the full three-body Coulomb break-up process. Understanding the dynamics in this simple, two-electron system is crucial to understanding more complex atoms and even simple molecules [1–12]. Until recently, the focus of these studies was on one-photon double ionization, where a single photon (with an energy of $\hbar\omega > 79\text{ eV}$) releases both electrons from the nucleus.

In recent years, technologies such as the free electron laser (FEL) [13–22] and high harmonic generation (HHG) from a driving infrared (IR) laser [23–32] have made coherent, ultrashort, and intense pulses in the vacuum and extreme ultraviolet (VUV-XUV) region available. The continuing development of these novel light sources has led to an increased interest in multi-photon processes at high photon energies. Simultaneously, the ultrashort duration of the pulses in the femtosecond ($1\text{ fs} = 10^{-15}\text{ s}$) or even attosecond ($1\text{ as} = 10^{-18}\text{ s}$) domain enables the study of *time-resolved* electron dynamics, starting the field of *attosecond science* [33–37].

In this thesis, we study the role of electronic correlation in double ionization by such ultrashort, highly intense pulses. We focus on the helium atom, which is the simplest many-electron atom, yet displays rich correlation effects. This investigation is performed by solving the time-dependent Schrödinger equation (TDSE) in its full dimensionality. Some of the contents of this thesis have been previously reported on, most importantly in the diploma theses of Stefan Nagele [38] and Renate Pazourek [39]. In addition, some of the results obtained have been published in refereed journals [40–42].

The first part of the thesis introduces the method for solving the TDSE that we have developed in the past few years. Some sections of this part are based on the previously published diploma theses from our group [38, 39]. The main idea behind our approach is to solve the full two-electron TDSE with very good accuracy, providing reliable results for a wide range of experimental parameters. The high demand on the level of accuracy means that two-electron systems are at the limit of current computational power and a direct extension of the approach to more complicated systems is out of reach. We start (chapter 3) by presenting time-dependent close coupling (TDCC) [7, 43, 44]. The general idea behind this approach is to expand the angular degrees of freedom in the eigenbasis of angular momentum, transforming the six-dimensional Schrödinger equation to an (infinite) set of two-dimensional coupled equations. In chapter 4, we discuss the methods used

to transform these equations to a discrete system that can be solved numerically. This is followed in [chapter 5](#) by a discussion of the computational implementation of the resulting (matrix) equations, including a description of the approach used to parallelize the method to enable the use of large computing clusters. This was necessary to achieve well-converged results within reasonable time. We then turn to the extraction of observables from the final wave function after time propagation, described in [chapter 6](#), and finish the discussion of the method by comparing the properties of some bound and quasi-bound eigenstates of the He Hamiltonian to published results ([chapter 7](#)).

In the second part, we discuss a number of results on the two-photon double ionization (TPDI) of atomic helium. This is one of the simplest multi-photon processes involving electron correlation, and has been the subject of intense theoretical studies in the past few years [[40–42](#), [45–90](#)]. The main fields of interest that have been studied are (i) cross sections in the *nonsequential* regime of TPDI, for which the limit of infinite pulse lengths is most interesting, and (ii) effects of ultrashort (attosecond) XUV pulses in the *sequential* regime of TPDI. Although the cross sections for nonsequential TPDI have attracted a significant amount of interest by theoreticians, the published results show large discrepancies between the different approaches. There are much fewer experimental studies yet, all of which are concerned with the nonsequential regime [[81](#), [91–94](#)]. For these, the experimental uncertainties are still too large to help in resolving the discrepancies in the theoretical results.

We first discuss the convergence properties of our method ([chapter 9](#)). Having established the approach, we discuss the total cross sections in the nonsequential regime in [chapter 10](#), comparing to a number of previously published results. Parts of the results in these two chapters are contained in [[40](#)]. In [chapter 11](#), we then discuss the long-time limit of TPDI for different photon energies, focusing on different measures to observe and quantify correlations. Finally, we investigate the dependence on pulse duration ([chapter 12](#)), for pulses from less than a hundred attoseconds up to a few femtoseconds duration. In particular, we show a novel interference effect between sequential contributions with excitation (shake-up) of the intermediate ion and nonsequential contributions without shake-up. Some of the results in these two chapters were published in [[41](#), [42](#)].

2 The helium atom

2.1 The non-relativistic Hamiltonian

The helium atom consists of a nucleus (mass m_n , charge number $Z = 2$) and two electrons (mass m_e , charge $-e$). Hence, the non-relativistic Hamiltonian is given by

$$\hat{H} = \frac{\hat{\mathbf{p}}_n^2}{2m_n} + \frac{\hat{\mathbf{p}}_{e,1}^2}{2m_e} + \frac{\hat{\mathbf{p}}_{e,2}^2}{2m_e} - \frac{Ze^2}{|\hat{\mathbf{r}}_{e,1} - \hat{\mathbf{r}}_n|} - \frac{Ze^2}{|\hat{\mathbf{r}}_{e,2} - \hat{\mathbf{r}}_n|} + \frac{e^2}{|\hat{\mathbf{r}}_{e,1} - \hat{\mathbf{r}}_{e,2}|}, \quad (2.1)$$

where $\hat{\mathbf{r}}_n$ and $\hat{\mathbf{p}}_n$ are the position and momentum (operators) of the nucleus, and $\hat{\mathbf{r}}_{e,i}$ and $\hat{\mathbf{p}}_{e,i}$ are the position and momentum (operators) of the electrons.

The center-of-mass motion can be separated from the internal dynamics of the atom [95] by introducing the center-of-mass coordinate

$$\hat{\mathbf{R}} = \frac{1}{M} (m_n \hat{\mathbf{r}}_n + m_e \hat{\mathbf{r}}_{e,1} + m_e \hat{\mathbf{r}}_{e,2}), \quad M = m_n + 2m_e \quad (2.2)$$

and the relative coordinates

$$\hat{\mathbf{r}}_i = \hat{\mathbf{r}}_{e,i} - \hat{\mathbf{r}}_n \quad (2.3)$$

together with their associated momenta $\hat{\mathbf{P}}$ and $\hat{\mathbf{p}}_i$. Using

$$\hat{\mathbf{p}}_n = \frac{m_n}{M} \hat{\mathbf{P}} - \hat{\mathbf{p}}_1 - \hat{\mathbf{p}}_2, \quad \hat{\mathbf{p}}_{e,i} = \frac{m_e}{M} \hat{\mathbf{P}} + \hat{\mathbf{p}}_i, \quad \mu = \frac{m_e m_n}{m_e + m_n}, \quad (2.4)$$

the Hamiltonian describing the internal degrees of freedom (i.e. neglecting the center-of-mass kinetic energy) can be written as

$$\hat{\mathbf{H}}_{\text{int}} = \frac{\hat{\mathbf{p}}_1^2}{2\mu} + \frac{\hat{\mathbf{p}}_2^2}{2\mu} - \frac{Ze^2}{|\hat{\mathbf{r}}_1|} - \frac{Ze^2}{|\hat{\mathbf{r}}_2|} + \frac{e^2}{|\hat{\mathbf{r}}_1 - \hat{\mathbf{r}}_2|} + \frac{\hat{\mathbf{p}}_1 \hat{\mathbf{p}}_2}{m_n}. \quad (2.5)$$

The *mass polarization term* $\hat{\mathbf{p}}_1 \hat{\mathbf{p}}_2 / m_n$ is a consequence of the fact that the center of mass is not identical with the position of the nucleus. Since the nuclear mass is much larger than the electron mass ($m_n / m_e \approx 7340$), this term, as well as the influence of the *reduced mass* μ , are small and can usually be neglected.

The reduced mass affects all levels of the helium atom in the same manner (as it amounts to using different atomic units) and can be taken into account by scaling their energies by a constant factor according to

$$E_\mu = \frac{\mu}{m_e} E_{m_e} \approx 0.99986 E_{m_e}, \quad (2.6)$$

$I_1(\text{a.u.})$	$\Delta E_{\text{rm}}(\text{a.u.})$	$\Delta E_{\text{mp}}(\text{a.u.})$	$\Delta E_{\text{r}}(\text{a.u.})$	$\Delta E_{\text{L}}(\text{a.u.})$
0.9037244	$1.239 \cdot 10^{-6}$	$2.18 \cdot 10^{-7}$	$2.56 \cdot 10^{-8}$	$6.11 \cdot 10^{-8}$

Table 2.1: Corrections to the first ionization potential of helium due to the reduced mass (ΔE_{rm}), mass polarization (ΔE_{mp}), relativistic contributions (ΔE_{r}), and the Lamb shift (ΔE_{L}) [96]. All quantities are given in atomic units, cf. [section 2.7](#).

$$\Rightarrow \Delta E_{\text{rm}} = E_{\mu} - E_{m_e} = E_{m_e} \left(\frac{\mu}{m_e} - 1 \right) \simeq -\frac{m_e}{m_n} E_{m_e}, \quad (2.7)$$

where E_{m_e} are the energies as obtained for infinite nuclear mass and E_{μ} includes the corrections due to the reduced mass [96]. The mass polarization term, on the other hand, depends on the correlation of the two electron momenta and influences all levels individually [97]. In first order perturbation theory the resulting energy correction is given by

$$\Delta E_{\text{mp}} = \frac{1}{m_n} \langle \Psi | \hat{\mathbf{p}}_1 \hat{\mathbf{p}}_2 | \Psi \rangle. \quad (2.8)$$

As an example, the energy corrections ΔE_{rm} and ΔE_{mp} to the first ionization potential I_1 of helium are given in [Table 2.1](#). For comparison we also show the contributions from relativistic corrections ΔE_{r} and the Lamb shift ΔE_{L} . Note that since the expectation value $\langle \hat{\mathbf{p}} \rangle$ is zero for bound states, ΔE_{mp} vanishes for (uncorrelated) wave functions $|\Psi\rangle$ which are described by a single Slater determinant.

Neglecting the effects of mass polarization and the reduced mass is equivalent to assuming *infinite* nuclear mass and leads to the Hamiltonian

$$\hat{\mathbf{H}}_0 = \frac{\hat{\mathbf{p}}_1^2}{2m_e} + \frac{\hat{\mathbf{p}}_2^2}{2m_e} - \frac{Ze^2}{r_1} - \frac{Ze^2}{r_2} + \frac{e^2}{|\hat{\mathbf{r}}_1 - \hat{\mathbf{r}}_2|}. \quad (2.9)$$

Due to the two-body interaction of the electrons the resulting time-independent Schrödinger equation

$$\hat{\mathbf{H}}_0 |\Psi\rangle = E |\Psi\rangle \quad (2.10)$$

is not separable and has no analytical solution. In other words, there is no complete set of commuting observables that diagonalizes the Hamiltonian.

2.2 Spin and symmetry

The Hamiltonian (2.9) does not take into account any relativistic effects, spin-orbit coupling, and spin-spin coupling. The operators are given by [96]

$$\hat{\mathbf{H}}_{\text{LS}_i} = \frac{Ze^2}{2m_e^2 c^2} \frac{\hat{\mathbf{L}}_i \cdot \hat{\mathbf{S}}_i}{r_i^3}, \quad (2.11)$$

$$\hat{\mathbf{H}}_{\text{SS}} = \frac{\mu_0}{4\pi} \frac{4\mu_B^2}{\hbar^2} \left[\frac{\hat{\mathbf{S}}_1 \cdot \hat{\mathbf{S}}_2}{r_{12}^3} - 3 \frac{(\hat{\mathbf{S}}_1 \cdot \hat{\mathbf{r}}_{12})(\hat{\mathbf{S}}_2 \cdot \hat{\mathbf{r}}_{12})}{r_{12}^5} \right]. \quad (2.12)$$

Neglecting these terms is a reasonable approximation for light atoms such as helium since the overall correction scales with Z^4 . Even though the Hamilton operator itself is spin-independent, the influence of the electron spin is taken into account indirectly by the requirements of the *Pauli exclusion principle*.

The Hamiltonian (2.9) commutes with the permutation operator \hat{P}_{12} , which is defined by

$$\hat{P}_{12}\Psi(\mathbf{r}_1, \mathbf{r}_2) := \Psi(\mathbf{r}_2, \mathbf{r}_1), \quad (2.13)$$

and has eigenstates that are either symmetric ($P = 0$) or antisymmetric ($P = 1$) under exchange of the two electrons,

$$\hat{P}_{12}\Psi(\mathbf{r}_1, \mathbf{r}_2) = (-1)^P \Psi(\mathbf{r}_1, \mathbf{r}_2). \quad (2.14)$$

Consequently, the Hamiltonian can be diagonalized simultaneously with the permutation operator, and its eigenstates are either symmetric or antisymmetric

$$\hat{P}_{12}\Psi_s(\mathbf{r}_1, \mathbf{r}_2) = \Psi_s(\mathbf{r}_1, \mathbf{r}_2) \quad (2.15)$$

$$\hat{P}_{12}\Psi_{\text{as}}(\mathbf{r}_1, \mathbf{r}_2) = -\Psi_{\text{as}}(\mathbf{r}_1, \mathbf{r}_2). \quad (2.16)$$

The Pauli principle demands that the total wave function of the electrons has to be antisymmetric. We construct the states of the system as products of spatial and spin functions, such that space-symmetric wave functions require antisymmetric singlet spin states ($S = 0$), whereas antisymmetric spatial wave functions require symmetric triplet spin states ($S = 1$) (see [98] for details). Consequently, the two possible solutions are

$$|\Phi_p\rangle = |\Psi_s\rangle \otimes \frac{1}{\sqrt{2}} (|\uparrow\downarrow\rangle - |\downarrow\uparrow\rangle) \quad (2.17)$$

and

$$|\Phi_o\rangle = |\Psi_{\text{as}}\rangle \otimes \begin{cases} |\uparrow\uparrow\rangle \\ \frac{1}{\sqrt{2}} (|\uparrow\downarrow\rangle + |\downarrow\uparrow\rangle) \\ |\downarrow\downarrow\rangle \end{cases}. \quad (2.18)$$

The states described by space-symmetric wave functions (2.17) are called *para* states, while those corresponding to space-antisymmetric wave functions (2.18) are referred to as *ortho* states. When treating the interaction with a time-dependent laser field in electric dipole approximation (and thus neglecting magnetic fields), the Hamilton operator is still spin-independent, cf. (2.41) and (2.33). Radiative transitions between single and triplet spin states (*intercombination*) are therefore negligible. As a consequence the total spin is conserved and the spatial wave function is either symmetric or antisymmetric for all times.

The ground state wave function of helium is space-symmetric (and therefore a spin-singlet, $S = 0$) because a configuration in which both electrons occupy the $1s$ state is not possible for $S = 1$ due to the Pauli principle. As we simulate the interaction of laser pulses with helium atoms that are initially in the ground state, we deal solely with space-symmetric wave functions in this work.

2.3 Classification of levels

If the Hamiltonian (2.9) contained only the one-body interaction terms, it would be possible to uniquely characterize all levels of the helium atom by an (anti-)symmetrized product of single particle states (e.g. $|1s\rangle_1|1s\rangle_2$ for the ground state, $|1s\rangle_1|2s\rangle_2$ and $|1s\rangle_1|2p\rangle_2$ for the first excited states, ...). This simple picture is disturbed by the two-body interaction. However, a large part of the electron-electron interaction can be treated by employing a *mean field* potential which retains the independence of the electrons and formally allows the same classification as outlined above.¹ This approach works well for the helium bound states, for instance, but completely fails for *doubly excited states* where both electrons are excited.

The residual two-body interaction that cannot be included in mean single-particle potentials is referred to as (true) *electron correlation* and is of great interest in ongoing research. A large part of this work is dedicated to studying its effects.

Although the Hamiltonian (2.5) is not separable and consequently does not support a complete set of commuting observables, there are nonetheless some operators that commute with it, such that the eigenstates of the Hamiltonian can be labeled by the eigenvalues of these operators. Specifically, the operators are the (squared) total orbital angular momentum $\hat{\mathbf{L}}^2$ and the total spin $\hat{\mathbf{S}}^2$, given by

$$\hat{\mathbf{L}} = \hat{\mathbf{L}}_1 + \hat{\mathbf{L}}_2, \quad \hat{\mathbf{S}} = \hat{\mathbf{S}}_1 + \hat{\mathbf{S}}_2, \quad (2.19)$$

and the parity operator $\hat{\Pi}$, which plays an important role in connection with the selection rules for electromagnetic transitions (see section 3.4.2), defined by

$$\hat{\Pi}\Psi(\mathbf{r}_1, \mathbf{r}_2) = \Psi(-\mathbf{r}_1, -\mathbf{r}_2). \quad (2.20)$$

¹ Refer to e.g. [95] for a detailed description.

The eigenfunctions of the parity operator fulfill

$$\hat{\Pi}\Psi(\mathbf{r}_1, \mathbf{r}_2) = (-1)^\pi\Psi(\mathbf{r}_1, \mathbf{r}_2), \quad (2.21)$$

with $\pi = 0$ signifying *even* parity and $\pi = 1$ signifying *odd* parity.

As these three operators commute with the Hamiltonian (2.9),

$$[\hat{\mathbf{L}}^2, \hat{\mathbf{H}}] = [\hat{\mathbf{S}}^2, \hat{\mathbf{H}}] = [\hat{\Pi}, \hat{\mathbf{H}}] = 0, \quad (2.22)$$

they are constants of motion and all eigenstates of the Hamiltonian (2.9) can be classified by their associated quantum numbers. The states are therefore labeled by

$$^{2S+1}L^\pi, \quad (2.23)$$

where $2S + 1$ gives the *spin multiplicity* of the level, $L = S, P, D, F, \dots$ gives the total angular momentum, and $\pi = e$ ($\pi = o$) signifies even (odd) parity. The parity of a given configuration is directly related to the single-particle orbital angular momentum quantum numbers l_i , resulting in odd parity if $l_1 + l_2$ is odd and vice versa for even parity. This also holds for configuration mixing, where l_1 and l_2 are not well-defined, because only states with the same parity can be combined if (2.21) has to be fulfilled (see section 3.4.1) [95, 99].

2.4 Spectral properties

As pointed out above, spin-orbit and spin-spin interactions can be neglected for helium. Consequently, the spectrum consists of two almost completely independent systems of levels. In addition, intercombinations (i.e. light-induced transitions between those two level systems) are forbidden in the electric dipole approximation (and thus strongly suppressed in reality). For that reason it is common to speak about two different species of helium, *parahelium* and *orthohelium* (see figure 2.1).

Note that the singly excited states in Fig. 2.1 converge to the first ionization threshold, which is given by the ground state ($|1s\rangle$) energy of the singly charged positive helium ion He^+ ,

$$E_{\text{He}^+,n} = -\frac{Z^2}{2n^2}, \quad (2.24)$$

with $Z = 2$. The ground state energy of the helium atom is about $E_0 = -79.01$ eV (see chapter 7), the first ionization potential is $I_1 = -E_0 + E_{\text{He}^+,1} = 24.59$ eV, and the second ionization potential is $I_2 = -E_{\text{He}^+,1} = 2$ a.u. = 54.42 eV.

The *doubly excited states* on the other hand form *infinitely many* (perturbed) Rydberg series that are embedded in the single continua and converge to the ionization thresholds $I_{1,n}$ which are characterized by the excited state n of the remaining inner electron. Accordingly, they form *resonances* which can decay by *auto-ionization* due to energy transfer between the two electrons (see chapter 7).

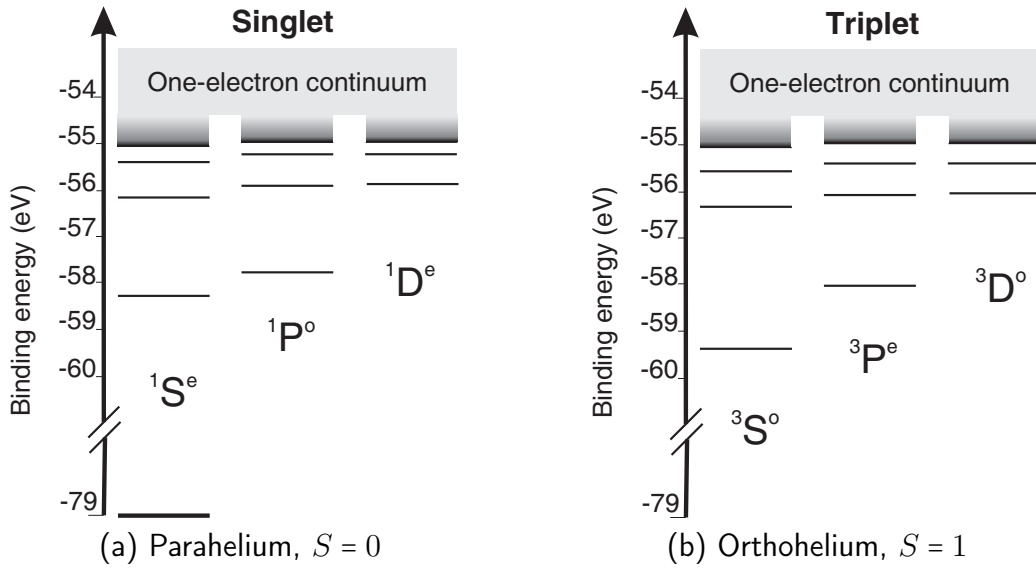


Figure 2.1: Level scheme for the S , P , and D bound states of helium for $S = 0$ and $S = 1$.

For instance, a ${}^1P^o$ $|2s2p\rangle$ state decays when one electron relaxes to the $\text{He}^+(1s)$ ground state, transferring the additional energy to the other electron which is then ejected. The lifetimes of the doubly excited states are therefore determined by the strength of their coupling to the continuum.

Thus, even though it is the simplest many-electron atom, the helium atom exhibits a complex spectral structure which gets more complicated with increasing (double) excitation [100]. Accurate results for bound-states can be obtained with the help of Hartree-Fock methods [101], i.e. by effective single-particle calculations. Nevertheless, these methods fail in the case of doubly excited states where electron correlation becomes more important and the full two-body interaction has to be taken into account.

2.5 Interaction with electromagnetic radiation

The non-relativistic interaction of a single free electron (charge $-e$) with an electromagnetic field is given by the gauge-dependent *minimal-coupling* Hamiltonian

$$\hat{H}_{\text{mc}} = \frac{[\hat{\mathbf{p}} + \frac{e}{c}\mathbf{A}(\hat{\mathbf{r}}, t)]^2}{2m} - e\Phi(\hat{\mathbf{r}}, t) \quad (2.25)$$

where the canonical momentum is modified by an additional term $\hat{\mathbf{p}} \rightarrow \hat{\mathbf{p}} + \frac{e}{c}\mathbf{A}(\hat{\mathbf{r}}, t)$. Physical observables are of course gauge-independent.

2.5.1 Semi-classical approximation

The quantized nature of the electromagnetic fields can be neglected for fields containing many photons, such as produced by lasers. For coherent fields, the potentials $\mathbf{A}(\mathbf{r}, t)$ and $\Phi(\mathbf{r}, t)$ can be inserted in the Hamiltonian (2.25) as real functions which are related to the physical fields (in cgs-units) by

$$\mathbf{B} = \nabla \times \mathbf{A}, \quad \mathbf{E} = -\nabla\Phi - \frac{1}{c} \frac{\partial \mathbf{A}}{\partial t}. \quad (2.26)$$

The Hamiltonian (2.25) then describes the *semi-classical* interaction of an electron with an external electromagnetic field. Note that the attribute “semi-classical” refers to the neglect of quantization effects of the electromagnetic field. The atom is described fully quantum-mechanically.

In radiation gauge (also called Coulomb gauge or transverse gauge)

$$\nabla \cdot \mathbf{A} = 0 \Leftrightarrow [\hat{\mathbf{p}}, \mathbf{A}] = 0 \quad (2.27)$$

$$\Phi(\hat{\mathbf{r}}, t) = 0, \quad (2.28)$$

Eq. 2.25 becomes

$$\hat{\mathbf{H}}_{\text{mc}} = \frac{\hat{\mathbf{p}}^2}{2m_e} + \frac{e}{m_e c} \hat{\mathbf{p}} \mathbf{A}(\hat{\mathbf{r}}, t) + \frac{e^2}{2m_e c^2} \mathbf{A}^2(\hat{\mathbf{r}}, t) := \hat{\mathbf{H}}_{\text{kin}} + \hat{\mathbf{H}}_{\text{em}}, \quad (2.29)$$

where the interaction with the electromagnetic field is described by the term

$$\hat{\mathbf{H}}_{\text{em}} = \frac{e}{m_e c} \hat{\mathbf{p}} \mathbf{A}(\hat{\mathbf{r}}, t) + \frac{e^2}{2m_e c^2} \mathbf{A}^2(\hat{\mathbf{r}}, t). \quad (2.30)$$

2.5.2 Dipole approximation

For a monochromatic electromagnetic wave the vector potential $\mathbf{A}(\hat{\mathbf{r}}, t)$ may be written as

$$\mathbf{A}(\hat{\mathbf{r}}_0 + \hat{\mathbf{r}}, t) = \mathbf{A}(t) \frac{1}{2} \exp[i\mathbf{k}(\hat{\mathbf{r}}_0 + \hat{\mathbf{r}})] + c.c., \quad (2.31)$$

where we choose $\hat{\mathbf{r}}_0 = 0$ in the following. In the *dipole approximation*, this reduces to

$$\mathbf{A}(\hat{\mathbf{r}}, t) = \mathbf{A}(t) \frac{1}{2} (1 + i\mathbf{k}\hat{\mathbf{r}} + \dots) + c.c. \approx \mathbf{A}(t). \quad (2.32)$$

This approximation is justified when the wavelength of the radiation is much larger than the distance over which the photon absorption takes place. This only happens close to the nucleus, where momentum and energy conservation can be fulfilled by imparting a recoil momentum to the nucleus, such that the dipole approximation is valid even when the final wave function spreads over regions larger than the field wavelength. Since the vector potential becomes independent of the spatial

coordinate the dipole approximation also implies the neglect of magnetic fields which is justified when the field strengths are not too high,²

Velocity Gauge

Employing the dipole approximation to (2.30) gives the Hamiltonian of the electron-field interaction in the so-called *velocity gauge*

$$\hat{\mathbf{H}}_{\text{em}}^{\text{v}} = \frac{e}{m_e c} \hat{\mathbf{p}} \mathbf{A}(t) + \frac{e^2}{2m_e c^2} \mathbf{A}^2(t) \quad (2.33)$$

and the corresponding time-dependent Schrödinger equation (TDSE) becomes

$$i\hbar \frac{\partial}{\partial t} |\Psi_{\text{v}}\rangle = (\hat{\mathbf{H}}_{\text{kin}} + \hat{\mathbf{H}}_{\text{em}}^{\text{v}}) |\Psi_{\text{v}}\rangle. \quad (2.34)$$

The quadratic term \mathbf{A}^2 can be removed by including a global phase factor, given by

$$\exp\left(\frac{ie^2}{2\hbar m_e c^2} \int_{-\infty}^t \mathbf{A}^2(t') dt'\right), \quad (2.35)$$

in the wave function, which does not change any physical observables and yields

$$\hat{\mathbf{H}}_{\text{em}}^{\text{v}} = \frac{e}{m_e c} \hat{\mathbf{p}} \mathbf{A}(t). \quad (2.36)$$

Length Gauge

A new wave function $|\Psi_1\rangle$ can be defined by the unitary *Göppert-Mayer transformation*³ [105, 106]

$$|\Psi_1\rangle = \hat{\mathbf{T}} |\Psi_{\text{v}}\rangle = \exp\left(+\frac{ie}{\hbar c} \mathbf{A}(t) \hat{\mathbf{r}}\right) |\Psi_{\text{v}}\rangle \quad (2.37)$$

and its inverse

$$|\Psi_{\text{v}}\rangle = \hat{\mathbf{T}}^\dagger |\Psi_1\rangle = \exp\left(-\frac{ie}{\hbar c} \mathbf{A}(t) \hat{\mathbf{r}}\right) |\Psi_1\rangle. \quad (2.38)$$

Substituting (2.38) into (2.34) gives

$$i\hbar \frac{\partial}{\partial t} \Psi_1(\mathbf{r}, t) = \left(\frac{\hat{\mathbf{p}}^2}{2m_e} + e\hat{\mathbf{r}}\mathbf{E}(t)\right) \Psi_1(\mathbf{r}, t), \quad (2.39)$$

² Thus, the laser intensities should also stay low enough such that the electron does not reach relativistic speeds (around 10^{16} W/cm² for laser wavelengths of 800 nm [102, 103]), so that Lorentz forces and interactions of the magnetic field with the electron spin can be neglected.

³ This class of transformations is sometimes called *gauge transformations of the second kind* [104].

and accordingly

$$i\hbar \frac{\partial}{\partial t} |\Psi_1\rangle = (\hat{\mathbf{H}}_{\text{kin}} + \hat{\mathbf{H}}_{\text{em}}^1) |\Psi_1\rangle. \quad (2.40)$$

In *length gauge* the contribution of the field interaction to the Hamiltonian thus reads

$$\hat{\mathbf{H}}_{\text{em}}^1 = e\hat{\mathbf{r}}\mathbf{E}(t). \quad (2.41)$$

Note that the result above can also be derived by directly transforming the Hamiltonian according to

$$\hat{\mathbf{H}}_{\text{kin}} + \hat{\mathbf{H}}_{\text{em}}^1 = \hat{\mathbf{T}}(t) (\hat{\mathbf{H}}_{\text{kin}} + \hat{\mathbf{H}}_{\text{em}}^v) \hat{\mathbf{T}}^\dagger(t) + i\hbar \left[\frac{d\hat{\mathbf{T}}(t)}{dt} \right] \hat{\mathbf{T}}^\dagger(t). \quad (2.42)$$

In principle, the expressions (2.40) and (2.34) are equivalent, and all physical observables give the same result in the two gauges. However, in practice, length and velocity gauge show different behavior with respect to basis truncations, especially when the wave function is represented in the angular momentum basis [107], and discretization errors which are an unavoidable consequence of *computational* implementations. Hence, comparison of the results obtained for the two gauges offers a test for numerical convergence.

A detailed treatment of gauge transformations in QED and related problems can be found in [106].

2.6 Resulting Hamiltonian

With the results from section 2.1 and 2.5 the full Hamiltonian for the semi-classical interaction of a non-relativistic helium atom (with infinite nuclear mass) with an electromagnetic field reads

$$\hat{\mathbf{H}}^1 = \frac{\hat{\mathbf{p}}_1^2}{2m_e} + \frac{\hat{\mathbf{p}}_2^2}{2m_e} - \frac{Ze^2}{r_1} - \frac{Ze^2}{r_2} + \frac{e^2}{|\hat{\mathbf{r}}_1 - \hat{\mathbf{r}}_2|} + e\mathbf{E}(t)(\hat{\mathbf{r}}_1 + \hat{\mathbf{r}}_2) \quad (2.43)$$

in length gauge and

$$\hat{\mathbf{H}}^v = \frac{\hat{\mathbf{p}}_1^2}{2m_e} + \frac{\hat{\mathbf{p}}_2^2}{2m_e} - \frac{Ze^2}{r_1} - \frac{Ze^2}{r_2} + \frac{e^2}{|\hat{\mathbf{r}}_1 - \hat{\mathbf{r}}_2|} + \frac{e}{m_e c} \mathbf{A}(t)(\hat{\mathbf{p}}_1 + \hat{\mathbf{p}}_2) \quad (2.44)$$

in velocity gauge.

2.7 Atomic units

For simplicity we will use *atomic units* in all subsequent chapters, which are obtained by setting

$$m_e = e = \hbar = 4\pi\epsilon_0 \stackrel{!}{=} 1. \quad (2.45)$$

For improved readability, we will sometimes show constants that are equal to one in atomic units, e.g. when giving the energy $\hbar\omega$ of a photon.

This is particularly useful for atomic physics because the basic units are well adjusted to the atomic scale. For example, 1 a.u. corresponds to

- a length of $a_0 = 5.29 \cdot 10^{-11}$ m (one Bohr radius),
- an energy of 27.21 eV (twice the ionization potential of hydrogen), and to
- a time of 24.19 as (the time scale of electronic motion in atoms).

The speed of light in atomic units is given by $c = \alpha^{-1} \approx 137$ a.u., where α is the fine structure constant. [Table 2.2](#) shows the conversion factors of some basic quantities into atomic units.

Quantity (1 a.u.)	Symbol	Value in SI units
charge	e	$1.602176487(40) \cdot 10^{-19}$ C
mass	m_e	$9.10938215(45) \cdot 10^{-31}$ kg
action	\hbar	$1.054571628(53) \cdot 10^{-34}$ J s
length	a_0	$0.52917720859(36) \cdot 10^{-10}$ m
energy	E_h	$4.35974394(22) \cdot 10^{-18}$ J
time	\hbar/E_h	$2.418884326505(16) \cdot 10^{-17}$ s
force	E_h/a_0	$8.23872206(41) \cdot 10^{-8}$ N
velocity	$a_0 E_h/\hbar$	$2.1876912541(15) \cdot 10^6$ m s ⁻¹
momentum	\hbar/a_0	$1.992851565(99) \cdot 10^{-24}$ kg m s ⁻¹
current	$e E_h/\hbar$	$6.62361763(17) \cdot 10^{-3}$ A
charge density	e/a_0^3	$1.081202300(27) \cdot 10^{12}$ C m ⁻³
electric potential	E_h/e	27.21138386(68) V
electric field	E_h/ea_0	$5.14220632(13) \cdot 10^{11}$ V m ⁻¹
electric field gradient	E_h/ea_0^2	$9.71736166(24) \cdot 10^{21}$ V m ⁻²
electric dipole moment	ea_0	$8.47835281(21) \cdot 10^{-30}$ C
electric quadrupole moment	ea_0^2	$4.48655107(11) \cdot 10^{-40}$ Cm ²

Table 2.2: Conversion factors for some basic quantities into atomic units [108].

Part I
Method

3 Time-dependent close coupling method

In order to simulate the interaction of laser pulses with the helium atom, we solve the time-dependent Schrödinger equation (TDSE)

$$i \frac{\partial}{\partial t} |\Psi(t)\rangle = \hat{\mathbf{H}} |\Psi(t)\rangle. \quad (3.1)$$

The wave function $|\Psi(t)\rangle$ is an element of a six-dimensional Hilbert space (three spatial degrees of freedom for each electron). In addition, it explicitly depends on time t .

To solve the TDSE, we employ the time-dependent close coupling (TDCC) method [7, 43, 44]. The basic idea of this approach is to expand the four angular degrees of freedom in the basis $|l_1 l_2 LM\rangle$ of coupled angular momenta. Here, L is associated with the total angular momentum, M gives its projection on the z -axis, and l_1 and l_2 give the single-electron angular momenta. The coupled angular basis functions are defined as

$$|l_1 l_2 LM\rangle = \sum_{m_1, m_2} |l_1 m_1 l_2 m_2\rangle \langle l_1 m_1 l_2 m_2 | l_1 l_2 LM\rangle, \quad (3.2)$$

where m_1 and m_2 are the z -projections of the individual angular momenta, while $\langle l_1 m_1 l_2 m_2 | l_1 l_2 LM\rangle$ are the Clebsch-Gordan coefficients. For basis functions of the coupled basis, L , M , l_1 , and l_2 are good quantum numbers, whereas m_1 and m_2 are not. This basis is well adapted to the problem at hand, as the field-free Hamiltonian displays spherical symmetry. Therefore, both L and M remain good quantum numbers. In linearly polarized laser fields, the spherical symmetry is reduced to cylindrical symmetry, such that only M is conserved. This effectively removes one degree of freedom from the calculation, strongly reducing the computational effort. The wave function is then represented as

$$|\Psi(t)\rangle = \sum_{L, M} \sum_{l_1, l_2} |\chi_{l_1, l_2}^{LM}(t)\rangle \otimes |l_1 l_2 LM\rangle, \quad (3.3)$$

where the $|\chi_{l_1, l_2}^{LM}(t)\rangle$ are the (partial) wave functions in radial space. This expansion is thus also called a *partial wave expansion* of the wave function. In the following,

we use the explicit representation

$$\langle r_1 r_2 | \chi_{l_1, l_2}^{LM}(t) \rangle = \frac{R_{l_1, l_2}^{LM}(r_1, r_2, t)}{r_1 r_2} \quad (3.4)$$

of the partial waves in radial space. The projection of the angular momentum basis functions $|l_1 l_2 LM\rangle$ onto angular space $(\Omega_1, \Omega_2) \equiv (\theta_1, \varphi_1, \theta_2, \varphi_2)$ is given by the coupled spherical harmonics (sometimes referred to as bipolar spherical harmonics),

$$\begin{aligned} \langle \Omega_1 \Omega_2 | l_1 l_2 LM \rangle &= \mathcal{Y}_{l_1, l_2}^{LM}(\Omega_1, \Omega_2) = \\ &= \sum_{m_1, m_2} \langle l_1 m_1 l_2 m_2 | l_1 l_2 LM \rangle Y_{m_1}^{l_1}(\Omega_1) Y_{m_2}^{l_2}(\Omega_2), \end{aligned} \quad (3.5)$$

where $Y_m^l(\Omega) = \langle \Omega | lm \rangle$ are the ordinary spherical harmonics.

Inserting the partial wave expansion into (3.1) and multiplying by $\langle l'_1 l'_2 L' M' |$ leads to

$$i \frac{\partial}{\partial t} \frac{R_{l'_1, l'_2}^{L' M'}(r_1, r_2, t)}{r_1 r_2} = \sum_{L, M} \sum_{l_1, l_2} \langle l'_1 l'_2 L' M' | \hat{\mathbf{H}} | l_1 l_2 LM \rangle \frac{R_{l_1, l_2}^{LM}(r_1, r_2, t)}{r_1 r_2}. \quad (3.6)$$

The seven-dimensional Schrödinger equation is thus transformed to a set of *infinitely* many coupled partial differential equations in r_1 , r_2 and t . In practice, the partial wave expansion (3.3) only has to include those partial waves that are physically relevant for a given process.

As mentioned before, linearly polarized electromagnetic fields in the dipole approximation conserve cylindrical symmetry about their polarization axis, which we choose as the z -axis. This means that one degree of freedom is removed from the system, and M is a conserved quantum number. As we always use initial states with $M = 0$ (e.g. the helium ground state), we can restrict ourselves to basis states $|l_1 l_2 L 0\rangle$. Expressed in angular variables $(\Omega_1, \Omega_2) \equiv (\theta_1, \varphi_1, \theta_2, \varphi_2)$, this means that the wave function only depends on $\varphi_1 - \varphi_2$, but is independent of $\varphi_1 + \varphi_2$. This drastically reduces the numerical effort needed. In the following, we drop the label $M = 0$ from all further equations. A discussion of the general case $M \neq 0$ can be found in [103].

To evaluate equation (3.6), the matrix elements $\langle l'_1 l'_2 L' M' = 0 | \hat{\mathbf{H}} | l_1 l_2 LM = 0 \rangle$ are needed. We split the Hamilton operator $\hat{\mathbf{H}}$ into separate parts, with

$$\hat{\mathbf{H}} = \hat{\mathbf{H}}_0 + \hat{\mathbf{H}}_{\text{em}} = \hat{\mathbf{T}}_1 + \hat{\mathbf{T}}_2 + \hat{\mathbf{W}} + \hat{\mathbf{H}}_{\text{em},1} + \hat{\mathbf{H}}_{\text{em},2} \quad (3.7)$$

and

$$\hat{\mathbf{T}}_i = \frac{\hat{\mathbf{p}}_i^2}{2} - \frac{Z}{r_i}, \quad \hat{\mathbf{W}} = \frac{1}{|\hat{\mathbf{r}}_1 - \hat{\mathbf{r}}_2|} = \frac{1}{\hat{r}_{12}} \quad (3.8)$$

$$\hat{\mathbf{H}}_{\text{em},i}^l = \hat{\mathbf{r}}_i \cdot \mathbf{E}, \quad \hat{\mathbf{H}}_{\text{em},i}^v = \hat{\mathbf{p}}_i \cdot \mathbf{A} + \frac{1}{2} \mathbf{A}^2, \quad (3.9)$$

where the $\hat{\mathbf{T}}_i$ include the kinetic energies and the electron-nucleus interaction, $\hat{\mathbf{W}}$ describes the electron-electron interaction, and the $\hat{\mathbf{H}}_{\text{em},i}$ describe the electron-laser interaction in either length gauge or velocity gauge.

The following calculations are based on the angular momentum algebra techniques presented in [Appendix B](#).

3.1 Kinetic energy and electron-nucleus interaction

The kinetic energy and electron-nucleus interaction terms $\hat{\mathbf{T}}_i$ are one-body operators. In addition, they conserve the single-particle and total angular momenta, as the electron-nucleus interaction is spherically symmetric. The associated matrix elements are therefore diagonal in the angular momentum basis. We proceed in coordinate space, where

$$\hat{\mathbf{r}} \rightarrow \mathbf{r}, \hat{\mathbf{p}} \rightarrow -i\nabla \quad (3.10)$$

and use

$$\Delta_i = \frac{\partial^2}{\partial r_i^2} + \frac{2}{r_i} \frac{\partial}{\partial r_i} - \frac{\mathbf{L}_i^2}{r_i^2}. \quad (3.11)$$

We then get

$$\hat{\mathbf{T}}_i = -\frac{1}{2}\Delta_i - \frac{Z}{r_i} = -\frac{1}{2} \left(\frac{\partial^2}{\partial r_i^2} + \frac{2}{r_i} \frac{\partial}{\partial r_i} - \frac{\mathbf{L}_i^2}{r_i^2} \right) - \frac{Z}{r_i} \quad (3.12)$$

and with the help of

$$\left(\frac{\partial^2}{\partial r_i^2} + \frac{2}{r_i} \frac{\partial}{\partial r_i} \right) \frac{R_{l_1 l_2}^L}{r_i} = \frac{1}{r_i} \frac{\partial^2 R_{l_1 l_2}^L}{\partial r_i^2} \quad (3.13)$$

the matrix element reads

$$\langle l'_1 l'_2 L' 0 | \hat{\mathbf{T}}_i | l_1 l_2 L 0 \rangle \frac{R_{l_1 l_2}^L}{r_1 r_2} = \frac{1}{r_1 r_2} \left(-\frac{1}{2} \frac{\partial^2}{\partial r_i^2} + \frac{l_i(l_i+1)}{2r_i^2} - \frac{Z}{r_i} \right) R_{l_1 l_2}^L \delta_{LL'} \delta_{l_1 l'_1} \delta_{l_2 l'_2}. \quad (3.14)$$

3.2 Electron-electron interaction

The electron-electron interaction operator is spherically symmetric (under rotation of both particle momenta), and therefore conserves the total angular momentum L . Consequently, the matrix elements associated with it are diagonal in L, L' . Using the expansion of $1/r_{12}$ into (renormalized) spherical harmonics as defined in [\(B.39\)](#)

$$\begin{aligned} \frac{1}{r_{12}} &= \sum_{\lambda=0}^{\infty} \frac{4\pi}{2\lambda+1} \frac{r_{<}^{\lambda}}{r_{>}^{\lambda+1}} \sum_{q=-\lambda}^{\lambda} Y_q^{\lambda*}(\Omega_1) Y_q^{\lambda}(\Omega_2) \\ &= \sum_{\lambda=0}^{\infty} \frac{r_{<}^{\lambda}}{r_{>}^{\lambda+1}} \sum_{q=-\lambda}^{\lambda} (-1)^q C_{-q}^{(\lambda)}(\Omega_1) C_q^{(\lambda)}(\Omega_2) \end{aligned} \quad (3.15)$$

we can write the matrix element for the electron-electron interaction operator

$$\begin{aligned} \langle l'_1 l'_2 L' 0 | \hat{\mathbf{W}} | l_1 l_2 L 0 \rangle &= \langle l'_1 l'_2 L' 0 | \frac{1}{r_{12}} | l_1 l_2 L 0 \rangle = \\ &= \sum_{\lambda=0}^{\infty} \frac{r_{<}^{\lambda}}{r_{>}^{\lambda+1}} \sum_{q=-\lambda}^{\lambda} (-1)^q \langle l'_1 l'_2 L' 0 | C_{-q}^{(\lambda)}(\Omega_1) C_q^{(\lambda)}(\Omega_2) | l_1 l_2 L 0 \rangle. \end{aligned} \quad (3.16)$$

With the help of formula (B.28) for the scalar product of two tensor operators in their coupled basis we obtain

$$\begin{aligned} \sum_{q=-\lambda}^{\lambda} (-1)^q \langle l'_1 l'_2 L' 0 | C_{-q}^{(\lambda)}(\Omega_1) C_q^{(\lambda)}(\Omega_2) | l_1 l_2 L 0 \rangle = \\ (-1)^{L'+l_2+l_1} \langle l'_1 || C^{(\lambda)} || l_1 \rangle \langle l'_2 || C^{(\lambda)} || l_2 \rangle \begin{Bmatrix} l'_1 & l'_2 & L' \\ l_2 & l_1 & \lambda \end{Bmatrix} \delta_{LL'}. \end{aligned} \quad (3.17)$$

After evaluating the reduced matrix elements by virtue of (B.40) and reordering the 6j-symbol according to (B.33), inserting (3.17) in (3.16) gives

$$\begin{aligned} \langle l'_1 l'_2 L' 0 | \hat{\mathbf{W}} | l_1 l_2 L 0 \rangle &\equiv \sqrt{(2l_1+1)(2l'_1+1)(2l_2+1)(2l'_2+1)} \\ &\times \sum_{\lambda=0}^{\infty} (-1)^{L'+\lambda} \frac{r_{<}^{\lambda}}{r_{>}^{\lambda+1}} \begin{pmatrix} l_1 & \lambda & l'_1 \\ 0 & 0 & 0 \end{pmatrix} \begin{pmatrix} l_2 & \lambda & l'_2 \\ 0 & 0 & 0 \end{pmatrix} \begin{Bmatrix} L' & l'_2 & l'_1 \\ \lambda & l_1 & l_2 \end{Bmatrix} \delta_{LL'} =: W_{l_1, l_2, l'_1, l'_2}^L(r_1, r_2). \end{aligned} \quad (3.18)$$

Note that when implemented computationally, the sum over λ will be truncated at a certain λ_{\max} .

3.3 Electron-laser interaction

The electron-laser interaction operators (in dipole approximation) are one-particle operators. They do not conserve angular momentum, but obey the selection rules for dipole transitions. In the coupled angular momentum basis this means that only matrix elements where L and either l_1 or l_2 change by one unit are non-zero. In addition, the operator has odd parity and therefore only couples partial waves with opposite parity. These selection rules are independent of the gauge employed.

3.3.1 Length gauge

Writing the dipole operators $z_i = r_i \cos \theta_i$ for linearly polarized fields in spherical coordinates and expressing $\cos \theta_i$ by renormalized spherical harmonics (Racah-tensors), the matrix element for the laser interaction in length gauge takes the

form

$$\begin{aligned} \langle l'_1 l'_2 L' 0 | \hat{\mathbf{H}}_{\text{em}}^1 | l_1 l_2 L 0 \rangle &\equiv \langle l'_1 l'_2 L' 0 | E(t) (z_1 + z_2) | l_1 l_2 L 0 \rangle = \\ &E(t) \langle l'_1 l'_2 L' 0 | r_1 C_0^{(1)}(\Omega_1) + r_2 C_0^{(1)}(\Omega_2) | l_1 l_2 L 0 \rangle. \end{aligned} \quad (3.19)$$

To evaluate the expressions $\langle l'_1 l'_2 L' 0 | C_0^{(1)}(\Omega_i) | l_1 l_2 L 0 \rangle$ it is necessary to switch to the uncoupled basis $|l_1 m_1 l_2 m_2\rangle$

$$\begin{aligned} \langle l'_1 l'_2 L' 0 | C_0^{(1)}(\Omega_1) | l_1 l_2 L 0 \rangle &= \\ \sum_{\substack{m_1, m'_1 \\ m_2, m'_2}} \begin{bmatrix} l_1 & l_2 & L \\ m_1 & m_2 & 0 \end{bmatrix} \begin{bmatrix} l'_1 & l'_2 & L' \\ m'_1 & m'_2 & 0 \end{bmatrix} \langle l'_1 m'_1 l'_2 m'_2 | C_0^{(1)}(\Omega_1) | l_1 m_1 l_2 m_2 \rangle \end{aligned} \quad (3.20)$$

where the rectangular brackets represent Clebsch-Gordan (CG) coefficients which are related to the 3j-symbols (round brackets) as described in (B.6). The remaining matrix element can then be calculated with the help of the Wigner-Eckart theorem (B.37)

$$\begin{aligned} \langle l'_1 l'_2 m'_1 m'_2 | C_0^{(1)}(\Omega_1) | l_1 l_2 m_1 m_2 \rangle &= \begin{bmatrix} l_1 & 1 & l'_1 \\ m_1 & 0 & m'_1 \end{bmatrix} \frac{\langle l'_1 || C^{(1)} || l_1 \rangle}{\sqrt{2l'_1 + 1}} \delta_{l'_2 l_2} \delta_{m'_2 m_2} = \\ &(-1)^{l_1 - l'_1 + 1} \begin{bmatrix} 1 & l_1 & l'_1 \\ 0 & m_1 & m'_1 \end{bmatrix} \frac{\langle l'_1 || C^{(1)} || l_1 \rangle}{\sqrt{2l'_1 + 1}} \delta_{l'_2 l_2} \delta_{m'_2 m_2}. \end{aligned} \quad (3.21)$$

Note that the relation (B.14) has been used to change the ordering of the columns in the CG coefficient. Inserting (3.21) in (3.20) gives

$$\begin{aligned} \langle l'_1 l'_2 L' 0 | C_0^{(1)}(\Omega_1) | l_1 l_2 L 0 \rangle &= (-1)^{l_1 - l'_1 + 1} \frac{\langle l'_1 || C^{(1)} || l_1 \rangle}{\sqrt{2l'_1 + 1}} \delta_{l'_2 l_2} \\ &\times \sum_{\substack{m_1 \\ m'_1, m_2, m'_2}} \begin{bmatrix} 1 & l_1 & l'_1 \\ 0 & m_1 & m'_1 \end{bmatrix} \begin{bmatrix} l_1 & l_2 & L \\ m_1 & m_2 & 0 \end{bmatrix} \begin{bmatrix} l'_1 & l'_2 & L' \\ m'_1 & m'_2 & 0 \end{bmatrix}. \end{aligned} \quad (3.22)$$

Due to selection rules only one index in the sum (3.22) is independent, which then can be evaluated using the relation (B.34). The reduced matrix element can be again calculated with the help of (B.40), giving

$$\begin{aligned} \langle l'_1 l'_2 L' 0 | C_0^{(1)}(\Omega_1) | l_1 l_2 L 0 \rangle &= \\ &(-1)^{l_1 - l'_1 + 1} (-1)^{l_1 + l_2 + L' + 1} (-1)^{l'_1} \sqrt{(2l_1 + 1)(2l'_1 + 1)(2L + 1)} \\ &\times \begin{bmatrix} 1 & L & L' \\ 0 & 0 & 0 \end{bmatrix} \begin{Bmatrix} 1 & l_1 & l'_1 \\ l_2 & L' & L \end{Bmatrix} \begin{Bmatrix} l_1 & 1 & l'_1 \\ 0 & 0 & 0 \end{Bmatrix} \delta_{l'_2 l_2}. \end{aligned} \quad (3.23)$$

After collecting the phase factors, converting the CG coefficient to a 3j-symbol with the help of (B.19) and slightly changing the ordering in the 6j-symbol by virtue of (B.32) and (B.33) the matrix element (3.20) finally becomes

$$\begin{aligned} \langle l'_1 l'_2 L' 0 | C_0^{(1)}(\Omega_1) | l_1 l_2 L 0 \rangle &= (-1)^{l_2} \sqrt{(2l_1 + 1)(2l'_1 + 1)(2L + 1)(2L' + 1)} \\ &\times \begin{pmatrix} L & 1 & L' \\ 0 & 0 & 0 \end{pmatrix} \begin{pmatrix} l_1 & 1 & l'_1 \\ 0 & 0 & 0 \end{pmatrix} \begin{Bmatrix} l_1 & l_2 & L \\ L' & 1 & l'_1 \end{Bmatrix} \delta_{l'_2 l_2}. \end{aligned} \quad (3.24)$$

The calculation for $\langle l'_1 l'_2 L' 0 | C_0^{(1)}(\Omega_2) | l_1 l_2 L 0 \rangle$ can be done in complete analogy, leading to the same result with $l_1 \leftrightarrow l_2$ and $l'_1 \leftrightarrow l'_2$. Therefore the final result for the total matrix element (3.19) is (in agreement with [7])

$$\begin{aligned} \langle l'_1 l'_2 L' 0 | \hat{\mathbf{H}}_{\text{em}}^1 | l_1 l_2 L 0 \rangle &\equiv E(t) \sqrt{(2L + 1)(2L' + 1)} \begin{pmatrix} L & 1 & L' \\ 0 & 0 & 0 \end{pmatrix} \\ &\times \left[r_1 (-1)^{l_2} \sqrt{(2l_1 + 1)(2l'_1 + 1)} \begin{pmatrix} l_1 & 1 & l'_1 \\ 0 & 0 & 0 \end{pmatrix} \begin{Bmatrix} l_1 & l_2 & L \\ L' & 1 & l'_1 \end{Bmatrix} \delta_{l'_2 l_2} \right. \\ &+ \left. r_2 (-1)^{l_1} \sqrt{(2l_2 + 1)(2l'_2 + 1)} \begin{pmatrix} l_2 & 1 & l'_2 \\ 0 & 0 & 0 \end{pmatrix} \begin{Bmatrix} l_2 & l_1 & L \\ L' & 1 & l'_2 \end{Bmatrix} \delta_{l'_1 l_1} \right] \\ &=: V_{l_1, l_2, l'_1, l'_2}^{LL'}(r_1, r_2, t). \end{aligned} \quad (3.25)$$

3.3.2 Velocity gauge

In velocity gauge, the dipole operator for linearly polarized fields reads

$$-\frac{i}{c} A(t) \partial_{z_i} = -\frac{i}{c} A(t) \nabla_i \cdot \hat{\mathbf{z}}_i, \quad (3.26)$$

where the $A(t)^2$ term has been transformed away as described in section 2.5.2.

Expression (3.26) can be recast using

$$\nabla_i = \frac{1}{2} [\Delta_i, \mathbf{r}_i] \quad (3.27)$$

and yields

$$-\frac{i}{c} A(t) \partial_{z_i} = -\frac{i}{2c} A(t) [\Delta_i, r_i \cos \theta_i]. \quad (3.28)$$

With the help of (3.11) and (3.13) we can write⁴

$$[\Delta_i, r_i \cos \theta_i] \frac{R_{l_1 l_2}^L}{r_i} = \frac{2}{r_i} \left[\cos \theta_i \frac{\partial}{\partial r_i} + \frac{-\mathbf{L}_i^2 \cos \theta_i + \cos \theta_i \mathbf{L}_i^2}{2r_i} \right] R_{l_1 l_2}^L \quad (3.29)$$

⁴ Note that $[\mathbf{L}^2, \cos \theta] \neq 0$.

and hence we have to calculate the matrix elements

$$\begin{aligned}
\langle l'_1 l'_2 L' 0 | \frac{-\mathbf{L}_i^2 \cos \theta_i + \cos \theta_i \mathbf{L}_i^2}{2r_i} | l_1 l_2 L 0 \rangle &= \\
\langle l'_1 l'_2 L' 0 | \frac{-l'_i(l'_i + 1) + l_i(l_i + 1)}{2r_i} \cos \theta_i | l_1 l_2 L 0 \rangle &= \\
\langle l'_1 l'_2 L' 0 | \frac{-l'_i(l'_i + 1) + l_i(l_i + 1)}{2r_i} C_0^{(1)}(\Omega_i) | l_1 l_2 L 0 \rangle. & \quad (3.30)
\end{aligned}$$

Since we have already worked out $\langle l'_1 l'_2 L' 0 | C_0^{(1)}(\Omega_i) | l_1 l_2 L 0 \rangle$ in (3.24) we can write the matrix elements for the laser interaction in velocity gauge

$$\begin{aligned}
\langle l'_1 l'_2 L' 0 | \hat{\mathbf{H}}_{\text{em}}^v | l_1 l_2 L 0 \rangle &\equiv \langle l'_1 l'_2 L' 0 | -\frac{i}{c} A(t) (\partial_{z_1} + \partial_{z_2}) | l_1 l_2 L 0 \rangle \frac{R_{l_1 l_2}^L}{r_1 r_2} = -\frac{1}{r_1 r_2} \\
&\times \left[\left(\frac{\partial}{\partial r_1} - \frac{l'_1(l'_1 + 1) + l_1(l_1 + 1)}{2r_1} \right) (-1)^{l_2} c_1 \begin{pmatrix} l_1 & 1 & l'_1 \\ 0 & 0 & 0 \end{pmatrix} \begin{Bmatrix} l_1 & l_2 & L \\ L' & 1 & l'_1 \end{Bmatrix} \delta_{l'_2 l_2} \right. \\
&+ \left. \left(\frac{\partial}{\partial r_2} - \frac{l'_2(l'_2 + 1) + l_2(l_2 + 1)}{2r_2} \right) (-1)^{l_1} c_2 \begin{pmatrix} l_2 & 1 & l'_2 \\ 0 & 0 & 0 \end{pmatrix} \begin{Bmatrix} l_2 & l_1 & L \\ L' & 1 & l'_2 \end{Bmatrix} \delta_{l'_1 l_1} \right] \\
&\times \frac{i}{c} A(t) \sqrt{(2L + 1)(2L' + 1)} \begin{pmatrix} L & 1 & L' \\ 0 & 0 & 0 \end{pmatrix} R_{l_1 l_2}^L \\
&=: \frac{1}{r_1 r_2} V_{l_1, l_2, l'_1, l'_2}^{LL'}(r_1, r_2, t) R_{l_1 l_2}^L \quad (3.31)
\end{aligned}$$

with

$$c_i = \sqrt{(2l_i + 1)(2l'_i + 1)}. \quad (3.32)$$

3.4 Close-coupling equations

Upon substitution of the matrix elements for the different parts of the Hamilton operator (3.14), (3.16), (3.25) or (3.31) into (3.6) and multiplying by $(r_1 r_2)$ the final close-coupling equations are given by

$$\begin{aligned}
i \frac{\partial}{\partial t} R_{l_1, l_2}^L(r_1, r_2, t) &= T_{l_1, l_2}(r_1, r_2) R_{l_1, l_2}^L(r_1, r_2, t) \\
&+ \sum_{l'_1, l'_2, L'} V_{l_1, l_2, l'_1, l'_2}^{LL'}(r_1, r_2, t) R_{l_1, l_2}^{L'}(r_1, r_2, t) \\
&+ \sum_{l'_1, l'_2} W_{l_1, l_2, l'_1, l'_2}^L(r_1, r_2) R_{l_1, l_2}^L(r_1, r_2, t). \quad (3.33)
\end{aligned}$$

3.4.1 Symmetry considerations

In chapter 2.2 we pointed out that the eigenfunctions of the field-free Hamiltonian are also eigenfunctions of the permutation and parity operators. The electron-laser interaction conserves the permutation symmetry, but not the parity. Instead, the parity switches from even to odd and vice versa for each transition induced by the laser field. By exploiting these symmetries, the number of partial waves needed in the partial wave expansion (3.3) is drastically reduced (typically by a factor of two to three), which in turn strongly reduces the numerical effort needed to solve the close-coupling equations (3.33).

Permutation

As we restrict ourselves to spin singlet states $S = 0$, the spatial part of the wave function is always symmetric under exchange of the two particles. In the partial wave expansion, this means that

$$\Psi_s(\mathbf{r}_2, \mathbf{r}_1) = \Psi_s(\mathbf{r}_1, \mathbf{r}_2) \Leftrightarrow R_{l_2, l_1}^L(r_2, r_1, t) = (-1)^{L+l_1+l_2} R_{l_1, l_2}^L(r_1, r_2, t), \quad (3.34)$$

where the phase factor occurs as the coupled spherical harmonics are either symmetric or antisymmetric under exchange of their arguments. In linearly polarized laser fields, $L + l_1 + l_2$ is constant because of parity conservation, such that this phase factor is always one in our case. Thus, interchanging both the radial coordinates r_1, r_2 and the single-particle angular momenta l_1, l_2 leaves the wave function invariant. We exploit this property by storing the functions $R_{l_1, l_2}^L(r_1, r_2, t)$ only for $l_2 > l_1$. If $R_{l_1, l_2}^L(r_1, r_2, t)$ with $l_1 > l_2$ is needed, the required value is instead taken from $R_{l_2, l_1}^L(r_2, r_1, t)$. Another possible way to exploit this would be to use explicitly symmetrized basis functions.

Parity

Application of the parity operator to the spherical harmonics transforms them according to

$$\hat{\Pi} Y_m^l(\theta, \varphi) = Y_m^l(\pi - \theta, \pi + \varphi) = (-1)^l Y_m^l(\theta, \varphi), \quad (3.35)$$

such that the parity of the spherical harmonics only depends on the absolute value of the angular momentum L^2 , but not on its direction. The coupled angular momentum basis conserves the single-particle angular momenta (i.e. l_1, l_2 remain good quantum numbers). Consequently, the parity of the coupled spherical harmonics is given by

$$\hat{\Pi} \mathcal{Y}_{l_1, l_2}^{LM}(\Omega_1, \Omega_2) = (-1)^{l_1+l_2} \mathcal{Y}_{l_1, l_2}^{LM}(\Omega_1, \Omega_2). \quad (3.36)$$

Taking into account the parity selection rules induced by the dipole operator leads to a significant reduction of the angular momentum basis functions that need to be used in the partial wave expansion, cf. section 3.4.2.

3.4.2 Selection rules

As mentioned previously, the field-free Hamiltonian $\hat{\mathbf{H}}_0$ conserves both total angular momentum and parity. The electron-laser interaction $V_{l_1, l_2, l'_1, l'_2}^{L, L'}$ (in either gauge) couples l_1, l_2 and L , but only for states that fulfill the *parity selection rules*, cf. (B.17)

$$l_1 = l'_1 \pm 1 \quad \text{and} \quad L = L' \pm 1 \quad (3.37)$$

or

$$l_2 = l'_2 \pm 1 \quad \text{and} \quad L = L' \pm 1. \quad (3.38)$$

This implies that when starting from the ground state with $^1S^e$, the states corresponding to each total angular momentum L must have parity $\pi = (-1)^L$, as each absorbed photon (i.e. unit of angular momentum) switches the parity. The partial wave expansion (3.3) therefore only needs to contain states with a given parity for any value of the total angular momentum L . Table 5.1 lists the first components of the partial wave expansion or alternatively, the reason why they are not needed in the computation.

4 Numerical methods

The use of time-dependent close-coupling, i.e. the expansion of the angular degrees of freedom in coupled spherical harmonics, does not introduce any approximations – the time-dependent close-coupling equations (3.33) are just one possible representation of the full Schrödinger equation. To solve these equations numerically, we introduce approximations to take care of both the radial degrees of freedom as well as the temporal propagation. The methods used are described in this chapter.

4.1 Radial discretization

The choice of the coupled angular momentum basis transforms four of the six spatial degrees of freedom from continuous variables to a discrete basis set, labeled by the angular momentum quantum numbers (l_1, l_2, L, M) . To be able to solve the resulting close-coupling equations (3.33), the remaining two radial degrees of freedom also have to be discretized, such that the operator $\hat{\mathbf{H}}$ can be represented by a matrix. While the choice of (coupled) angular momenta for the angular degrees of freedom is relatively straightforward because they fit the symmetry of the problem, the situation is more complex for the radial degrees. One common approach is the use of grid-based methods, where the value of the wave function is stored at a sequence of grid points and derivative operators are approximated by finite difference techniques. This has the favorable property that all operators are very sparse, i.e. operators that are local in space remain local in this representation, and derivative operators typically couple only a few adjacent grid points. This allows for efficient computation of the matrix-vector products representing the action of operators on a wave function. On the other hand, these approaches are typically not very accurate, i.e. require a high number of grid points to achieve converged results. Another common approach is the use of basis-set methods, where the wave function is represented by the coefficients of a (typically orthonormal) basis set $|\chi_i\rangle$. If the basis chosen is well adapted to the physical problem, this often requires much fewer basis functions than the number of grid points necessary in a grid-based approach. On the other hand, one has to calculate potentially complicated matrix elements $\langle\chi_i|\hat{\mathbf{O}}|\chi_j\rangle$ of the operators sandwiched between the basis functions. Additionally, the resulting matrix representations of the operators are often far from sparse, even for local operators such as potentials $V(x)$.

In order to obtain a matrix representation of the Hamiltonian that is both accurate and sparse, it is desirable to use a method that combines some of the features of both grid-based and basis-set approaches. One such approach is the *finite element discrete variable representation* (FEDVR), which, in turn, combines ideas from finite element approaches and the discrete variable representation.

4.1.1 Finite elements

The basic idea of *finite element* (FE) methods is to divide the underlying configuration space of a differential equation into small subdomains or finite elements. Typically, FE techniques are used to handle complex geometries – however, they are also useful for “simple” problems in one dimension (which is sufficient for our purposes). In our case, the radial variables r_i are split into finite elements with the FE boundaries

$$0 \leq r^{(1)} < r^{(2)} < \dots < r^{(N)} \leq r_{\max}. \quad (4.1)$$

Instead of using global basis functions, we expand the wave function in a basis of functions that are local to each finite element,

$$f_m^{(i)}(r), r \notin [r^{(i)}, r^{(i+1)}] \Rightarrow f_m^{(i)}(r) = 0 \quad \forall m. \quad (4.2)$$

In each finite element, we choose basis functions obtained from a *discrete variable representation* (DVR) approach, which also provides a prescription for calculating matrix elements. Apart from the basic idea of splitting space into smaller elements, we do not use the further features of FE methods. A more detailed treatment of the subject can be found in, e.g. [109].

4.1.2 Discrete variable representation

In this section we give a short introduction to the polynomial *discrete variable representation* (DVR), which is closely related to the well-known concept of the spectral (finite-basis) representation of wave functions. Following [110–113] we will outline the most important steps for one-dimensional problems in this section.

In coordinate space a wave function in its *spectral representation* (SR)

$$\langle x|\Psi\rangle = \sum_{m=1}^N \langle x|\Phi_m\rangle \langle \Phi_m|\Psi\rangle = \sum_{m=1}^N a_m \langle x|\Phi_m\rangle \quad (4.3)$$

is described by the expansion coefficients

$$a_m = \langle \Phi_m|\Psi\rangle = \int \langle \Phi_m|x\rangle \langle x|\Psi\rangle dx \quad (4.4)$$

in a given orthonormalized basis $\{|\Phi_m\rangle\}$ of the Hilbert space, where usually the basis is complete for $N \rightarrow \infty$. For $N \neq \infty$, this representation is also called a *finite*

basis representation (FBR). The basis functions are orthonormal and thus fulfill

$$\langle \Phi_m | \Phi_n \rangle = \int \langle \Phi_m | x \rangle \langle x | \Phi_n \rangle dx = \delta_{mn}. \quad (4.5)$$

Inserting this ansatz for the wave function in the time-independent Schrödinger equation gives

$$\sum_{m=1}^N \langle \Phi_n | \hat{\mathbf{H}} | \Phi_m \rangle a_m = \sum_{m=1}^N \hat{\mathbf{H}}_{nm} a_m = a_n E, \quad (4.6)$$

which is a matrix eigenvalue problem once the matrix elements $\hat{\mathbf{H}}_{nm} = \langle \Phi_n | \hat{\mathbf{H}} | \Phi_m \rangle$ have been calculated. Note that the coefficients a_n can be understood as variational parameters and as a consequence the solutions of (4.6) will always represent an upper bound to the true solution for $N \rightarrow \infty$. Thus, the SR is sometimes also called *variational basis representation* (VBR).

The idea behind the DVR is to choose a basis $\{|\Phi_m\rangle\}$ for which the overlap integrals in (4.5) can be evaluated *exactly* by numerical quadrature. In a polynomial DVR, these functions are polynomials up to order N , products of which can be integrated exactly by Gaussian quadrature of order N (see [Appendix A](#) for more details). Replacing the integral in (4.4) by its discrete approximation, we get

$$\tilde{a}_m = \sum_{j=1}^M w_j \langle \Phi_m | x_j \rangle \langle x_j | \Psi \rangle \quad (4.7)$$

with the spectral basis remaining orthonormal when using the quadrature,

$$\langle \Phi_m | \Phi_n \rangle = \sum_{j=1}^M w_j \langle \Phi_m | x_j \rangle \langle x_j | \Phi_n \rangle = \delta_{mn}. \quad (4.8)$$

The integrals are approximated with the help of the quadrature weights w_j . The wave function (4.3) then reads

$$\langle x | \Psi \rangle = \sum_{m=1}^N \tilde{a}_m \langle x | \Phi_m \rangle \simeq \sum_{m=1}^N \sum_{j=1}^M w_j \langle x | \Phi_m \rangle \langle \Phi_m | x_j \rangle \langle x_j | \Psi \rangle. \quad (4.9)$$

Note that consequently also matrix elements

$$\langle \Phi_m | \hat{\mathbf{V}} | \Phi_n \rangle = \int \Phi_m^*(x) V(x) \Phi_n(x) dx \simeq \sum_j w_j \Phi_m^*(x_j) V(x_j) \Phi_n(x_j) \quad (4.10)$$

are calculated approximately by grid based quadrature methods instead of continuous integration. In the DVR, this finite basis is transformed by a unitary transformation to a new basis $\{f_j(x)\}$. The functions $f_j(x)$ have the property that they are non-zero only at the quadrature point x_j , i.e.

$$f_j(x_i) = \frac{\delta_{ij}}{\sqrt{w_i}} \quad (4.11)$$

and in analogy to (4.3) and (4.8) they define an orthonormal basis (a rigorous proof can be found in [110]),

$$\langle f_i | f_j \rangle = \int f_i^*(x) f_j(x) dx \stackrel{!}{=} \sum_{m=1}^N w_m f_i^*(x_m) f_j(x_m) = \delta_{ij} \quad (4.12)$$

The DVR basis functions can be obtained from (note that the $\{\Phi_m\}$ do not form a *complete* basis if N is finite)

$$f_j(x) = \sqrt{w_j} \sum_{m=1}^N \langle x | \Phi_m \rangle \langle \Phi_m | x_j \rangle. \quad (4.13)$$

The wave function is then expressed as

$$\langle x | \Psi \rangle = \sum_{j=1}^N \langle x | f_j \rangle \langle f_j | \Psi \rangle = \sum_{j=1}^N \tilde{\Psi}_j f_j(x), \quad (4.14)$$

where the coefficients $\tilde{\Psi}_j = \langle f_j | \Psi \rangle$ are also directly connected to the values of the wave function at the grid points, $\tilde{\Psi}_j = \sqrt{w_j} \Psi(x_j)$. This is the reason that the DVR can be seen as a bridge between spectral basis methods and grid-based approaches – the coefficients of the basis functions f_j simultaneously give the values of the wave function at the grid points in coordinate space, which are chosen as the quadrature points of the underlying Gaussian quadrature.

A further consequence of this is that the coordinate operator is strictly diagonal in the DVR basis,

$$\langle f_i | \hat{x} | f_j \rangle = \delta_{ij} x_i. \quad (4.15)$$

Consequently, the functions $f_j(x)$ can be referred to as *coordinate eigenfunctions* because they depend only on the chosen quadrature and the corresponding mesh (which are, in turn, related to the corresponding equivalent finite-basis representation).

In a DVR the wave functions are thus represented by a complete and orthonormal set of basis functions that are uniquely related to the chosen grid and quadrature. Note that FBR and DVR are strictly equivalent (*isomorphic*) if the FBR consists of orthogonal polynomials, as we have chosen here [114, 115].

Therefore, a wave function in the DVR is effectively represented by an *interpolating polynomial*. For a given order this interpolating polynomial is unique [116] and we can express it without loss of generality by the Lagrange polynomials (A.11)

$$L_i(x) = \prod_{j \neq i} \frac{x - x_j}{x_i - x_j} \quad (4.16)$$

which fulfill

$$L_i(x_j) = \delta_{ij}. \quad (4.17)$$

As the representation is unique, i.e. the Lagrange polynomials form the only polynomial basis that fulfills (4.17), they are identical to the basis functions $f_j(x)$ (up to a factor $\sqrt{w_j}$). This is the reason why in many publications (following a series of papers by Baye *et al.* [117–119]) polynomial DVRs are referred to as Lagrange-mesh techniques. This notation emphasizes the two possible equivalent approaches to the DVR:

1. In the grid approach one chooses a quadrature and an according grid (usually given by the zeros of classical orthogonal polynomials). The DVR basis functions can then be expressed by Lagrange interpolating polynomials.
2. In the basis approach one selects a set of basis functions which imply a quadrature and constructs the DVR basis as in (4.13).

Potential matrix elements

A very attractive property of the DVR is that due to (4.11) and (4.15) the potential matrix elements are diagonal within quadrature accuracy

$$\langle f_i | \hat{V} | f_j \rangle \stackrel{!}{\simeq} V(x_i) \delta_{ij} \quad (4.18)$$

and thus equal to the potential evaluated at the grid points.

Note that the potential matrix elements are in general not calculated *exactly* by quadrature. The reason is that a N -point Gaussian quadrature just allows for an exact calculation of polynomial integrands of degree $2N - 1$ (see A.8 in Appendix A). Hence, assuming that all matrix elements of coordinate operators are diagonal is the *fundamental approximation* in DVR. In other words (referring to the isomorphic FBR) the quadrature is not exact for those components of $\hat{V}|\Phi_i\rangle$ (*aliasing terms*) that do not remain in the spectral basis [120]. In practice, those errors are removed *implicitly* by extending the basis size until numerical convergence is reached. However, the strict variational properties of (4.6) are lost in the DVR. A more detailed treatment of the problem is given in [114, 120].

Calculating derivatives

In the DVR basis the n -th derivative of a function $\Psi(x)$ is given by

$$\frac{\partial^n \Psi(x)}{\partial x^n} = \sum_{j=1}^N \tilde{\Psi}_j \frac{\partial^n f_j(x)}{\partial x^n}, \quad (4.19)$$

where the derivatives of the basis functions $\frac{\partial^n f_j(x)}{\partial x^n}$ have to be computed just once initially. If the n -th derivative is to be evaluated at the DVR points one gets

$$\frac{\partial^n \Psi(x_i)}{\partial x^n} = \sum_{j=1}^N \tilde{\Psi}_j \frac{\partial^n f_j}{\partial x^n}(x_i). \quad (4.20)$$

Multiplying both sides by $\sqrt{\omega_i}$ and using (4.14) then gives

$$\frac{\partial^n \tilde{\Psi}_i}{\partial x^n} = \sum_{j=1}^N \frac{\partial^n f_j}{\partial x^n}(x_i) \sqrt{\omega_i} \tilde{\Psi}_j := D_{ij} \tilde{\Psi}_j \quad (4.21)$$

which represents a matrix-vector multiplication. Thus, in a DVR basis derivatives are calculated by multiplying the vectors $\tilde{\Psi}_j$ by a differentiation matrix \mathbf{D} . Note that the matrix \mathbf{D} is full and hence the matrix-vector product is computationally expensive when the basis size is large.

4.1.3 Finite element discrete variable representation

In a finite element discrete variable representation (FEDVR or FEM-DVR) [121–124] the underlying configuration space of a problem is divided into elements in each of which the wave function is represented in a local DVR basis. Consequently, the main advantages of the two techniques are brought together:

- Since the DVR basis functions are only defined on *local* grids the kinetic energy matrix is not full as in the standard DVR approach (cf. Eq. 4.21) but consists of several blocks (one for each FE) which overlap at only one point (see Fig. 4.1 for a schematic diagram). Consequently, the matrix is sparse and matrix-vector products can be efficiently calculated when implemented computationally. This property also allows for a straight-forward way of *parallelization*. Nevertheless, it provides an accurate numerical expression of the derivatives [123].
- The potential matrix is diagonal, thus avoiding the need to calculate complex matrix elements as in SR or FBR methods.

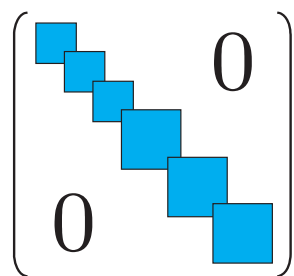


Figure 4.1: Schematic diagram of the kinetic matrix in a FEDVR basis. Due to the underlying division into finite elements the matrix consists of several blocks (one for each FE) which overlap at only one point. The remaining elements are zero.

Since the resulting grid is composed of many local sub-grids for each finite elements we have to use a quadrature where the end point in each node coincides with

the starting point for the neighboring finite element. This is necessary to impose continuity for the represented wave functions. For Gauss-Legendre quadratures the mesh points are given by the roots of the Legendre polynomials. As all these roots lie *inside* the sub-grids, we instead use a Gauss-Lobatto quadrature in each element (see [Appendix A](#)). In a Gauss-Lobatto quadrature, the first and last points are explicitly chosen, which leads to a slightly reduced accuracy. By choosing the first and last points to lie exactly at the FE boundaries, we can connect the last basis function in each element with the first function in the following element, forming a “bridge” function. Note that by employing a Gauss quadrature we implicitly choose a polynomial basis in the equivalent SR.

[Fig. 4.2](#) shows the first points of a typical FEDVR grid with eleven basis functions per finite element and the resulting grid spacing. The finite elements have a constant extension of 4 a.u.. The FEDVR parameters determine the maximum energy of electrons that can be well represented on the grid, which is around 4 a.u. for the parameters used here. Near the origin, the basis has to represent the Coulomb singularity of the nuclear potential, which is already done with good accuracy for the parameters given here (the ground state energy of the one-particle Hamiltonian has a relative error of $\approx 10^{-8}$). In order to increase the accuracy, it would be possible to use smaller finite elements close to the origin.

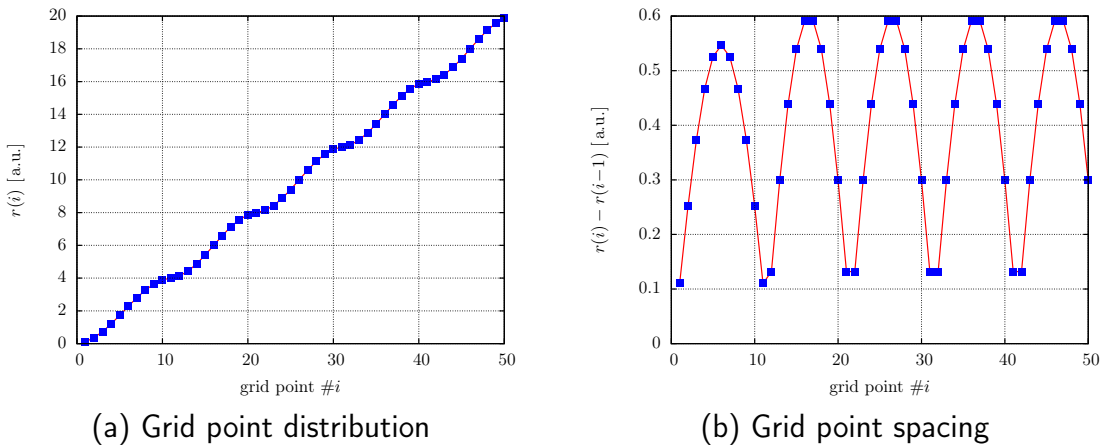


Figure 4.2: Mesh points of a typical FEDVR grid with eleven basis functions per finite element. The oscillatory structure in the grid spacing is a consequence of the Gauss-Lobatto quadrature.

From a Lagrange basis for each element

$$L_m^{(i)}(r) := \begin{cases} \prod_{j \neq m} \frac{r - r_j^{(i)}}{r_m^{(i)} - r_j^{(i)}} & r^{(i)} \leq r \leq r^{(i+1)}, 1 \leq i \leq N \\ 0 & \text{else} \end{cases} \quad (4.22)$$

we thus obtain (in agreement with [123]) the normalized FEDVR basis functions

$$f_m^{(i)}(r) := \begin{cases} \frac{L_1^{(i)}(r) + L_{M_i}^{(i-1)}(r)}{\sqrt{w_1^{(i)} + w_{M_i}^{(i-1)}}} & m = 1 \\ \frac{L_m^{(i)}(r)}{\sqrt{w_m^{(i)}}} & m = 2, \dots, M_i - 1 \\ \frac{L_{M_i}^{(i)}(r) + L_1^{(i+1)}(r)}{\sqrt{w_{M_i}^{(i)} + w_1^{(i+1)}}} & m = M_i \end{cases} \quad (4.23)$$

which fulfill the orthonormality relation

$$\langle f_m^{(i)} | f_n^{(j)} \rangle = \int f_m^{(i)*}(r) f_n^{(j)}(r) dr \simeq \sum_{l=1}^N \sum_{k=1}^{M_l} w_k^{(l)} f_m^{(i)*}(r_k^{(l)}) f_n^{(j)}(r_k^{(l)}) = \delta_{ij} \delta_{mn}. \quad (4.24)$$

In contrast to equation (4.12) the FEDVR basis functions are only approximately orthogonal because for each element the integrand in (4.24) is a polynomial of degree $(2M_i - 2)$ whereas the integration is only exact for polynomials up to degree $(2M_i - 3)$, cf. (A.15). This deficiency of FEDVR compared to DVR has little effect in practice since it can be compensated by increasing the number of basis functions.

Note that the definitions for the *bridge functions* (at $m = 1$ and $m = M_i$) in (4.23) ensure that $f_{M_i}^{(i)}(r) = f_1^{(i+1)}(r)$ and thus the continuity of the represented wave functions at the FE boundaries. In contrast, the first derivative is not continuous, since the finite elements have an overlap of only one grid point. As pointed out in [125] the matrix elements of the momentum operator (which is equivalent to the derivative operator) and the kinetic energy operator (which relies on the calculation of the second derivative) are nevertheless correctly defined. The integrals $\langle f_m^{(i)} | d/dr | f_n^{(j)} \rangle$ for the first derivative operator can be directly calculated, while the second derivative integrals need to be performed by partial integration, such that only first derivatives remain to be evaluated.

In analogy to (4.14) a wave function $\Psi(r)$ can be written as

$$\Psi(r) = \sum_{j=1}^N \sum_{k=1}^{M_j} \tilde{\Psi}_k^{(j)} f_k^{(j)}(r) \quad (4.25)$$

and the scalar product of two wave functions in FEDVR representation is given by

$$\langle \varphi | \psi \rangle = \int \left(\sum_{i,k} \varphi_k^{(i)*} f_k^{(i)*}(r) \sum_{j,l} \psi_l^{(j)} f_l^{(j)}(r) \right) dr \simeq \sum_{i,k} \varphi_k^{(i)*} \psi_k^{(i)} \quad (4.26)$$

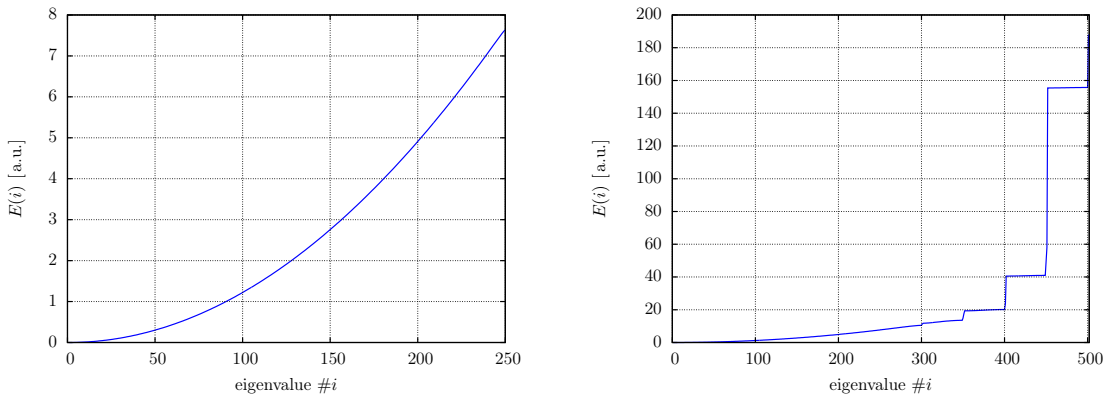
Consequently also the potential matrix elements are approximately diagonal, cf. (4.18)

$$\langle f_m^{(i)} | \hat{\mathbf{V}} | f_n^{(j)} \rangle \simeq V(x_i^{(m)}) \delta_{ij} \delta_{mn} \quad (4.27)$$

and derivatives are calculated by deriving the basis functions, cf. (4.19)

$$\frac{\partial^n \Psi(r)}{\partial r^n} = \sum_{j=1}^N \sum_{k=1}^{M_j} \tilde{\Psi}_k^{(j)} \frac{\partial^n f_k^{(j)}(r)}{\partial r^n}. \quad (4.28)$$

Fig. 4.3 shows the eigenvalues of the *discrete* Laplace operator on a FEDVR grid as obtained from (4.28). The step-like behavior for higher eigenvalues is a consequence of the division into finite elements. For physical problems one has to ensure that the occurring energies are in the region where the eigenvalues grow quadratically (and mimic the dispersion relation of a free particle).



(a) The first eigenenergies of a FEDVR grid grow quadratically.

(b) For higher energies the spectrum contains “unphysical” steps due to the division into finite elements.

Figure 4.3: Eigenvalues of the *discrete* Laplace operator on a FEDVR grid with $r_{\max} = 200$ and eleven basis functions per finite element. The finite elements have an extension of 4 a.u.. The resulting number of grid points is 501.

Boundary conditions

The FEDVR method, as outlined above, provides a flexible and accurate way of discretizing differential equations. In addition it is also necessary to properly implement the boundary conditions. In our case it is crucial to ensure

$$\Psi(r = 0) = \Psi(r_1^{(1)}) = 0 \quad (4.29)$$

due to the Coulomb singularity at the origin. This can be easily taken into account by omitting the first basis function $f_1^{(1)}$ in (4.25), i.e. by starting the first inner sum at $k = 2$.

Accordingly, keeping the last basis function at the outermost edge of the grid is equivalent to imposing open boundary conditions, since the derivative of $\Psi(r)$ at r_{\max} depends solely on $(M_N - 1)$ function values for $r < r_{\max}$. For bound states it is sufficient to choose r_{\max} such that

$$\Psi(r \rightarrow \infty) \simeq \Psi(r = r_{\max}) = 0 \quad (4.30)$$

can be fulfilled.

Note that if a wave packet reaches r_{\max} during propagation, it encounters “hard walls” in any case since $\Psi(r > r_{\max}) = 0$ is imposed implicitly due to the end of the grid. The resulting unphysical reflections have to be avoided by either extending the grid so that the boundary is never reached or by implementing *absorbing boundaries* (see [chapter 5](#)).

4.2 Temporal discretization

With the help of the time evolution operator

$$\hat{U}(t, t + \Delta t) = \mathcal{T} \exp\left(-i \int_t^{t+\Delta t} \hat{H}(t') dt'\right) \quad (4.31)$$

the solution of the TDSE for a given initial state $|\Psi(t_0)\rangle$ can formally be written as

$$|\Psi(t_0 + \Delta t)\rangle = \hat{U}(t_0, t_0 + \Delta t) |\Psi(t_0)\rangle = \mathcal{T} \exp\left(-i \int_{t_0}^{t_0+\Delta t} \hat{H}(t') dt'\right) |\Psi(t_0)\rangle \quad (4.32)$$

where \mathcal{T} denotes the time-ordering operator for the exponential with non-commuting argument ($[\hat{H}(t_1), \hat{H}(t_2)] \neq 0$).

Direct evaluation of (4.32) is cumbersome since the time evolution operator has to be expanded in a Dyson series to represent the time-ordering. However, for small time intervals Δt the Hamiltonian can be assumed to be constant, thus giving

$$\hat{U}(t, t + \Delta t) \simeq \exp(-i\hat{H}(t)\Delta t) \quad (4.33)$$

and

$$|\Psi(t + \Delta t)\rangle \simeq \exp(-i\hat{H}(t)\Delta t) |\Psi(t)\rangle. \quad (4.34)$$

Note that the time evolution operator (4.31) is *transitive*

$$\hat{U}(t, t + 2\Delta t) = \hat{U}(t + \Delta t, t + 2\Delta t) \hat{U}(t, t + \Delta t) \quad (4.35)$$

and *unitary*

$$\hat{U}^\dagger(t, t + \Delta t) = \hat{U}^{-1}(t, t + \Delta t) \quad (4.36)$$

$$\Rightarrow \langle \Psi(t) | \Psi(t) \rangle = \langle \Psi(t + \Delta t) | \Psi(t + \Delta t) \rangle \quad \forall t, \Delta t. \quad (4.37)$$

Larger times can therefore be reached by successive application of (4.33). The norm of the wave function is conserved for all times. For many practical problems the exponential in (4.33) can not be evaluated exactly but there exist many propagation schemes that provide different approximations (see [126] for a comprehensive review of different time-stepping techniques). In our approach, we use the *Short Iterative Lanczos* (SIL) propagation scheme, which will be briefly outlined below.

4.2.1 Lanczos propagation

The Lanczos algorithm relies on Krylov subspace techniques that were originally introduced to calculate eigenvalues and eigenvectors of (large) matrices [127]. In the form presented here, it is only applicable for Hermitian matrices. The procedure works as follows:

A Krylov subspace of order $N + 1$ is generated by the repeated action of $\hat{\mathbf{H}}$ on an initial state $|\Psi_0\rangle$ (assumed to be normalized)

$$K_{N+1} = \{|\Psi_0\rangle, |\Psi_1\rangle, |\Psi_2\rangle, \dots, |\Psi_N\rangle\} \quad (4.38)$$

$$|\Psi_k\rangle = \hat{\mathbf{H}}^k |\Psi_0\rangle. \quad (4.39)$$

Orthonormalizing the basis vectors in the subspace by the Gram-Schmidt procedure produces a new basis,

$$Q_{N+1} = \{|q_0\rangle, |q_1\rangle, |q_2\rangle, \dots, |q_N\rangle\}. \quad (4.40)$$

The Hamilton operator $\hat{\mathbf{H}}$ is then approximated as a $(N + 1) \times (N + 1)$ matrix $\hat{\mathbf{H}}^{(Q)}$ in the Q_{N+1} basis. N is chosen much smaller than the dimension of the matrix representation of $\hat{\mathbf{H}}$ (which can be up to 10^9), with typical values of 12 – 15 in our case. Direct diagonalization of this small matrix can be efficiently performed. In the limit $N \rightarrow \infty$, the eigenvalues and eigenvectors of the transformed Hamiltonian converge to those of the full Hamiltonian, with the extreme (i.e. largest and smallest) eigenvalues converging first.

The Lanczos algorithm is very effective because in practice it is not necessary to explicitly build up the Krylov space and perform the full orthonormalization to all previous vectors, since the matrix $\hat{\mathbf{H}}^{(Q)}$ is tridiagonal and its elements can be obtained from a three-term recursion relation. This construction proceeds analogously to the construction of orthogonal polynomials, cf. [section A.1](#).

We thus get a *three-term recurrence relation*

$$|q_0\rangle := |\Psi_0\rangle \quad (4.41)$$

$$\beta_0 |q_1\rangle = \hat{\mathbf{H}} |q_0\rangle - \alpha_0 |q_0\rangle \quad (4.42)$$

$$\beta_j |q_{j+1}\rangle = \hat{\mathbf{H}} |q_j\rangle - \alpha_j |q_j\rangle - \beta_{j-1} |q_{j-1}\rangle \quad (4.43)$$

where $|\Psi_0\rangle$ is assumed to be normalized and

$$\alpha_j = \langle q_j | \hat{\mathbf{H}} | q_j \rangle \quad (4.44)$$

$$\beta_j = \|\hat{\mathbf{H}}|q_j\rangle - \alpha_j|q_j\rangle - \beta_{j-1}|q_{j-1}\rangle\| = \langle q_{j-1} | \hat{\mathbf{H}} | q_j \rangle = \langle q_{j+1} | \hat{\mathbf{H}} | q_j \rangle, \quad (4.45)$$

where both α_j and β_j are real. The Hamilton operator in the subspace Q_{N+1} is thus real and tridiagonal and is given by

$$\hat{\mathbf{H}}_{ij}^{(Q)} = \langle q_i | \hat{\mathbf{H}} | q_j \rangle \hat{=} \begin{pmatrix} \alpha_0 & \beta_0 & 0 & \cdots & 0 \\ \beta_0 & \ddots & \ddots & \ddots & \vdots \\ 0 & \ddots & \ddots & \ddots & 0 \\ \vdots & \ddots & \ddots & \ddots & \beta_{N-1} \\ 0 & \cdots & 0 & \beta_{N-1} & \alpha_N \end{pmatrix}. \quad (4.46)$$

To perform time propagation, we replace the Hamiltonian in the time evolution operator by its approximation in the Krylov subspace,

$$\hat{\mathbf{U}}^{(Q)} = \exp(-i\hat{\mathbf{H}}^{(Q)}\Delta t). \quad (4.47)$$

Consequently, $\hat{\mathbf{U}}^{(Q)}$ is restricted to the same Krylov subspace, where the exponential can be evaluated by direct diagonalization

$$\hat{\mathbf{U}}^{(Q)} = \sum_l |Z_l\rangle \exp(-ih_l^{(Q)}\Delta t) \langle Z_l|. \quad (4.48)$$

Here, $|Z_l\rangle$ denotes the eigenvector of $\hat{\mathbf{H}}^{(Q)}$ with the eigenvalue $h_l^{(Q)}$.

The approximation for the propagated wave function then reads

$$|\Psi(t + \Delta t)\rangle = \hat{\mathbf{U}}^{(Q)}|\Psi(t)\rangle = \hat{\mathbf{U}}^{(Q)}|\Psi_0\rangle = \sum_{k=0}^N a_k |q_k\rangle \quad (4.49)$$

with

$$a_k = \langle q_k | \hat{\mathbf{U}}^{(Q)} | q_0 \rangle = \sum_l \langle q_k | Z_l \rangle \exp(-ih_l^{(Q)}\Delta t) \langle Z_l | q_0 \rangle. \quad (4.50)$$

Since the $|q_k\rangle$ are linear combinations of the $|\Psi_k\rangle$ which, in turn, are given by $|\Psi_k\rangle = \hat{\mathbf{H}}^k|\Psi_0\rangle$, equation (4.49) is effectively a N -th order polynomial expansion of the exponential in (4.33). Moreover, the Lanczos procedure generates a set of orthogonal polynomials and for a finite K -dimensional operator (such as a Hamiltonian in a DVR representation) the approximation gets *exact* for $N \rightarrow K-1$ [126]. In contrast to a standard N -th order Taylor or Chebyshev expansion the coefficients a_k are optimized to give the best approximation for a given $|\Psi_0\rangle$ and in addition unitarity is conserved.

Note that the Lanczos procedure can also be adopted for non-Hermitian operators. For complex symmetric operators, it can be adapted to lead to a tridiagonal

matrix as well, by performing the dot products without complex conjugation of the vectors. Another approach (known as the Arnoldi-Lanczos procedure [128]) leads to an upper Hessenberg matrix, which has zero entries below the first subdiagonal, in (4.46). This, however, means that the vectors have to be explicitly orthogonalized to all previous Krylov vectors, and therefore entails more numerical work. Both of these approaches can be used to include complex absorbing potentials in the propagation scheme, as the Hamiltonian is then complex symmetric instead of Hermitian. We use a different approach to include absorbing boundaries, as explained in chapter 5.

Stability and unitarity considerations

The Krylov subspace approximation (4.48) for the time evolution operator is explicitly unitary. Therefore, the Lanczos algorithm is *unconditionally stable* and the propagation scheme is norm conserving for Hermitian Hamiltonians. Consequently, the algorithm is also energy conserving for time-independent operators.

Even though the propagation is explicitly unitary regardless of the properties of the discrete Hamiltonian, its spectrum still affects the propagation because large spectral ranges require small time steps or high orders to get accurate results. Thus, smaller grid spacings and more FEDVR basis functions make the temporal propagation computationally more costly.

Propagation error

The Lanczos algorithm allows for a convenient error estimation since the propagation error (i.e. the difference between the exact and the numerically propagated wave function) is proportional to the magnitude of the coefficient a_{N+1} of the first vector $|q_{N+1}\rangle$ lying outside the employed Krylov subspace. Following [129, 130] the error is approximately given by

$$\epsilon_{\text{Lan}} \approx \frac{\Delta t^N}{(N)!} \prod_{i=0}^N \beta_i. \quad (4.51)$$

This error estimation (or a direct calculation of the coefficient a_{N+1} with the help of (4.41)) can be used as a *tolerance parameter* to dynamically adjust the step-size or order N to obtain a constant error for each time step. For small time steps usually a few iterations (i.e. low orders) are sufficient for the last coefficients a_{N+1} to become negligible. Thus, the Lanczos algorithm is particularly effective as a short-time propagator and the method is often referred to as *short iterative Lanczos* (SIL) procedure.

5 Computational implementation

In this chapter, we describe the actual implementation of the computational methods described in the previous chapters in some detail. In particular, we discuss the choices made to minimize the amount of computational work and at the same time allow for efficient implementation of the associated operations. Additionally, we describe the parallelization of the program, which enables the concurrent use of a few hundred processors. The speed of the computation is shown to scale almost perfectly linearly with the number of processors.

5.1 Representation of the wave function

5.1.1 Partial waves

To discretize the close-coupling equations, we represent the functions $R_{l_1, l_2}^L(r_1, r_2)$ in a FEDVR product basis (one for each variable r_1 and r_2), indexed by j_1 and j_2 . In addition, we combine the angular quantum numbers L , l_1 , and l_2 to one index k , such that the wave function is represented by a 3-dimensional array,

$$R_{l_1, l_2}^L(r_1, r_2) \rightarrow R_{j_1, j_2, k}. \quad (5.1)$$

The mapping from angular momenta L, l_1, l_2 to the combined index k depends on the size of the angular momentum expansion. This expansion is determined by the three parameters L_{\max} , $l_{>, \max}$, and $l_{<, \max}$. These impose the following conditions on L, l_1, l_2 :

$$L \leq L_{\max}, \quad (5.2)$$

$$\max(l_1, l_2) \leq l_{>, \max}, \quad (5.3)$$

$$\min(l_1, l_2) \leq l_{<, \max}. \quad (5.4)$$

Thus, L_{\max} gives the maximum value for the total angular momentum L , $l_{>, \max}$ describes the maximum value for the single electron angular momenta l_1 and l_2 , and $l_{<, \max}$ restricts the expansion to partial waves where at least one of the two single electron angular momenta is smaller than or equal to $l_{<, \max}$. In many applications, we will choose $l_{<, \max} = l_{>, \max}$. By choosing $l_{>, \max} > l_{<, \max}$, it is however possible to use expansions where only one of the electrons can gain a large amount of angular momentum. Because of exchange symmetry, it is of course not possible to specify

which electron may attain high angular momentum. We only specify that at most one of the two indistinguishable electrons can reach high angular momentum at any point any time. When only single ionization is of interest, this can be used in simulations including an infrared (IR) field, which transfers a large amount of angular momentum to free electrons.

As already pointed out in [section 3.4.1](#), because of the exchange symmetry between electrons, the array $R_{j_1, j_2, k}$ actually contains redundant information if all values of j_1, j_2, L, l_1, l_2 are taken into account. One possible way around this would be to use explicitly symmetrized basis functions. However, this necessitates adding normalization prefactors to the basis functions, as well as making the structure of the matrix representing the Hamiltonian slightly more complicated. Therefore, we choose a different route: We store only those parts of the wave function that are needed, and use the exchange symmetry $j_1 \leftrightarrow j_2, l_1 \leftrightarrow l_2$ to reconstruct the remainder of the wave function when needed. In particular, we only include partial waves $k \equiv (L, l_1, l_2)$ with $l_1 \leq l_2$, and use the transpose $R_{j_2, j_1, k}$ when the partial wave with values (l_2, l_1) is required.

Applying the above considerations as well as the selection rules from [section 3.4.2](#) considerably reduces the number of partial waves, see [Table 5.1](#) for an example. The number of partial waves needed strongly depends on the nature of the physical problem and the observables of interest. Some points of interest are listed in the following:

- For calculations with XUV pulses of moderate intensities ($< 10^{15}$ W/cm²), only a few photons (typically at most two) are absorbed, such that the total angular momentum will only reach values of $L = 2$. In order to ensure numerical convergence, it is usually sufficient to use $L_{\max} = 3$.
- Angle-integrated variables are usually converged for relatively small values of $l_{<, \max}, l_{>, \max} \approx 3$. In order to get accurate angular distributions, it is however often necessary to include much larger values of up to $l_{<, \max} = l_{>, \max} = 10$. An expansion with $(L_{\max}, l_{<, \max}, l_{>, \max}) = (3, 3, 3)$ needs $N_{PW} = 15$ partial waves, while $(3, 10, 10)$ gives $N_{PW} = 57$.
- For simulations including intense infrared or optical pulses, the electrons absorb many more photons, such that it is necessary to use considerably larger bases with $L_{\max} \gtrsim 20$, and similar values for the single electron angular momenta.
- If only situations where one electron always stays bound are of interest, it is possible to set $l_{<, \max}$ to much smaller values, e.g. 5, even in IR fields. An expansion with $(L_{\max}, l_{<, \max}, l_{>, \max}) = (20, 5, 20)$ needs $N_{PW} = 349$ partial waves, while $(20, 20, 20)$ would require $N_{PW} = 1331$ partial waves.

$L l_1 l_2$	parity	angular index k / reason for exclusion
0 0 0	e	1
0 1 1	e	2
0 2 2	e	3
0 3 3	e	$l_1 > l_{<,max}$
1 0 1	o	4
1 1 0	o	redundant
1 1 1	e	parity forbidden
1 1 2	o	5
1 2 1	o	redundant
1 2 2	e	parity forbidden
1 2 3	o	6
1 3 2	o	redundant
1 3 3	e	parity forbidden
2 0 2	e	7
2 2 0	e	redundant
2 1 1	e	8
2 1 2	o	parity forbidden
2 2 1	o	parity forbidden
2 1 3	o	9
2 3 1	o	redundant
2 2 2	e	10
2 2 3	o	parity forbidden
2 3 2	o	parity forbidden
2 3 3	e	$l_1 > l_{<,max}$

Table 5.1: Reduction of partial waves fulfilling $\Delta(l_1, l_2, L)$ due to exchange symmetry or selection rules for $(L_{max}, l_{<,max}, l_{>,max}) = (2, 2, 3)$.

5.1.2 FEDVR basis

In choosing the parameters of the FEDVR grid, different objectives have to be fulfilled. For one, the discretized operators on the grid have to be a sufficiently good approximation to the real operators. The Coulomb singularity demands a high density of grid points near the nucleus, while the necessary density of grid points at large values of r is determined by the need to represent waves with the highest energy the electrons attain. These requirements can be fulfilled both by choosing small finite elements and/or by using high orders for the quadrature in each element. The second objective is to maximize computational speed, which depends on a number of factors. In general, the cost of applying each operator scales at least linearly with the total number of grid points. The higher the order

for the FEDVR, the fewer grid points are needed to attain the same precision. However, using higher orders for the FEDVR also increases the maximum energy of the grid eigenfunctions. This is illustrated in Fig. 5.1 which shows the maximal eigenvalue of the *discrete* Laplace operator (which dominates the spectral range of the Hamiltonian) as a function of the number of FEDVR basis functions for a grid with an element size of 4 a.u..

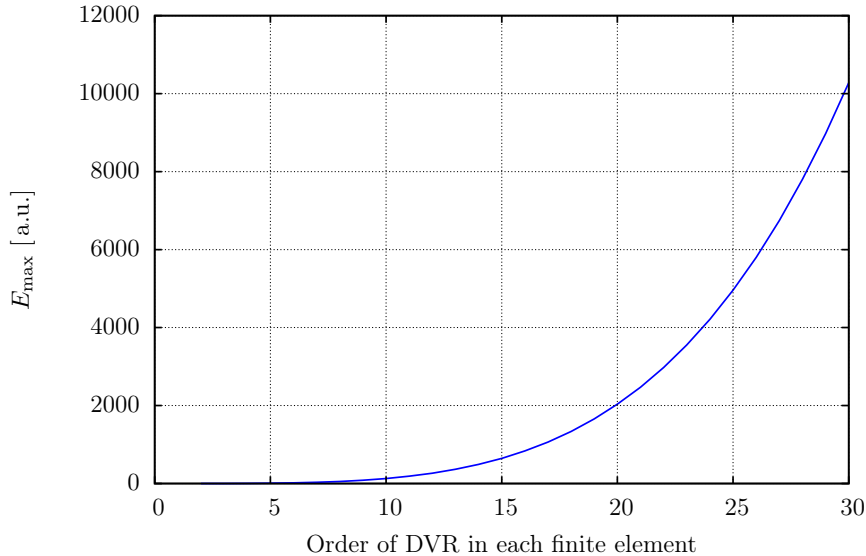


Figure 5.1: Maximal eigenenergy of the discrete Laplace operator as a function of the number of FEDVR functions for a grid with a finite element size of 4 a.u..

As the total computational cost is also determined by the number of time steps necessary, and the maximum possible time step scales inversely with the highest energy on the grid, it is favorable to use moderate orders. We have found that finite elements of extension 4 a.u. and order 11 in each element generally provide a good compromise for the above requirements, giving a good approximation of the wave function while not supporting too high energies. The total number of basis functions (or grid points) for a given grid is $N_{\text{FEDVR}} = N_{\text{FE}}(N_{\text{DVR}} - 1) + 1$, where N_{FE} is the number of finite elements, N_{DVR} is the order of the DVR in each element, and we have taken into account that one basis function is shared between adjacent finite elements and that we drop the first function at $r = 0$ to enforce the boundary condition at the origin.

The necessary extension of the FEDVR grid of course depends strongly on the physical problem at hand. Typically, the grids reach up to a few hundred atomic units. The largest grids we have used had an extension of $r_{\text{max}} = 1400$ a.u., which corresponds to 3201 basis functions for each variable r_1, r_2 . The grid points have to be dense enough to resolve the oscillation of the highest energy electrons that will

be produced in the calculation. In addition, the Coulomb singularity at the origin has to be treated with sufficient precision. In most cases, the grid point density necessary to represent the high energy electrons was also high enough to represent the Hamiltonian close to the Coulomb singularity with sufficient accuracy. For cases where only low energy electrons are produced, the grid can be sparser far from the origin. In these cases, the finite elements are chosen smaller near the origin and larger away from it.

The total number of basis functions needed to represent the wave function is

$$N = N_{\text{FEDVR}}^2 \cdot N_{\text{PW}} \quad (5.5)$$

and can reach values as large or even larger than $N = 10^9$. Just the storage requirement for each wave function (stored as double precision complex values, needing 16 byte per value) is then almost 15 Gbyte. Thus, one quickly reaches the limits of memory capacity and CPU power on single machines, and even calculations on large clusters take significant amounts of time.

5.2 Implementation of the electron-electron interaction

The electron-electron interaction Hamiltonian $\hat{\mathbf{W}}$ is represented in TDCC (cf. Eq. 3.18) by

$$\langle k' | \hat{\mathbf{W}} | k \rangle = \sum_{\lambda=0}^{\infty} \frac{r_{<}^{\lambda}}{r_{>}^{\lambda+1}} \hat{\mathbf{W}}_{k,k',\lambda}^{\text{ang}}, \quad (5.6)$$

where $\hat{\mathbf{W}}_{k,k',\lambda}^{\text{ang}}$ is the angular part of the electron-electron interaction operator, k and k' are the combined angular indices (L, l_1, l_2) and (L', l'_1, l'_2) , $r_{<}$ is $\min(r_1, r_2)$ and $r_{>}$ is $\max(r_1, r_2)$. The usual approximation for potentials in the FEDVR approach is to represent them as a diagonal matrix, with the entries just being the values of the potential at the grid points. However, this approach would entail a large error for the electron-electron interaction operator, as the radial part $r_{<}^{\lambda}/r_{>}^{\lambda+1}$ has a derivative discontinuity at $r_1 = r_2$, which can not simply be represented in the FEDVR basis. This can be fixed following the recipe of McCurdy *et al.* [131], a short summary of which is given in the following. The general idea behind this is to evaluate one of the radial integrals over FEDVR basis functions analytically, instead of using the Gauss-Lobatto quadrature associated with the grid. The radial parts of the interaction operator are given by the integrals

$$\langle f_{j_1} f_{j_2} | \frac{r_{<}^{\lambda}}{r_{>}^{\lambda+1}} | f_{j'_1} f_{j'_2} \rangle = \int_0^{r_{\max}} dr_1 \int_0^{r_{\max}} dr_2 f_{j_1}(r_1) f_{j'_1}(r_1) \frac{r_{<}^{\lambda}}{r_{>}^{\lambda+1}} f_{j_2}(r_2) f_{j'_2}(r_2), \quad (5.7)$$

where $f_j(r)$ is the j^{th} FEDVR basis function. Instead of directly employing Gauss-Lobatto quadrature, we define the function

$$\begin{aligned} y(r) &= r \int_0^{r_{\max}} dr' \frac{r_{<}^\lambda}{r_{>}^{\lambda+1}} f_{j_2}(r') f_{j_2'}(r') \\ &= \int_0^r dr' \frac{r'^\lambda}{r^\lambda} f_{j_2}(r') f_{j_2'}(r') + \int_r^{r_{\max}} dr' \frac{r'^{\lambda+1}}{r'^{\lambda+1}} f_{j_2}(r') f_{j_2'}(r'), \end{aligned} \quad (5.8)$$

which satisfies the radial Poisson equation,

$$\left(\frac{d^2}{dr^2} - \frac{\lambda(\lambda+1)}{r^2} \right) y(r) = -\frac{2\lambda+1}{r} f_{j_2}(r) f_{j_2'}(r) \quad (5.9)$$

with the boundary conditions $y(0) = 0$ and $y(r_{\max}) = r_i^\lambda / r_{\max}^\lambda \delta_{j_2, j_2'}$. Expanding $y(r)$ in the basis of FEDVR functions, inserting into (5.9), solving the resulting matrix equation, and finally adding a solution of the homogeneous radial Poisson equation to satisfy the boundary conditions leads to

$$y(r) = (2\lambda+1) \sum_{i=1}^N [T^\lambda]_{i, j_2}^{-1} \frac{f_i(r)}{r_{j_2} \sqrt{w_{j_2}}} \delta_{j_2, j_2'} + \frac{r_{j_2}^\lambda r_{\max}^{\lambda+1}}{r_{\max}^{2\lambda+1}} \delta_{j_2, j_2'}, \quad (5.10)$$

where

$$T_{i, j}^\lambda = \langle f_i | -\frac{d}{dr^2} + \frac{\lambda(\lambda+1)}{r^2} | f_j \rangle \quad (5.11)$$

is twice the single-electron kinetic energy operator for angular momentum λ in the FEDVR basis, $[T^\lambda]_{i, j}^{-1}$ is the element i, j of its inverse, and w_j is the Gauss-Lobatto integration weight associated with grid point r_j . Inserting this expression for $y(r)$ back into the original equation (5.7) and performing the integral using the Gauss-Lobatto quadrature gives the final result

$$\langle f_{j_1} f_{j_2} | \frac{r_{<}^\lambda}{r_{>}^{\lambda+1}} | f_{j_1'} f_{j_2'} \rangle = \delta_{j_1, j_1'} \delta_{j_2, j_2'} \left(\frac{2\lambda+1}{r_{j_1} r_{j_2} \sqrt{w_{j_1} w_{j_2}}} [T^\lambda]_{j_1, j_2}^{-1} + \frac{r_{j_1}^\lambda r_{j_2}^\lambda}{r_{\max}^{2\lambda+1}} \right), \quad (5.12)$$

which remarkably is still diagonal in the FEDVR grid indices j_1, j_2 . The inverse matrices only have to be calculated once at the start of the program, which does not incur a large computational overhead. The improved precision of this expression for the electron-electron interaction is considerable. As an example, the error in the ground state energy (i.e. the deviation from the “real” ground state of the non-relativistic Hamiltonian) is only $5.3 \cdot 10^{-5}$ a.u. using this improved expression, while the error is $1.2 \cdot 10^{-2}$ a.u. when using the “naive” expression for the interaction operator. This example was calculated using typical parameters for our simulations (FEDVR elements of order 11 with 4 a.u. extension, $l_{<, \max} = l_{>, \max} = 9$).

5.3 Temporal propagation

For temporal propagation we use the Short Iterative Lanczos (SIL) algorithm with fixed order (usually $N \approx 12 - 15$) and an *adaptive* time step to fulfill a tolerance criterion for the magnitude of the first component outside the Krylov subspace (as described in 4.2.1). As the magnitude of the time step only enters in the exponential of the $N \times N$ matrix representing the Hamiltonian in the Krylov subspace, changing the time step incurs essentially no computational cost. The routine was written such that all calculations are performed within the $\{|q_j\rangle\}$ -basis as long as possible, only switching to the full basis at the very last step.

In addition to the SIL algorithm, we have also implemented a *second-order differencing* or *leapfrog* scheme, described in more detail in [38], as well as a Runge-Kutta-Fehlberg time integrator, which compares the 4th and 5th-order Runge-Kutta time steps to estimate the integration error. Both of these alternative propagation schemes are considerably less efficient than the SIL propagator and are therefore only used as a cross-check and consistency test.

5.3.1 Calculation of the ground state

To obtain the initial wave function (i.e. the ground state of the helium atom), we propagate an arbitrary state in negative *imaginary time* by substituting $\partial_t \rightarrow -i\partial_t$ in the field-free TDSE. In addition, we renormalize the resulting wave function after each time step. As a consequence, all eigenstates of the Hamiltonian, apart from the ground state, are damped out exponentially. Therefore, after some time only the ground state remains from the superposition [132]. Note that convergence can be sped up by choosing a starting state that is close to the ground state. We therefore start the imaginary time propagation with an uncorrelated product of $|1s\rangle$ states.

5.4 Absorbing boundaries

In practice, it is often unavoidable that parts of the wave function reach the boundary of the grid at r_{\max} . In order to prevent reflections, we impose a *complex* absorbing potential of the form

$$A(r) = i\alpha\theta(r - r_{\text{cut}}) \ln \cos\left(\frac{r - r_{\text{cut}}}{r_{\max} - r_{\text{cut}}}\right) \quad (5.13)$$

where α determines the strength of the absorption, to dampen the wave function to zero before it reaches the boundary. The potential and its first derivative are continuous functions, while the second derivative is discontinuous at r_{cut} . The form of this particular potential is similar to a cosine-shaped “absorbing edge” masking

function (as also employed in e.g. [72]) and proved to be suitable for our purposes. However, the effectiveness of such potentials always depends on the energy and the form of the incoming wave packet. In general, it is hard to completely avoid reflections. However, it is possible to suppress them below a certain level, see e.g. [133, 134] for a detailed treatment of the problem.

As adding this potential to the full Hamiltonian would make it non-Hermitian, we do not include it in the SIL procedure, but apply it after every time step. Formally, this is equivalent to a split-operator approach to the full time evolution operator (including the absorbing potential), where the third-order error term is ignored,

$$\begin{aligned}\hat{U}(t, t + \Delta t) &= \exp(-i\hat{\mathbf{H}}(t)\Delta t - i\hat{A}\Delta t) \\ &= \exp\left(-i\hat{A}\frac{\Delta t}{2}\right)\exp(-i\hat{\mathbf{H}}(t)\Delta t)\exp\left(-i\hat{A}\frac{\Delta t}{2}\right) + O(\Delta t^3).\end{aligned}\quad (5.14)$$

5.5 Parallelization

As we have seen in the previous sections, the computational cost for many problems quickly becomes too big to handle them on single machines. We have therefore implemented a parallelized version of the code which can run on large clusters, using a few hundred CPU cores simultaneously. This version uses the MPI (Message Passing Interface) library [135] for communication. This implies that a separate process runs on each core, and data is exchanged between the processes by calls to MPI library routines. In this section, we give a short overview of the implementation and show some benchmark results demonstrating linear scaling of the computation speed with the number of used processes. This favorable scaling as well as the access to large clusters enabled us to perform the extensive numerical studies presented in this thesis. The clusters used were provided through Institutional Computing at Los Alamos National Laboratory (LANL) and through two TeraGrid grants by the National Science Foundation (NSF).

5.5.1 Splitting the grid

In order to efficiently utilize cluster architectures, we split the wave function into parts such that the operators that we apply on the wave function are mostly local, i.e. such that little communication between processes is necessary. In the current version, only the radial grid is split into parts, and each process gets the full angular momentum expansion for the radial parts it is responsible for. The total matrix representing the radial part of the wave functions is split into square parts of identical size, i.e. each part has $N_{\text{local}} \times N_{\text{local}}$ grid points. The splitting occurs along finite element boundaries, with an overlap of one grid point, such that adjacent processes both store the coefficient of the bridge function.

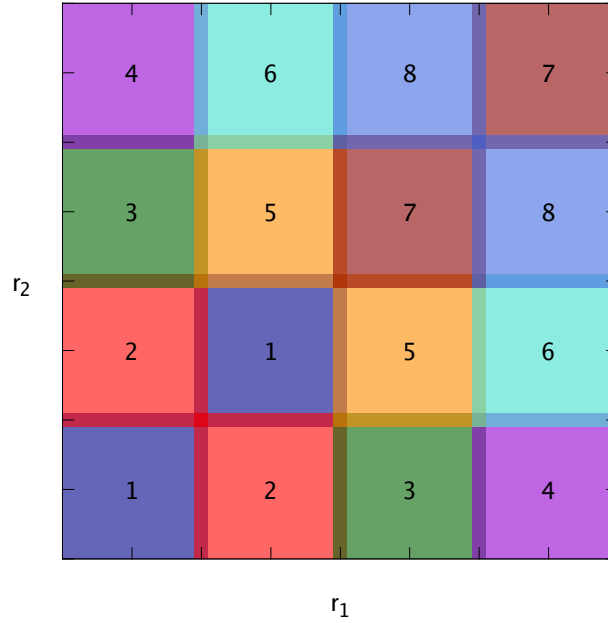


Figure 5.2: Sketch of the split of the radial (r_1, r_2) space into parts of equal size and distribution among processes for the parallelized implementation of the program. The colors and numbers encode the process number that stores each part of the wave function.

As all operators in the FEDVR approach are either local in radial space (such as the operators representing the potentials) or at most couple across elements via the bridge functions, this ensures that only the coefficients of the bridge functions have to be synchronized after each application of an operator containing derivatives (such as the kinetic energy operator). There is one additional complication because of the way we use exchange symmetry – if an operator couples to a partial wave (L, l_1, l_2) with $l_1 > l_2$, we instead use the transposed spatial part of the partial wave (L, l_2, l_1) . To ensure that each process has this part of the wave function in his local memory, we distribute *two* of the square parts of the wave function to each process, such that each process either gets two parts along the diagonal $r_1 = r_2$, or a part and its transpose ($r_1 \leftrightarrow r_2$). This pattern is shown in Fig. 5.2 for the case of 8 processes, which means that the radial grid is split into 16 parts in a 4×4 grid.

In order to allow more flexibility in choosing the number of processes when simulating a specific grid, it is possible to assign more than 2 parts of the wave function to each process. For example, 4 processes can be used to calculate the grid in Fig. 5.2 simply by modifying the mapping of processors to parts of the wave function. For example, process 1 would get the parts assigned to processes 1 and 2 in the figure, process 2 would get the parts for process 3 and 4, and so on.

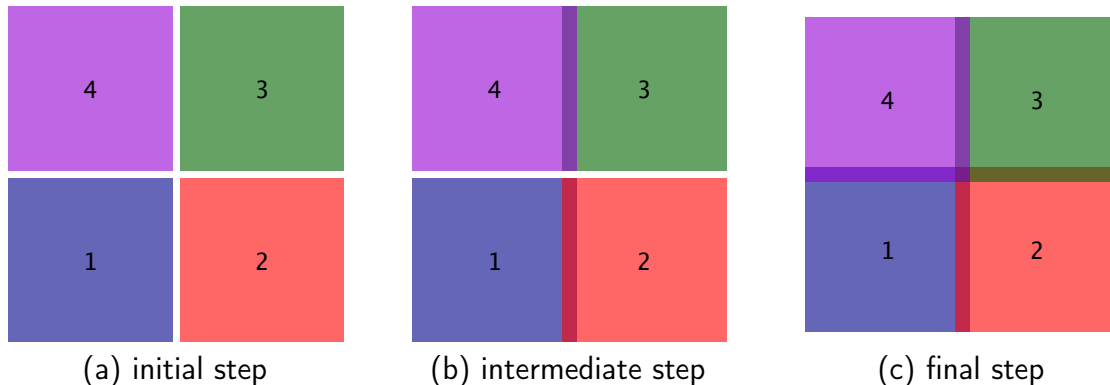


Figure 5.3: Synchronization procedure for parts of the wave function using MPI. This synchronization has to be done after applying an operator containing a derivative to the wave function.

5.5.2 Communication pattern

After applying an operator containing derivatives, the wave function parts of the separate processes have to be synchronized to ensure consistency. The distribution amongst processes is chosen such that only one spatial grid point, representing the coefficient of the bridge function connecting the finite elements, has to be communicated between the different processes. Before synchronization, each process only has that contribution to the new wave function that comes from coupling of the bridge function to the finite element that the process itself owns, while there is a second contribution from coupling to the finite element at the adjacent process.

Fig. 5.3 demonstrates the two steps that the synchronization takes: First, each process sends the “right” and “left” edges (i.e. along the r_1 -direction) of its wave function part to the adjacent processes, such that the processes in one row afterwards agree on the value of the bridge function coefficients at the edge. In the second step, the processes communicate “up” and “down”, i.e. along the direction of r_2 . Note that there is one point at the corner of the four parts that all four processes share in their representation. By doing the communication in two steps and only doing the second step after the first one has completed, this point is already included correctly (i.e. all processes get the sum of the contribution of all processes to this point) and we circumvent the need to communicate “diagonally”.

The other class of operations that need communication between the processes are the “global” operations such as calculating norms or dot products. For these, the sum over the contributions from all processes has to be calculated. Fortunately, only a single number (the contribution from all parts belonging to a process) has to be synchronized, such that the amount of data is small. Additionally, MPI provides specialized routines that do global reduction operations. Most implementations use

smart algorithms that perform this operation in a minimum number of steps, e.g. by performing the reduction on a logical tree structure for the processors, such that only $\log N$ steps are necessary for N processors.

5.5.3 L-shaped grid

The parallelized version of the program adds some flexibility to the total form of the radial grid. By not assigning any processes to the part of the wave function where both r_1 and r_2 exceed some value r_{small} , it is possible to easily implement an *L-shaped* grid. For example, using $r_{\text{small}} = r_{\text{max}}/2$ (corresponding to removing the parts of the wave function belonging to processors 7 and 8 in Fig. 5.2, and only using 6 processors) would reduce the computational effort by 25%. Such a grid can be used when only one of the two electrons can reach a distance larger than r_{small} from the nucleus, i.e. in situations where only single ionization is of interest. In combination with the asymmetric expansion in angular momenta provided by choosing $l_{>,\text{max}} > l_{<,\text{max}}$, as discussed in section 5.1.1, this provides a computationally tractable approach to calculate full-dimensional, fully correlated wave functions in IR laser fields, as long as one electron remains bound to the core, such as in *high harmonic generation* (HHG).

5.6 Benchmarks

In order to compare the different machines that we have access to, a standard benchmark run was performed on each of them with varying numbers of processes. The parameters were chosen such as to allow a wide range of process numbers for splitting the wave function. For the benchmark calculations, the radial grid had an extension of $r_{\text{max}} = 480$ a.u., with finite elements of size 4 a.u. and order 11 for the DVR in each element. The angular momentum parameters were chosen similar to the ones used for the two-photon double ionization runs presented in Part II, with $L_{\text{max}} = 3$ and $l_{<,\text{max}} = l_{>,\text{max}} = 7$. In order to get reasonably short simulation runtimes, only a very short XUV pulse was used, with a \sin^2 envelope and a total duration of 80 as.

The program first needs some time for setup (especially for the inversion of the kinetic energy matrix for the electron-electron interaction). As these times are negligible for “real” runs (a few minutes) and are not implemented to profit from parallelization, including them in the measured time for the very short run we do here would distort the results heavily. Therefore, we use the total wall clock time taken just for the real time propagation (measured with the routine `MPI_WTIME` provided by the MPI library). In order to facilitate comparison, this time is then multiplied with the number of processes (i.e. CPU cores) used in the calculation. This gives the total CPU time consumed for each run. Linear

scaling of the computation speed with number of cores is indicated by a constant value for this number, which signifies that the total computational effort necessary to solve a given problem is independent of the number of CPUs. CPU hours (or SUs, Service Units) are also the relevant unit for accounting on TeraGrid. Therefore, it is useful to choose the number of processors for each run such that a minimum number of CPU hours is used to finish the calculation.

5.6.1 Available machines

The different clusters that were used for the benchmarking runs are listed in [Table 5.2](#). These clusters were either provided by the Information Technology Services (Zentraler Informatikdienst, ZID) of the Vienna University of Technology (ICP5), by Institutional Computing at Los Alamos National Laboratory (Coyote and Lobo), or accessed through TeraGrid grants by the National Science Foundation.

Name	Site	CPUs	GHz	cores/CPU	CPUs / cores per node
ICP5	VUT	IBM Power5+	1.90	1	2/2
Coyote	LANL	AMD Opteron	2.60	1	2/2
Lobo	LANL	AMD Opteron 8354	2.20	4	4/16
Kraken	NICS	AMD Opteron 2376	2.30	4	2/8
Ranger	TACC	AMD Opteron 8356	2.30	4	4/16
Lonestar	TACC	Intel Xeon 5100	2.66	2	2/4
Abe	NCSA	Intel Xeon 5300	2.33	4	2/8
Queen Bee	LONI	Intel Xeon 5300	2.33	4	2/8

Table 5.2: Systems used for benchmarking.

5.6.2 Total runtime

[Fig. 5.4](#) shows the total amount of CPU hours consumed for the same run on the different clusters and for different numbers of cores (MPI processes) used in the simulation. Note that the results shown do not include any averaging, i.e. each run was only performed once. During testing, we noticed that sometimes, a run would complete much slower than expected. As far as we could determine, these hiccups occur because of temporary problems with one or a few nodes of the clusters, so that these runs were repeated, and the runtimes without these problems are shown. This is discussed in more detail in [Appendix D](#).

There are a number of interesting features and results that can be observed in this plot:

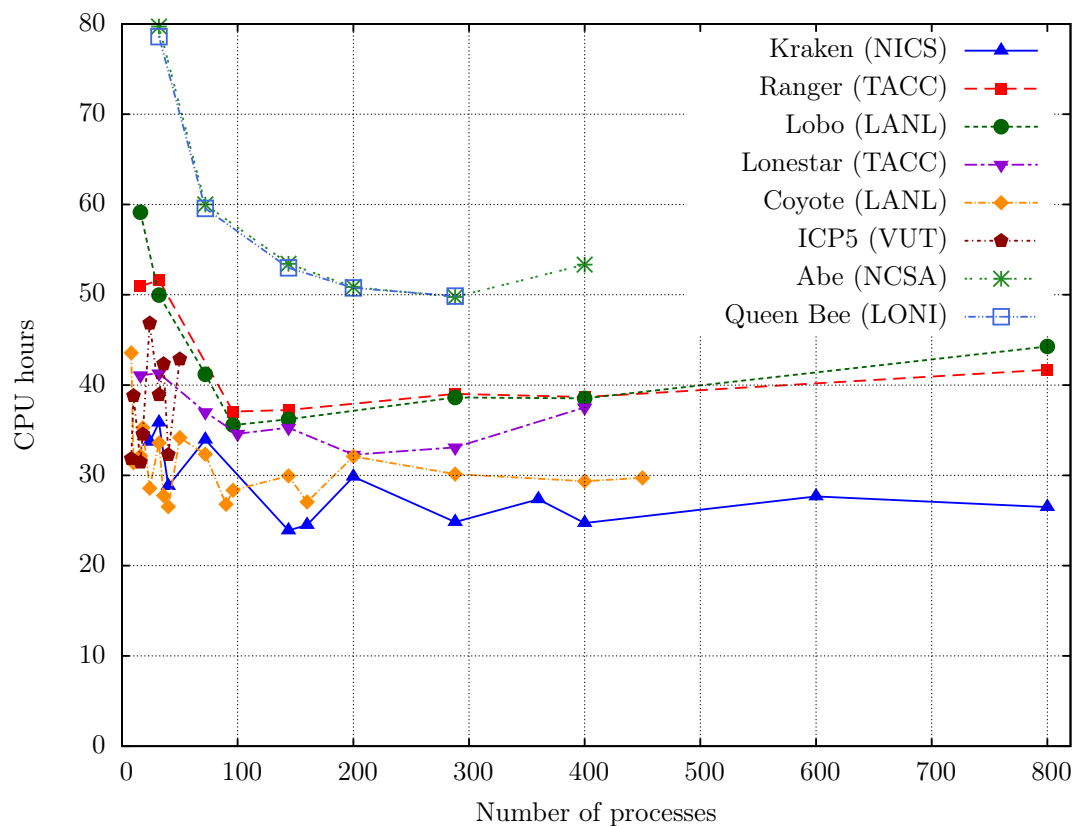


Figure 5.4: Total CPU hours used for the benchmark run on different LANL and TeraGrid clusters.

- The scaling is roughly linear on most clusters, i.e. the lines are reasonably flat. For small numbers of processes, the runtimes actually increase – this comes from the fact that each process then gets bigger parts of the wave function and the caches of the CPUs can not work as effectively anymore.
- The clusters can be clearly ordered in terms of computational speed per core, from fastest to slowest: 1) Kraken, 2) Coyote, 3) Lonestar, 4) Ranger and Lobo, and 5) Abe and Queen Bee. These results correlate with the memory bandwidth available per core. This is expected due to the sparse structure of most interaction matrices. Because of this, most elements of the wave function are only used once in the application of the Hamiltonian, and consequently, the deciding factor for the computational speed is the speed with which the wave function can be read from and written to main memory, i.e. the memory bandwidth.
- There are large fluctuations in speed for small numbers of processes for the

parameters used in the benchmarking run. This can be explained by the way in which the parts of the wave functions are assigned to the processes, as explained in [section 5.5.1](#). When each process gets more than two parts of the wave function, each part is smaller. Depending on the size of the parts, this can lead to improved caching efficiency, and consequently, improved speeds. This leads to the large fluctuations for small numbers of cores. This effect is more visible on the clusters with fewer cores per node because of the fact that more benchmark runs were done on these clusters. As we used only full nodes, we only did benchmarks with 16, 32, . . . , processes on clusters with 16 cores per node. Conversely, on clusters with 2 cores per node, we also did runs with 8, 10, 12, . . . processes. In addition, the caching behavior depend on the specific cache hierarchies and sizes of the processors in use.

- As is to be expected, clusters with similar architectures also perform very similarly, such as Queen Bee and Abe, or Lobo and Ranger.

In order to achieve good scaling to high numbers of processes, it was necessary to ensure parallelization of all time-consuming parts in the calculation. In particular, the writing of the wave functions to disk had to be optimized to occur in parallel from different processes in order not to become a bottleneck. Additionally, when scaling to large numbers of processors, the part of the wave function in radial space that each process gets can become small – down to only one finite element. In order to achieve good scaling even in that limit it was necessary to minimize the overhead in each routine. For example, it is crucial to not have to recompute the angular momentum coupling matrix elements in the electron-laser and electron-electron interaction for each application of the Hamiltonian. This is in contrast to the single processor code, where it does not matter if they are evaluated on the fly for each application of the Hamiltonian.

An additional observation during benchmarking was that the results are considerably more stable on some machines than on others. On some of the machines (e.g. Coyote), some runs are slower than the others by a factor of almost two without any apparent reason. Redoing those runs, using exactly the same executable and parameters, usually shows the “normal” computation speed. The reason for these discrepancies is not clearly known up to now. The investigations in this direction are explained in [Appendix D](#).

6 Observables

Using the methods presented in the previous chapters, we solve the time-dependent Schrödinger equation for a wide variety of laser pulses and obtain the fully correlated wave function after the end of the pulse. The last step is then to extract the physically relevant information that we are interested in from the wave function represented in radial and angular space in our FEDVR/TDCC basis. We are interested in quantities that are accessible in experiment as well as quantities that might not be (currently) accessible in experiments, but which reveal information about the processes that occurred. Many of these quantities can be accessed by projecting the final wave function on eigenstates of the full field-free Hamiltonian (2.9) with specific boundary conditions or asymptotic behavior. For example, we are interested in the double ionization probability distribution $P^{DI}(\mathbf{k}_1, \mathbf{k}_2)$, where \mathbf{k}_1 and \mathbf{k}_2 are the asymptotic momenta of the two electrons. Unfortunately, there are no analytic solutions for the eigenstates of the full Hamiltonian, due to the electron-electron interaction term in (2.9) and the resulting non-separability of the Schrödinger equation. Numerical diagonalization of the full Hamiltonian, apart from being computationally very expensive, suffers from the problem that specifying the boundary conditions or asymptotic behavior is very difficult, as there is a high amount of degeneracy in the final states. For example, if the total energy E_{tot} is positive, there are infinitely many eigenstates of the Hamiltonian with that energy: a continuum of double ionized states with $\frac{1}{2}(\mathbf{k}_1^2 + \mathbf{k}_2^2) = E_{\text{tot}}$, as well as infinitely many singly ionized states with the bound electron in state n of the He^+ ion and $\frac{1}{2}\mathbf{k}_1^2 - 2/n_2^2 = E_{\text{tot}}$. When diagonalizing the Hamiltonian in a box, the eigenstate at a specific energy would in general contain a superposition of these (quasi-)degenerate states.

We therefore choose a different approach to extract the final single and double ionization probability distributions: we use final states that represent the true eigenstates reasonably well in the asymptotic region, where the electrons are far away from each other, and propagate the wave function until this asymptotic limit is reached. The validity of this approach is tested and discussed in detail in [chapter 9](#).

6.1 Continuum wave functions

We exploit the fact that our time-dependent approach allows propagation of the wave packet for long times after the conclusion of the pulse. Once the distance

between the two electrons has reached a large enough value, we can neglect the electron-electron interaction term, $\hat{\mathbf{H}}_{12} = |\hat{\mathbf{r}}_1 - \hat{\mathbf{r}}_2|^{-1}$, which becomes insignificant for asymptotic distances. Consequently, we approximate the continuum by the exact solution of the (separable) stationary Schrödinger equation with the Hamiltonian without electron-electron interaction,

$$\hat{\mathbf{H}}_0 = \frac{\hat{\mathbf{p}}_1^2}{2} + \frac{\hat{\mathbf{p}}_2^2}{2} - \frac{Z}{r_1} - \frac{Z}{r_2}. \quad (6.1)$$

If both electrons are far away from the nucleus and/or have high energies, it would also be possible to neglect the electron-nucleus interaction when constructing final states for double ionization. However, as we are also interested in situations where there is only single ionization, we retain the electron-nucleus interaction term. This also ensures that the approximate single continuum and double continuum eigenstates are orthogonal to each other.

The separable Hamiltonian (6.1) is just the sum of two independent one-particle Hamiltonians. Before constructing the two-electron product states for the single and double continuum, we summarize some of the properties of the eigenstates of the (analytic) eigenfunctions of the single-particle Hamiltonian of a hydrogen-like atom, with

$$\hat{\mathbf{H}}_1 = \frac{\hat{\mathbf{p}}^2}{2} - \frac{Z_{\text{eff}}}{r}. \quad (6.2)$$

As (6.2) is spherically symmetric, its eigenstates can be separated into a radial and an angular part,

$$\Phi_{k,l,m}(\mathbf{r}) = \frac{\phi_{k,l}(r)}{r} Y_m^l(\Omega), \quad (6.3)$$

where the angular part is described by the spherical harmonics $Y_m^l(\Omega)$. For the *bound states*, the radial part of the regular eigenfunction is given by [95]

$$\phi_{n,l}(r) = \frac{\sqrt{Z_{\text{eff}}}}{n} \sqrt{\frac{(n-l-1)!}{(n+l)!}} \left(\frac{2Z_{\text{eff}}r}{n}\right)^{l+1} L_{n-l-1}^{2l+1}\left(\frac{2Z_{\text{eff}}r}{n}\right) \exp\left(-\frac{Z_{\text{eff}}r}{n}\right) \quad (6.4)$$

where L stands for the generalized Laguerre polynomial and $n \geq 1$ is the main quantum number. The eigenenergies of the bound states are given by

$$E_n = -\frac{Z_{\text{eff}}^2}{2n^2}. \quad (6.5)$$

The regular solution for the *unbound states* is given by the regular radial *Coulomb function* $F_l(\eta, kr)$ [95]

$$\begin{aligned} \phi_{k,l}(r) &= \sqrt{\frac{2}{\pi}} F_l(\eta, kr), \\ F_l(\eta, kr) &= 2^l e^{-\frac{1}{2}\pi\eta} \frac{|\Gamma(l+1+i\eta)|}{(2l+1)!} e^{-ikr} (kr)^{l+1} F(l+1-i\eta, 2l+2; 2ikr), \end{aligned} \quad (6.6)$$

with the confluent hypergeometric series F

$$F(a, b; z) = \sum_{n=0}^{\infty} \frac{\Gamma(a+n)}{\Gamma(a)} \frac{\Gamma(b)}{\Gamma(b+n)} \frac{z^n}{n!}, \quad (6.7)$$

which in the limit $r \rightarrow \infty$ behave as

$$F_l(\eta, kr) \rightarrow \sin\left(kr - \eta \ln 2kr - \frac{l\pi}{2} + \sigma_l\right). \quad (6.8)$$

In (6.6) we introduced the Coulomb parameter η which determines the strength of the Coulomb term in (6.2)

$$\eta = -\frac{Z_{\text{eff}}}{k}. \quad (6.9)$$

Inserting the radial part (6.6) back into (6.3) yields the *spherical Coulomb waves* $\Phi_{k,l}(\mathbf{r})$, which are eigenfunctions of (6.2), orthonormalized in momentum k , total angular momentum \mathbf{L}^2 , and the z -component L_z of angular momentum,

$$\langle \Phi_{k,l,m} | \Phi_{k',l',m'} \rangle = \delta(k - k') \delta_{ll'} \delta_{mm'}. \quad (6.10)$$

Since k is a continuous variable, wave functions are normalized to the Dirac delta function (or distribution), while the discrete quantum numbers l, m are orthonormalized to a Kronecker delta. Instead of normalizing in momentum space, we can also use *energy normalized* radial Coulomb functions. Due to

$$\delta(k - k') = \frac{dE}{dk} \delta(E - E'), \quad k = \sqrt{2E}, \quad (6.11)$$

they are related to the momentum normalized functions (6.6) according to

$$\phi_{E,l}(r) = \frac{\phi_{k,l}(r)}{\sqrt{k}}. \quad (6.12)$$

If we are not interested in the angular momentum quantum numbers, but want to specify a 3-vector $\mathbf{k} \equiv (k, \Omega_k)$ for the momentum, we can use the expansion

$$\psi_{\mathbf{k}}(\mathbf{r}) = \sum_{l=0}^{\infty} \sum_{m=-l}^l i^l e^{-i\sigma_l} Y_m^{l*}(\Omega_k) \Phi_{k,l}(\mathbf{r}), \quad (6.13)$$

with the *Coulomb phase* $\sigma_l = \arg[\Gamma(l+1+i\eta)]$. These functions are the solutions (for a Coulomb potential) satisfying scattering boundary conditions that converge asymptotically to eigenstates of linear momentum \mathbf{k} . *Incoming* boundary conditions are the appropriate basis states for extracting ionization probabilities [136–138].

Using these *one-electron* eigenfunctions, we construct the *double continuum* wave functions as symmetrized product states of two unscreened Coulomb waves (6.13)

with effective charge $Z_{\text{eff}} = 2$, where the symmetrization is necessary to account for the indistinguishability of the two electrons. For $\mathbf{k}_1 \neq \mathbf{k}_2$, these states are given by

$$\Psi_{\mathbf{k}_1, \mathbf{k}_2}^{DC}(\mathbf{r}_1, \mathbf{r}_2) = \frac{1}{\sqrt{2}} [\psi_{\mathbf{k}_1}(\mathbf{r}_1)\psi_{\mathbf{k}_2}(\mathbf{r}_2) + \psi_{\mathbf{k}_1}(\mathbf{r}_2)\psi_{\mathbf{k}_2}(\mathbf{r}_1)]. \quad (6.14)$$

The use of a product final state amounts to neglecting the effect of electron-electron interaction, which is a good approximation only in the asymptotic regime ($r_{12} \rightarrow \infty$).

It should be noted that in our approach of solving the TDSE, we only need the double continuum wave functions in the asymptotic region for extraction of the final momentum distributions. The correlation is thus included in the calculation at each step, the only approximation is the identification of the momenta $\mathbf{k}_1, \mathbf{k}_2$ in the product state with the asymptotic momenta of the two electrons.

In other approaches, such as time-independent perturbation theory, it is much more crucial to use an accurate representation of the continuum. This can be achieved in a number of ways, e.g. by using so-called 3C wave functions [139, 140] which consist of a product of three two-body Coulomb functions. Another approach is to use the techniques of exterior complex scaling (ECS), which can be used to transform the projection on the final states to a surface integral at the edge of the box, where the product of Coulomb waves is again a good approximation if the box is large enough [131, 141, 142]. A third approach to get the double ionization wave function is to use the J -matrix method to generate fully correlated multichannel scattering wave functions for the single continuum and then obtain the double ionization wave packet by subtracting the bound and singly ionized parts from the total wave function [62].

Inserting the partial-wave expansion (6.13) in (6.14) and switching to coupled spherical harmonics yields the double-continuum wave function in coordinate space,

$$\begin{aligned} \Psi_{\mathbf{k}_1, \mathbf{k}_2}^{DC}(\mathbf{r}_1, \mathbf{r}_2) &= \sum_{L, M} \sum_{l_1, l_2}^{\infty} i^{l_1 + l_2} e^{-i(\sigma_{l_1} + \sigma_{l_2})} [\mathcal{Y}_{l_1, l_2}^{LM}(\Omega_{k,1}, \Omega_{k,2})]^* \frac{1}{\sqrt{2}} \frac{1}{r_1 r_2} \\ &\times \left[\phi_{k_1, l_1}(r_1) \phi_{k_2, l_2}(r_2) \mathcal{Y}_{l_1, l_2}^{LM}(\Omega_{r,1}, \Omega_{r,2}) + \phi_{k_1, l_1}(r_2) \phi_{k_2, l_2}(r_1) \mathcal{Y}_{l_1, l_2}^{LM}(\Omega_{r,2}, \Omega_{r,1}) \right]. \end{aligned} \quad (6.15)$$

In analogy, we construct the *single continuum* as a symmetrized product state of a *bound state* $\Phi_{n,l,m}(\mathbf{r})$ of the He^+ ion and a Coulomb wave $\psi_{\mathbf{k}}(\mathbf{r})$ with effective charge $Z_{\text{eff}} = 1$

$$\Psi_{n,l,m,\mathbf{k}}^{SC}(\mathbf{r}_1, \mathbf{r}_2) = \frac{1}{\sqrt{2}} [\Phi_{n,l,m}(\mathbf{r}_1)\psi_{\mathbf{k}}(\mathbf{r}_2) + \Phi_{n,l,m}(\mathbf{r}_2)\psi_{\mathbf{k}}(\mathbf{r}_1)]. \quad (6.16)$$

Inserting the partial wave expansion for the Coulomb wave and the coordinate representation of $\Phi_{n,l,m}(\mathbf{r})$ yields the single continuum wave function in coordinate space. Note that the bound state is not expanded into a function of a wave vector

(as in (6.13) for the continuum wave) leaving a Clebsch-Gordan coefficient from switching to the coupled angular momentum representation.

$$\begin{aligned} \Psi_{n,l,m,\mathbf{k}}^{SC}(\mathbf{r}_1, \mathbf{r}_2) &= \sum_{L,M} \sum_{l_k=0}^{\infty} \sum_{m_k=-l_k}^{l_k} i^{l_k} e^{-i\sigma_{l_k}} [Y_{m_k}^{l_k}(\Omega_k)]^* \langle l m l_k m_k | l l_k L M \rangle \frac{1}{\sqrt{2}} \frac{1}{r_1 r_2} \\ &\times \left[\phi_{n,l}(r_1) \phi_{k,l_k}(r_2) \mathcal{Y}_{l_1, l_2}^{LM}(\Omega_{r,1}, \Omega_{r,2}) + \phi_{n,l}(r_2) \phi_{k,l_k}(r_1) \mathcal{Y}_{l_1, l_2}^{LM}(\Omega_{r,2}, \Omega_{r,1}) \right]. \end{aligned} \quad (6.17)$$

6.2 Ionization probability distributions

6.2.1 Fully differential probability distributions

By projecting the single- and double-continuum functions constructed in the previous section onto the fully correlated final state wave function, we obtain momentum probability distributions. The electron momentum distribution for *double ionization* is given by

$$P^{DI}(\mathbf{k}_1, \mathbf{k}_2) = P^{DI}(k_1, k_2, \Omega_{k,1}, \Omega_{k,2}) = |\langle \Psi_{\mathbf{k}_1, \mathbf{k}_2}^{DC} | \Psi \rangle|^2. \quad (6.18)$$

Using the expression (6.15) for the double continuum and (3.3) for the calculated wave function yields

$$\begin{aligned} P^{DI}(\mathbf{k}_1, \mathbf{k}_2) &= \frac{1}{2} \left| \sum_{L,M} \sum_{l_1, l_2}^{\infty} i^{-l_1 - l_2} e^{i(\sigma_{l_1} + \sigma_{l_2})} \mathcal{Y}_{l_1, l_2}^{LM}(\Omega_{k,1}, \Omega_{k,2}) \right. \\ &\times \left. \int_0^{\infty} \int_0^{\infty} dr_1 dr_2 R_{l_1, l_2}^L(r_1, r_2) [\phi_{k_1, l_1}(r_1) \phi_{k_2, l_2}(r_2) + \phi_{k_1, l_1}(r_2) \phi_{k_2, l_2}(r_1)] \right|^2, \end{aligned} \quad (6.19)$$

where we used the orthonormality relation

$$\langle \mathcal{Y}_{l_1, l_2}^{LM} | \mathcal{Y}_{l'_1, l'_2}^{L'M'} \rangle = \delta_{LL'} \delta_{l_1 l'_1} \delta_{l_2 l'_2} \delta_{MM'} \quad (6.20)$$

for the evaluation of the angular part of the integral in position space. Furthermore, we can use the exchange symmetry for the wave function $|\psi\rangle$

$$R_{l_2, l_1}^L(r_2, r_1) = (-1)^{(l_1 + l_2 - L)} R_{l_1, l_2}^L(r_1, r_2) \quad (6.21)$$

and obtain for the double ionization probability distribution

$$P^{DI}(\mathbf{k}_1, \mathbf{k}_2) = \left| \sum_L \sum_{l_1, l_2}^{\infty} i^{-l_1 - l_2} e^{i(\sigma_{l_1} + \sigma_{l_2})} \mathcal{Y}_{l_1, l_2}^{L0}(\Omega_{k,1}, \Omega_{k,2}) P_{l_1, l_2}^L(k_1, k_2) \right|^2 \quad (6.22)$$

with

$$P_{l_1, l_2}^L(k_1, k_2) = \sqrt{2} \int_0^\infty \int_0^\infty dr_1 dr_2 R_{l_1, l_2}^L(r_1, r_2) \phi_{k_1, l_1}^*(r_1) \phi_{k_2, l_2}^*(r_2). \quad (6.23)$$

For the six-dimensional *single ionization* probability distribution we find a similar expression,

$$P^{SI}(n, l, m, \mathbf{k}) = \left| \sum_L \sum_{l_k=0}^\infty \sum_{m_k=-l_k}^{l_k} (-i)^{l_k} e^{i\sigma_{l_k}} Y_{m_k}^{l_k}(\Omega_k) \langle l m l_k m_k | l l_k L 0 \rangle P_{l_1, l_2}^L(n, k) \right|^2 \quad (6.24)$$

with

$$P_{l_1, l_2}^L(n, k) = \sqrt{2} \int_0^\infty \int_0^\infty dr_1 dr_2 R_{l_1, l_2}^L(r_1, r_2) \phi_{n, l}^*(r_1) \phi_{k, l_k}^*(r_2). \quad (6.25)$$

Instead of using distributions differential in *momentum*, it is equally possible to use *energy* differential distributions, which can be described by the the same expressions, except for the use of energy-normalized Coulomb functions $\phi_{E, l}$ (6.12) instead of $\phi_{k, l}$ in (6.23) and (6.25).

The fully differential probability distributions (6.22) and (6.24) contain all the information about the final state momenta of the electrons. Often, it is more interesting to look at lower-dimensional distributions, obtained either by integrating out some variables of the full distribution or by choosing specific *cuts* in the six-dimensional space.

6.2.2 Energy probability distributions

Integrating out the angles Ω_1, Ω_2 in (6.22) gives the joint energy probability distribution for the two (ejected) electrons in a double ionization process

$$P^{DI}(E_1, E_2) = \sum_L \sum_{l_1, l_2}^\infty \left| P_{l_1, l_2}^L(E_1, E_2) \right|^2. \quad (6.26)$$

Integrating over E_1 or E_2 gives the single-electron energy probability distribution for double ionization,

$$P^{DI}(E) = \int_0^\infty P^{DI}(E_1, E_2) dE_1 = \int_0^\infty P^{DI}(E_1, E_2) dE_2, \quad (6.27)$$

i.e. the probability for one detected electron to have the energy E .

6.2.3 Angular probability distributions

More detailed information about a double ionization event is provided by angular differential distributions. The joint angular distribution is obtained by integrating over the energies of both electrons,

$$P^{DI}(\Omega_{k,1}, \Omega_{k,2}) = \int_0^\infty \int_0^\infty P^{DI}(E_1, E_2, \Omega_{k,1}, \Omega_{k,2}) dE_1 dE_2. \quad (6.28)$$

This gives the distribution in angles, regardless of the energies of the electrons. By dropping the integration over one of the energies, one obtains the angle-energy probability distribution, which can reveal correlations between the angular and energy degrees of freedom.

An additional observable of interest is the one-electron angular distribution, which can be characterized by the anisotropy parameters β_j , as shown in the following. The one-electron probability distribution $P^{DI}(E_1, \Omega_{k,1})$ for one electron with respect to the laser polarization axis is given by integrating (6.22) over E_2 and $\Omega_{k,2}$. Because of the total cylindrical symmetry in our system, the resulting one-electron probability distribution is independent of the azimuthal angle φ_1 . In the following, we therefore integrate over φ_1 , and consequently, $P^{DI}(E_1, \theta_1) = 2\pi P^{DI}(E_1, \Omega_{k,1})$.

$$P^{DI}(E_1, \theta_1) = \iiint P^{DI}(E_1, E_2, \Omega_{k,1}, \Omega_{k,2}) dE_2 d\Omega_{k,2} d\varphi_1. \quad (6.29)$$

Note that due to the indistinguishability of the two electrons it follows that

$$P^{DI}(E_1, \theta_1) = P^{DI}(E_2, \theta_2) = P^{DI}(E, \theta). \quad (6.30)$$

This expression can be characterized by the angular anisotropy parameters β_j , cf. e.g. [74], or $\beta = \beta_2$ and $\gamma = \beta_4$ [61] that are obtained by projecting $P(E, \theta)$ on Legendre polynomials $P_l(\cos \theta)$

$$P^{DI}(E, \theta) = P^{DI}(E) \sum_{j=0}^{\infty} \beta_j(E) P_j(\cos \theta), \quad (6.31)$$

where the energy dependence $P^{DI}(E)$ has been factored out of the sum and $\beta_0(E) = 1$, as the integral over the Legendre polynomials is zero for $j \neq 0$. As we only study ionization by either one or two photons, the coefficients of Legendre polynomials with odd j vanish. This can be seen in equation (6.35) from the 3j-symbol containing j , L and L' , with all magnetic quantum numbers equal to zero (the *parity 3j-symbol*), which is zero for odd $j + L + L'$. As L and L' are either both odd or both even ($L = 1$ for one-photon transitions, $L = 0, 2$ for two-photon transitions, $L = 1, 3, 5$ for three-photon transitions, ...) $L + L'$ is always even. Therefore, j also has to be even. In addition, because of the triangle inequality in the parity 3j-symbol, the highest j occurring in an n -photon transition is $j = 2n$.

The anisotropy parameters can be expressed by inserting the electron momentum distribution for double ionization (6.22) into equation (6.29) and analytically performing the integration

$$P^{DI}(E_1, \theta_1) = \int_0^\infty \int_{\Omega_2} \int_0^{2\pi} P^{DI}(E_1, E_2, \Omega_1, \Omega_2) dE_2 d\Omega_2 d\varphi_1 = \int_0^\infty \int_{\Omega_2} \int_0^{2\pi} \left| \sum_L \sum_{l_1, l_2} i^{-l_1-l_2} e^{i(\sigma_{l_1} + \sigma_{l_2})} \mathcal{Y}_{l_1, l_2}^{L0}(\Omega_1, \Omega_2) P_{l_1, l_2}^L(E_1, E_2) \right|^2 dE_2 d\Omega_2 d\varphi_1. \quad (6.32)$$

For brevity we will use

$$D_{l_1, l_2}^L(E_1, E_2) = i^{-l_1-l_2} e^{i(\sigma_{l_1} + \sigma_{l_2})} P_{l_1, l_2}^L(E_1, E_2) \quad (6.33)$$

in the following formulas. This corresponds to an expansion in our coupled basis representation in energy space, thus expressing the doubly ionized wave function $\Psi^{DI}(E_1, E_2, \Omega_{k,1}, \Omega_{k,2})$ in coupled spherical harmonics

$$\Psi^{DI}(E_1, E_2, \Omega_1, \Omega_2) = \sum_L \sum_{l_1, l_2} D_{l_1, l_2}^L(E_1, E_2) \mathcal{Y}_{l_1, l_2}^{L0}(\Omega_1, \Omega_2). \quad (6.34)$$

The integrals over the angles can be performed analytically by using the techniques of angular momentum coupling (as described in detail in [Appendix C](#)). The final result for the angular probability distribution $P(E_1, \theta_1)$ is then

$$P^{DI}(E_1, \theta_1) = \sum_j \sum_{\substack{L', l_1' \\ L, l_1, l_2}} (-1)^{j-L-L'-l_2} \sqrt{(2l_1+1)(2l_1'+1)(2L+1)(2L'+1)(2j+1)} \begin{pmatrix} l_1 & l_1' & j \\ 0 & 0 & 0 \end{pmatrix} \begin{pmatrix} j & L & L' \\ 0 & 0 & 0 \end{pmatrix} \begin{Bmatrix} j & l_1 & l_1' \\ l_2 & L' & L \end{Bmatrix} (D_{l_1', l_2}^{L'})^* D_{l_1, l_2}^L P_j(\cos \theta_1). \quad (6.35)$$

For $j = 2$ this formula coincides with the expression for β parameters presented by Kheifets *et al.* [74] and an analogous expression for β parameters of two-photon single ionization by Gribakin *et al.* [143].

6.2.4 Angular distribution for single ionization

Similar to the one-electron angular distribution for double ionization expressed in terms of the anisotropy parameters, we define the analogous probability distribution for single ionization by summing over the states of the bound electron

$$P^{DI}(E, \theta) = \sum_{n, l, m} \int P^{SI}(n, l, m, E, \Omega_k) d\varphi, \quad (6.36)$$

with $P^{SI}(n, l, m, E, \Omega)$ defined in (6.24). We follow the derivation for the double ionization angular distribution in Appendix C but use the singly ionized wave function ψ^{SI}

$$\psi^{SI}(n, l, m, E, \Omega_k) = \sum_{L, M} \sum_{l_k=0}^{\infty} \sum_{m_k=-l_k}^{l_k} (-i)^{l_k} e^{i\sigma_{l_k}} Y_{m_k}^{l_k}(\Omega_k) \begin{bmatrix} l & l_k & L \\ m & m_k & 0 \end{bmatrix} P_{l_1, l_2}^L(n, E), \quad (6.37)$$

with $P_{l_1, l_2}^L(n, E)$ given in equation (6.25). Instead of performing the integral over the continuum states of the second electron, we take the sum over the bound states

$$\int dE_2 d\Omega_{k,2} \longrightarrow \sum_{n,l} \sum_{m=-l}^l. \quad (6.38)$$

This yields

$$P(E, \theta_k) = \sum_j \beta_j(E) P_j(\cos \theta_k), \quad (6.39)$$

with

$$\beta_j(k) = \sum_{n,l} \sum_{\substack{L', l'_k \\ L, l_k}} (-1)^{j-L-L'-l} \sqrt{(2l_k+1)(2l'_k+1)(2L+1)(2L'+1)(2j+1)} \\ \begin{pmatrix} l_k & l'_k & j \\ 0 & 0 & 0 \end{pmatrix} \begin{pmatrix} j & L & L' \\ 0 & 0 & 0 \end{pmatrix} \left\{ \begin{matrix} j & l_k & l'_k \\ l & L' & L \end{matrix} \right\} \left((-i)^{l'_k} e^{i\sigma_{l'_k}} P_{l'_k, l}^{L'}(n, k) \right)^* \left((-i)^{l_k} e^{i\sigma_{l_k}} P_{l_k, l}^L(n, k) \right). \quad (6.40)$$

The different bound states (n, l, m) are summed up incoherently in (6.40). For a fixed n, l, m , we get the probability distribution for the free electrons associated with production of the He^+ ion in different excited (shake-up) states (e.g. $1s, 2s, 2p, \dots$).

6.3 Recoil ion momentum distribution

While the fully differential probability distribution provides very detailed information about the kinematics of a double ionization process, it is very difficult to measure this quantity in experiments. In principle, cold target recoil ion momentum spectroscopy (COLTRIMS) [144–146] can be used to measure the energies and emission directions of all three involved particles (the nucleus and the two electrons). The count rate of the events of interest is usually low, such that fully differential distributions would require very long measurement times to acquire sufficient statistics. By focusing on integrated quantities, the statistics can be improved. One possibility is to measure the momentum distribution of the recoiling nucleus. As the target gas in such an experiment consists of cold atoms with negligible speed, the final momentum of the nucleus is just the recoil obtained from the

two electrons, i.e.

$$\mathbf{Q} = -(\mathbf{k}_1 + \mathbf{k}_2). \quad (6.41)$$

Introducing the relative momentum of the electrons $\mathbf{q} = \mathbf{k}_1 - \mathbf{k}_2$, the double ionization probability distribution can be expressed as [147]

$$P^{DI}(E_Q, E_q, \Omega_Q, \Omega_q) = \left(\frac{qQ}{8k_1k_2} \right) P^{DI}(E_1, E_2, \Omega_{k,1}, \Omega_{k,2}) \quad (6.42)$$

with the Jacobian arising from the coordinate transformation from $(\mathbf{k}_1, \mathbf{k}_2)$ to (\mathbf{Q}, \mathbf{q}) and the change to the energy representation with $E_i = k_i^2/2$. Integration over the relative momentum \mathbf{q} then yields the recoil ion momentum distribution (which is again cylindrically symmetric),

$$P^{DI}(\mathbf{Q}) = \iint dE_q d\Omega_q \left(\frac{qQ}{8k_1k_2} \right) P^{DI}(E_1, E_2, \Omega_{k,1}, \Omega_{k,2}). \quad (6.43)$$

We show the recoil ion momentum distribution (which is rotationally symmetric about the laser polarization axis) integrated over one of the transversal directions, i.e. we show $P^{DI}(Q_x, Q_z) = \int dQ_y P^{DI}(\mathbf{Q})$. In our representation of the six-fold differential cross section with the expansion in coupled spherical harmonics the evaluation of (6.43) is computationally very expensive. One possible approach to evaluate this is described in [80]. We choose a different approach to generate the nuclear recoil probability distributions. We use *Monte Carlo* techniques to “simulate” a real experiment. In particular, we generate a large number N of pairs of electron momenta $(\mathbf{k}_1, \mathbf{k}_2)$ distributed according to the full probability distribution $P^{DI}(\mathbf{k}_1, \mathbf{k}_2)$ (6.22). From the momenta $(\mathbf{k}_1, \mathbf{k}_2)$ we calculate the recoil ion momentum and use this to fill a histogram, as is done in a real experiment with N counts. The accuracy of this method depends on the number N of electron pairs that we generate and the accuracy of the grid on which the probability distribution is calculated. As the nuclear recoil is an effectively only two-dimensional quantity, the accuracy requirements are not extremely critical.

6.3.1 Generation of randomly distributed electron configurations

In order to generate electron pairs distributed according to $P^{DI}(\mathbf{k}_1, \mathbf{k}_2)$, it is necessary to create random variables distributed according to an arbitrary probability density function (PDF) $\omega(x)$ over $[a, b]$ with

$$\int_a^b \omega(x) dx = 1. \quad (6.44)$$

We therefore need a change of variables [148] from the uniform distribution $u(r)$ over $[0, 1]$ generated by a random variable generator (we use the Mersenne Twister

generator [149], which has very good statistical properties and fast execution speed) to our PDF. We build up the electron pairs distributed over the whole six-dimensional $(\mathbf{k}_1, \mathbf{k}_2)$ -space in subsequent steps, using the different differential distributions presented in the last sections.

We start with the one electron energy distribution $P^{DI}(E)$ (6.27) to generate the first coordinate k_2 . In momentum space the PDF then reads

$$\omega(k_2) = \frac{P^{DI}(k_2)}{P^{DI}}, \quad \int_0^\infty \frac{P^{DI}(k_2)}{P^{DI}} dk_2 = 1. \quad (6.45)$$

For the mapping $r \rightarrow k_2$ from the uniformly distributed r we use the *cumulative distribution function* (CDF)

$$W(k_2) = \int_0^{k_2} dk'_2 \frac{P^{DI}(k'_2)}{P^{DI}}, \quad (6.46)$$

which is obtained by numerical integration. We use the uniform distribution $u(r)$ to randomly pick a value for $W(k_2)$, from which k_2 is obtained by inversion, such that we get k_2 distributed according to $P^{DI}(k_2)/P^{DI}$.

For the next step we use the joint energy distribution $P^{DI}(k_1, k_2)$ to obtain k_1 . Subsequent use of the angular distribution and fully differential probability distribution yields the full set $k_1, \theta_1, \varphi_1, k_2, \theta_2, \varphi_2$ for one electron configuration. Note that the flexibility of this approach allows to easily generate *any* probability distribution of the two electrons, although we currently only use it for the nuclear recoil distributions. We have, however, tested the accuracy of the approach by comparing to the analytically calculated distributions given in the previous sections.

7 Eigenstates

As a test for our method, we present some results on the eigenstates of the non-relativistic Hamiltonian (2.9). We compare these results with various published data.

Solving the eigenproblem of the Hamiltonian (i.e. the time-independent Schrödinger equation) is not possible for realistic problem sizes by direct diagonalization of the matrix representation of the Hamiltonian in our basis. This is because we have chosen a representation that is optimized for a computationally cheap evaluation of the Hamiltonian and a good representation of *many* eigenstates, from the lowest-lying bound states up to high-lying doubly ionized states. We therefore use an approach based on Krylov subspace methods to calculate just some of the eigenvalues and eigenvectors of the Hamiltonian. We utilize the ARPACK package [150], which implements a variant of the Implicitly Restarted Arnoldi Method [151]. This package can be used to calculate the lowest eigenstates of a sparse matrix without having to construct the matrix explicitly – the only required operation is the application of the matrix to a vector. In the following, we give some benchmark results obtained with this method, both for bound states as well as for doubly excited resonances. In our approach, the accuracy of the eigenenergies of the Hamiltonian depends on both the quality of the radial grid as well as the size of the angular momentum expansion (determined by $l_{<,max}$, $l_{>,max}$ for a fixed L). The results we give in the following were obtained using typical grids used for time propagation, i.e. not optimized to give the best possible energies. The finite elements of the radial FEDVR grid had an extension of 4 a.u., with order 11 for the DVR, while the angular momentum expansion used $l_{<,max} = l_{>,max} = 8$.

The “exact” ground state energy of the infinite-mass nonrelativistic Hamiltonian (2.9) is [152]

$$E_0 = -2.903724377 \dots \text{ a.u. .} \quad (7.1)$$

Relativistic corrections give a value of -2.903700023 a.u. [100, 153], while the experimentally measured value is -2.903693775 a.u. [154]. Standard (single-configuration) Hartree-Fock calculations [101] yield a ground state energy of about -2.86168 a.u. and the difference to the exact value is sometimes (especially in the field of quantum chemistry) referred to as *correlation energy* $E_C = 0.042044$ a.u. since this contribution from the residual two-body interaction cannot be obtained from a mean-field potential. Our method using the numerical parameters given above yields a ground

state energy of $E_0 = -2.90366$ a.u., i.e. an absolute error of $\approx 6 \cdot 10^{-5}$ a.u., which translates to a relative error of $\approx 2 \cdot 10^{-3}\%$.

In table 7.1 we compare our results for the first $^1S^e$ bound states with “exact” values taken from [155] and find excellent agreement, with all but the ground state agreeing on at least 6 digits.

	exact values	our values
ground state	-2.90372	-2.90366
$1s\ 2s$	-2.14597	-2.14597
$1s\ 3s$	-2.06127	-2.06127
$1s\ 4s$	-2.03359	-2.03359

Table 7.1: Comparison of the calculated energies (in a.u.) for the first $^1S^e$ bound states (characterized by the approximate single particle states) with the exact values.

7.1 Doubly excited resonances

The doubly excited states of (ortho-)helium are all embedded in (single) ionization continua (cf. section 2.4). Hence, they are not bound integrable states, but auto-ionizing *resonances* with a finite lifetime. These states are therefore characterized not only by their energy E_R , but also by their *width*⁵ Γ , which is related to the lifetime as $\Gamma = \tau^{-1}$. In the doubly excited states, the electron-electron interaction has considerably higher influence on the states, as the electrons are further away from the nucleus, and the coupling to the continuum is mediated by this interaction. Therefore, the labeling of states by the dominant independent particle-configuration (which can be done for singly excited states) breaks down, and the classification is usually done by the introduction of new approximate quantum numbers. We do not discuss this here in more detail, and simply identify the states by their total symmetry, energy and width. In order to obtain the resonance energies as well as the widths, the complex absorbing potential (cf. section 5.4) has to be included in the Hamiltonian, such that the operator is no longer Hermitian, but complex symmetric.

In Table 7.2 we present the energies and widths of some of the resonances (doubly excited states) for total symmetries $^1S^e$, $^1P^o$, and $^1D^e$ as obtained by our method. The values are compared with results from an exterior complex scaling (ECS) calculation by Scrinzi and Piraux which are accurate up to 10^{-4} a.u. [155, 156] and results for the $^1S^e$ states from Bürgers *et al.* [157], who employ perimetric coordinates and a complex scaling technique. The agreement between the three different methods is very good.

⁵ which together form the quasi-energy $E = E_R - i\Gamma/2$

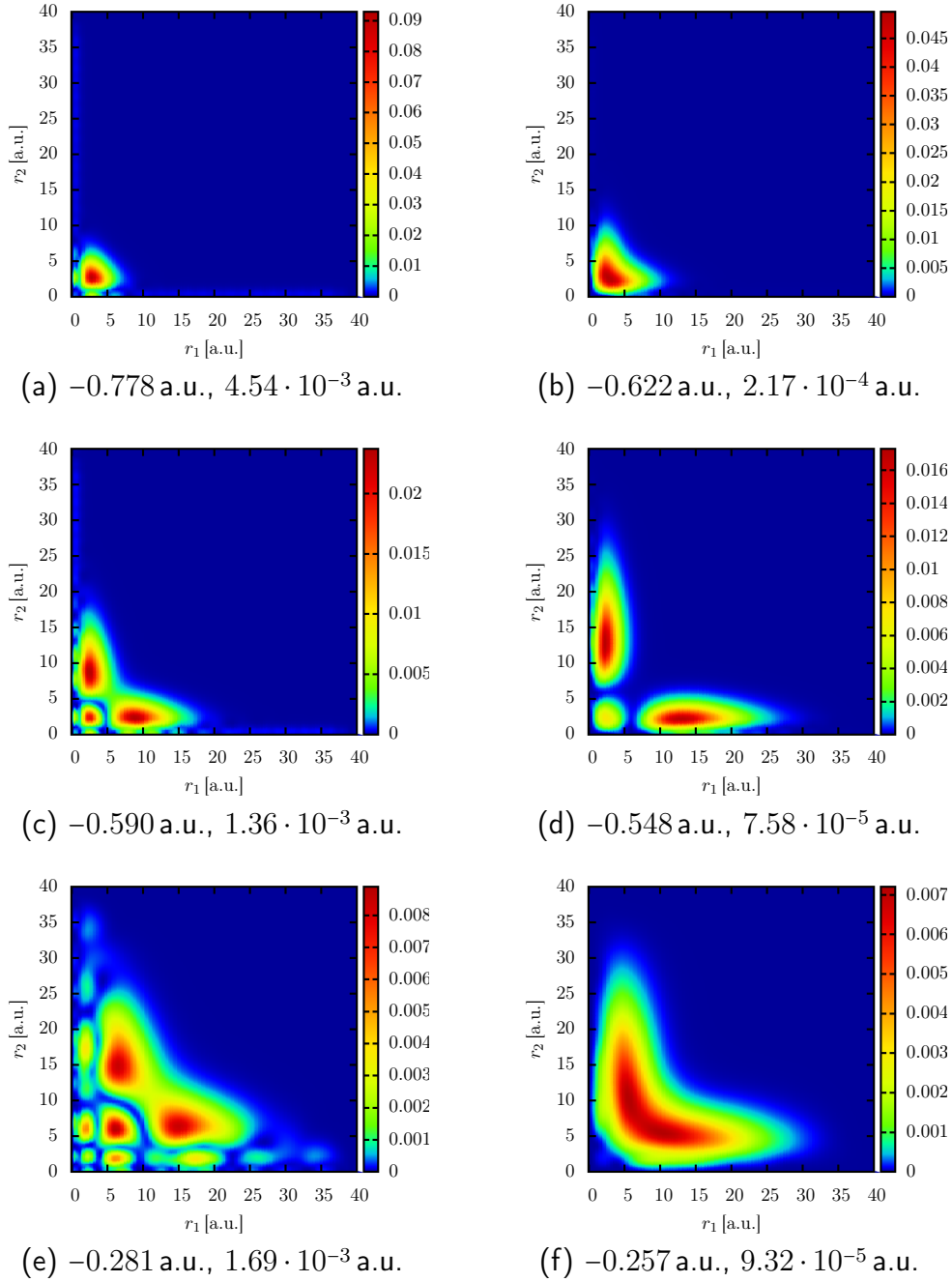


Figure 7.1: Radial probability distributions $P(r_1, r_2)$ of some doubly excited states associated with total symmetry $^1S^e$. The labels give the energies E_R and widths Γ .

	values from [155] (a.u.)		calculated values (a.u.)		values from [157] (a.u.)	
	energy	width	energy	width	energy	width
$^1S^e$	-0.77787	4.55E-03	-0.77786	4.54E-03	-0.77787	4.54E-03
	-0.62193	2.16E-04	-0.62174	2.17E-04	-0.62192	2.16E-04
	-0.58989	1.37E-03	-0.58989	1.36E-03	-0.58989	1.36E-03
	-0.54809	6.83E-05	-0.54806	7.58E-05	-0.54809	7.48E-05
	-0.35352	2.98E-03	-0.35351	2.48E-03	-0.35354	3.01E-03
$^1P^o$	-0.69313	1.37E-03	-0.69306	1.37E-03		
	-0.59707	3.86E-06	-0.59707	3.84E-06		
	-0.56409	2.93E-04	-0.56407	3.01E-04		
	-0.33561	6.92E-03	-0.33652	9.25E-03		
$^1D^e$	-0.70194	2.36E-03	-0.70188	2.37E-03		
	-0.56925	6.93E-04	-0.56920	5.58E-04		
	-0.55640	3.60E-04	-0.55642	1.99E-05		
	-0.34309	5.17E-03	-0.34365	5.35E-03		

Table 7.2: Energies and widths (all in a.u.) obtained using ARPACK for some $^1S^e$, $^1P^o$, and $^1D^e$ resonances of helium compared with the results in [155] and [157] for $^1S^e$.

Fig. 7.1 shows the radial probability distributions of the eigenstates associated with some of these doubly excited states. We only show eigenstates with total symmetry $^1S^e$, as the general forms are similar for other total symmetries. The figure demonstrates the strongly differing character of the various resonances. For resonances with a short lifetime (large width), the singly ionized continuum contribution to the state can be seen as a faint light blue region close to the axes. The lifetimes of the more highly excited states are not extremely accurate, as part of the bound part of the wave function already reaches the absorbing boundary layer.

The signature of the doubly excited states can also be seen in the single ionization cross section by photon impact. Here, the double excited resonance acts as an additional pathway for photon absorption. The interference between the direct coupling to the continuum and the indirect coupling through the doubly excited state gives rise to the well-known *Fano resonances* [158, 159] in the electron emission spectrum. This represents one of the most direct processes which reveals many-electron effects in atomic transitions [160].

Part II

Two-photon double ionization

8 Introduction

Two-photon double ionization (TPDI) of helium is one of the simplest multi-photon processes involving electron correlation. Consequently, TPDI of atomic helium has been the subject of intense theoretical studies in the past few years [40–42, 45–90]. Most of the existing literature deals with either (i) cross sections in the *nonsequential* regime of TPDI, or with (ii) the effects of ultrashort (attosecond) XUV pulses in the *sequential* regime of TPDI. Although the cross sections for nonsequential TPDI have attracted a significant amount of interest by theoreticians, the published results show large discrepancies between some different approaches. However, in the last few years, agreement has been observed between some quite different approaches for which the convergence has been extensively tested [40, 80, 88]. There are much fewer experimental studies as of yet, all of which are concerned with the nonsequential regime [81, 91–94]. For these, the experimental uncertainties are still too large to help in resolving the discrepancies in the theoretical results.

These investigations are motivated by the development of novel light sources in recent years. These sources produce coherent, intense and ultrashort pulses in the vacuum ultraviolet (VUV) and extreme ultraviolet (XUV) region. One technology is the free electron laser (FEL) [13–22], where a beam of electrons at relativistic velocities traverses an undulator. Through the process of self-amplified spontaneous emission (SASE), the electrons produce a high-intensity beam at XUV energies. Currently, there are two FELs in the VUV-XUV and X-ray regime (XFELs) in operation: FLASH at DESY in Hamburg, Germany [20, 21], and LCLS in Stanford, USA, which has just achieved lasing at the design wavelength. FLASH has reached focused intensities of up to 10^{16} W/cm², and photon energies as high as 190 eV, while LCLS reaches energies up to a few keV. The duration and temporal structure of the individual FEL pulses is not well known, but is of the order of 10–50 femtoseconds for FLASH. In addition, there have been a number of proposals aimed to decrease the duration of these pulses to a few hundred attoseconds [22, 161–166].

Another approach to produce intense ultrashort pulses at XUV wavelengths is to use high harmonic generation (HHG) from a driving infrared (IR) laser [23–32]. This technique has been successfully used to create the shortest pulses available today, with durations down to 80 as [31]. With current technology, attosecond pulses are much less intense than FEL pulses. The focused intensities are not well known but typically do not exceed $\approx 10^{12}$ W/cm². The main problem preventing higher intensities in HHG from gas targets is the loss of phase matching as the XUV and IR propagate in the generating gas medium. Various ways to increase

the maximally available intensity have been proposed, such as circumventing the loss of phase matching [167–169] or using solid targets, which allow for the use of far higher driving IR intensities, creating a relativistic plasma and harmonics up to very high orders [170–173].

The continuing development of such intense sources has led to an increased interest in multi-photon processes. An important aspect of these sources is their ability to produce *ultrashort* pulses, with durations of a few femtoseconds for FELs and down to less than a hundred attoseconds for HHG. This has in turn enabled the study of *time-resolved* electronic dynamics, starting the field of *attosecond science* [33–37].

Calculations for two-photon ionization employ either a time-independent (TI) or a time-dependent (TD) approach. TI methods involve either lowest-order perturbation theory (LOPT) or *R*-matrix Floquet theory, and are only applicable in the limit of (infinitely) long pulses. TD methods are based on a direct solution of the time-dependent Schrödinger equation and are therefore not restricted to any given order of the perturbation or pulse duration. The results we present in the following are mostly calculated at moderate intensities of the XUV field ($\sim 10^{12}$ W/cm²). At this intensity, corrections to LOPT are expected to be small. The decisive advantage of TD methods here stems from a different aspect. Namely, TI calculations of processes involving correlated two-electron final states in the continuum, $\Psi_{\mathbf{k}_1, \mathbf{k}_2}(\mathbf{r}_1, \mathbf{r}_2)$, require the knowledge of the final state in the entire configuration space in order to calculate the two-photon transition amplitude $t_{i \rightarrow \mathbf{k}_1, \mathbf{k}_2}^{(2)}$ (cf. (8.4a)). As the numerical or analytical determination of accurate correlated continuum final states remains a challenge, evaluation of $t_{i \rightarrow \mathbf{k}_1, \mathbf{k}_2}^{(2)}$ involves, inevitably, additional approximations that are difficult to control. Adding the time as an additional degree of freedom to the six spatial dimensions of the two-electron problem allows one to bypass the determination of $\Psi_{\mathbf{k}_1, \mathbf{k}_2}$. Instead, we propagate the wave packet for sufficiently long times such that we can extract the relevant dynamical information entirely from the asymptotic region where electron correlations become negligible. Moreover, residual errors can be controlled by systematically varying the propagation time. This advantage comes along with a distinct disadvantage: Results will, in general, depend on the time-structure imposed on the external perturbation, specifically on the duration and temporal shape of the XUV pulse. A comparison with TI calculations on the level of (generalized) cross sections therefore requires a careful extraction of information and checks of the independence from pulse parameters.

8.1 Sequential and nonsequential regimes of TPDI

The nature of the two-photon double ionization (TPDI) process depends strongly on the photon energy $\hbar\omega$. In order to doubly ionize the helium atom, $\hbar\omega$ has to be large enough so that two photons can fully ionize the helium atom, i.e. $2\hbar\omega > I_1 + I_2 = -E_0$,

where $I_1 \approx 24.6$ eV and $I_2 \approx 54.4$ eV are the first and second ionization potentials of helium, while $E_0 \approx -79$ eV is the total ground state energy. In a “long” pulse with an approximately delta-like energy spectrum, there are two distinct regimes of TPDI, depending on the photon energy. In “real” pulses with finite spectral width, the photon energy is described by a distribution $\mathcal{F}(\omega)$. The following arguments thus depend on the assumption that the width of that distribution is sufficiently small for the regime to be identified unambiguously.

For $\hbar\omega > I_2$, one photon has enough energy to ionize the He^+ ion in its ground state. In this regime, an independent-particle picture is applicable for long pulses: each electron absorbs one photon and electron-electron interaction is a priori not required for double ionization to occur. Therefore, the double ionization can proceed in two well-separated steps, and this energy regime is called the *sequential* regime. The first electron is ejected with energy $E_1 = \hbar\omega - I_1$, carrying with it the energy contained in the electron-electron interaction in the ground state. At a later time, when the first electron is well separated from the remaining ion, the second electron is ejected with the energy $E_2 = \hbar\omega - I_2$. In long pulses, this is the dominant process, leading to an electron energy spectrum with two sharp peaks at E_1 and E_2 . In the limit of low pulse intensities, where depletion can be neglected, the total yield is proportional to the square of the pulse duration ($P_{\text{seq}}^{DI} \propto T^2$), taken to be the signature of the sequential (two-step) nature of the process.

For high photon energies, different sequential pathways become accessible. The first photon absorption can produce *shake-up* in the remaining He^+ ion, leaving it in an excited state, with the second absorption proceeding from this excited state. These pathways are accessible for the sequential process when one photon provides enough energy to strip one electron from the atom and simultaneously excite the ion to a higher state, i.e. if $\hbar\omega > I_1 + \mathcal{E}_n$, where $\mathcal{E}_n = (2 - 2/n^2)$ a.u. is the excitation energy to the n th shell of the He^+ ion. In long pulses and for high photon energies, this leads to shake-up satellite lines in the electron energy spectrum [174]. While the first ionization potential is increased for shake-up ionization, the second ionization potential is decreased ($I'_2 = I_2/n^2$). Consequently, the peak positions $E'_1 = \hbar\omega - I_1 - \mathcal{E}_n$, $E'_2 = \hbar\omega - I_2 + \mathcal{E}_n$ are different from those without shake-up, but the overall picture of sequential and independent photoionization events remains unchanged. There are, however, two reasons why some correlation between the electrons can be expected even for long pulses: for one, the electron that is emitted later is *faster* than the first electron in the shake-up pathway. If the electrons are emitted in the same direction, the second electron can thus collide with the first one, modifying the independent-particle behavior. In addition, the excited states of the He^+ ion are (almost) degenerate in angular momentum, such that the He^+ ion can remain in a superposition of excited states, with the coefficients depending on the emission angle of the first electron. This can also cause non-vanishing correlation between the electrons even in very long pulses. As the photon energy approaches the threshold for one-photon double ionization at $\hbar\omega = -E_0$,

successively higher shake-up states become accessible. However, the probability for shake-up quickly decreases with the quantum number n of the leftover excited state, such that typically, only the first few excited states play a role even if more are energetically accessible.

If the photon energy $\hbar\omega$ is smaller than the second ionization potential I_2 , the sequential process can not occur. The two photons still provide enough energy to doubly ionize the helium atom, but only if the two electrons share the available energy. This regime is called the *nonsequential* regime. This implies that the process can only happen if both photons are absorbed almost simultaneously. The two consequences of this are that the energy of the intermediate state, which is only populated transiently, does not need to be $\hbar\omega - I_1$ (because of the quantum mechanical time-energy uncertainty), and that the electrons can interact and exchange energy. Consequently, the asymptotic energies of the electrons in the final state do not have to be $E_1 = \hbar\omega - I_1$ and $E_2 = \hbar\omega - I_2$ (where for $\hbar\omega < I_2$, E_2 would be negative and therefore not correspond to a free electron). Because the photons have to be absorbed quasi-simultaneously, the total double ionization yield in the nonsequential regime is linearly proportional to the pulse duration, $P_{\text{nonseq}}^{DI} \propto T$ as long as depletion can be neglected.

It should be stressed that even in the sequential spectral regime, there are non-sequential contributions to the total double ionization which can be identified by their T^k ($k = 1$) scaling. In particular, final states where the electron energies are not at the sequential peaks are only reached by nonsequential processes.

8.2 Second-order perturbation theory

Before turning to the numerical results, we discuss the structure of the two-photon transition by examining the second-order time-dependent perturbation theory expression describing the transition. In the interaction or Dirac picture of quantum mechanics, the wave function in time-dependent perturbation theory is given up to second order by

$$|\Psi_I(t)\rangle = |\Psi_I^{(0)}(t)\rangle + |\Psi_I^{(1)}(t)\rangle + |\Psi_I^{(2)}(t)\rangle + \dots \quad (8.1a)$$

$$|\Psi_I^{(0)}(t)\rangle = |\Psi_I(t_0)\rangle \quad (8.1b)$$

$$|\Psi_I^{(1)}(t)\rangle = \frac{1}{i} \int_{t_0}^t dt_1 \hat{V}_I(t_1) |\Psi_I(t_0)\rangle \quad (8.1c)$$

$$|\Psi_I^{(2)}(t)\rangle = \frac{1}{i^2} \int_{t_0}^t dt_1 \hat{V}_I(t_1) \int_{t_0}^{t_1} dt_2 \hat{V}_I(t_2) |\Psi_I(t_0)\rangle, \quad (8.1d)$$

where we have split the Hamiltonian according to $\hat{H} = \hat{H}_0 + \hat{V}(t)$ and $V_I(t) = U_0^\dagger(t, t_0) \hat{V}(t) U_0(t, t_0)$, with $U_0(t, t_0) = \exp(-i\hat{H}_0(t - t_0))$. $|\Psi_I(t_0)\rangle = |\Psi(t_0)\rangle = |i\rangle$ is

the initial state at time t_0 , in our case the ground state of the helium atom. The transition amplitude to a final state $|f\rangle$ is given by $t_{i \rightarrow f} = \langle f | \Psi_I(t_f) \rangle$, where t_f is a time after the perturbation has been turned off.

As we are interested in two-photon double ionization, we drop the zero-order and first-order terms in (8.1a). In addition, we choose $t_0 = 0$, insert a complete set of eigenstates of \hat{H}_0 (which has discrete and continuous parts) between the interaction operators, and assume that the final state is an eigenstate of \hat{H}_0 with energy E_f . The expression for the second-order transition amplitude after the end of the laser pulse is then

$$t_{i \rightarrow f}^{(2)} = - \sum_n \int_0^{t_f} dt_1 \int_0^{t_1} dt_2 \langle f | e^{iH_0 t_1} \hat{V}(t_1) e^{-iH_0 t_1} | n \rangle \langle n | e^{iH_0 t_2} \hat{V}(t_2) e^{-iH_0 t_2} | i \rangle \quad (8.2)$$

$$t_{i \rightarrow f}^{(2)} = - \sum_n \int_0^{t_f} dt_1 \int_0^{t_1} dt_2 e^{iE_f t_1} e^{iE_n t_2} \langle f | \hat{V}(t_1) | n \rangle \langle n | \hat{V}(t_2) | i \rangle, \quad (8.3)$$

with $E_{fn} = E_f - E_n$ and $E_{ni} = E_n - E_i$. We insert the specific form of our interaction operator in velocity gauge, $\hat{V}(t) = (\hat{p}_{z,1} + \hat{p}_{z,2})A(t) = \hat{\mu}A(t)$, where we define $\hat{\mu}$ as the total dipole operator. Each term in the sum over intermediate states then factorizes into a product of a function that just depends on the energies of the involved states and the temporal shape of the interaction potential, and a matrix element describing the transition via two dipole operators,

$$t_{i \rightarrow f}^{(2)} = - \sum_n \langle f | \hat{\mu} | n \rangle \langle n | \hat{\mu} | i \rangle \mathcal{G}(E_{fn}, E_{ni}, A(t)) \quad (8.4a)$$

$$\mathcal{G}(E_{fn}, E_{ni}, A(t)) = \int_0^{t_f} dt_1 \int_0^{t_1} dt_2 e^{iE_{fn} t_1} e^{iE_{ni} t_2} A(t_1) A(t_2). \quad (8.4b)$$

We first analyze the shape function \mathcal{G} in more detail. This function contains that part of the information about the probability amplitudes of the transition that stems just from the temporal shape of the driving pulse, but does not contain any system-specific information. To represent an ultrashort laser pulse, we choose a specific shape for the time dependence of the laser vector potential, a sine-squared pulse of total duration T at mean frequency ω and with peak vector potential A_0 (other choices, such as a Gaussian envelope, lead to essentially the same results),

$$A(t) = A_0 \cos(\omega t) \begin{cases} \sin(\pi t/T)^2 & 0 < t < T \\ 0 & \text{otherwise} \end{cases}. \quad (8.5)$$

Inserting $A(t)$ into \mathcal{G} , setting $t_f = T$, using $\cos(\omega t) = \frac{1}{2}(\exp(i\omega t) + \exp(-i\omega t))$ and keeping only the exponential corresponding to *absorption* of a photon (rotating

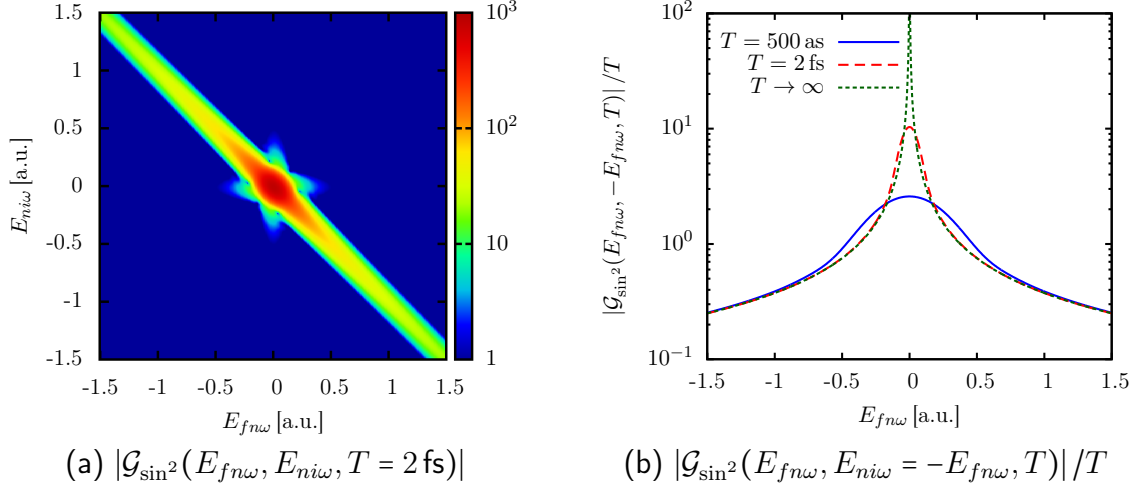


Figure 8.1: Pulse-dependent shape function $|\mathcal{G}_{\sin^2}(E_{fn\omega}, E_{ni\omega}, T)|$ in two-photon transitions. The color scale in (a) is logarithmic. The values on the diagonal $E_{fn\omega} = -E_{ni\omega}$, shown in (b), have been rescaled with $1/T$ to allow direct comparison between different pulse durations. The shapes differ only around the peak $E_{fn\omega} = 0$, while the tails converge to $1/|E_{fn\omega}|$.

wave approximation) leads to

$$\mathcal{G}_{\sin^2}(E_{fn\omega}, E_{ni\omega}, A_0, T) = \frac{A_0^2}{4} \int_0^T dt_1 \int_0^{t_1} dt_2 e^{iE_{fn\omega}t_1} e^{iE_{ni\omega}t_2} \sin\left(\pi \frac{t_1}{T}\right)^2 \sin\left(\pi \frac{t_2}{T}\right)^2, \quad (8.6)$$

where $E_{fn\omega} = E_{fn} - \omega$ and $E_{ni\omega} = E_{ni} - \omega$ quantify the deviation from energy conservation in each step. This is a definite integral that can be evaluated explicitly. However, the final result is unwieldy and does not directly provide much insight, so it is not reproduced here.

Fig. 8.1 shows $|\mathcal{G}_{\sin^2}(E_{fn\omega}, E_{ni\omega}, A_0, T)|$ for a laser pulse of total duration $T = 2 \text{ fs}$ with $A_0 = 1$. In the limit of long pulses, energy conservation for the whole two-photon process implies that $E_f - E_i = 2\omega$, i.e. $E_{fn\omega} = -E_{ni\omega}$. This is clearly seen in Fig. 8.1a – there is only significant probability for a transition around the diagonal $E_{fn\omega} = -E_{ni\omega}$. If energy conservation is fulfilled separately in each step, i.e. if $E_{fn\omega} = E_{ni\omega} = 0$, the shape function shows a pronounced peak. In this case, both transitions are resonant, and there can be an “infinite” time delay between the two photon absorptions. This peak thus corresponds to the sequential process, where the absorption proceeds in two separate steps. The width of this main peak at $E_{fn\omega} = E_{ni\omega} = 0$ is determined by the uncertainty in the photon energy, i.e. the spectral bandwidth of the laser pulse. Specifically, for the \sin^2 pulse the FWHM

of $|\mathcal{G}_{\sin^2}|^2$ along the diagonal $E_{fn\omega} = -E_{ni\omega}$ is given by $11.17/T$ (for width and T in atomic units, corresponding to ≈ 7.35 eV for $T = 1$ fs). This is almost identical to the FWHM of the spectral distribution, which is given by $9.05/T$ (again in atomic units, or ≈ 5.96 eV for $T = 1$ fs).

The spectral bandwidth (and thus, the duration) of the pulse thus determine the width of the main peak, where both steps satisfy energy conservation separately. However, if the intermediate state is only populated transiently, the quantum-mechanical time-energy uncertainty allows for violation of energy conservation. The intermediate state thus does not have to be on-shell. Stated differently, the system can “borrow” energy from the field if it “returns” it quickly enough. The larger the deviation from energy conservation, the shorter the time that the intermediate state can be occupied. This is *not* related to the uncertainty in the photon energy. Accordingly, even in long pulses, the shape function is non-zero for large absolute values of $E_{ni\omega}$ and $E_{fn\omega}$, as long as the final state is on-shell (i.e. $E_{ni\omega} = -E_{fn\omega}$). For large values of $|E_{fn\omega}|$, the value of the shape function approaches the infinite-pulse limit even for short pulses, with an agreement of better than 3% for $|E_{ni\omega}| > 30.4/T$ (in atomic units). Conversely, for a given value of $|E_{ni\omega}|$, the total pulse duration T has to be larger than $30.4/|E_{ni\omega}|$ to observe linear scaling with the pulse duration to within 3%. This again demonstrates that the intermediate states are only transiently populated for large $|E_{ni\omega}|$ – even a short pulse is then much longer than the population time of the state, such that the long-pulse limit is reached earlier.

In the limit of infinite pulse duration, the rate of the process, i.e. the modulus squared of the shape function divided by the pulse duration, reduces to

$$\lim_{T \rightarrow \infty} \frac{|\mathcal{G}(E_{fn\omega}, E_{ni\omega}, A(t))|^2}{T} \propto \lim_{\eta \rightarrow 0} A_0^4 \frac{\delta(E_{fn\omega} + E_{ni\omega})}{|E_{ni\omega} + i\eta|^2}. \quad (8.7)$$

The (omitted) prefactors depend on the pulse shape used. The total transition is then described by the well-known expression for Fermi’s golden rule in second-order perturbation theory. **Fig. 8.1b** shows the diagonal of $|\mathcal{G}_{\sin^2}|^2$ along the line $E_{ni\omega} = -E_{fn\omega}$, along with the limiting value of $1/|E_{ni\omega}|$. Even for a relatively short pulse of total duration 2 fs, the time-dependent expression reaches the time-independent limit about 0.3 a.u. away from the main peak.

In addition to the shape function, which does not contain any system-specific information, there is a second ingredient necessary to calculate the transition amplitudes $t_{i \rightarrow f}$. These are the matrix elements $\langle f | \hat{\mu} | n \rangle \langle n | \hat{\mu} | i \rangle$ in (8.4a). The system under consideration determines both the available spectrum of initial, intermediate and final states as well as the numerical values for the matrix elements.

If the system of interest were a few-level system with a purely discrete spectrum, the shape function would only have to be evaluated for a few specific values of $E_{fn\omega}, E_{ni\omega}$. In the case of double ionization of helium, however, there is a continuum

of states for both the intermediate as well as the final states. The initial state is the ground state, denoted by $|1s^2\rangle$, while the final state is $|\Psi_{\mathbf{k}_1, \mathbf{k}_2}\rangle$, where \mathbf{k}_1 and \mathbf{k}_2 are the final asymptotic momenta of the two electrons. The intermediate states are, in principle, *all* eigenstates of the field free Hamiltonian (2.9). The dipole selection rules from the ground state reduce these to only states with symmetry $^1P^o$. Even with this restriction, the sum contains excited states, singly ionized states (possibly with excitation of the remaining ion), and doubly ionized states. However, it is possible to determine the most important contributions to the total transition amplitude based on qualitative arguments. These arguments depend on the final state of interest, and therefore also on the regime. The importance of the contribution of a given intermediate state to some final state depends on both the shape factor \mathcal{G} for that intermediate state as well as the matrix elements associated with it.

We first analyze the sequential regime, where the photon energy ω is larger than the second ionization potential $I_2 = 54.4\text{eV}$. We also assume that the photon energy is below the energy needed to produce shake-up ionization, i.e. ionization with associated excitation of the remaining ion. In that case, there is only one intermediate state that is on-shell ($E_{ni\omega} = 0$). This state is the singly ionized state $|\epsilon_1 p 1s\rangle$, with $\epsilon_1 = \omega - I_1$. The matrix element of the first transition, $\langle \epsilon_1 p 1s | \hat{\mu} | 1s^2 \rangle$, is proportional to the square root of the well-known single-ionization cross section of He. From this intermediate state, there is a continuum of final states that can be reached while fulfilling energy conservation. These are states of the form $|E_1 l_1 E_2 l_2\rangle$, with total symmetry $^1S^e$ or $^1D^e$ and where E_1 and E_2 are the asymptotic energies of the two electrons, with the energy conservation condition $E_1 + E_2 = E_0 + 2\omega$. While all of these states are energetically allowed, the matrix elements for the second transition, $\langle E_1 l_1 E_2 l_2 | \hat{\mu} | \epsilon_1 p 1s \rangle$, strongly differ. Unfortunately, because of the correlation in both the intermediate and final states, there are no explicit expressions for these transition matrix elements, and even numerical approximations are very difficult to calculate. However, the value of the transition elements is strongly peaked around $E_1 = \epsilon_1$. This can be understood because in the part of configuration space where the electrons are far apart from each other, the fully correlated eigenstates are reasonably well approximated by the product of solutions of the single-particle Hamiltonian without electron-electron interaction. If the eigenfunctions in this element are approximated by the uncorrelated product of the single-particle functions, the absolute value of the matrix element is just the product of a delta function and the single-ionization cross section of He^+ , i.e. $\langle E_1 l_1 E_2 l_2 | \hat{\mu} | \epsilon_1 p 1s \rangle \approx \delta_{l_1, p} \delta(E_1 - \epsilon_1) \delta_{l_2, p} \langle E_2 l_2 | \hat{p}_z | 1s \rangle$. This approximation is employed in [75, 80, 83, 88], where it is shown to give relatively good agreement for the singly differential cross section $d\sigma/dE$. It can not, however, explain the angular and angle-energy correlations that are observed in the full calculation.

The above approximation, which only includes a single intermediate state for any given final state, neglects the coherent superposition of intermediate states that are

all coupled to the same final state. As we have established before, transitions where energy conservation for the intermediate state is not fulfilled are exactly those transitions for which the intermediate state is only populated transiently. This means that in (8.1d), t_1 is only slightly larger than t_2 . Consequently, the second transition only probes the part of the intermediate wave packet where the first electron is still close to the core. This also implies that the two electrons are close to each other and have not yet reached their asymptotic energies. The transition via an off-shell intermediate state therefore probes exactly the part of the wave function where the electronic interaction is strong, i.e. where there is strong correlation. Therefore, the final states reached in the transition through an off-shell intermediate state should display clear signs of correlation.

We adopt the following convention for the nomenclature (i.e. when to call a transition “nonsequential” or “sequential”): (i) If the population in the final states of interest is linearly proportional to the duration of the pulse (equivalently, if the rate of the transition converges to a stable value as $T \rightarrow \infty$), we call this a *nonsequential* process. (ii) If the population in the final states is proportional to the square of the pulse duration, we call it a *sequential* process. These definitions agree with the intuitive meaning of “nonsequential” and “sequential” – nonsequential processes only occur if the two photon absorptions are confined to within a short time of each other, while in a sequential process, there can be an arbitrary delay between the photon absorptions. The definitions also agree with the usual nomenclature of the sequential vs. the nonsequential regime. Nonsequential processes are also often called “direct” transitions. In particular, this is the more common notion when only discrete states are involved – a direct transition is then one where the single intermediate state is off-resonant. In the case of TPDI of helium, there is a continuum of intermediate and final states, some of which are resonant and some of which are not, but all of which contribute to the total ionization. Note that the scaling behavior with T and T^2 implicitly assumes that the laser intensity, determined by A_0 , is small enough such that depletion can be neglected.

After this discussion of the general properties of two-photon transitions, we now turn to specific examples of TPDI in helium. In [chapter 9](#), we discuss the convergence properties of our method, with a particular focus on the validity of the projection onto products of Coulomb waves for extracting the final double ionization momentum distribution. After having established the convergence of our method, we discuss the nonsequential regime in [chapter 10](#), where total cross sections have been calculated by a number of authors. The well-defined cross section and the plethora of available results affords the opportunity to discuss the advantages and disadvantages of our approach. Parts of this work were published in [40].

In [chapter 11](#), we then discuss the long-time limit of TPDI as the photon energy is scanned from the nonsequential to the sequential regime and across the threshold for shake-up (excitation) ionization. Here, we focus on different measures to observe and quantify correlations, with a focus on angular correlation. In [chapter 12](#), we

investigate the dependence on pulse duration in the sequential regime. We discuss both the limit of ultrashort pulse durations as well as the behavior in longer pulses up to a few femtoseconds duration. In particular, we show an interference effect between nonsequential and sequential contributions from the channel without and with shake-up of the remaining ion. Some of the results presented in these two chapters were published in [41, 42].

9 Convergence issues

In this section, we investigate the convergence behavior of our approach, utilizing the test case of TPDI. Particular focus will be put on the convergence of the cross sections in nonsequential TPDI. To this end, we test the validity of the projection onto uncorrelated products of Coulomb waves as the final states and show that this is, indeed, a good approximation if one waits long enough after the end of the pulse, such that the electrons have reached the asymptotic region where interactions become negligible. In addition, we have performed detailed convergence tests as a function of gauge, spatial grid structure, and partial wave decomposition. Furthermore, we investigate the role of the pulse duration and pulse shape for extracting cross sections.

For the two-photon double ionization cross section in the photon energy range 40eV to 50eV, we reach an accuracy below the 2% level. In addition to total cross sections and total DI yields, we present differential quantities such as singly differential and triply differential cross sections (TDCS), where just one electron energy or one electron energy and the emission angles of both electrons are specified. We first focus on angle-integrated quantities, which are relatively insensitive to the size of the partial wave expansion, but clearly show the influence of the pulse shape and duration, as well as some dependence on the time of projection. We then investigate the convergence behavior of angular-resolved quantities. Here we focus on the joint angular distribution and the TDCS, which reveal the angular correlation between the electrons. We show that the convergence of the TDCS is very sensitive to the total number of partial waves that are included in the simulation. Once the TDCS is converged, all integrated quantities, such as one-electron angular distributions, which are just integrals over the TDCS, should be converged as well.

9.1 Dependence on pulse parameters

As described in [section 6.2](#), we obtain the electron momentum distribution after TPDI by projecting the wave function $|\Psi(t_f)\rangle$ onto a product of uncorrelated Coulomb waves, where t_f is some time after the end of the laser pulse. We only take into account those two-electron partial waves that can be reached by two-photon processes from the ground state, i.e. partial waves with $L = 0$ or $L = 2$. We thus obtain the TPDI momentum probability distribution $P^{DI}(E_1, E_2, \Omega_1, \Omega_2)$, cf. [\(6.19\)](#).

In the notation we use, all arguments of P^{DI} that are not given are assumed to be integrated over, such that, e.g., $P^{DI}(E_1)$ is the one-electron energy spectrum, where E_2 , Ω_1 , and Ω_2 have been integrated over. Integrating $P^{DI}(E_1, E_2, \Omega_1, \Omega_2)$ over all variables gives the total double ionization yield P^{DI} . The dependence on the primary photon energy is only implicit through the electromagnetic pulse entering the propagation. Within a time-dependent calculation, the resulting double ionization probability depends on the spectral distribution, i.e. the shape and duration of the laser pulse. If one is interested in effects in (ultra)short pulses, this can be used as a control knob to probe the dynamics of the system. However, the generalized DI cross section (DICS) at a fixed frequency of the ionizing radiation is independent of pulse parameters. If this is the quantity of interest, special care is required in the extraction.

For one-photon ionization, a straightforward relationship exists between the energy-dependent ionization yield and the cross section. From a single pulse calculation, one can thus obtain the cross section for all energies contained within the pulse [62, 84]. This can be easily seen by inserting the explicit shape of the laser pulse into the first-order perturbation theory expression (8.1c). The transition probability to a final state $|f\rangle$ is then given by

$$P_{i \rightarrow f}^{(1)} = |\langle f | \hat{\mu} | i \rangle|^2 |\mathcal{F}(E_f - E_i)|^2, \quad (9.1)$$

where $\hat{\mu}$ is the dipole transition operator, E_f (E_i) is the energy of the final (initial) state, and $\mathcal{F}(\omega)$ is the Fourier transform of the temporal shape of the laser pulse. In velocity gauge, the transition operator $\hat{\mu}$ is the momentum operator and the laser pulse is described by the vector potential, while in length gauge the transition operator is the position operator and the laser pulse is described by the electric field. This separation into a direct product of the laser pulse shape and the dipole matrix elements is not possible without additional approximations (such as used in [84]) for two-photon or multi-photon ionization, since the relation between the energy-dependent cross section and the total yield in a finite laser pulse contains an integral over intermediate states. For the evaluation of this integral, the intermediate states and energies would have to be explicitly available. In the current approach, this is not easily possible without losing the key advantage of the time-dependent method of not having to construct intermediate or final states explicitly.

The alternative is to use a sufficiently long pulse with narrow spectral width. It is then necessary to check that the limiting value of the quantity of interest for $T \rightarrow \infty$ has been reached for the pulse duration T employed. For example, one can calculate the cross section from the total yield with the approximation that it is constant over the width of the pulse. For this approximation to be valid, the spectral width of the pulse must be smaller than the energy width over which the cross section significantly changes.

Another requirement when calculating cross sections is that the pulse has to be weak enough such that lowest-order perturbation theory is applicable and ground

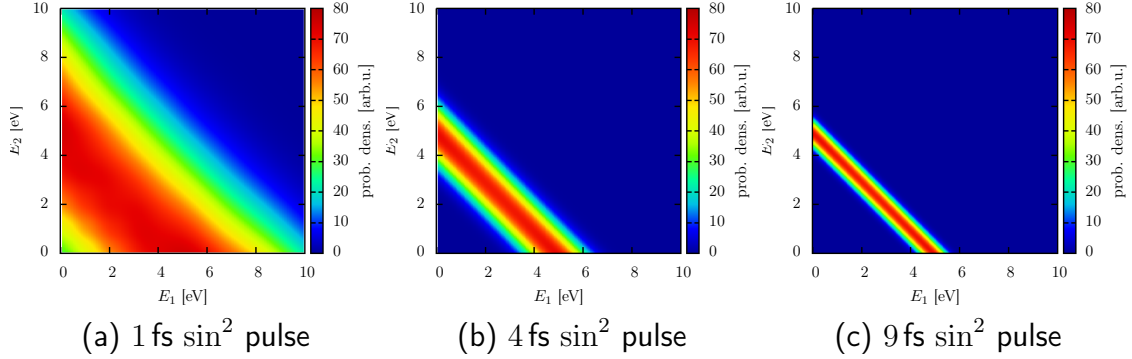


Figure 9.1: Energy distribution after two-photon double ionization from three different laser pulses with a mean energy of $\langle\omega\rangle = 42$ eV. All three pulses have a \sin^2 envelope for the vector potential, with total durations (a) 1 fs (~ 10 cycles), (b) 4 fs (~ 40 cycles), (c) 9 fs (~ 90 cycles). The distributions are centered around the line $E_1 + E_2 = 2\langle\omega\rangle - I_1 - I_2 \approx 5$ eV. The width of the distribution directly shows the energy uncertainty due to Fourier broadening.

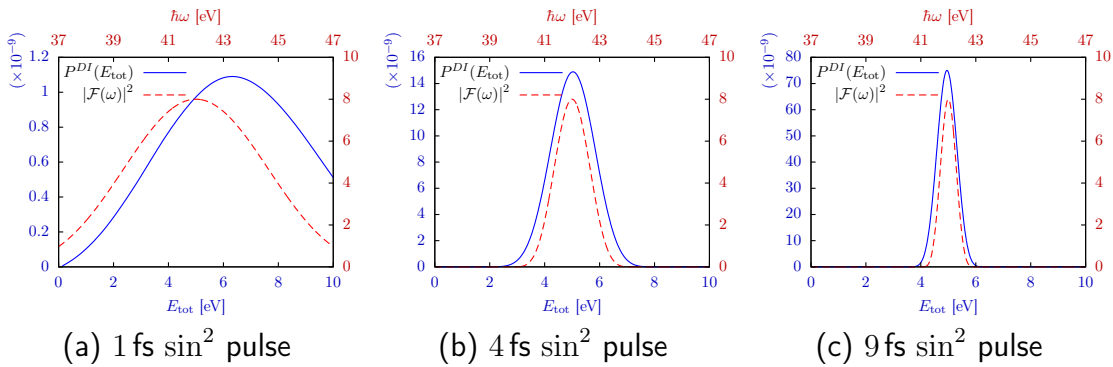


Figure 9.2: Total energy distribution $P^{DI}(E_{\text{tot}})$ and Fourier spectra 1 fs, 4 fs and 9 fs \sin^2 laser pulses. $P^{DI}(E_{\text{tot}})$ is the integral over lines with $E_{\text{tot}} = E_1 + E_2$ from Fig. 9.1. The left and lower axes describe $P^{DI}(E_{\text{tot}})$, the right and upper axes describe $|\mathcal{F}(\omega)|^2$, the Fourier transform of $A(t)$. For the 4 fs and 9 fs pulses, the double ionization probability directly reflects the Fourier spectrum. For the shorter pulse the electron energy distribution is strongly influenced by the energy dependence of the cross section (cf. Fig. 10.3).

state depletion can be neglected. Choosing a peak intensity of $I_0 = 10^{12} \text{ W/cm}^2$ ensures this even for “long” pulses up to durations of some tens of femtoseconds. In the nonsequential regime, variation between 10^{11} W/cm^2 and 10^{13} W/cm^2 results in deviations for the total cross section at 42 eV of less than 0.3%. For an intensity of 10^{13} W/cm^2 , the two-photon yield is a factor of 10^4 higher than at 10^{11} W/cm^2 .

A second test for the applicability of perturbation theory is the linear (quadratic) scaling of the total yield with the pulse duration T in the nonsequential (sequential) regime. In the nonsequential regime, this means that the transition rate must be proportional to $\Phi(t)^N$, where $\Phi(t) = I(t)/\omega$ is the photon flux and N is the minimum number of photons required for the process to take place. The double ionization yield is then given by

$$P_{\text{nonseq}}^{DI} = \int_{-\infty}^{\infty} dt \sigma_N \Phi(t)^N, \quad (9.2)$$

where σ_N is the total generalized N -photon cross section for double ionization of He. Accordingly, the cross section is given by

$$\sigma_N \approx \left(\frac{\omega}{I_0}\right)^N \frac{1}{T_{\text{eff},N}} \iiint dE_1 dE_2 d\Omega_1 d\Omega_2 P^{DI}(E_1, E_2, \Omega_1, \Omega_2), \quad (9.3)$$

where the effective time $T_{\text{eff},N}$ for an N -photon process is defined as

$$T_{\text{eff},N} = \int_{-\infty}^{\infty} dt \left(\frac{I(t)}{I_0}\right)^N. \quad (9.4)$$

For a \sin^2 pulse envelope and a two-photon process, $T_{\text{eff},2}$ is found to be $35T/128$ [54, 62, 68]. Eq. 9.3 is valid for direct, i.e. nonsequential, double ionization when no on-shell intermediate state is involved. On the other hand, the (two-photon) sequential ionization yield can be written as

$$P_{\text{seq}}^{DI} = \int_{-\infty}^{\infty} dt \sigma_1 \Phi(t) \int_t^{\infty} dt' \sigma_2 \Phi(t'), \quad (9.5)$$

where σ_1 is the one-photon cross section for single ionization of He, and σ_2 is the one-photon cross section for ionization of the He^+ ion. Using the symmetry of the integrand yields

$$P_{\text{seq}}^{DI} = \sigma_1 \sigma_2 \frac{1}{2} \left(\int_{-\infty}^{\infty} dt \Phi(t) \right)^2 = \frac{\sigma_1 \sigma_2 I_0^2}{2\omega^2} (T_{\text{eff},1})^2, \quad (9.6)$$

which is proportional to the square of the total pulse duration T . Proceeding along the same lines as for Eq. 9.3 by dividing the yield P_{seq}^{DI} by the pulse duration

results in an apparent “cross section” that increases linearly with the pulse length, contradicting the notion of a pulse shape and duration independent quantity. It is, however, possible to extract the product of the two cross sections σ_1 and σ_2 by dividing the total yield by the square of the pulse duration.

We first investigate the joint energy distribution $P^{DI}(E_1, E_2)$ (Fig. 9.1) and the distribution in total energy $P^{DI}(E_{\text{tot}})$ (Fig. 9.2, i.e. the integral along lines of constant total energy $E_1 + E_2$ in Fig. 9.1) for three different pulses with a \sin^2 envelope, with total durations $T = 1$ fs, $T = 4$ fs, and $T = 9$ fs, containing about 10, 40, and 90 optical cycles, respectively. We here choose a mean photon energy in the nonsequential regime, $\langle\omega\rangle = 42$ eV. This means that there is no peak from the sequential process in the energy distribution, and the electrons have to exchange energy for the double ionization process to occur. Consequently, both photons have to be absorbed within a short time of each other and the pulses should not have to be extremely long to achieve convergence. Still, the pulse with $T = 1$ fs (frequently employed, see refs. [54, 58, 62, 68, 82, 175]) results in averaging over a broad range of energies and can thus only give reasonable results where the cross section changes slowly. The 4 fs pulse is sufficient to resolve the cross section a few eV above the threshold for TPDI, but will fail close to the sequential threshold at $\hbar\omega = 54.4$ eV, where contamination from sequential contributions will occur. Using $T = 9$ fs or even longer pulses allows to approach the sequential threshold more closely.

Contrary to the total cross section, it is possible to define a meaningful singly differential cross section $d\sigma/dE_1$ even in the sequential regime. This cross section is proportional to the single-electron energy spectrum $P^{DI}(E_1)$ and diverges at the peaks of the sequential process, but is well-defined away from the peaks, where the ionization probability scales linearly with the pulse duration (cf. section 8.2).

9.2 Differential distributions and cross sections

The singly differential cross section (SDCS) for emitting an electron with energy E_1 follows from Eq. 9.3 as

$$\frac{d\sigma_N}{dE_1} = \left(\frac{\omega}{I_0}\right)^N \frac{1}{T_{\text{eff},N}} \iiint dE_2 d\Omega_1 d\Omega_2 P^{DI}(E_1, E_2, \Omega_1, \Omega_2) = \left(\frac{\omega}{I_0}\right)^N \frac{1}{T_{\text{eff},N}} P^{DI}(E_1). \quad (9.7)$$

Likewise, the triply differential cross section (TDCS) for emitting one electron with energy E_1 into the solid angle Ω_1 , while the second one is emitted into Ω_2 , is given by

$$\frac{d\sigma_N}{dE_1 d\Omega_1 d\Omega_2} = \left(\frac{\omega}{I_0}\right)^N \frac{1}{T_{\text{eff},N}} \int dE_2 P^{DI}(E_1, E_2, \Omega_1, \Omega_2). \quad (9.8)$$

In the limit of an infinitely long laser pulse with well-defined energy (i.e. a delta-like spectrum), the fully differential distribution $P^{DI}(E_1, E_2, \Omega_1, \Omega_2)$ reduces to

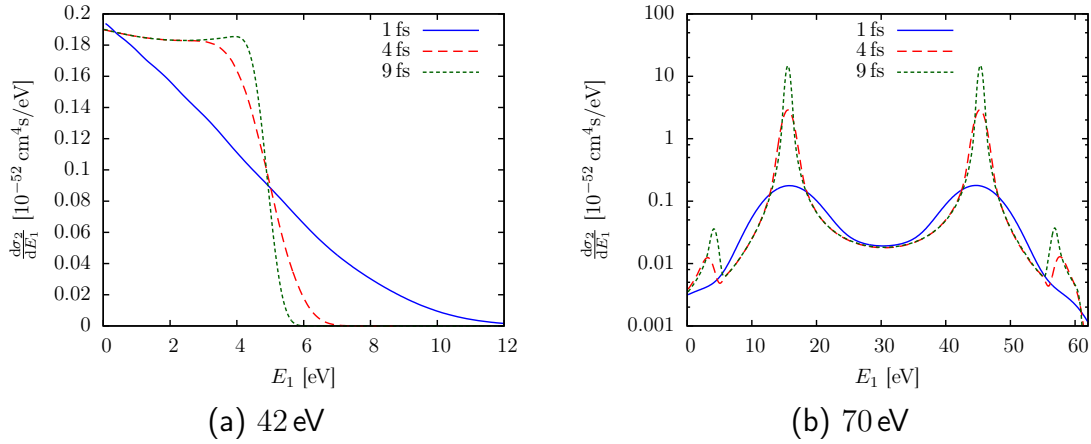


Figure 9.3: Singly differential cross section $d\sigma_2/dE_1$ for 1 fs, 4 fs and 9 fs \sin^2 laser pulses at $\hbar\omega = 42$ eV and $\hbar\omega = 70$ eV. (a) is in the nonsequential regime, where the distribution is flat, and corresponds to integration of Fig. 9.1 along E_2 . Apart from the shortest pulse, the distribution at low energies is relatively insensitive to the spectral bandwidth of the laser field. The sharpness of the cutoff at high energies, on the other hand, is directly determined by Fourier broadening. (b) is at an energy above the sequential threshold, where the peaks of the sequential process are clearly visible (note the logarithmic scale). Away from the peaks, the singly differential cross section also converges, even though the total cross section does not. The structure around the peaks associated with the shake-up process (at $E_1 \approx 5$ eV and $E_1 \approx 55$ eV) is discussed in more detail in section 12.2.

a delta-function in total energy (i.e. $\delta(N\hbar\omega - E_1 - E_2)$) times $P^{DI}(E_1, \Omega_1, \Omega_2)$, which is the quantity that is calculated in time-independent approaches. Unlike the joint two-electron energy distribution, which directly shows the Fourier width, the SDCS and TDCS as calculated by (9.7) and (9.8) are, within reasonable limits, more insensitive to the pulse shape used in the time-dependent approach since the Fourier width of the pulse is accounted for by the integration over the energy of the second electron.

Fig. 9.3 shows the SDCS for 42 eV and 70 eV pulses and for different pulse durations. For the shortest pulses, the Fourier broadening strongly distorts the results. For the 42 eV pulse, the cross section is already converged at low energies for the two longer pulses, while the cutoff at $E_1 = 2\hbar\omega - E_0$ directly shows the spectral broadening. For the 70 eV pulse, the cross section is converged away from the sequential peaks, but shows interesting effects close to the peaks associated with shake-up ionization. This is discussed in more detail in section 12.2.

Note that $P^{DI}(E_1)$ is not symmetric around the point of equal energy sharing in pulses with finite duration. It is therefore sometimes advantageous to transform the

coordinates (E_1, E_2) to new coordinates that directly reflect the exchange symmetry between the electrons. One possibility is to use $(E_{\text{tot}}, \Delta E)$, where $E_{\text{tot}} = E_1 + E_2$ is the total energy, and $\Delta E = E_1 - E_2$ is the energy difference between the two electrons. The distribution integrated over total energy then explicitly shows the exchange symmetry, as exchange of the two electrons ($1 \leftrightarrow 2$) corresponds to $\Delta E \rightarrow -\Delta E$. Another commonly used possibility is to specify energy sharing $\tan(\alpha) = E_1/E_2$. The exchange $1 \leftrightarrow 2$ of the two electrons then corresponds to $\alpha \rightarrow \pi/2 - \alpha$. Finally, it is also possible to fix momentum sharing, $\tan \alpha' = k_1/k_2$. The frequently investigated case of equal energy sharing corresponds to $\alpha' = \alpha = \pi/2$, $\Delta E = 0$. For the calculation of the SDCS and TDCS, the total energy E_{tot} is then integrated over. In the limit of vanishing pulse width, all the possibilities to define the differential cross sections (i.e. differential in E_1 , ΔE , α , or α') are equivalent, and changing the variables can be performed by a simple transformation (in essence, multiplying with the Jacobian of the transformation). In finite pulses with nonvanishing spectral width, this is, however, not possible, because the integration over E_{tot} proceeds along different lines in the space (E_1, E_2) (cf. Fig. 9.1), depending on whether E_1 , ΔE , α , or α' is held fixed. Only in the limit $T \rightarrow \infty$, where the width of the distribution in E_{tot} tends to zero, do these different variants coincide. In the following, we mostly concentrate on the definition where the energy E_1 of one electron is held fixed, as this corresponds most closely to the measurement obtained in an electron spectrometer in experiment.

For comparing the distributions obtained from different photon energies to each other, it is more convenient to choose the distribution $P^{DI}(\Delta E)$, as the positions of the sequential peaks in this distribution are independent of the laser pulse energy. The main sequential peaks, associated with leaving the He^+ ion in its ground state, are located at $E_1 = \hbar\omega - I_1$ and $E_2 = \hbar\omega - I_2$, such that $\Delta E = E_1 - E_2 = I_2 - I_1 \approx 29.8 \text{ eV}$. This affords the opportunity to directly compare the energy distributions obtained from different photon energies (cf. chapter 11).

9.3 Influence of final-state correlations

Since the extraction of double ionization observables eventually proceeds by projection onto uncorrelated Coulomb final states, controlling and monitoring the effect of residual electron-electron correlations becomes important. The key point is that electronic correlations are fully included in the initial state and in the time propagation and therefore in the wave packet at the point of projection. The only approximation is that we identify the probability amplitude in the uncorrelated final state $|\mathbf{k}_1\rangle|\mathbf{k}_2\rangle$ with the probability amplitude in the fully correlated state $|\Psi_{\mathbf{k}_1, \mathbf{k}_2}\rangle$. If the electrons are far apart and thus do not interact strongly, this is a good approximation, just as plane waves can be used to extract the momentum distribution of a single-electron wave packet in a Coulomb potential if the wave packet is localized

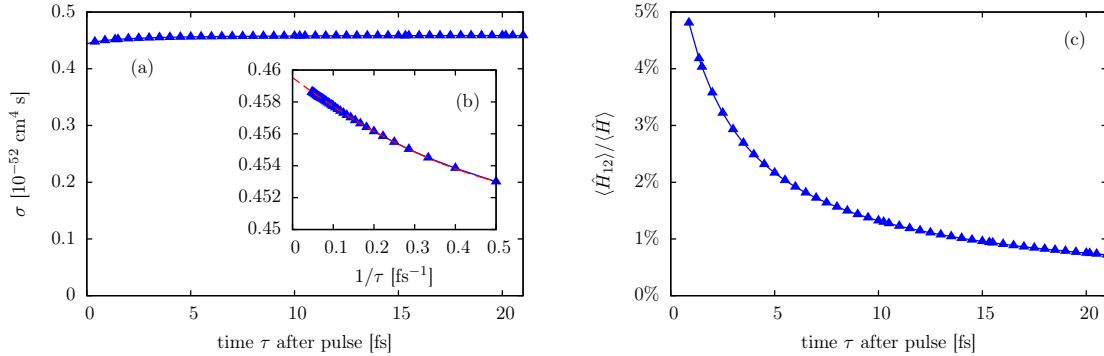


Figure 9.4: Convergence of the total cross section with propagation time τ . The cross section is calculated at different times τ after the 4 fs \sin^2 pulse from Fig. 9.1, with intensity 10^{12} W/cm^2 (angular momentum expansion with $L_{\max} = 3$ and $l_{<, \max} = l_{>, \max} = 7$). Plot (a) shows that while there is some noticeable change for short times, the results are stable at later times and seem to converge to a limiting value. This is confirmed in the inset (b), which shows the same data vs. $1/\tau$. Extrapolation to $1/\tau \rightarrow 0$ using a quadratic fit shows a limiting value of $0.4595 \cdot 10^{-52} \text{ cm}^4 \text{ s}$, only slightly higher than the result obtained at $\tau = 21$ fs. Plot (c) shows the temporal evolution of the ratio of the expectation values of the electron-electron interaction energy $\langle \hat{H}_{12} \rangle = \langle |\hat{\mathbf{r}}_1 - \hat{\mathbf{r}}_2|^{-1} \rangle$ and the total energy $\langle \hat{H} \rangle$.

far away from the nucleus. We monitor the residual error by further propagating the wave function for a time τ after the conclusion of the laser pulse (i.e. letting the electrons move further apart) and varying the time of projection. If the final state were an eigenstate of the full Hamiltonian, the results would be time-independent. The residual dependence on the time of projection is thus a direct measure of the error introduced by the neglect of final-state correlation during projection. As that time is extended, this error should become negligible. The maximum time one can wait is limited in practice by the box size, as the ionized wave packet will eventually hit the box boundaries and be reflected. To test for convergence we performed one calculation with a box size of 800 a.u., using the same 4 fs \sin^2 laser pulse at 42 eV as in Fig. 9.1b, and let the wave function propagate for an additional 21 fs after the end of the pulse. The doubly ionized part is still completely contained in the box after this time.

Fig. 9.4 displays the convergence of the total cross section at 42 eV as a function of the field-free propagation time τ . Delaying the projection from $\tau = 1$ fs to $\tau = 21$ fs changes the total cross section by less than 2%. Extrapolating to infinite time (and therefore to an infinite separation of the two electrons, Fig. 9.4b) changes the cross section by less than 0.2% from the value at $\tau = 21$ fs. This gives an estimate of the error due to projection of that order of magnitude. Furthermore, the electron-electron interaction energy is responsible for less than 1% of the total energy of the

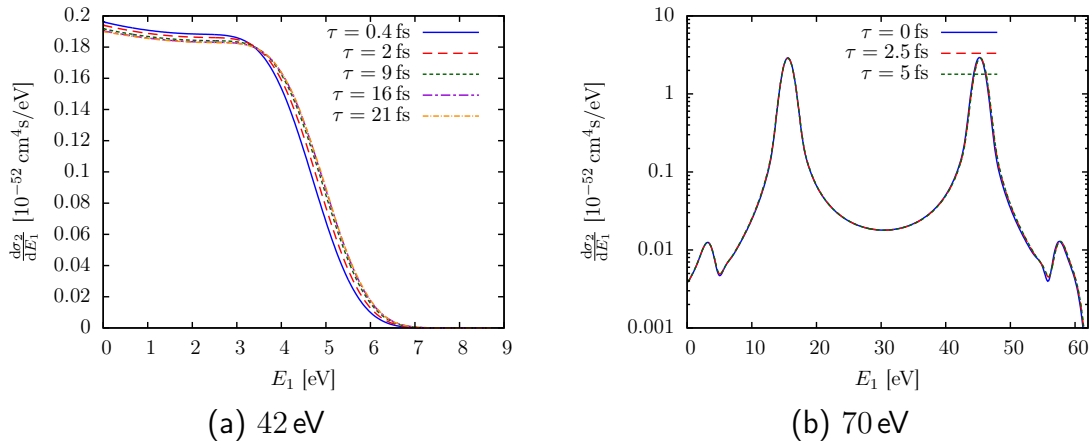


Figure 9.5: Convergence of the singly differential cross section with propagation time τ . The cross section is calculated at different times τ after a 4 fs \sin^2 pulse with (a) $\hbar\omega = 42$ eV or (b) $\hbar\omega = 70$ eV, with intensity 10^{12} W/cm² (angular momentum expansion with $L_{\max} = 3$ and $l_{<,\max} = l_{>,\max} = 7$). While the electrons at low photon energy (a) are slow and therefore need a relatively long time to reach the asymptotic limit, the distribution at $\hbar\omega = 70$ eV (b), where the electrons are faster, is almost fully converged directly after the pulse.

wave packet at $\tau = 21$ fs (Fig. 9.4c).

The singly differential cross sections (Fig. 9.5) show the same qualitative convergence behavior with projection time as the total cross section. In the nonsequential regime, at photon energies close above the TPDI threshold (Fig. 9.5a), the electrons are slow and need long times to reach the asymptotic regime. As the energy stored in the electronic interaction is converted into kinetic energy for the two electrons as time progresses, the singly differential cross section extends to slightly higher energies for later times. This is only a small effect, though, and the SDCS at $\tau = 9$ fs looks almost identical to the one at $\tau = 21$ fs.

At higher photon energies (Fig. 9.5b), there are two effects that decrease the importance of the electronic interaction for the final state: In the first place, the kinetic energy of the electrons is larger, such that the relative importance of the interaction energy is lower, and secondly, the electrons move faster and consequently reach the asymptotic regime earlier. Therefore, the SDCS at $\hbar\omega = 70$ eV has already almost converged even when projecting directly after the end of the laser pulse. It converges fully within a few femtoseconds.

The triply differential cross sections (Fig. 9.6) show an even faster convergence behavior with projection time than the singly differential cross sections. We have chosen equal energy sharing, for which the singly differential cross section also quickly converges. The insensitivity to the time of projection can be understood

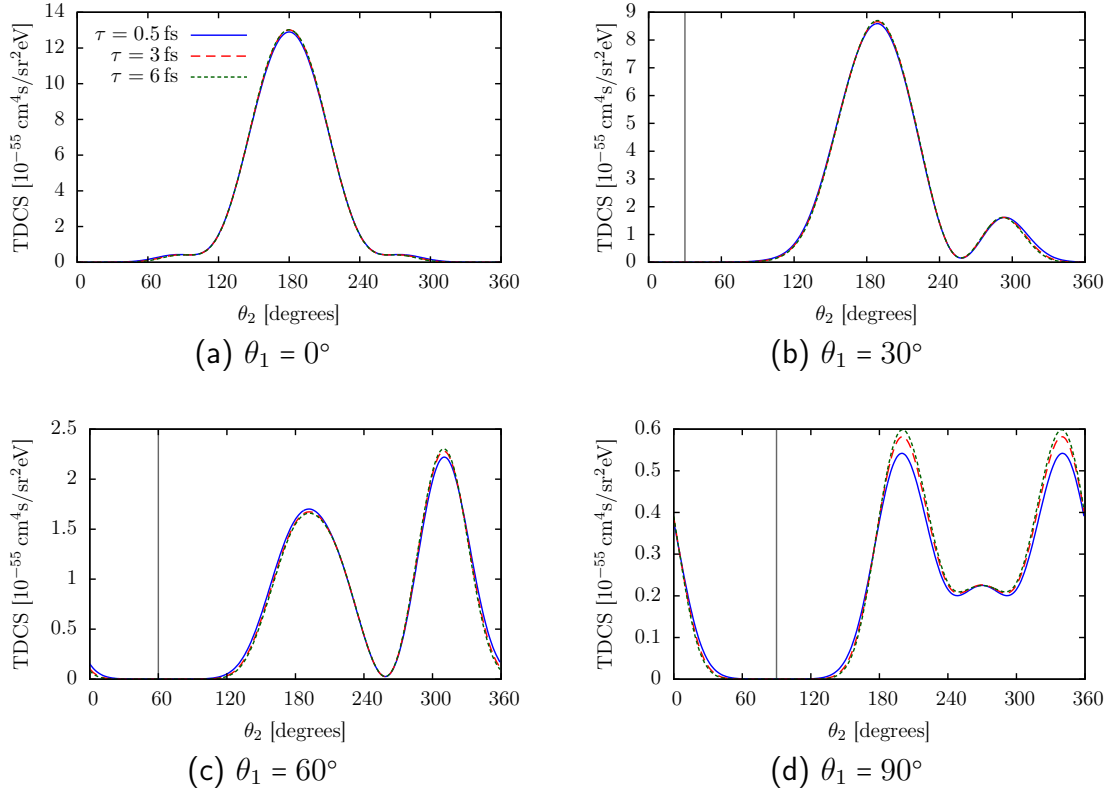


Figure 9.6: Convergence of the triply differential cross section $d^3\sigma/dE_1d\Omega_1d\Omega_2$ with propagation time τ . The vertical gray line shows the ejection angle θ_1 of the first electron. The cross section is calculated at different times τ after a 4 fs \sin^2 pulse with mean photon energy $\hbar\omega = 42$ eV and intensity 10^{12} W/cm². E_1 is chosen as 2.5 eV, i.e. at equal energy sharing. The azimuthal angles are chosen in coplanar geometry, $\phi_1 = \phi_2 = 0^\circ$. The angular momentum expansion includes values up to $L_{\max} = 4$ and $l_{<,\max} = l_{>,\max} = 9$. The cross section quickly converges with τ .

by the fact that the electrons predominantly move in opposite directions. In that case, they may exchange energy as they propagate outwards, but cease to change direction.

The investigations above show that projecting onto products of Coulomb waves is not a serious limitation for most applications. In other words, when the electrons have had time to move apart, their interaction can be neglected when extracting the final momenta. This can be ensured by propagating the wave function after the end of the laser pulse until the electrons are a few hundred atomic units away from the core and each other. The error quickly decreases for higher photon energies as the electron energies are also higher. This approach is problematic, however, when the wave packet contains a wide range of electron energies. The propagation

time necessary to achieve convergence for the slowest electrons then necessitates the use of a very large radial box to contain the fastest electrons until the time of projection.

Due to the fact that the coordinate space representation of the fully correlated wave packet is available at the time of projection, an alternative, semi-quantitative check and error estimate for double ionization exists. By inspecting the joint radial distribution $P^{DI}(r_1, r_2) = \iint d\Omega_1 d\Omega_2 |\Psi(r_1, r_2, \Omega_1, \Omega_2)|^2$ at different times (Fig. 9.7), final states representing double ionization can be separated from those representing single ionization. While the singly ionized part of the wave function moves parallel to the r_i axes, the doubly ionized parts of the wave function have positive radial momentum for both electrons so that they move away from both axes. With increasing time, the spatial overlap between singly and doubly ionized states decreases, and the two contributions can be identified visually. An estimate for an upper bound for the total double ionization cross section can thus be found by just integrating the radial density over the area that the doubly ionized wave packet occupies (which visual inspection reveals to be roughly $r_1, r_2 > 70$ a.u. at $\tau = 20$ fs after the end of the pulse, see Fig. 9.7d). This integral, which still contains a small portion of single ionization accompanied by excitation to Rydberg states, gives an *upper bound* for the total double ionization cross section. In the case of a pulse with photon energy $\hbar\omega = 42$ eV (Fig. 9.7), the extracted estimate is about 25% higher than the value determined by projection. This discrepancy is predominantly caused by the existence of high-lying Rydberg states which also have contributions at large values of r . The error of the estimate increases to about 45% when using the smaller value of $r_1, r_2 > 40$ a.u. obtained from the radial density at $\tau = 8$ fs.

One can expect that the choice of the final state is even more important when calculating differential cross sections because fewer degrees of freedom are integrated over. Specifically, the triply differential cross section (TDCS) depends on the partial-wave phase shifts, which may not have fully converged at the time of projection. In order to monitor possible errors in the angular distribution, we have also extracted the TDCS by a complementary method employing the coordinate representation of the two-electron wave packet at large propagation time, bypassing projection. In order to compare with the TDCS at equal energy sharing, we take only the part of the wave packet with $r_1 = r_2$, the part where both electrons have moved out to the same distance from the nucleus in the same time. This is what a (microscopic) time-of-flight detector would identify as equal-energy electrons. We then directly determine the angular distribution for this part of the wave function

$$\frac{d\sigma^{\text{WP}}(E_1 = E_2)}{dE_1 d\Omega_1 d\Omega_2} \propto \int dr |\Psi(r, r, \Omega_1, \Omega_2)|^2. \quad (9.9)$$

This estimate for the TDCS, referred to in the following as the wave packet (WP) method, is compared with the projection onto Coulomb waves (Eq. 9.8) in Fig. 9.8.

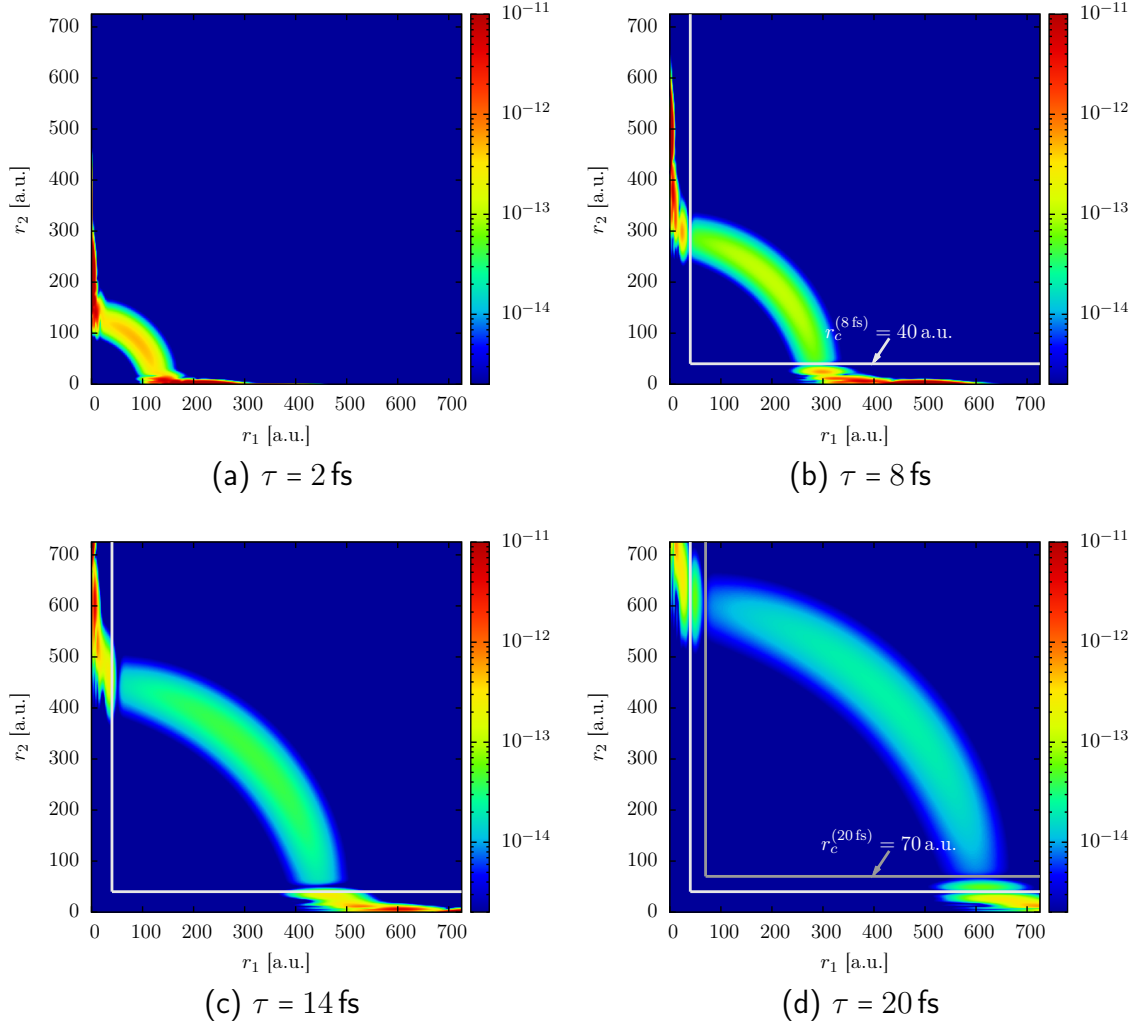


Figure 9.7: Radial density for various times τ after the end of the pulse, for the same pulse as in Fig. 9.4. At $\tau = 20$ fs, the doubly ionized part of the wave function is completely contained in the box with $r_1, r_2 > 70$ a.u. . By integrating the probability density over this region, an upper bound for the double ionization yield can be established. The gray lines indicate the border between singly and doubly ionized parts, identified by visual inspection. The lighter gray line at $r_c = 40$ a.u. is the apparent border at $\tau = 8$ fs, while the darker gray line at $r_c = 70$ a.u. is suggested by the distribution at $\tau = 20$ fs. The density located between the two borders contains singly ionized parts that would erroneously be identified as being doubly ionized at $\tau = 8$ fs due to the lack of spatial separation.

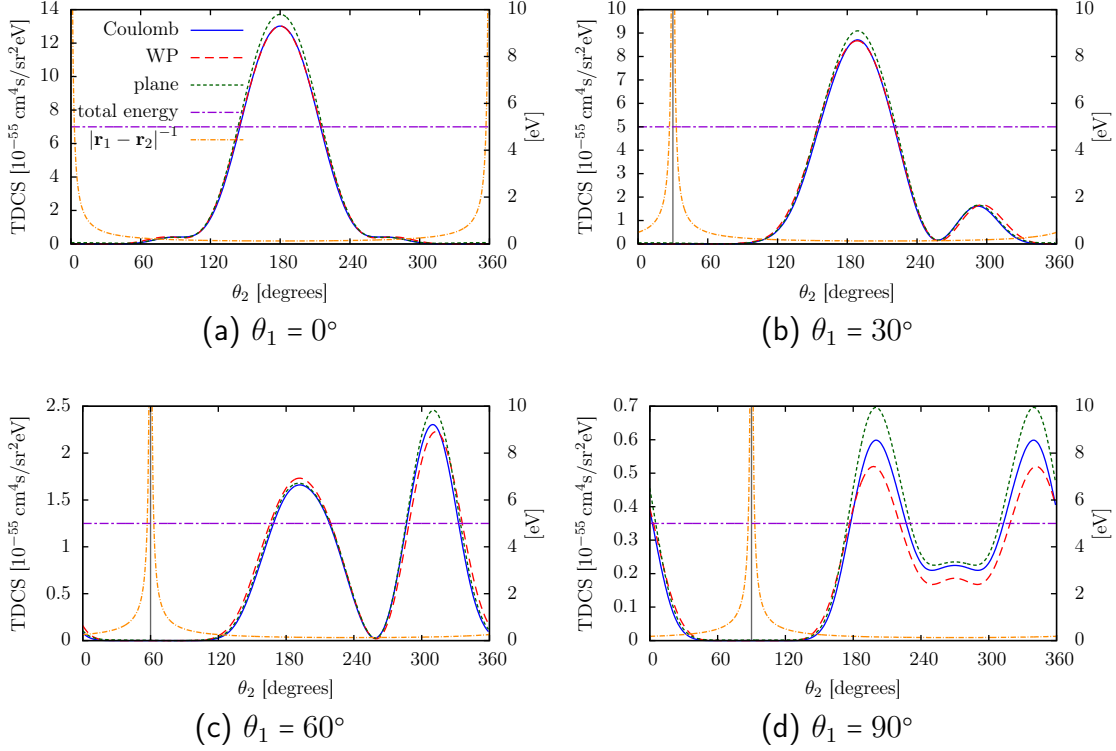


Figure 9.8: Comparison of different methods for extracting the triply differential cross sections (TDCS) at 42 eV photon energy, with a 4 fs \sin^2 laser pulse. The data for Coulomb projection are obtained from Eq. 9.8 (at $E_1 = 2.5$ eV) while the results labeled wave packet (WP) were obtained without transforming to momentum space (Eq. 9.9). The angularly resolved value of the electron-electron interaction energy at the position of the wave packet ($r_{1,2} \approx 150$ a.u.) is also shown in comparison to the total energy of the doubly ionized wave packet (~ 5 eV). The vertical gray line shows the ejection angle θ_1 of the first electron. The angular momentum expansion used values of $L_{\max} = 4$ and $l_{<,\max} = l_{>,\max} = 9$. The radial box had an extension of 400 a.u., with FEDVR elements of 4 a.u. and order 11.

The excellent agreement we find attests to the fact that residual errors due to final-state correlations at the point of projection are, indeed, negligible. In addition, we show the projection onto plane waves, where even the Coulomb potential of the ionic core is neglected. Up to a global scaling factor of about 1.1, the TDCS at equal energy sharing obtained from projection onto plane waves almost exactly agrees with the result obtained from projection onto Coulomb waves. This suggests that the Coulomb potential of the ionic core can also be neglected in the asymptotic region when only the angular differential behavior is of interest.

In addition to the TDCS as extracted through different methods, Fig. 9.8 shows

the angularly resolved value of the electron-electron interaction energy. The radial distance of both electrons was taken as $r_{1,2} = 150$ a.u., which corresponds to the position of the doubly ionized wave packet at the point of projection. Clearly, the electrons only move into directions where their interaction energy is negligible compared to the total energy of the doubly ionized wave packet. This also supports the finding that the electron interaction can be neglected when projecting at late times.

9.4 Numerical convergence tests

In addition to the convergence of our approach with respect to the final time of projection, it is necessary to check for convergence and stability of the numerical methods employed. In order to ensure the reliability of the calculated cross sections, we have performed extensive numerical testing and have found our results to be well converged. The convergence issues addressed are (i) the radial discretization, (ii) the temporal propagation, and (iii) the angular momentum expansion.

Convergence with respect to the radial grid (i) is easy to achieve within the FEDVR approach. Most results shown were obtained with finite elements of 4 a.u. extension and of order 11. Results with order 13 for elements of 4 a.u. were virtually identical (within 0.02% for the total cross sections in the nonsequential regime). Convergence of the time propagation (ii) using our SIL method is equally uncritical. Even when relaxing the convergence criterion used for time propagation by two orders of magnitude, the results do not change perceptibly from those presented here. In addition, we also checked that our results do not depend on the gauge used in Eq. 2.9. The change in the total cross section when switching from velocity gauge to length gauge is only 0.01%.

The final question regarding convergence concerns the truncation of the angular momentum expansion Eq. 3.3. As the total angular momentum L is conserved for the field-free Hamiltonian (because of spherical symmetry), the expansion does not require much higher values for L_{\max} than the minimum number of photons absorbed by the system. We have indeed found that there was no noticeable difference in any of the results between $L_{\max} = 3$ or $L_{\max} = 4$. At the low intensities used here, the result is well converged with $L_{\max} = 3$ when employing length gauge. Using velocity gauge, even $L_{\max} = 2$ produces well-converged results. The convergence with respect to the single-particle angular momenta (l_1, l_2) , which are mixed by the electron-electron interaction, is much more critical. The size of the expansion in (l_1, l_2) strongly influences the accuracy of the angular distribution of the electrons and the degree of angular correlation.

While the total cross section shows variations of less than 0.3% when $(l_{<,\max}, l_{>,\max})$ is increased from (3, 3) to (9, 9) (Fig. 9.9), a different picture emerges when the two-electron angular distribution is considered. The TDCS shows a strong depen-

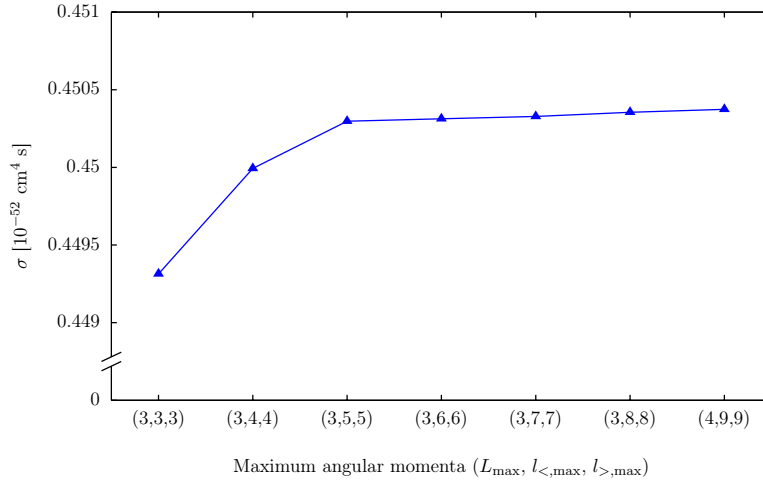


Figure 9.9: Convergence of the total cross section with the size of the angular momentum expansion. The total cross section is converged to within the accuracy of the method even for the smallest expansion in angular momenta. The differences in the result due to different angular basis sizes are much smaller than those observed when performing the projection at different times after the end of the pulse (Fig. 9.4) (4 fs \sin^2 pulse at 42 eV as in Fig. 9.1)

dence on the number of included partial waves. For the present case, convergence is reached when single electron angular momenta up to $l_{<, \max} = l_{>, \max} = 7$ are included (see Fig. 9.10 below). In particular, the TDCS at $\theta_1 = 90^\circ$ (where the cross section is very small) is very sensitive to the size of the partial wave expansion.

9.5 Conclusions

In the preceding chapter, we have presented extensive tests of the convergence properties of our method. In particular, we have demonstrated that projecting onto products of Coulomb waves to extract the double ionization momentum distribution is valid as long as one delays the projection until the electrons are far enough apart from each other. This was tested by a number of approaches: For one, we investigated the asymptotic behavior of the projection by propagating the electrons to a distance of more than 400 a.u. from the nucleus. In addition, we compared the double ionization probability obtained from projection with the value obtained from performing a cut in radial space. In addition, we have shown that a wave-packet method can be used to extract the joint angular distributions at equal energy sharing with high precision, without transforming to momentum space. Furthermore, even projecting onto plane waves only introduces an error of

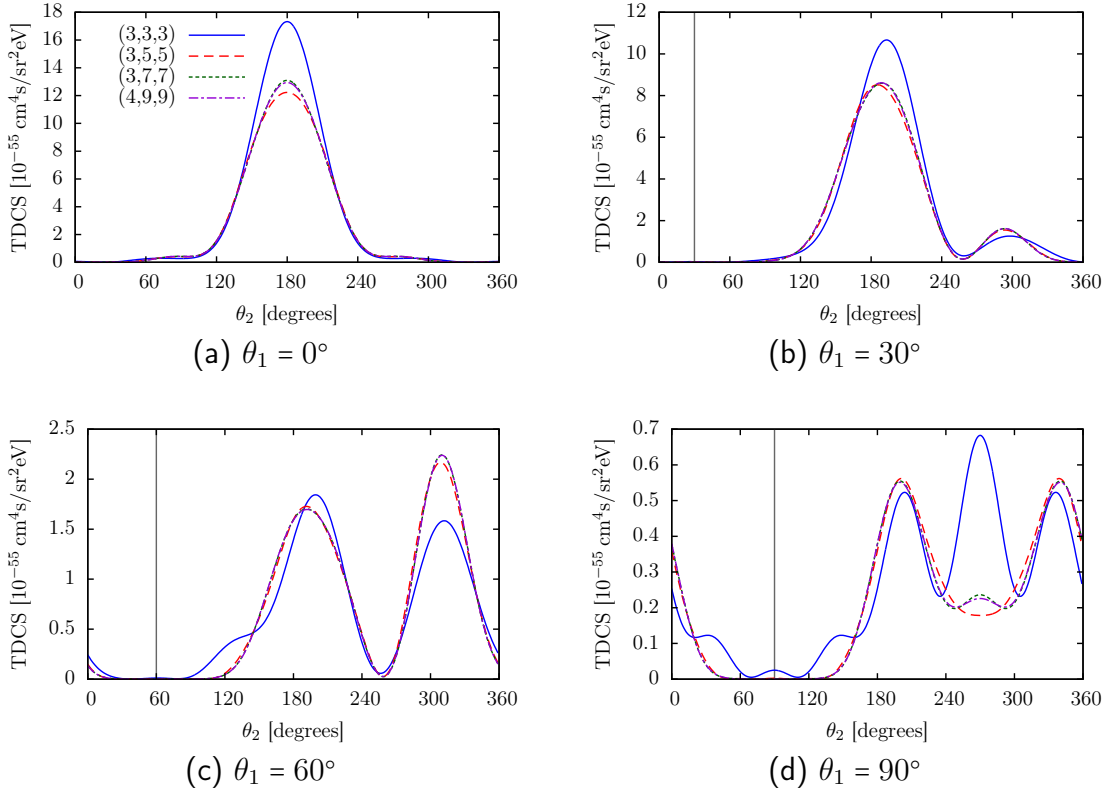


Figure 9.10: Convergence of the triply differential cross section (TDCS) with the size of the angular momentum expansion. The labels specify the maximum values ($L_{\max}, l_{<,\max}, l_{>,\max}$) used in the angular momentum expansion. The vertical gray lines show the ejection angle θ_1 of the first electron. The TDCS converges only for relatively large values in the angular momentum expansion (4 fs \sin^2 pulse at 42 eV as in Fig. 9.1).

a few percent, provided the projection is delayed long enough.

The good convergence behavior can be understood by a simple argument. The full wave function contains the electron correlation regardless of which basis it is expressed in. The only ambiguity exists in identifying which parts of the wave packet at time τ after the end of the pulse will asymptotically correspond to the situation of interest (in our case, double ionization). If τ is chosen large enough, the electrons have separated in space and their interaction energy is low (cf. Fig. 9.4c). This implies that the electrons will neither significantly deflect each other nor exchange energy at later times. Therefore, both the angular and the energy distribution are stable, and the momenta of the electrons at time τ correspond to the asymptotic momenta for $t \rightarrow \infty$. Similarly, channels where one of the electrons did not gain enough energy to escape the Coulomb potential of the nucleus by the time $t = \tau$ correspond to singly ionized final states, as the electron interaction does not provide

enough energy to change this situation at later times.

In addition to testing the validity of projection onto products of Coulomb waves, we have demonstrated that well-converged angular distributions require the inclusion of large numbers of single-electron angular momenta. These are necessary to correctly represent the correlated angular distribution of the electrons.

10 Cross sections for nonsequential TPDI

Having established the convergence of our method, we present results for the cross sections for nonsequential TPDI of helium. The first quantity of interest is the *total cross section*, which has been calculated by a number of groups over the past few years. In order to achieve converged values, the spectral bandwidth of the laser pulse used to calculate the cross section (according to Eq. 9.3) has to be sufficiently small. The spectral width of the pulse depends both on the pulse shape as well as on the total duration of the pulse. In addition to the \sin^2 pulses used for most results shown in this thesis, we also used the following pulse shapes: (i) a Gaussian pulse envelope and (ii) a flat-top pulse envelope with a \sin^2 ramp on for a quarter of the pulse duration, constant intensity for half the pulse duration, and a \sin^2 ramp off for the last quarter of the pulse (cf. Fig. 10.1a). The durations of the Gaussian and flat-top pulses were chosen such that the FWHM of the spectral distribution was identical to that of a \sin^2 pulse of 4 fs duration. Although all three pulses have the same spectral width, the distributions look different. Specifically, the spectral distribution of the flat-top pulse contains significant side lobes (ringing) (cf. Fig. 10.1b). In Fig. 10.2a, we show that the results obtained for the total cross section are almost identical with all three pulse shapes, apart from close to the step discontinuity at the threshold for sequential double ionization. Note that T_{eff} is dependent on the pulse shape, which has to be taken into account properly (cf. (9.4)). Fig. 10.2b shows the dependence of the extracted cross sections on the duration of the pulse. As the threshold for sequential TPDI is approached, successively longer pulses are necessary to resolve the rapidly growing cross section. The calculations were performed with differing box sizes depending on the pulse duration, with $r_{\text{max}} = 240$ a.u. for the smallest boxes and $r_{\text{max}} = 1400$ a.u. for the largest boxes. The FEDVR elements contained 11 basis functions each and spanned 4 – 4.4 a.u.. The maximum angular momentum values used were $L_{\text{max}} = 3$ for the total angular momentum and $l_{<,\text{max}} = l_{>,\text{max}} = 7$ for the individual angular momenta. The peak intensity was chosen as $I_0 = 10^{12}$ W/cm². The ionization yields were extracted 1 fs after the pulse. Following the results of section 9.3 the projection error should be less than 2%.

In Fig. 10.3, we compare the present results for the total cross section with published data. For Fig. 10.3a, we used the longest available \sin^2 pulse for each data point (cf. Fig. 10.2b), i.e. 4 fs pulses for $\hbar\omega \leq 51$ eV, 11 fs pulses for $\hbar\omega \leq 53$ eV

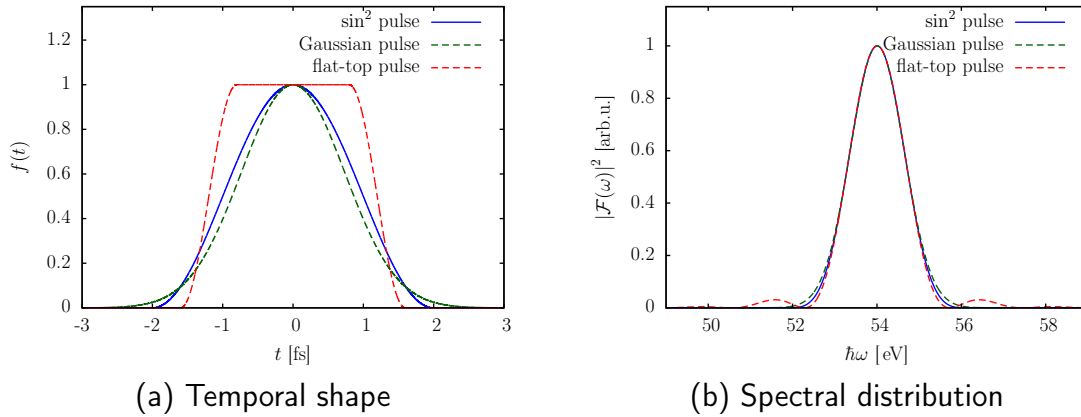
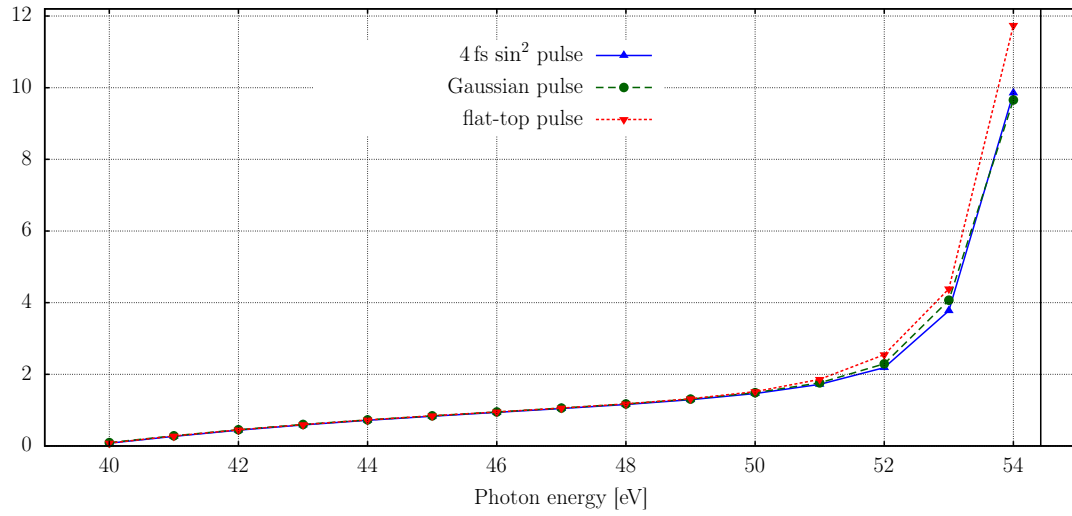


Figure 10.1: Different pulse shapes used for extracting cross sections for nsTPDI. In (a), we show the temporal profile of the pulse envelope of the three pulse shapes used: a 4 fs \sin^2 pulse, a Gaussian pulse, and a flat-top pulse. In (b), we show the corresponding spectral distributions (modulus squared of the Fourier transforms). The durations of the pulses were chosen so that the FWHMs of the spectral distributions coincide.

and 20 fs pulses for $\hbar\omega = 53.5$ eV and $\hbar\omega = 54$ eV.

For photon energies below around 50 eV, the total cross section for TPDI is a relatively smooth function of photon energy, showing an approximately linear increase. Above the threshold (54.4 eV), the cross section is not defined, as the yield then scales with the square of the pulse duration, whereas a cross section requires linear scaling with pulse duration. In order to extract the cross section close to the threshold, it is therefore necessary to ensure that the spectral width of the pulses is small enough such that the total yield only contains negligible contributions from the sequential process. By using successively longer pulses, we were able to resolve the threshold behavior up to less than one eV below the threshold, with the result for 53.5 eV being converged for $T = 20$ fs. In order to resolve the behavior for energies even closer to the threshold, still longer pulses would have to be used, which becomes prohibitively expensive. Close to the sequential threshold, the cross section rises steeply with photon energy. The sequential process is then *almost* possible, i.e. the energy of the intermediate state is close to being on-shell. As the long-time limit $T \rightarrow \infty$ of second-order perturbation theory shows, the transition amplitude is proportional to $E_{ni\omega}^{-1}$, i.e. the inverse of the deviation from the on-shell process. As the threshold is approached, this deviation becomes small, leading to the observed rise in the cross section. This has been called the signature of the “virtual” sequential process by Horner *et al.* [75].

The present results show a more pronounced variation with photon energy than other results obtained by direct integration of the time-dependent Schrödinger equa-



(a) Three different pulse shapes

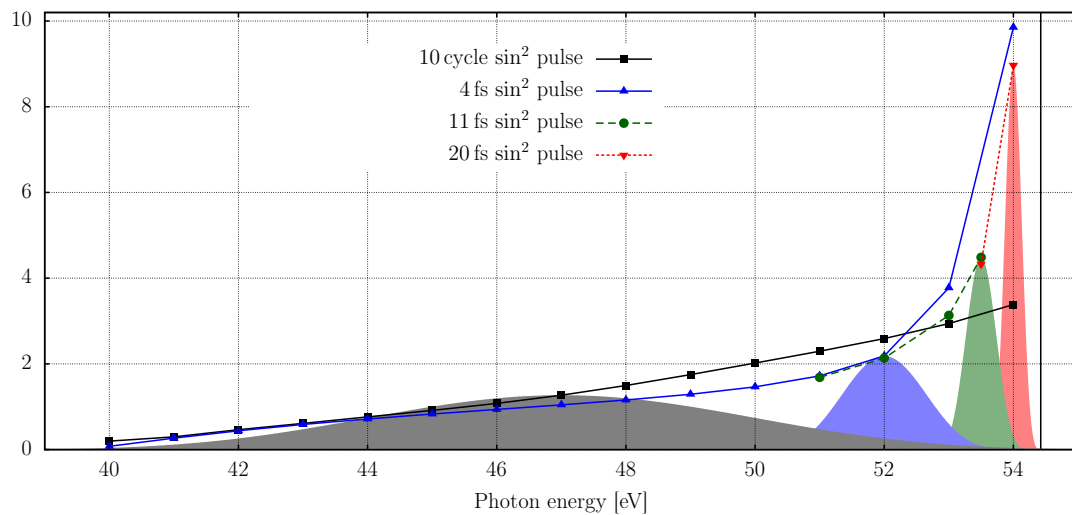
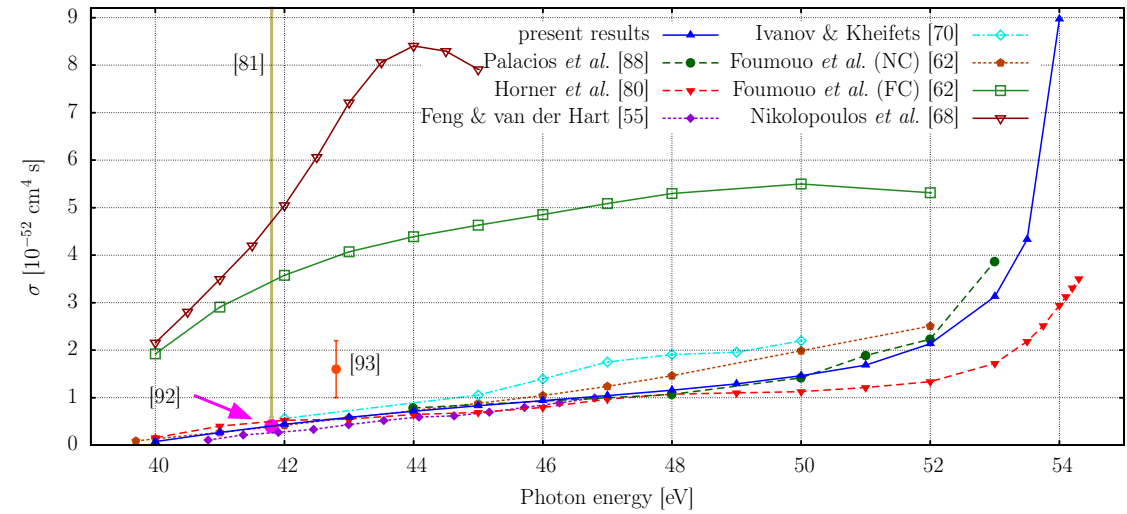
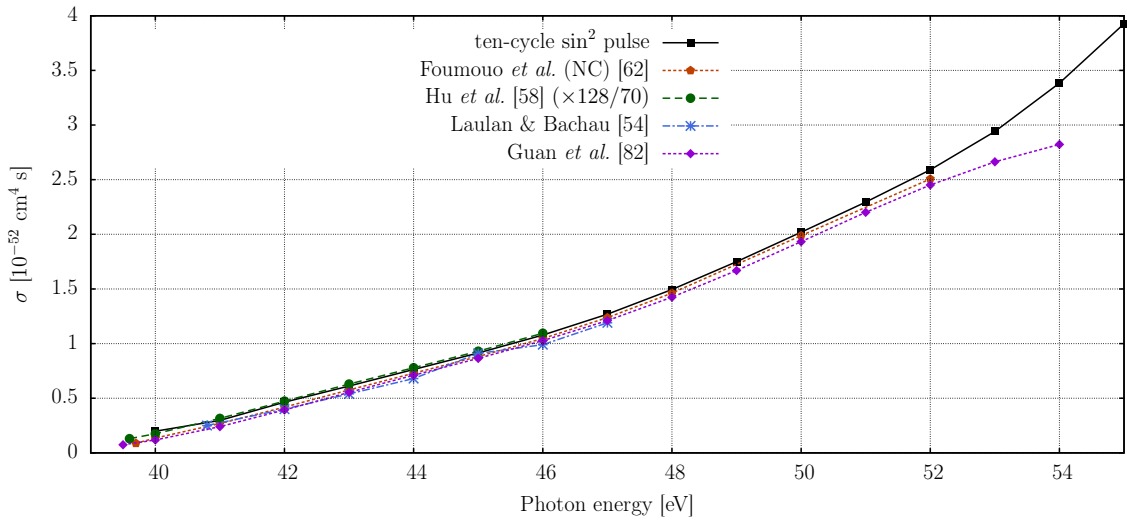
(b) \sin^2 pulses of differing duration

Figure 10.2: Total TPDI cross sections obtained using different pulse shapes and durations. In (a), we compare three pulse shapes with the same spectral FWHM of ~ 1.5 eV: a 4 fs \sin^2 pulse, a Gaussian pulse, and a flat-top pulse. In (b), \sin^2 pulses of different total durations were used. For each of the pulse durations, the spectral distribution of the pulse is plotted below the curve at one of the data points, showing the area over which the cross section obtained was effectively integrated. The angular momenta were allowed to go up to $L_{\max} = 3$ for the total angular momentum, and $l_{<,\max} = l_{>,\max} = 7$ for the single electron angular momenta. The radial boxes had different extensions depending on the pulse duration, with a maximum of $r_{\max} = 1400$ a.u. for the 20 fs pulses. The FEDVR elements used order 11 and an extension of at most 4.4 a.u..



(a) Longest available pulses



(b) Ten-cycle pulses

Figure 10.3: Comparison of the total two-photon double ionization (TPDI) cross sections, obtained from Eq. 9.3, with $T_{\text{eff}} = 35T/128$. In (a), “present results” labels the data obtained with the longest \sin^2 pulse that we calculated at each energy (cf. Fig. 10.2b), all with a peak intensity of 10^{12} W/cm^2 . For the results of Fomouo *et al.* [62], (NC) labels the results obtained by projecting onto uncorrelated Coulomb waves, while (FC) labels the results obtained using the J -matrix method. (b) shows the results obtained with ten-cycle pulses compared to other approaches using the same pulses. The results of Hu *et al.* [58] were rescaled by a factor of $128/70$ in order to include the correct T_{eff} .

tion. This can be easily explained by the fact that most previous work employed ten-cycle pulses. At photon energies of 42-54 eV, this corresponds to about 1 fs total duration, and consequently, a spectral width (FWHM) of about 6 eV (for \sin^2 pulses). The results are therefore an average over a rather large energy window. In contrast, we use pulses of up to 20 fs duration with a narrower spectrum (FWHM ~ 0.3 eV). To facilitate the comparison with previous calculations we have also performed a calculation using ten-cycle pulses (Fig. 10.3b) for which we indeed find better agreement. The pulse duration dependence becomes, in particular, critical near the threshold for sequential ionization at 54.4 eV.

We compare our results with data from both time-dependent and time-independent approaches. Laulan and Bachau [54] solved the TDSE by means of a B -spline method and an explicit Runge-Kutta propagation scheme. The double ionization probability was obtained by projecting onto uncorrelated Coulomb functions. They also included first-order correction terms in the representation of the double continuum (thus partly taking into account radial correlations). However, they found little difference with respect to the uncorrelated functions, as expected from our investigations. Hu, Colgan, and Collins [58] solved the time-dependent close-coupling equations using finite-difference techniques for the spatial discretization and the real-space product formula as well as a leapfrog algorithm for temporal propagation. The double ionization probability was also extracted by projection onto uncorrelated Coulomb waves. Guan, Bartschat and Schneider [82] used an approach very similar to ours, employing the FEDVR and using the Lanczos method for time propagation. Palacios *et al.* [88] also used an FEDVR basis, combined with a Crank-Nicholson time propagator. They extracted the double ionization yields by application of exterior complex scaling (ECS) and a formal propagation to $t \rightarrow \infty$, such that the volume integral for projection can be rewritten as a surface integral, performed at asymptotic distances to the core. This approach thus also includes correlation in the final state.

Foumouo *et al.* [62] employed a spectral method of configuration interaction type (involving Coulomb-Sturmian functions) and an explicit Runge-Kutta time propagation to solve the TDSE. The double ionization probability is calculated by closure, i.e. by subtracting the singly ionized states from the total wave function and taking the remaining probability as the double ionization probability. The singly ionized states were constructed by using the J -matrix method, which should contain angular and radial correlations to the full extent. In addition, they also performed projection on the uncorrelated product of Coulomb waves. The more recent results from Ivanov and Kheifets [70] are based on the time-dependent convergent close-coupling (CCC) method, taking into account correlations in the final state to some degree. Nikolopoulos and Lambropoulos [68] solved the TDSE using an expansion in correlated multichannel wave functions.

Within the time-independent methods, Nikolopoulos and Lambropoulos in an earlier paper [50] applied lowest-order non-vanishing perturbation theory (LOPT)

to determine the generalized cross sections. Feng and van der Hart [55] employed R -matrix Floquet theory in combination with B -splines basis sets. The data from Horner *et al.* [75, 80] also result from LOPT calculations. They solved the Dalgarno-Lewis equations for two-photon absorption in LOPT employing exterior complex scaling (ECS) and also account for correlation in initial, intermediate, and final states.

Overall, our results are in reasonable to good agreement with those of [54, 55, 58, 62, 80, 82, 88] while sizable discrepancies exist in comparison with those of [50, 68] as well as those of [62] in which corrections due to final-state correlations are included. Clearly, the degree of convergence of the present results on the few percent level as well as the upper bound extracted from the radial wave packet analysis preclude any change of cross section by a factor of 5 – 10, which would be necessary to obtain values of the same magnitude as [50, 62, 68]. The only other calculations approaching the threshold for sequential TPDI are those by the Berkeley group [75, 80, 88], which also show the strong increase of the total cross section as the threshold is approached. In particular, the data of Palacios *et al.* [88] agree with ours almost perfectly up to 52 eV. The deviation at 53 eV can be explained by the fact that they used pulses of total duration $T = 3$ fs, while we used longer pulses up to $T = 20$ fs close to threshold.

The experimental values of Hasegawa, Nabekawa *et al.* [91, 92] at 41.8 eV and of Sorokin *et al.* [93] at 42.8 eV (cf. Fig. 10.3) are compatible with most of the theoretical data. Antoine *et al.* [81] provide an experimental lower bound for the cross section at 41.8 eV, which is right at the value of the cross section obtained by most time-dependent approaches. Due to the experimental uncertainties (e.g. the harmonic intensity in [91, 92] or the assumptions on the pulse shape and focusing conditions in [93]), the currently available data are not sufficient to strongly support or rule out any of the theoretical results.

We turn now to the triply differential cross section (TDCS), the quantity most sensitive to the level of the underlying approximations. The present results show qualitative agreement with the published data [58, 70, 80], but there are pronounced quantitative differences. While the prominent back-to-back emission lobe (anti-)parallel to the laser polarization direction is well reproduced in most calculations (Fig. 10.4), the angular distribution for less favored emission directions (e.g. $\theta_1 = 90^\circ$) differs significantly from other calculations. One reason is the sensitivity to the partial-wave expansion. In contrast to the *total* cross section, the TDCS needs a larger number of angular momentum combinations (L, l_1, l_2) in the expansion of the wave function to converge. In order to resolve angular correlations in the triply differential cross section (TDCS), it is necessary to use large expansions in single electron angular momenta. More specifically, good convergence of the TDCS is only reached for values as high as $l_{<,max} = l_{>,max} = 7$ (cf. Fig. 9.10), which exceeds the angular momentum content of most other calculations [58, 70]. As discussed in section 9.3, we have alternatively determined the TDCS by directly analyzing the

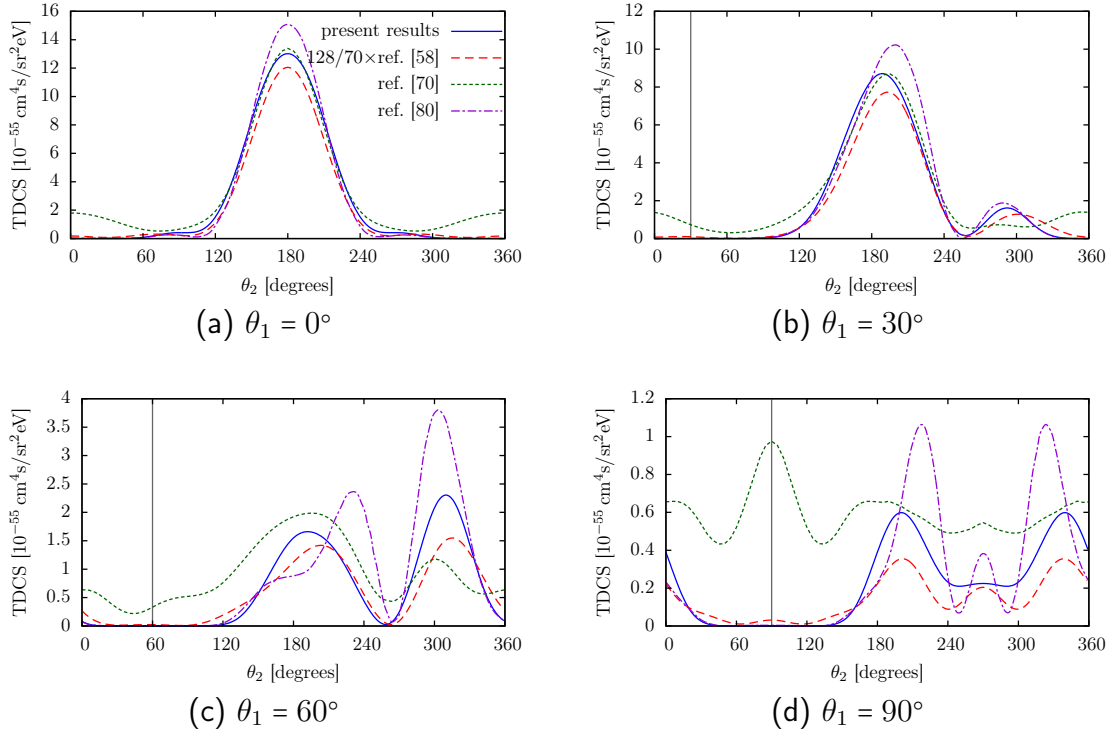


Figure 10.4: Comparison of triply differential cross sections (TDCS) at 42 eV photon energy. Our data are obtained from Eq. 9.8, at $E_1 = 2.5$ eV, i.e. equal energy sharing, using a 4 fs \sin^2 laser pulse. In comparison, the results of Hu *et al.* [58] and Ivanov and Kheifets [70] are shown. The vertical gray line shows the ejection angle θ_1 of the first electron. The angular momentum expansion used values of $L_{\max} = 4$ and $l_{<, \max} = l_{>, \max} = 9$. The radial box had an extension of 400 a.u., with FEDVR elements of 4 a.u. and order 11.

angular distribution of the wave packet for equal energy sharing by a radial integral constrained to equal radii. We find remarkably close agreement with the Coulomb projection method (Fig. 9.8). The residual small deviations can be taken as an estimate for the uncertainty of the extraction method of the TDCS by Coulomb projection.

Horner *et al.* [80] solve the Dalgarno-Lewis equations for LOPT using an exterior complex scaling technique. In order to produce converged results, a small imaginary part has to be added to the photon energy in the first step of the calculation. The obtained results then have to be extrapolated to zero imaginary part, leading to some uncertainty in the relative phases of different contributions, which strongly influence the TDCS. Ivanov and Kheifets [70] take correlation in the final states into account using a convergent close-coupling (CCC) method. While the magnitude of their results is similar to those presented here, the shape differs considerably. In

particular, they find significant probability for emission of both electrons in the same direction ($\theta_1 = \theta_2$), where the mutual repulsion of the electrons should be strongest. Fomouo *et al.* [87] calculated the TDCS for equal energy sharing at 45 eV photon energy using two different methods. The results obtained by projecting the final wave function on products of Coulomb waves resemble ours (not shown here for 45 eV, but the behavior is similar as for 42 eV). However, when correlation in the final state is taken into account using their J -matrix method, the results are much larger in magnitude (as for the total cross section, cf. Fig. 10.3) and display a shape reminiscent of the one obtained by Ivanov and Kheifets [70], with the same surprising feature of emission in the same direction at equal energy sharing.

11 Differential distributions: Photon energy dependence

In this section, we investigate the changing character of the TPDI process as the photon energy is scanned from the nonsequential to the sequential regime. In particular, we start by focusing on the single electron energy distribution, $P^{DI}(\Delta E)$, which is closely related to the singly differential cross section (SDCS) (Eq. 9.7). The SDCS is well defined in both the nonsequential and the sequential regime, except at the peaks of the sequential process, where it diverges. In time-dependent calculations, the yield contained in the sequential peaks scales with T^2 , where T is (proportional to) the pulse duration. In order to facilitate comparison between different photon energies, we plot $P^{DI}(\Delta E)$, i.e. the probability distribution as a function of the difference in energy of the two electrons, $\Delta E = E_1 - E_2$. In the limit $T \rightarrow \infty$ (and in time-independent calculations), this quantity is related to the singly differential cross section $d\sigma/dE$ by a simple variable transformation. As elaborated in section 9.2, the positions of the main sequential peaks in this distribution are independent of the laser pulse energy, lying at $\Delta E = \pm(I_2 - I_1) \approx \pm 29.8 \text{ eV}$.

Fig. 11.1 shows the TPDI probability distribution $P^{DI}(\Delta E)/P^{DI}(\Delta E = 0)$, i.e. the singly differential energy distribution as a function of energy difference, normalized to a value of 1 at $\Delta E = 0$ to allow for comparison of the shape of the function at different photon energies. We show this function for various photon energies from slightly above the threshold for TPDI (at 39.5 eV) to just above the single-photon double ionization threshold, where all shake-up channels are accessible for TPDI. Remarkably, the form of the singly differential distribution depends only on the relative energy sharing $\Delta E = E_1 - E_2$ between the electrons, but is largely independent of the pulse energy. For an energy difference smaller than $|\Delta E| \approx 45 \text{ eV}$, the curves agree excellently. This can be understood as a consequence of the fact that the energy-differential distribution is almost fully determined by the shape function in the second-order time-dependent perturbation theory expression (8.4a). To verify this, we rely on the approximations presented in section 8.2: we only include intermediate states of the form $|\epsilon_1 p 1 s\rangle$, i.e. singly ionized states where the ion remains in the ground state, and we assume that the final state is $|\epsilon_1 p E_2 p\rangle$, i.e. that the second transition does not influence the first electron ($\epsilon_1 = E_1$). In addition, we here neglect the energy dependence of the dipole matrix elements in the transition, in order to show just the influence of the shape factor $\mathcal{G}_{\text{sin}^2}$. To reach a specific final state $|E_1 p E_2 p\rangle$, there are then two relevant intermediate states, $|E_1 p 1 s\rangle$ and

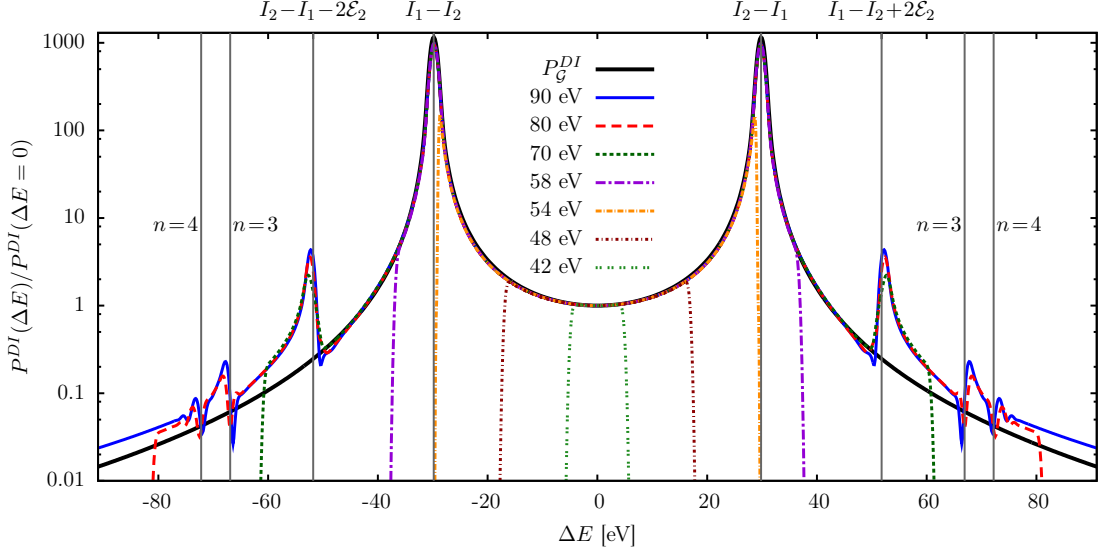


Figure 11.1: Double ionization probability $P^{DI}(\Delta E)$ as a function of the energy difference ΔE of the two electrons. All calculations were done with pulses with total duration $T = 9$ fs and a \sin^2 envelope for the vector potential, apart from the one at $\hbar\omega = 54$ eV, where the pulse with $T = 20$ fs was used. The distributions are normalized to a value of 1 at $\Delta E = 0$. For the explanation of how P_G^{DI} is determined, see the text. The gray lines show the expected positions of the peaks for the sequential process (with and without shake-up)

$|E_2 p 1 s\rangle$. The transition probability to the final state $|E_1 p E_2 p\rangle$ in this approximation (and for \sin^2 pulses) is then given by

$$P_G^{DI}(E_1, E_2) \propto \left| \mathcal{G}_{\sin^2}(E_{fn\omega}^1, E_{ni\omega}^1, T) + \mathcal{G}_{\sin^2}(E_{fn\omega}^2, E_{ni\omega}^2, T) \right|^2, \quad (11.1)$$

with $E_{ni\omega}^{1,2} = E_{1,2} + I_1 - \omega$ and $E_{fn\omega}^{1,2} = E_{2,1} + I_2 - \omega$, where $I_1 = E_{1s} - E_0$ and $I_2 = -E_{1s}$ are the first and second ionization potentials.

Finally, we assume the pulse is long enough such that the total energy of the final state is well-determined, $E_1 + E_2 = 2\omega + E_0$. This enforces $E_{ni\omega} = -E_{fn\omega}$. Switching to the variable $\Delta E = E_1 - E_2$, the arguments of \mathcal{G}_{\sin^2} then become independent of the photon energy, as $E_1 = \omega + E_0/2 + \Delta E/2$ and $E_2 = \omega + E_0/2 - \Delta E/2$, and

$$E_{fn\omega}^1 = E_0/2 - E_{1s} - \Delta E/2 = (I_2 - I_1 - \Delta E)/2, \quad (11.2)$$

$$E_{fn\omega}^2 = E_0/2 - E_{1s} + \Delta E/2 = (I_2 - I_1 + \Delta E)/2. \quad (11.3)$$

We thus obtain

$$P_G^{DI}(\Delta E) \propto \left| \mathcal{G}_{\sin^2}((I_2 - I_1 - \Delta E)/2, -(I_2 - I_1 - \Delta E)/2, T) + \mathcal{G}_{\sin^2}((I_2 - I_1 + \Delta E)/2, -(I_2 - I_1 + \Delta E)/2, T) \right|^2. \quad (11.4)$$

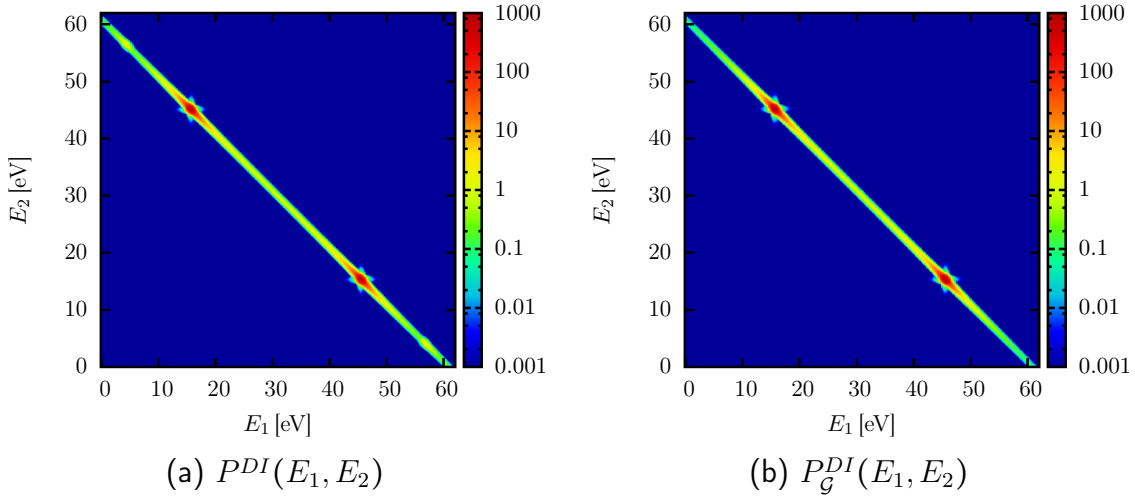


Figure 11.2: Energy distribution for TPDI from a 9 fs \sin^2 pulse at $\hbar\omega = 70$ eV. (a) shows the distribution obtained from the full solution of the TDSE, (b) shows the strongly simplified model P_G^{DI} . The agreement is remarkably good.

This expression does not contain any system-specific information apart from the difference in the ionization potentials for the two steps, as $E_0 - 2E_{1s} = I_2 - I_1 \approx 29.8$ eV. This is also the energy difference of the He atom without electron-electron interaction ($2E_{1s}$) to the “real” He atom (E_0), and has been previously called the “correlation energy” E_C of the He ground state⁶ [53, 56, 78, 86]. This determines a timescale $T_C = 2\pi/E_C \approx 139$ as. For pulses approaching this duration, the shape of the energy distribution can be expected to change strongly, cf. chapter 12.

The quantity $P_G^{DI}(\Delta E)/P_G^{DI}(\Delta E = 0)$ is also shown in Fig. 11.1. The agreement of this extremely simple approximation with the full solutions obtained from the TDSE is excellent for a wide range of photon energies. Fig. 11.2 shows that this agreement extends to the joint energy distribution $P^{DI}(E_1, E_2)$ of the two electrons. In the regions where shake-up ionization starts to play a role, i.e. for $|\Delta E| > 50$ eV, the neglect of intermediate states with shake-up excitation of the intermediate state causes the failure of the model. Including these states would require the determination of the relative phases of the relevant cross sections, which can not be done easily. The agreement of the model presented here with the full calculations can be slightly improved by using the square root of the product of the single-ionization cross sections for single-photon absorption in He and He⁺ to approximate the transition matrix elements, instead of assuming them to be independent of energy. Doing so also allows quantitative comparison of the model with the full results, i.e. without normalizing $P^{DI}(\Delta E = 0) = 1$. The model without

⁶ Note that this is different from the “correlation energy” as commonly used in quantum chemistry, which is defined as the difference of the real energy to the Hartree-Fock energy, cf. chapter 7.

normalization then agrees with the full calculations to within an error of $\sim 10\%$, as shown by Palacios *et al.* [88].

The validity of the simple model (which does not include any correlations) shows that the single-electron energy distribution (or singly differential cross section) is not a good observable to determine the amount of electronic correlation in the process. A further topic of discussion is whether the model should be called “purely sequential”. As we do not include any explicit correlation effects in the matrix elements, this might seem justified. On the other hand, as discussed in [section 8.2](#), the inclusion of off-shell transitions automatically corresponds to the inclusion of nonsequential (or direct) processes, where the intermediate state is only transiently occupied. Without the inclusion of off-shell transitions, only electrons at the peaks of the sequential process would be observed. We thus keep the nomenclature as before, and simply use “nonsequential” for these transitions to final states that are only possible through the inclusion of off-shell intermediates. Another point to note is that the existence of electron interaction is crucial for the model as well – this causes the difference of the ionization potentials for the first and second transition. Consequently, in the model, all the energy contained in the electron interaction is taken away by the first electron, such that the second electron feels only the Coulomb attraction of the core. If this were not taken into account, i.e. if the electron-electron interaction did not have any effect, the final two-electron distribution would just be the product of two independent one-electron distributions.

11.1 Angular correlations

In order to reveal the electron correlation in the TPDI process, we now turn to angularly resolved quantities. The first quantity of interest is the joint angular distribution $P^{DI}(\Omega_1, \Omega_2)$. For this, the electron energies are integrated over, so that the angular distribution of those electrons that are preferentially emitted is seen. We choose a coplanar geometry, i.e. we set both azimuthal angles to zero, $\varphi_1 = \varphi_2 = 0^\circ$. As the system shows cylinder symmetry, the distributions are independent of $\varphi_1 + \varphi_2$, and there is only a possible dependence on $\varphi_1 - \varphi_2$. Closer investigation shows that this dependence does not influence the conclusions presented here, and we thus restrict ourselves to coplanar geometry.

In [Fig. 11.3](#), the joint angular distribution $P^{DI}(\theta_1, \theta_2)$ is plotted for different photon energies from the nonsequential to the sequential regime. In order to allow comparison between the different energies, the plots are normalized to the value of $P^{DI}(\theta_1 = 0^\circ, \theta_2 = 180^\circ)$. We here plot the angular distributions in a polar plot, where we use a quadratic scale, such that the distance from the origin is determined by $\sqrt{P^{DI}(\theta_1, \theta_2)}$. The area enclosed by the curve then represents the value of the cross section. This allows for a better comparison of the distributions and also has the advantage to more clearly show the behavior at angles where the

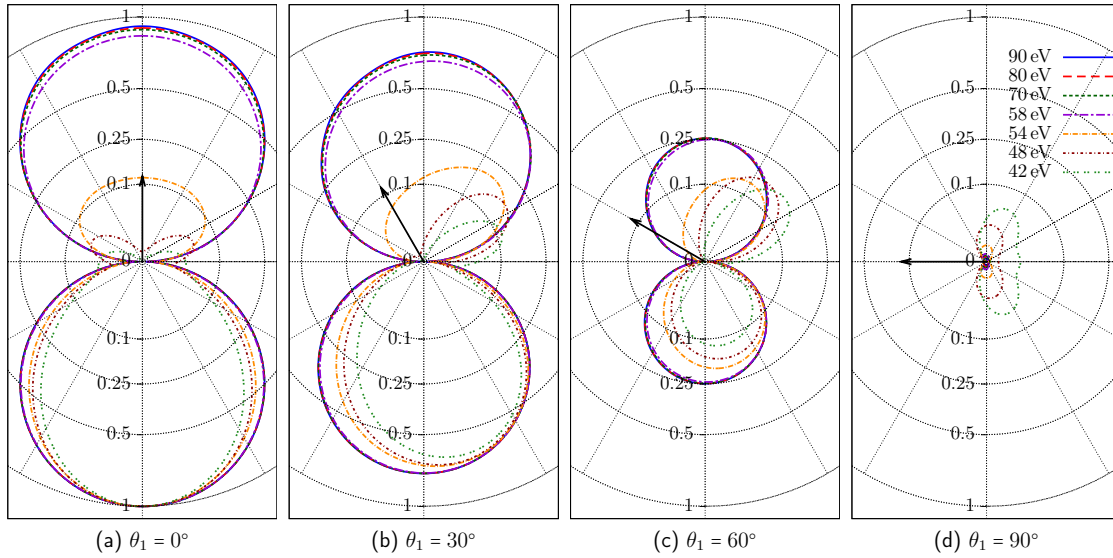


Figure 11.3: Joint angular distribution $P^{DI}(\theta_1, \theta_2)$ for TPD from 9 fs \sin^2 pulses at different photon energies. For each plot, θ_1 is fixed to a specific value (indicated by the black arrow), while θ_2 is scanned. At photon energies below the sequential threshold, the electrons are preferentially emitted in a back-to-back configuration, while above the threshold, the joint distributions resemble independent dipolar distributions for the two electrons. Note that the contour lines are progressively spaced on a quadratic scale in order to ensure that the area under the curve in the polar plot graphically corresponds to the probabilities.

probability is small. The figure clearly shows the transition from the nonsequential to the sequential regime: In the sequential regime, where almost all electrons are emitted within the sequential peaks, the angular distributions of the electrons are independent of each other, such that the distribution for the second electron is always the Hertz dipole (\cos^2) expected from a dipolar transition from the $1s$ state, with very little dependence on the ejection angle of the first electron. Going to the nonsequential regime ($\hbar\omega < 54.4$ eV), this changes dramatically – in this regime the electrons have to interact for double ionization to occur. Accordingly, the second electron is emitted at a time when the first electron is still close to the nucleus. The dipolar shape of the angular distribution is then modified in such a way that the probability for ejection of the two electrons in the same direction is strongly reduced. Even at $\hbar\omega = 54$ eV, just below the threshold, this is a strong effect. At $\hbar\omega = 48$ eV, the probability for ejection in the same direction is extremely reduced, and at $\hbar\omega = 42$ eV, where the total excess energy of the two electrons is just $E_{\text{tot}} = 2\hbar\omega + E_0 \approx 5$ eV, the probability for ejection in the same direction is almost negligible. In addition, although the two lobes of the Hertz dipole are still visible, they are strongly distorted in the nonsequential regime.

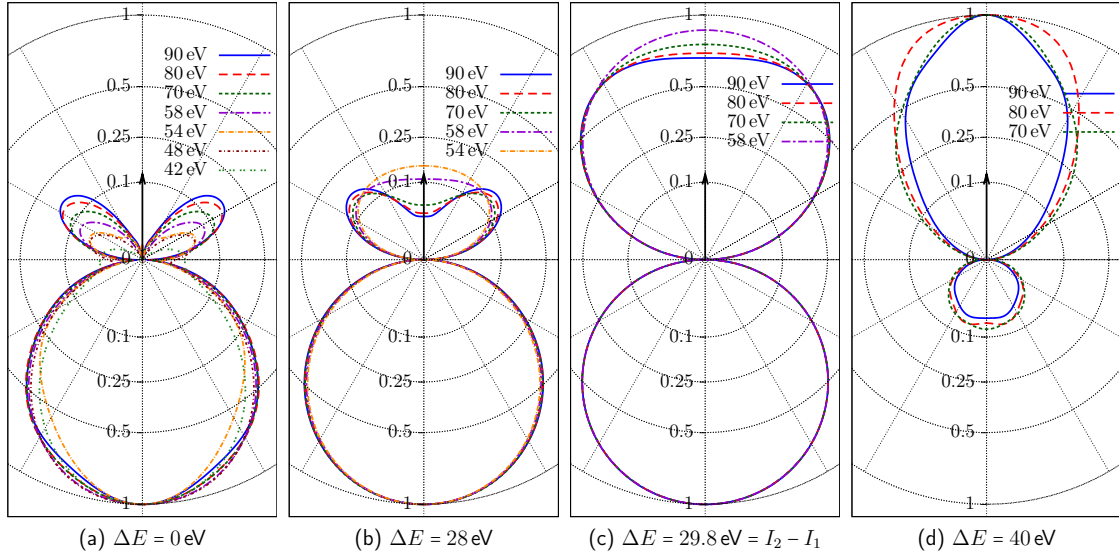


Figure 11.4: Joint energy-angle distribution $P^{DI}(\Delta E, \theta_1 = 0^\circ, \theta_2)$ for TPDI from 9 fs \sin^2 pulses at different photon energies. For each fixed energy difference, the distributions look very similar regardless of the photon energy. For ΔE “inside” the main peaks ((a) and (b)), the electrons are mainly emitted in a back-to-back configuration, at the main peaks they are largely independent of each other (c), while outside the main peaks they are preferentially emitted in the same direction (d). Note that the scale is quadratic in order to ensure that the area under the curve in the polar plot graphically corresponds to the probabilities.

Instead of integrating over all energies and thus observing the angular distribution averaged over *all* electrons that are emitted, we now investigate the distribution under the constraint of a specific energy difference ΔE between the electrons, i.e. the angle-energy distribution $P^{DI}(\Delta E, \theta_1, \theta_2)$, while the total energy E_{tot} is integrated over. Fig. 11.4 shows this distribution for various values of the energy sharing, from equal energy sharing $\Delta E = 0$ to energy sharings outside the main sequential peaks. For each fixed value of ΔE , the distributions look similar regardless of the photon energy. For energies inside the interval delimited by the main sequential peaks, i.e. $|\Delta E| < 29.8 \text{ eV}$, the electrons are mainly emitted in a back-to-back configuration. At the main sequential peaks, i.e. the energies where most electrons are ejected, the electrons are largely independent of each other and are emitted in an independent dipolar configuration. Finally, outside the main sequential peaks, they are preferentially emitted in the same direction. As energy sharings away from the main peaks are only reached if both electrons, which repel each other, are emitted within a short time of each other, it seems surprising at first that they would be emitted in the same direction. However, it should be kept in mind that at these large values of ΔE , one of the electrons is significantly faster than the other one,

such that they do not stay close to each other even if they are emitted in the same direction. The strong preference for emission in the same direction can then be understood by the fact that this asymmetric energy distribution is easily reached if both electrons are initially emitted in the same direction, such that the slower electron interacts with the faster electron through *post-collision interaction* (PCI) [176–179], essentially giving it an additional “push”.

To better quantify the amount of correlation between the electrons, we examine the *mutual information* [180] contained within their combined angular distribution. Mutual information is one of many possible quantities used in probability theory to measure the amount of correlation between two variables. In essence, it measures the information that the two variables share – i.e. how much information one gains about the second variable by knowing the first. For continuous variables, it is defined by

$$\mathcal{I}(X; Y) = \iint dx dy P(x, y) \log_2 \left(\frac{P(x, y)}{P(x)P(y)} \right), \quad (11.5)$$

where $P(x, y)$ is the joint probability distribution of the two variables, while $P(x) = \int dy P(x, y)$ and $P(y) = \int dx P(x, y)$ are the reduced one-variable distributions. All integrations are performed over the whole domain of the distribution. If the two variables are independent, the total distribution is identical to the product of the one-variable distributions ($P(x, y) = P(x)P(y)$), and the argument of the logarithm is always 1, such that the mutual information vanishes. The mutual information is closely related to the concept of information entropy (or Shannon entropy), and can be expressed by $\mathcal{I}(X; Y) = H(X) + H(Y) - H(X, Y)$, where $H(X) = -\int dx P(x) \log_2 P(x)$ is the Shannon entropy of the reduced probability distribution $P(x)$. We are interested in the mutual information in the angular distribution of the two electrons, which we define by

$$\mathcal{I}_{\Omega_1, \Omega_2} = \iint d\Omega_1 d\Omega_2 P_n^{DI}(\Omega_1, \Omega_2) \log_2 \left(\frac{P_n^{DI}(\Omega_1, \Omega_2)}{P_n^{DI}(\Omega_1)P_n^{DI}(\Omega_2)} \right), \quad (11.6)$$

$$\mathcal{I}_{\Omega_1, \Omega_2}(\Delta E) = \iint d\Omega_1 d\Omega_2 P_{n, \Delta E}^{DI}(\Omega_1, \Omega_2) \log_2 \left(\frac{P_{n, \Delta E}^{DI}(\Omega_1, \Omega_2)}{P_{n, \Delta E}^{DI}(\Omega_1)P_{n, \Delta E}^{DI}(\Omega_2)} \right), \quad (11.7)$$

with

$$P_n^{DI}(\Omega_1, \Omega_2) = P^{DI}(\Omega_1, \Omega_2) / \iint d\Omega_1 d\Omega_2 P^{DI}(\Omega_1, \Omega_2), \quad (11.8)$$

$$P_{n, \Delta E}^{DI}(\Omega_1, \Omega_2) = P^{DI}(\Omega_1, \Omega_2, \Delta E) / \iint d\Omega_1 d\Omega_2 P^{DI}(\Omega_1, \Omega_2, \Delta E). \quad (11.9)$$

We either examine the total mutual information in the angular distribution for all electrons for which we get a single number $\mathcal{I}_{\Omega_1, \Omega_2}$, or we fix the energy difference ΔE of the electrons and examine the mutual information in the distribution

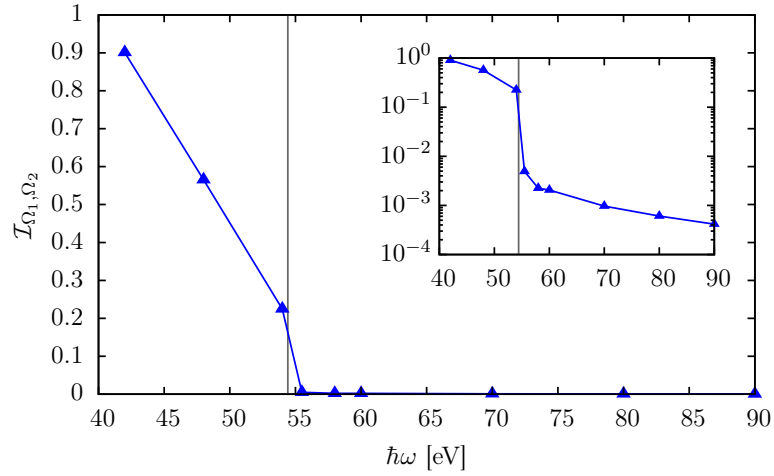


Figure 11.5: Mutual information $\mathcal{I}_{\Omega_1, \Omega_2}$ for TPDI for different photon energies $\hbar\omega$. The pulses had a 9 fs \sin^2 envelope, apart from the data point at 54 eV, where a 20 fs \sin^2 pulse was used to suppress the sequential contribution. The gray line at 54.4 eV indicates the threshold for sequential TPDI. The inset shows the same data on a logarithmic scale. The mutual information decreases as the threshold is approached, showing a steep drop after the threshold, with little dependence on the photon energy for $\hbar\omega > 54.4$ eV.

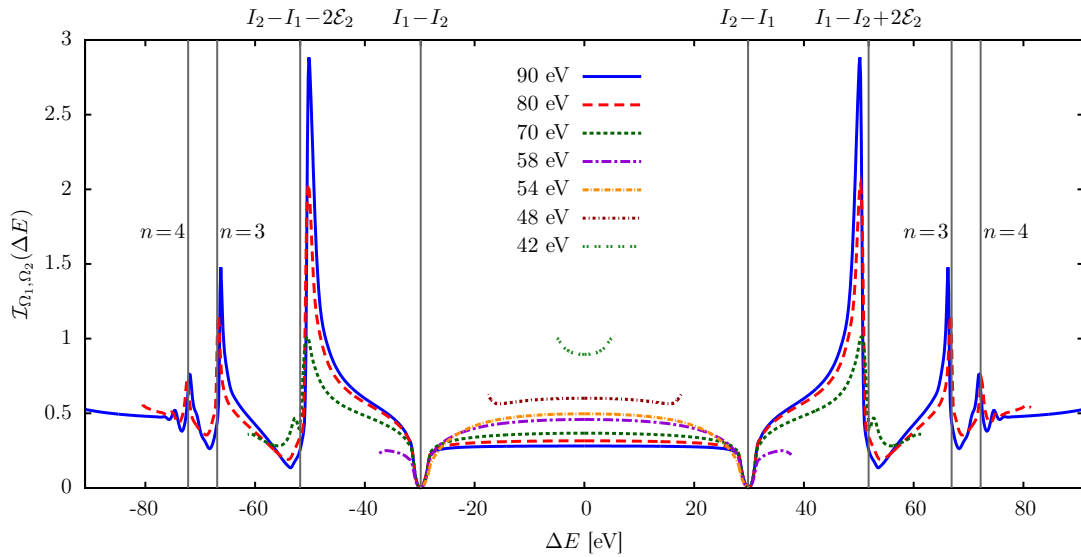


Figure 11.6: Mutual information $\mathcal{I}_{\Omega_1, \Omega_2}(\Delta E)$ for TPDI for different photon energies $\hbar\omega$ as a function of ΔE . The pulses had a 9 fs \sin^2 envelope, apart from the data for photon energy $\hbar\omega = 54$ eV, where a 20 fs \sin^2 pulse was used.

$P^{DI}(\Omega_1, \Omega_2, \Delta E)$. For the calculation of the mutual information, the probability distributions have to be normalized, cf. (11.8) and (11.9).

We first determine the total mutual information in the angular probability distribution of the two electrons, shown in Fig. 11.5. The mutual information in the angular distribution decreases as the threshold for sequential two-photon double ionization is approached, but stays at appreciable values below the threshold. Once the threshold is crossed (i.e. above $\hbar\omega = 54.4$ eV) the value of the mutual information steeply drops to almost negligible values, and slowly keeps on decreasing for higher photon energies. This confirms the expected behavior – below the threshold for sequential TPDI, the electrons strongly interact during the ionization process and are therefore correlated. In contrast to this, the main channel above the sequential threshold contains two independent photon absorptions from $1s$ states, such that the angular distribution is a product of \cos^2 distributions and there is almost no angular correlation, leading to vanishing mutual information. In the nonsequential regime, the angular distributions are well-converged and have already reached the values obtained in the limit $T \rightarrow \infty$, such that the mutual information should be independent of a further increase in pulse duration. In contrast, the (negligible) value of the total mutual information in the sequential regime depends on the pulse duration T , as the nonsequential contribution to the total angular distribution decreases with $\approx T^{-1.4}$, cf. section 12.3. The character of the angular correlation is seen even more clearly when plotting the mutual information as a function of the energy difference ΔE between the electrons (Fig. 11.6). In contrast to the energy spectrum (cf. Fig. 11.1), which is almost completely determined by the shape factor from second-order time-dependent perturbation theory, the mutual information strongly depends on the photon energy. The lower the photon energy, the slower the first electron, and consequently, the stronger the influence of the electron-electron interaction, leading to increased angular correlation. Therefore, around $\Delta E = 0$, the pulse at $\hbar\omega = 42$ eV shows high values of $\mathcal{I}_{\Omega_1, \Omega_2}$, with a monotonic decrease as the photon energy is increased. At the peaks of the main sequential process, $\Delta E = \pm(I_2 - I_1)$, the mutual information vanishes almost completely, as expected from an angular distribution that is a product of Hertz dipoles. For photon energies where shake-up of the remaining ion is possible, the mutual information at the energies of the shake-up process shows large peaks followed by dips. As the behavior around the shake-up peaks strongly depends on the pulse length even for these relatively long pulses, we discuss this phenomenon in the section on pulse-length dependence of the TPDI process, chapter 12.

An alternative measure for the angular correlation is given by the von Neumann entropy of the one-particle angular density matrix $\gamma_{1, \Omega}(\Omega, \Omega')$, which is obtained from the full density matrix $\gamma_2(\mathbf{k}_1, \mathbf{k}_2, \mathbf{k}'_1, \mathbf{k}'_2) = \psi(\mathbf{k}_1, \mathbf{k}_2)\psi^*(\mathbf{k}'_1, \mathbf{k}'_2)$ by performing a partial trace over all coordinates of the second electron and the magnitude of the

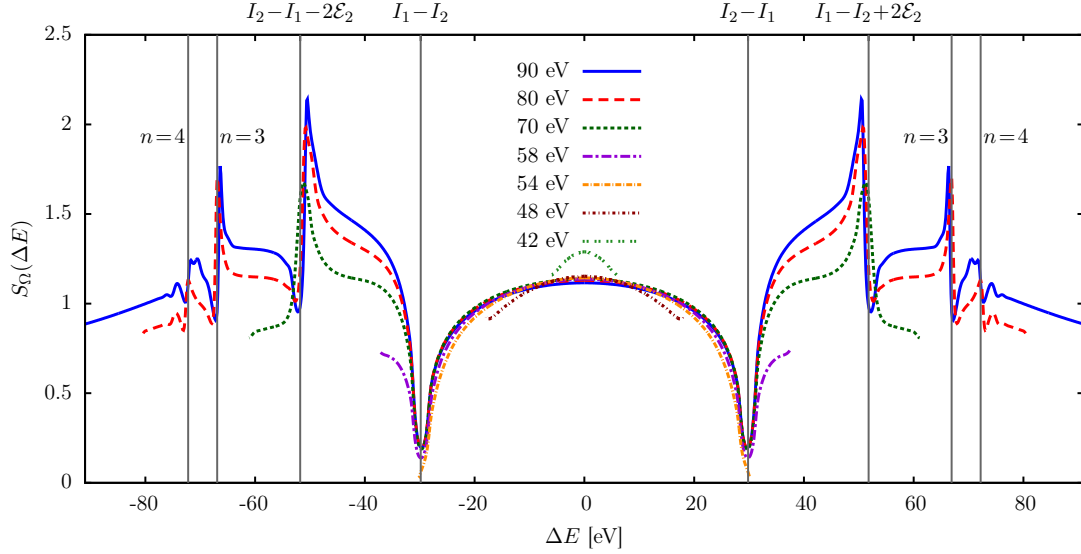


Figure 11.7: Energy-resolved angular von Neumann entropy $S_{\Omega}(\Delta E)$ for TPDI for different photon energies $\hbar\omega$. The pulses had a 9 fs \sin^2 envelope, apart from the run at 42 eV, where a 20 fs \sin^2 pulse was used.

momentum k_1 of the first electron. The angular von Neumann entropy, given by

$$S_{\Omega} = -\text{Tr}(\gamma_{1,\Omega} \ln \gamma_{1,\Omega}), \quad (11.10)$$

determines the amount of uncertainty about the angular state of one electron. This uncertainty stems from the dependence of the angular state on the state of the second electron. If the electrons are in an independent product state (as in the sequential process), the von Neumann entropy becomes zero. We show the angular von Neumann entropy under the condition that the energy difference is fixed to ΔE , i.e.

$$S_{\Omega}(\Delta E) = -\text{Tr}(\gamma_{1,\Omega}(\Delta E) \ln \gamma_{1,\Omega}(\Delta E)), \quad (11.11)$$

where $\gamma_{1,\Omega}(\Delta E)$ is the one-particle angular density matrix with the trace performed only over states with $E_1 - E_2 = \Delta E$. In addition, these density matrices have to be normalized such that their trace is 1. Fig. 11.7 shows that this measure displays very similar behavior as the angular mutual information. In particular, the maxima and minima appear at the same values of ΔE . This verifies that both of these measures give a reasonable indication for the amount of angular correlation in the final states. However, there are some differences: most strikingly, the minimum value of the entropy at the energy of the sequential process is still clearly non-zero, reaching about 0.2, while the mutual information decreases to very small values of the order of 10^{-3} . One possible explanation is that the von Neumann entropy also captures phase information, as it deals with the quantum mechanical density

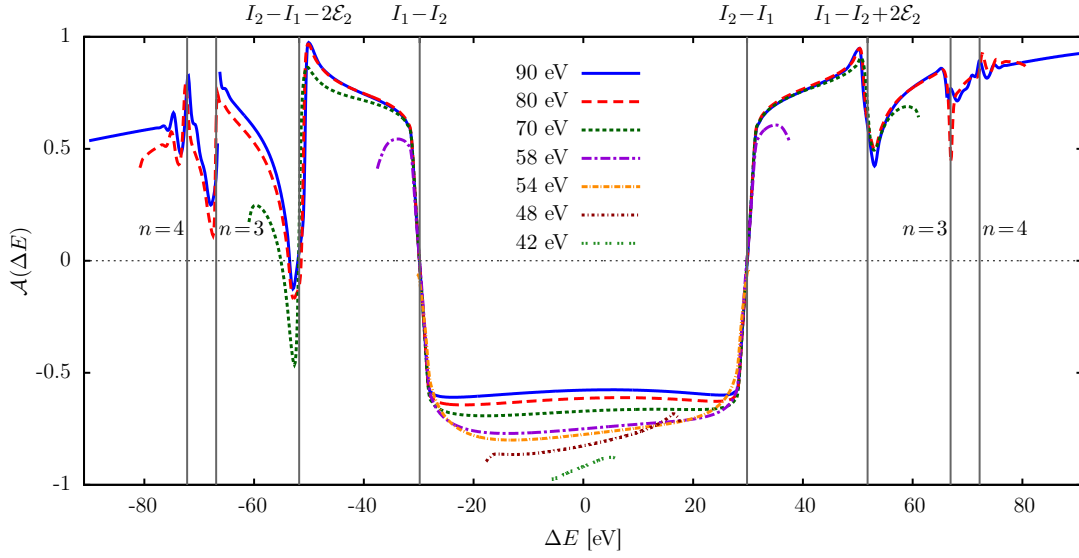


Figure 11.8: Forward-backward asymmetry $\mathcal{A}(\Delta E)$ for TPDI for different photon energies $\hbar\omega$. The pulses had a 9 fs \sin^2 envelope, apart from the run at 54 eV, where a 20 fs \sin^2 pulse was used.

matrix, while the mutual information only depends on the classical probability distribution. This would point to the fact that even when the angular probability distributions of the two electrons are almost independent, their relative emission direction still influences the phases in the final state.

To get more information on the relative emission directions of the two electrons, we introduce the forward-backward asymmetry distribution $\mathcal{A}(E_1, E_2)$, obtained by fixing the ejection direction of one electron in the direction of the laser polarization ($\theta_1 = 0^\circ$) and calculating the probability for the second electron to be emitted into the forward half-space $\theta_2 < \pi/2$ or backward half-space $\theta_2 > \pi/2$. The probabilities thus defined are

$$P^\pm(E_1, E_2) = 4\pi^2 \int_{\substack{\theta_2 < \pi/2 \\ \theta_2 > \pi/2}} P(E_1, E_2, \theta_1 = 0^\circ, \theta_2) \sin \theta_2 d\theta_2, \quad (11.12)$$

where the factor $4\pi^2$ stems from integration over ϕ_1 and ϕ_2 . The forward-backward asymmetry is then given by

$$\mathcal{A}(E_1, E_2) = \frac{P^+(E_1, E_2) - P^-(E_1, E_2)}{P^+(E_1, E_2) + P^-(E_1, E_2)}, \quad (11.13)$$

which varies in the range $[-1, 1]$. Values close to zero indicate equal probability for the second electron to be emitted in the forward or backward half-space, while large absolute values identify strong angular correlations. Positive values ($\mathcal{A} > 0$) indicate a preference for ejection of both electrons in the same direction while negative

values ($\mathcal{A} < 0$) indicate ejection in opposite directions. Note that $\mathcal{A}(E_1, E_2)$ is not symmetric under exchange of E_1 and E_2 , as the emission direction of the electron with energy E_1 is fixed in the laser polarization direction. Analogously, the reduced one-electron asymmetry $\mathcal{A}(E_1)$ can be determined by integrating $P^\pm(E_1, E_2)$ over the energy of the second electron, i.e. $P^\pm(E_1) = \int P^\pm(E_1, E_2)dE_2$, and

$$\mathcal{A}(E_1) = \frac{P^+(E_1) - P^-(E_1)}{P^+(E_1) + P^-(E_1)}. \quad (11.14)$$

Fixing the energy difference ΔE and integrating over total energy analogously gives the closely related quantity $\mathcal{A}(\Delta E)$. This is shown in Fig. 11.8 to allow easy comparison to Fig. 11.1 and Fig. 11.6. As we have seen before, the electrons are essentially uncorrelated at the “sequential” peaks, leading to vanishing asymmetry. For energies in between the two main peaks at $\Delta E = \pm(I_2 - I_1)$, the electrons are emitted in opposite directions, leading to negative values for $\mathcal{A}(\Delta E)$. The asymmetry is stronger for lower energies, again confirming that the electron-electron interaction has a stronger influence on the final distribution when the electrons are slower.

For energies outside the energy interval delimited by the sequential peaks, the asymmetry is equally strong, but now positive, pointing to the same emission direction for both electrons. When the second electron is emitted in the same direction as the first one, the well-known post-collision interaction [176–179] tends to increase the asymmetric sharing of the available energy [42]. The dividing line between the two different regimes of ejection (in opposite or in the same direction) is quite sharp and lies directly at the position of the sequential peaks.

At the positions of the shake-up peaks, we see large fluctuations of the forward-backward asymmetry, as also observed in the mutual angular information. For completeness we note that in the region between the two main peaks, only electrons emitted in opposite directions are observed both in “sequential” ($\hbar\omega > 54.4\text{ eV}$) and “nonsequential” ($39.5\text{ eV} < \hbar\omega < 54.4\text{ eV}$) TPDI. The main difference is that in nonsequential TPDI, only that region is energetically accessible, such that no other angular configurations are observed.

11.2 Nuclear recoil and one-electron angular distributions

We now turn to the investigation of *less* differential probability distributions, which are easier to access experimentally. Specifically, we investigate the *recoil ion momentum* probability distributions $P^{DI}(Q_x, Q_z)$ (cf. section 6.3) and the one-electron angular distributions $P^{DI}(E, \theta)$ (cf. section 6.2.3). The recoil ion momentum distribution can be experimentally obtained using COLTRIMS (COLd Target Re-

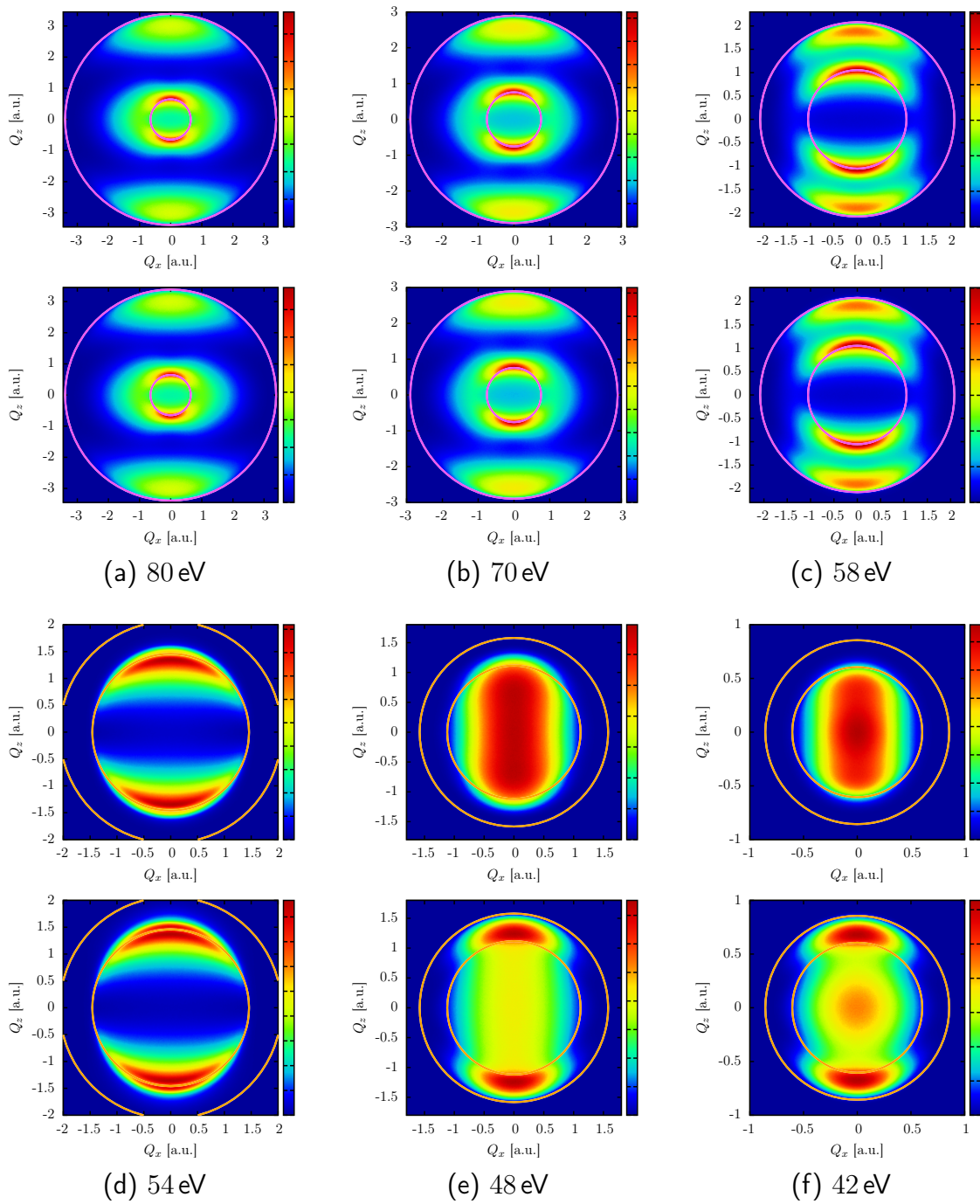


Figure 11.9: Recoil ion momentum distribution for TPDI from 9 fs \sin^2 pulses at different photon energies. For each energy, the upper plot shows the actual distribution, while the lower plot shows the distribution obtained with a product of dipoles as the angular distribution. The z -axis is chosen to coincide with the laser polarization axis.

coil Ion Momentum Spectroscopy) setups⁷. This has been done at FLASH (Free-electron LASer in Hamburg) using XUV pulses at $\hbar\omega = 44\text{ eV}$ photon energy [94]. Our results are shown in Fig. 11.9. In order to clearly see the effects of angular correlation, we compare the actual distributions with distributions obtained by assuming a product of $\cos^2\theta$ angular distributions for the electrons, i.e. with $P_{\text{dipole}}^{DI}(E_1, E_2, \Omega_1, \Omega_2) = P^{DI}(E_1, E_2) \frac{9}{4} \cos^2\theta_1 \cos^2\theta_2$. In the sequential regime (Fig. 11.9(a-c)), two distinct rings can be observed – these stem from electrons that are either emitted with momentum $k_1 = \sqrt{2(\hbar\omega - I_1)}$ or $k_2 = \sqrt{2(\hbar\omega - I_2)}$, with I_n being the n th ionization potential ($I_1 = 24.6\text{ eV}$, $I_2 = 54.4\text{ eV}$). The angular emission pattern in the sequential regime is a Hertz dipole for both electrons, such that emission on the laser polarization axis (the z -axis in our convention) is strongly favored. Consequently, the ion momentum shows peaks close to $Q = \pm(k_1 \pm k_2)$. These positions are marked by the magenta circles in Fig. 11.9(a-c). In the sequential regime, the actual recoil ion momentum distributions look almost exactly identical to those with a pure product of dipoles for the angular distribution, as expected. It should be noted that for $\hbar\omega = 80\text{ eV}$, the highest energy we show, there is also one-photon double ionization, with a total excess energy of $\hbar\omega + E_0 = 1\text{ eV}$. We here only plot the distribution associated with the two-photon process. In reality, there would be a contribution from one-photon double ionization at very small ion momenta, the relative strength of which depends linearly on the laser pulse intensity.

In the nonsequential regime, on the other hand, the sequential peaks disappear, and the one-electron energy distribution becomes much flatter. The highest recoil ion momenta would be reached for equal energy sharing and emission in the same direction. These momenta are indicated by the outer orange circles in Fig. 11.9(d-f). However, the electrons are almost always emitted in a back-to-back configuration. Therefore, these maximum ion momenta are not reached. For the back-to-back configuration, the largest ion momenta are instead obtained when one electron takes *all* the available excess energy, with the second electron just barely gaining enough energy to escape the nuclear potential. The ion momenta in this configuration are indicated by the inner orange circles in Fig. 11.9(d-f). For energies just below the sequential threshold, this is also the most probable configuration, as the one-electron energy distribution still shows the signature of the sequential process, i.e. the flanks of the sequential peaks (dubbed the “virtual” sequential process by Horner *et al.* [75]). Therefore, in most double ionization events at $\hbar\omega = 54\text{ eV}$, one electron gets almost all the excess energy, and the recoil ion momentum distribution is peaked close to the inner circle. For lower photon energies, the one-electron energy probability distribution is almost completely flat, and consequently, the area inside the circle allowed for back-to-back emission is almost uniformly filled. The distribution is still slightly elongated along the laser polarization axis z , as the electrons are preferentially emitted along this axis. The results in the nonsequential

⁷ Also known as reaction microscopes

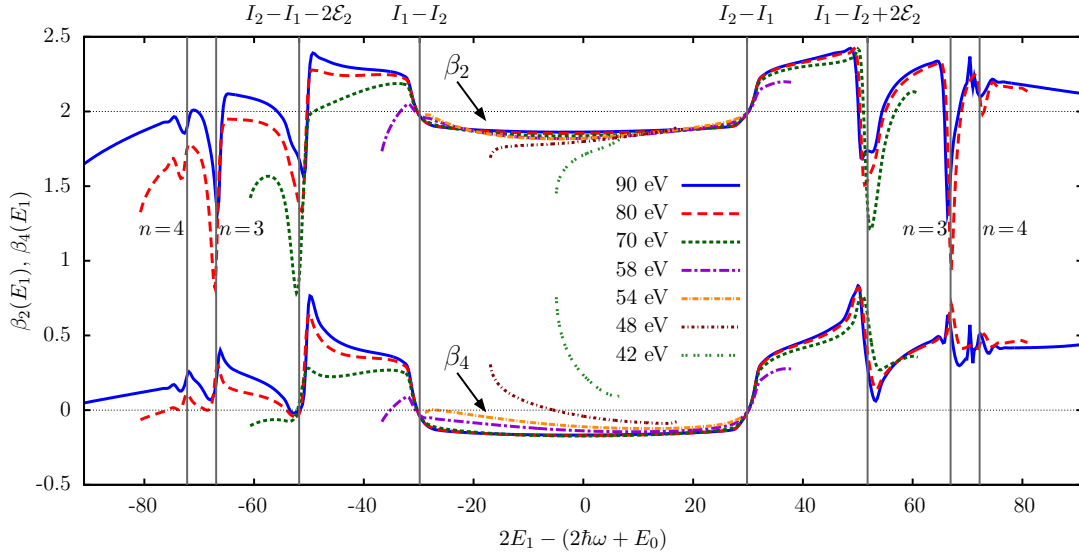


Figure 11.10: Angular asymmetry parameters $\beta_2(E_1)$, $\beta_4(E_1)$ for TPDI for different photon energies $\hbar\omega$. The pulses had a 9 fs \sin^2 envelope, apart from the run at 54 eV, where a 20 fs \sin^2 pulse was used. In order to compare more easily with the previous plots, the electron energy axis is shifted (see text). The upper group of lines gives β_2 , the lower group gives β_4 .

regime also show the influence of angular correlation most clearly. Using a product of dipoles instead of the real angular distribution leads to completely wrong recoil ion momentum distributions.

We now turn to the one-electron angle-energy distribution $P^{DI}(E, \theta)$. As explained in section 6.2.3, this distribution is cylindrically symmetrical and can (for two-photon double ionization) be parametrized as

$$P^{DI}(E, \theta) = P^{DI}(E)(1 + \beta_2(E)P_2(\cos \theta) + \beta_4(E)P_4(\cos \theta)), \quad (11.15)$$

where $P_l(x)$ are the Legendre polynomials. A Hertz dipole shape ($P^{DI}(E, \theta) \propto \cos^2(\theta)$) corresponds to $\beta_2 = 2$ and $\beta_4 = 0$. Although we want to use the one-electron distribution $P^{DI}(E, \theta)$ here because of its experimental relevance, we want to simultaneously compare with the previously obtained results plotted as a function of ΔE . As we are using relatively long pulses ($T = 9$ fs), the total energy is conserved, and we can use the transformation $\Delta E = E_1 - E_2 = 2E_1 - (E_1 + E_2) \approx 2E_1 - (2\hbar\omega + E_0)$. We therefore plot the one-electron angular asymmetry parameters vs. this shifted variable. Fig. 11.10 shows that in the sequential regime, the one-electron angular distribution at the main sequential peaks is indeed a simple Hertz dipole with $\beta_2 = 2$, $\beta_4 = 0$. At energies between the sequential peaks, both β_2 and β_4 decrease, producing a slightly broader distribution, but with the nodal line at $\theta = 90^\circ$ preserved for photon energies above the sequential threshold. This points to the fact

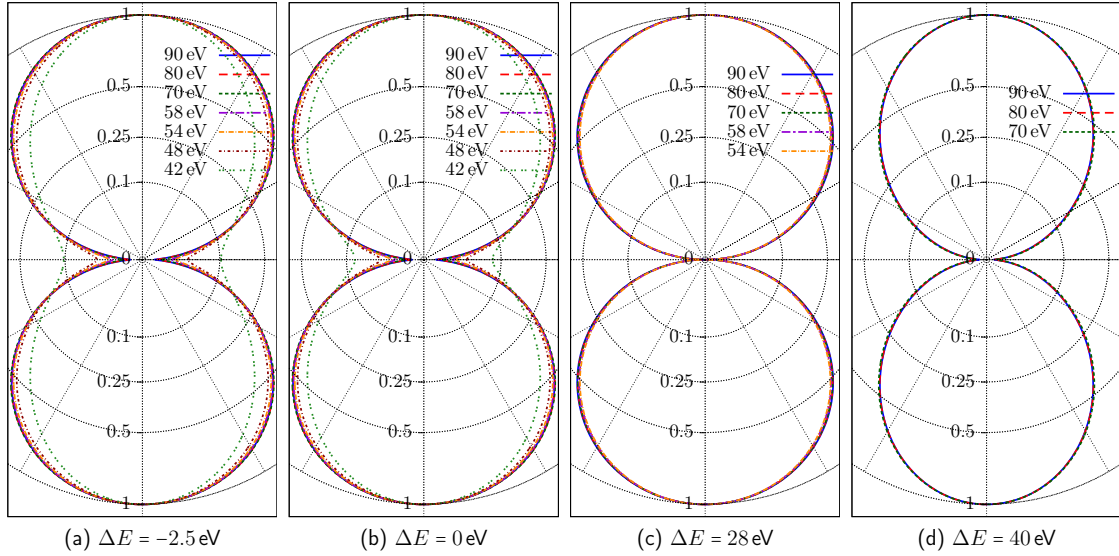


Figure 11.11: One-electron angular distributions $P^{DI}(E_1, \theta_1)$ for TPDI from 9 fs \sin^2 pulses at different photon energies. The energies E_1 were chosen so that they correspond to a fixed energy difference, $\Delta E = 2E_1 - (2\hbar\omega + E_0)$ (see text). Apart from the 42 eV pulse, the distributions for a fixed value of energy sharing again look very similar. Note that the scale is quadratic.

$\hbar\omega$ [eV]	90	80	70	58	55.5	54	48	42
β_2	1.993	1.991	1.988	1.984	1.957	1.947	1.806	1.688
$\beta_4(\times 10^2)$	-0.576	-0.718	-0.932	-1.611	-2.658	-3.904	-0.232	27.895

Table 11.1: Asymmetry parameters for energy-integrated angular distributions $P^{DI}(\theta)$, for TPDI by 9 fs \sin^2 pulses. Note that the values of β_4 were multiplied by 10^2 .

that the process is dominated by the absorption of one photon by each electron. At energies “outside” the main sequential peaks, the nodal line also survives, but the distribution becomes elongated. This fits with the mechanism of post-collision interaction described above – the higher energies are reached when the electrons are emitted in the same direction. Assuming an underlying \cos^2 distribution, this is most likely along the laser polarization axis. Therefore, high-energy electrons are most likely observed along that axis as well. The angular distributions are shown for some specific values of ΔE in Fig. 11.11. As the photon energy is decreased to just above the threshold for nonsequential TPDI, the electrons interact more strongly, and ejection at $\theta = 90^\circ$ becomes significant.

In addition to the energy-resolved angular distribution, Table 11.1 lists the asymmetry parameters for the energy-integrated angular distribution $P^{DI}(\cos \theta)$. Above the sequential threshold, where almost all electrons are emitted in the sequential

peaks with uncorrelated angular distributions, β_2 is close to two, while β_4 is negligible. This resembles a Hertz dipole, given by $\beta_2 = 2$, $\beta_4 = 0$. As the photon energy is decreased to below the sequential threshold, the asymmetry parameters significantly deviate from the Hertz dipolar shape, due to the stronger interaction between the electrons.

12 Differential distributions: Pulse duration dependence

In this section, we explore the dependence of TPDI on the pulse duration T ranging from ~ 100 attoseconds (the duration of the shortest pulses produced by high-harmonic generation [31]) to a few femtoseconds (the expected duration of XFEL pulse “bursts”).

In the nonsequential regime, energy-sharing between the electrons, and thus correlations, are a *conditio sine qua non* for double ionization to occur. By contrast, in “sequential” TPDI, each photon has sufficient energy to ionize one electron within an independent-particle model and electron-electron interaction, while present, is not a necessary prerequisite. As we have seen in the previous chapters, the final electron distribution contains contributions from pathways where the transitions happen within a short time of each other nonetheless. These are however strongly suppressed in long pulses and only visible on a logarithmic scale (cf. Fig. 11.1). By using the pulse duration as a control knob, it is possible to directly influence the *average* time delay between the two transitions (photon absorptions). In a pulse of just a few hundred attoseconds duration, the electrons are necessarily emitted within a short time of each other when double ionization occurs. Therefore, the concept of “sequential interactions”, valid for long pulses, becomes meaningless in attosecond pulses [53, 57, 61, 86]. Instead, the two-electron emission occurs almost simultaneously, and the strength of electron correlation in the exit channel can be tuned by the pulse duration T . In ionization by attosecond pulses, the duration of which corresponds to the timescale of the electronic motion in atoms, the breakdown of the independent-particle picture and strong coupling between the outgoing electrons is not imposed by the necessity of energy-sharing but is enforced by the ultrashort time between the two photoemission events occurring within T . Electron-electron interaction therefore plays a decisive role in the correlated final momentum distribution. In particular, the electrons are preferably emitted in a back-to-back configuration at approximately equal energy sharing, corresponding to a Wannier ridge configuration [40]. This configuration is usually observed when the available energy is just above the threshold for double ionization [181]. In that case, the only way for both electrons to be ejected is in a back-to-back configuration at approximately equal energy. In our case, the close proximity in time of the two photon absorption events induces this break-up mode. It has previously been observed in e-2e ionization processes [182] and also invoked in the classification of

doubly-excited resonances [100]. Because of the large instability of the Wannier orbit, its presence is more prevalent in break-up processes than in quasi-bound resonances.

We first discuss the evolution of the one- and two-electron energy spectra as the pulse duration is varied, showing non-uniform scaling with T . In [section 12.2](#), we show that the structures at the energies of the peaks associated with shake-up ionization of the He atom stem from interference between sequential and nonsequential contributions. Consequently, the strength of these interferences can be varied by changing the pulse duration, and from the size and shape of these Fano-like resonances, the pulse duration of XUV pulses might be deduced. We then discuss angular and angle-energy correlations present in ultrashort pulses, and finally show the nuclear recoil distributions obtained in ultrashort pulses. Note that we describe the \sin^2 pulses by their total duration T . The full width at half maximum (FWHM) of these pulses is given by $T/2$ for the envelope of the vector potential, and by $\approx 0.364T$ for the envelope of the pulse intensity (proportional to the square of the field). As attosecond pulses are usually described by the FWHM of their intensity envelope (e.g. [31]), a pulse with $T = 300$ as roughly corresponds to what is usually called a “100 as pulse”.

12.1 Energy spectrum

[Fig. 12.1](#) shows the two-electron energy distribution (previously investigated in [53, 57, 61, 86]) for two-photon double ionization at $\hbar\omega = 70$ eV, using \sin^2 pulses of different total durations T , ranging from $T = 150$ as up to $T = 9$ fs. For each pulse duration, the full distribution obtained from solving the TDSE is compared with the simple model from [Eq. 11.1](#). As before (cf. [Fig. 11.2](#)), the simple model agrees with the full results very well. Although a slight difference is clearly visible for the shortest pulses, the agreement is still good. Therefore, the energy distributions do not help to elucidate the change in the electron dynamics as the pulse duration is varied. It does, however, reveal the breakdown of the sequential ionization picture with decreasing pulse duration T . For long pulses, two distinct peaks signifying the emission of the “first” electron with energy $E_1 = \hbar\omega - I_1$ and the “second” electron with $E_2 = \hbar\omega - I_2$ are clearly visible. For pulses of the order of one hundred attoseconds, a dramatically different picture emerges: the two peaks merge into a single one located near the point of symmetric energy sharing. This effect is not simply due to the Fourier broadening of the pulse (cf. [86]), which determines the uncertainty in the total energy E_{tot} (i.e. the width along lines with $E_1 - E_2 = \text{const}$). Instead, the close proximity in time of the two emission events means that the energy of the intermediate state is not well defined, representing a clear departure from the independent-particle behavior. Differently stated, the time interval between the two ionization events is too short for the “remaining” electron to relax to

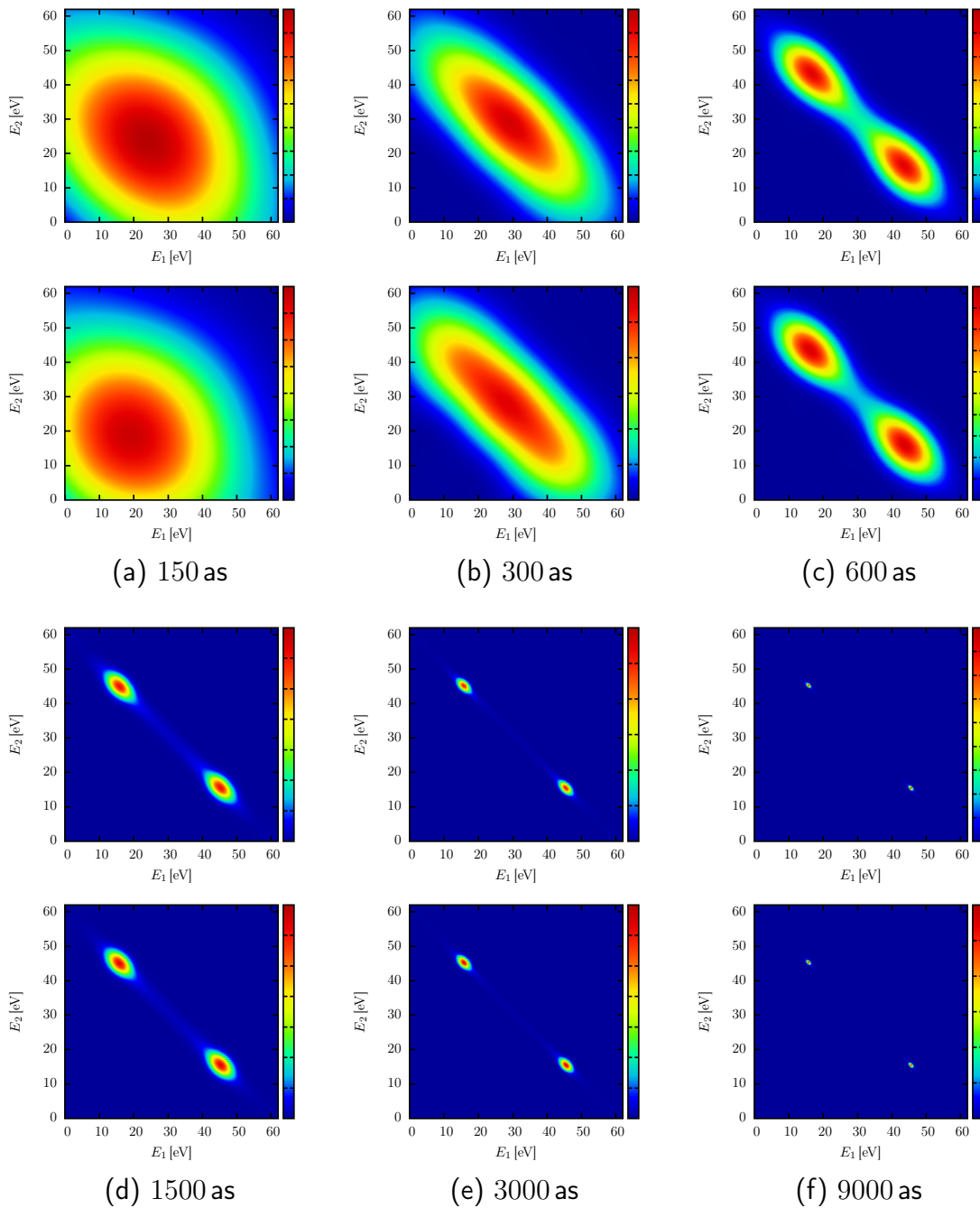


Figure 12.1: Energy distributions for TPDI with different pulse durations for \sin^2 pulses at $\hbar\omega = 70$ eV. For each duration, the upper plot shows the actual distribution, while the lower plot shows the distribution obtained with the simple model described in the text, obtained from second-order perturbation theory by neglecting correlation.

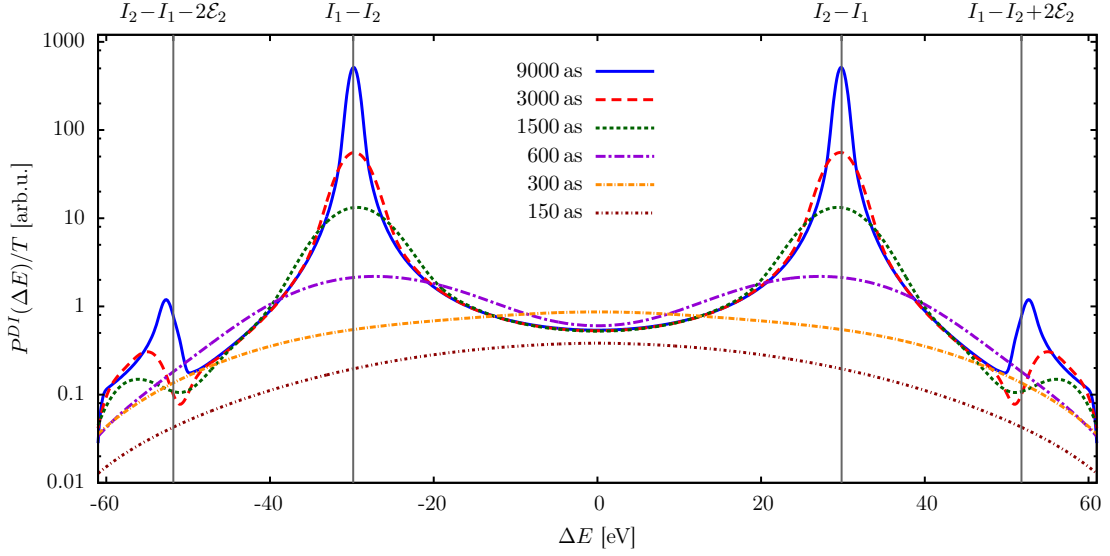


Figure 12.2: Double ionization rate $P^{DI}(\Delta E)/T$ (i.e. DI probability divided by the pulse duration) for TPDI by an XUV pulse at $\hbar\omega = 70\text{eV}$ with different pulse durations T . For sufficiently long pulse duration, the DI rate converges to a stable value except near the peaks of the sequential process.

a stationary ionic state. This demonstrates the fact that in the limit of ultrashort pulses, the distinction between “sequential” and “nonsequential” ionization loses its significance. Although electron interaction is not necessary to achieve double ionization, it has a significant effect on the outgoing electrons. This has been called the “transient” regime previously [86], where the duration of the XUV pulse is comparable to the “correlation time” defined by $T_C = 2\pi/E_C \approx 139\text{as}$, with $E_C = I_2 - I_1$ (cf. section 8.2). Note that the simple model presented previously does not include any electron correlation, but does include electron interaction in the sense that the ionization potentials for the first and second step are different. This amounts to the approximation that all the energy stored in the electrons’ mutual interaction is *immediately* converted into the kinetic energy of the free electron after the first transition.

Before turning to the observables showing the correlations induced by the electron interaction, we discuss the behavior of the energy distribution $P^{DI}(\Delta E)$ as the pulse duration is varied. A key indicator for sequential TPDI is that for sufficiently low intensities (when ground state depletion is negligible), the total yield scales with $P_{\text{seq}}^{DI} \propto \int_{-\infty}^{\infty} \int_t^{\infty} I(t)I(t')dt'dt \propto T^2$ [40, 57]. This is an immediate consequence of two independent subsequent emission processes, the probability for each of which increases linearly with T , such that $P_{\text{seq}}^{DI} \sim (P^I)^2 \propto T^2$. Equivalently, for each of the two processes a well-defined transition rate $W = \lim_{T \rightarrow \infty} P^I/T$ exists. This implies that the total rate P_{seq}^{DI}/T of the two-step process grows linearly with T

in the limit of long pulses, precluding the definition of a single cross section. By contrast, the nonsequential or direct double ionization probability P_{nonseq}^{DI} scales linearly with T and a converged transition rate exists in the limit of infinitely long pulses, $W = \lim_{T \rightarrow \infty} P_{\text{nonseq}}^{DI}/T$.

In the regime of sequential TPDI, the coexistence of both sequential and nonsequential contributions leads to a non-uniform scaling of the ionization yield with pulse duration over different regions of the electron emission spectrum. Fig. 12.2 shows the energy differential electron emission probability for different pulse durations, divided by T , $dW/d(\Delta E) = P^{DI}(\Delta E)/T$. This quantity converges to a duration-independent cross section value (apart from constant factors) except near those values of the energy where the sequential process (with or without shake-up) is allowed [75]. The areas of the main sequential peaks grow linearly with T , indicative of an overall quadratic scaling characteristic for the sequential process (cf. Fig. 12.3a). If one divides the yield contained in the peak areas by T^2 , the result is just proportional to the product of the single ionization cross sections for one-photon absorption from the He ground state and one-photon absorption from the He⁺ ground state.

The region within which the linear scaling prevails (white in Fig. 12.3b) is determined by the pulse duration for two different reasons:

(i) Due to Fourier broadening, the photon energy is not well defined for a finite pulse, limiting the energy resolution. This determines the width of the sequential peak. Thus, if the broadened sequential peak overlaps with the final energy of interest, the long-pulse limit $P^{DI}(E) \propto T$ can not be observed. This effect can be explained by the shape factor \mathcal{G} of second-order time-dependent perturbation theory and therefore is not connected directly to the dynamics of the process. As discussed in section 8.2, for a given deviation $|E_{ni\omega}|$ from energy conservation in each step, the total pulse duration T has to be larger than $T_c^{(i)} = 30.4/|E_{ni\omega}|$ (in atomic units) to observe linear scaling with the pulse duration to within 3%. This limiting value is shown in Fig. 12.3b as a purple dashed line. The agreement with the full numerical solution is very good, i.e. the purple line almost exactly determines the region where linear scaling with the pulse duration prevails.

(ii) In addition to the energy uncertainty of the pulse itself and of the intermediate state energy, the electrons can exchange energy through their mutual interaction. There is an intrinsic maximum time delay $t_c^{(ii)}$ between ionization events that can lead to a specific combination of final energies of the ejected electrons. When the second electron is ionized at a time when the first electron is already far from the nucleus, the electrons cannot exchange a sufficient amount of energy. This implies that the pulse has to be considerably longer than this maximal delay in order to resolve all contributions to a specific final state.

In order to estimate the size of effect (ii), we employ a simple classical model. We assume that the first electron is emitted satisfying energy conservation, i.e. with

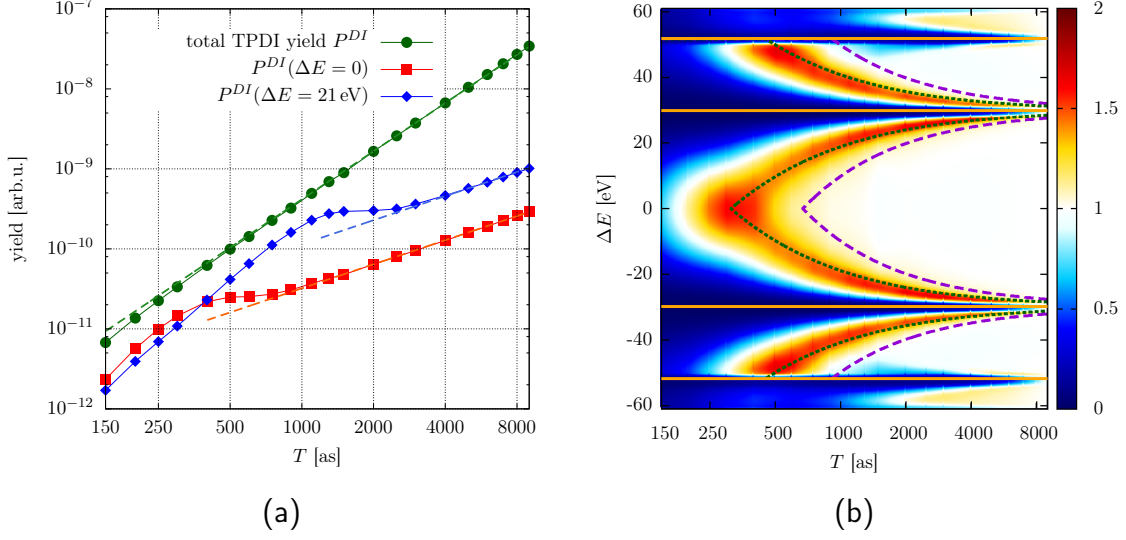


Figure 12.3: (a) Scaling of TPDI yields with pulse duration T at $\hbar\omega = 70$ eV. The green points are the total ionization yield P^{DI} , the red squares give the differential yield at equal energy sharing $P^{DI}(\Delta E = 0)$, and the blue diamonds give the differential yield closer to the sequential peak, at $\Delta E = 21$ eV. The dashed lines show fits to quadratic scaling with T for the total yield, and fits to linear scaling with T for the singly differential yield. At $\Delta E = 0$, i.e. far away from the sequential peaks, the scaling is linear for pulse durations of about 500 as, while closer to the peaks, the scaling only becomes linear for pulses longer than roughly 1500 as. (b) Contour plot of $P_{rel}^{DI}(E, T)$. A value of 1 for P_{rel}^{DI} (white in the color scale used here) marks the region where linear scaling of the singly differential yield with pulse duration T is observed. The orange lines indicate the positions of the peaks from the sequential process. The purple dashed and green dotted lines indicate the pulse durations $T_c^{(i)}$ and $T_c^{(ii)}$ after which linear scaling of the yield with T is expected due to Fourier broadening of the sequential peak and because of the maximum time delay between the photon absorptions (see text).

energy $E_{SI} = \hbar\omega - I_1$. In order to reach a specific final state with energies (E_1, E_2) , the liberated electron has to gain or lose the energy $E_{diff} = \min(|E_{SI} - E_1|, |E_{SI} - E_2|)$ by interacting with the second electron. Therefore, the first electron can be at most a distance $r_{SI}(t_c^{(ii)}) = 1/E_{diff}$ from the core at the moment of the second photon absorption. Solving the classical equation of motion for the electron in the (screened) field of the nucleus leads to a critical time

$$t_c^{(ii)} = \frac{2\sqrt{\alpha(\alpha+1)} - \ln\left(2\alpha + 2\sqrt{\alpha(\alpha+1)} + 1\right)}{(2E_{SI})^{3/2}}, \quad (12.1)$$

with $\alpha = E_{SI}/E_{diff}$. Note that $t_c^{(ii)}$ represents an upper limit for the maximum time

delay between the electron ejections, as it assumes that *all* the energy contained in the electron-electron interaction is transferred to only one of the electrons. In order to resolve all contributions leading to a specific final state, the pulse has to be considerably longer than the maximum classical time delay between the electron ejections. We here choose $T_c^{(ii)} \approx 10t_c^{(ii)}$, indicated in Fig. 12.3b as a dotted green line.

The fact that the timescale $T_c^{(ii)}$ obtained from the simple classical model is shorter than the time $T_c^{(i)}$ from the shape factor \mathcal{G} points to a possible explanation of why the simple model⁸ introduced earlier describes the energy spectrum so well: the intrinsic (classical) timescales of the process are of a similar magnitude, but shorter than the timescale introduced by the shape function, such that the spectrum is dominated by the effects from the system-independent shape function.

Fig. 12.3b displays the estimates $T_c^{(i,ii)}$ and the fraction of double ionization probability that scales linearly with T as a function of emission energy and pulse duration,

$$P_{\text{rel}}^{DI}(\Delta E, T) = \frac{P^{DI}(\Delta E, T)}{P^{DI}(\Delta E, T_{\text{max}})} \frac{T_{\text{max}}}{T}, \quad (12.2)$$

where $T_{\text{max}} = 9$ fs is the longest pulse we used. P_{rel}^{DI} takes on the value one when the double ionization probability at energy difference ΔE shows linear scaling with pulse duration. We note that the estimate of effect (ii) could be validated in a time-independent perturbation theory calculation. The latter does not show Fourier broadening but introduces an effective cutoff for the interaction time $t_c^{(ii)}$ because of the limited box size. The non-uniform scaling with T described here should occur for any photon energy where the sequential process is allowed. This is confirmed by calculations at $\hbar\omega = 91$ eV, shown in Fig. 12.5.

12.2 Shake-up interferences

The additional structures at higher ($E \approx \hbar\omega - I_2 + \mathcal{E}_2$) and lower ($E \approx \hbar\omega - I_1 - \mathcal{E}_2$) energies visible in Figs. 11.1, 11.6, 11.8, 11.10, and 12.2 originate from shake-up satellites in He^+ which can serve as intermediate states for two-photon double ionization. In the shake-up process, the He^+ ion is left in an excited state, while the free electron obtains an energy of $E'_1 = \hbar\omega - I_1 - \mathcal{E}_n$ (in the sequential limit). In the long-pulse limit, this simply leads to the appearance of shake-up satellite lines at energies E'_1 and $E'_2 = \hbar\omega - I_2 + \mathcal{E}_n$ in the one-electron energy spectrum. These lines are strongly suppressed compared to the “main” sequential lines without shake-up, as the transition matrix elements involved are smaller.

⁸ which includes only the shape factor and the difference in ionization energies for the first and second step, but neglects correlation

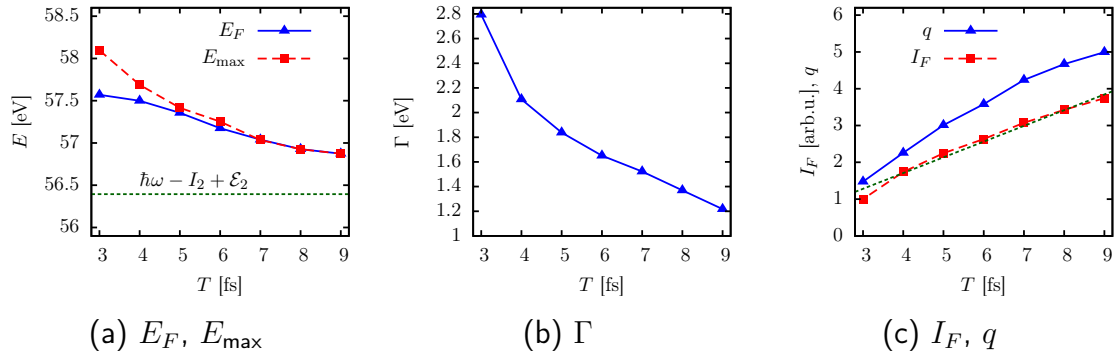


Figure 12.4: Parameters of the shake-up interference peaks around 57 eV for TPDI by an XUV pulse at $\hbar\omega = 70$ eV obtained from fitting to a Fano lineshape. (a) Fano resonance energy E_F and position E_{\max} of the maximum in the spectrum, (b) width Γ , (c) Fano parameter q and integrated yield I_F from the shake-up pathway. See text for details.

For short pulses up to a few femtoseconds duration, nonsequential (or direct) double ionization from the channel without shake-up is therefore larger or comparable to the contribution of the shake-up channel even at the positions of the peaks of the sequential process. The electrons can then reach the same final energies either through nonsequential TPDI without shake-up or through sequential TPDI via $\text{He}^+(nl)$ ($n > 1$) in the sequential process. Both indistinguishable pathways lead to the same final state and thus to an interference pattern in the double ionization yield, as observed in Fig. 12.2. This interference bears some resemblance to the well-known exchange interference between e.g. photo-electrons and Auger electrons [183–186]. There is, however, a fundamental difference: while the exchange interference is intrinsically controlled by atomic parameters, namely the energy and lifetime of the Auger electron, the novel interference observed here is truly a dynamical effect present only for short pulses and can be controlled by the pulse duration T . This interference effect, described in [41] was observed at about the same time by Palacios *et al.* [88].

As the dependence of the yield on the pulse duration is different for the different channels (proportional to T for the nonsequential channel, proportional to T^2 in the sequential channel), the observed spectrum strongly changes with pulse duration. For short pulses ($T < 1000$ as, cf. Fig. 12.2), the yield is completely dominated by the nonsequential channel without any trace of a shake-up interference. As the pulse duration is increased, the sequential channel with shake-up becomes increasingly important. As expected from the interference of a relatively sharp peak with a smooth background, the peak resembles a Fano lineshape [159]. Thus, the position of the maximum is shifted from the position expected in the limit of infinitely long pulses. Even for relatively long pulses ($T = 9$ fs), approaching the duration of

XFEL pulses, the position of the shake-up peak in the one-electron energy spectrum $P^{DI}(E)$ is shifted by a considerable fraction of an electron Volt. The structural similarity to a Fano resonance suggests to characterize the interference in terms of Fano resonance parameters for the position $E_F(T)$, width $\Gamma(T)$, and asymmetry $q(T)$, as well as its strength $I_F(T)$ (Fig. 12.4). To apply Fano's parametrization [159], the calculated energy spectrum $P^{DI}(E)$ is divided by the nonresonant spectrum $P_G^{DI}(E)$ (11.1). This simple model is similar to that proposed by Palacios *et al.* [88], as well as the time-independent model by Horner *et al.* [75, Eq. (8)]. As seen before, this fits the form of the spectrum away from the shake-up satellite peaks very well. A background contribution c_{bg} is added to account for the different angular distributions of the different channels, which prevent complete interference. This gives

$$\frac{P^{DI}(E)}{P_G^{DI}(E)} \approx c_{bg} + c_F \frac{(q\Gamma/2 + E - E_F)^2}{(E - E_F)^2 + (\Gamma/2)^2}. \quad (12.3)$$

The fitting procedure used here only works well for pulse durations $T \geq 3$ fs, as for shorter pulses, the shake-up peak is strongly suppressed and considerably broadened. Fig. 12.4 illustrates the dependence of the obtained parameters on the pulse duration, confirming the expected behavior: for long pulses, the peaks converge to the satellite lines, i.e. Lorentzians of vanishing width, such that $E_F \rightarrow \hbar\omega - I_2 + \mathcal{E}_n$ ($E_F \rightarrow \hbar\omega - I_1 - \mathcal{E}_n$), $\Gamma \rightarrow 0$, $|q| \gg 1$. The overall strength I_F of the shake-up peak relative to the nonresonant background is obtained from the integral over the Fano lineshape, $I_F \propto c_F(q^2 - 1)\Gamma$. I_F grows approximately linearly with T , confirming the scaling of the sequential shake-up channel with T^2 versus the scaling of the nonresonant background with T (Fig. 12.4c). Also shown in Fig. 12.4a is the position E_{\max} of the maximum of the spectrum $P^{DI}(E)$ without any further processing.

The effects of this shake-up interference could possibly be observed in XFEL pulses, which reach focused intensities of up to 10^{16} W/cm² [21]. To confirm that the results shown here (calculated for 10^{12} W/cm²) also apply for these high intensities, we performed an additional calculation at a peak intensity of $I_0 = 5 \cdot 10^{15}$ W/cm² with a \sin^2 pulse of total duration $T = 9$ fs. The shape of the differential yield $P^{DI}(E)$ (not shown) is almost unchanged compared to the result at 10^{12} W/cm² peak intensity, even though the ground state survival probability is only 20%. The total double ionization probability is $P^{DI} = 36\%$, i.e. more than a third of the helium atoms in the laser focus are doubly ionized. Even though the yield in the shake-up peak is only 0.6% of the total yield for that duration, this could be seen in experiment as only the integrated one-electron energy spectrum has to be observed. Moreover, from the position, strength and asymmetry of the interference peaks, information on the poorly known pulse duration of XFEL pulse ‘‘bursts’’ could possibly be deduced.

The results shown up to now were obtained at a photon energy of $\hbar\omega = 70$ eV, where only the $n = 2$ shake-up channel plays a role. While the qualitative behavior

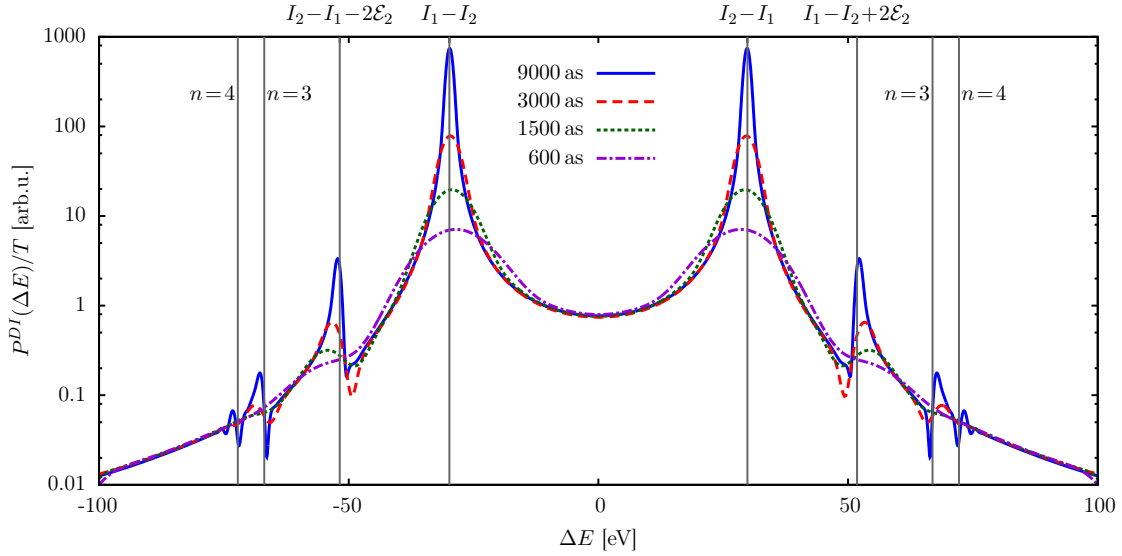


Figure 12.5: Double ionization (DI) rate $P^{DI}(\Delta E)/T$ (i.e. DI probability divided by the pulse duration) for TPDI by an XUV pulse at $\hbar\omega = 91$ eV with different pulse durations T . Shake-up peaks up to $n = 5$ are visible.

of each shake-up peak is expected to be independent of $\hbar\omega$, new intermediate ionic states $|nl\rangle$ become accessible at $\hbar\omega > I_1 + \mathcal{E}_n$, converging to $\hbar\omega > -E_0$ for $n \rightarrow \infty$. This is demonstrated in Fig. 12.5 at a photon energy of $\hbar\omega = 91$ eV. As the shake-up probability quickly decreases with increasing n , only the peaks up to $n = 4$ can clearly be identified at the pulse lengths used here (up to $T = 9$ fs), with $n = 5$ being just barely visible. For longer pulses, more highly excited states would start to play a role as well. In that case, one would need to take into account that the peaks for higher n overlap with each other as well as with the nonresonant background for a complete description.

It should be noted that in order to observe these interference effects, the asymptotic vectorial momenta $\mathbf{k}_1, \mathbf{k}_2$ (i.e. not only the asymptotic energies E_1, E_2) of the two pathways have to coincide. The shake-up channel has an angular distribution considerably different from that of the nonsequential channel, such that only partial interference between the final states is expected. This leads to a rich structure in the observed angular distributions (not shown), a more detailed analysis of which is given in the following section.

12.3 Angular correlations

The attosecond-pulse induced dynamical electron correlation becomes more clearly visible in the angular distributions. We again start by examining the energy-

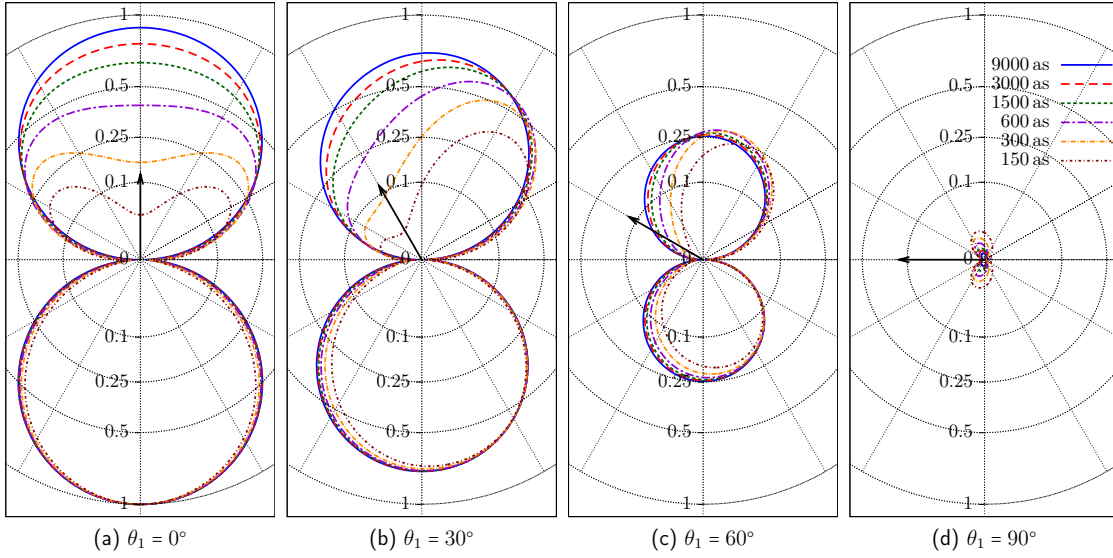


Figure 12.6: Joint angular distribution $P^{DI}(\theta_1, \theta_2)$ for TPDI from \sin^2 pulses at $\hbar\omega = 70$ eV for different pulse durations. For each plot, θ_1 is fixed to a specific value (indicated by the black arrow), while θ_2 is scanned. While long pulses $T \gtrsim 3$ fs show independent dipolar distributions for the two electrons, attosecond pulses lead to strong back-to-back emission. Note that the scale is quadratic in order to ensure that the area under the curve in the polar plot graphically corresponds to the probabilities.

integrated joint angular distribution $P^{DI}(\Omega_1, \Omega_2)$, cf. Fig. 12.6. We choose a coplanar geometry (azimuthal angles $\phi_1 = \phi_2 = 0^\circ$), as calculations in non-coplanar geometry lead to the same conclusions. In the limit of “long” pulses ($T = 9$ fs), the joint angular distribution approaches the product of two independent Hertz dipoles, each of which signifies the independent interaction of one electron with one photon. Consequently, also the conditional angular distribution $P^{DI}(\theta_1, \theta_2)$ corresponds to a Hertz dipole. With decreasing pulse duration, the distribution is strongly modified and develops a pronounced forward-backward asymmetry. The conditional probability for the second electron to be emitted in the same direction as the first is strongly suppressed. This strong preference for back-to-back emission for $T \leq 300$ as persists after integration over the electron energies, i.e. it does not only occur for some specific choice of energy sharing. Nevertheless, approximately equal energy sharing dominates (cf. Figs. 12.1 and 12.2). Thus, the dominant break-up mode induced by an attosecond pulse corresponds to the “Wannier ridge” configuration [181]. This resembles the nonsequential TPDI regime (cf. Fig. 12.7), where only back-to-back configurations are observed as well. As we have previously discussed, in that process only electrons ionized within a short time of each other can be observed even in long pulses. Thus, the similarity of the joint angular distributions in ultrashort pulses and in nonsequential TPDI is not surprising.

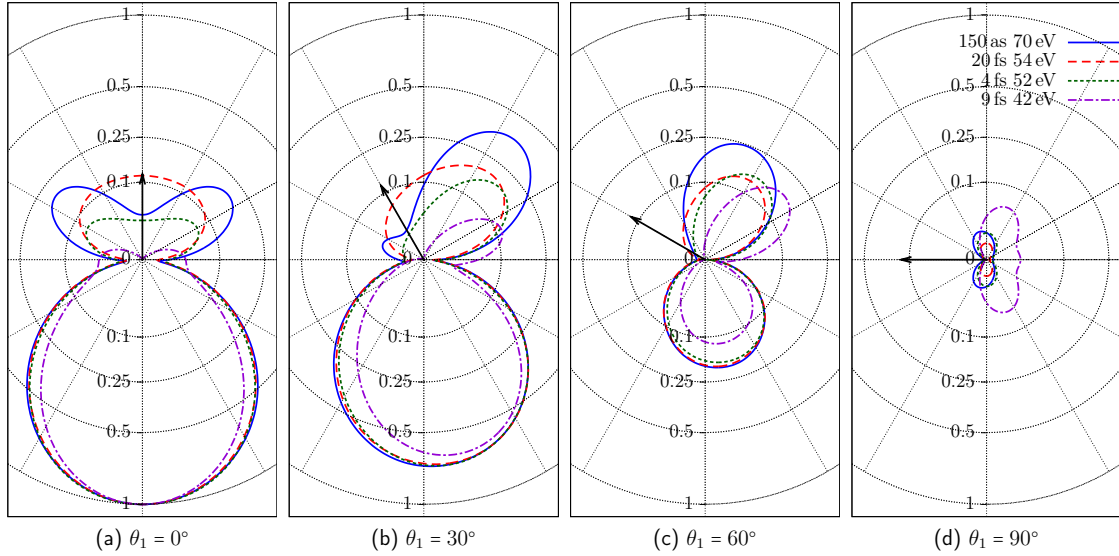


Figure 12.7: Joint angular distribution $P^{DI}(\theta_1, \theta_2)$ for TPDI for ultrashort sequential and long nonsequential pulses. All pulses had a \sin^2 envelope. For each plot, θ_1 is fixed to a specific value (indicated by the black arrow), while θ_2 is scanned. Note that the scale is quadratic in order to ensure that the area under the curve in the polar plot graphically corresponds to the probabilities.

In order to better quantify the attosecond-pulse induced correlation, we again investigate the *mutual information* $\mathcal{I}_{\Omega_1, \Omega_2}$ (11.6) of the joint angular distribution $P^{DI}(\Omega_1, \Omega_2)$. Fig. 12.8a shows that the mutual information, negligible in long pulses, strongly increases as the pulse duration is decreased. Furthermore, the pulse duration dependence of the mutual information follows a power law, $\mathcal{I}_{\Omega_1, \Omega_2} \propto 1/T^b$, with $b \approx 1.40$. The reason for this power law dependence as well as the significance of the exponent are still under investigation.

The power law decay of the mutual information persists up to the longest pulses considered here ($T = 9$ fs). However, the value of $\mathcal{I}_{\Omega_1, \Omega_2}$ is expected to converge to a non-zero value even in the limit of infinitely long pulses. While in that case, the nonsequential contributions are negligible, the (sequential) shake-up ionization processes always occur with the same relative probability compared to the main sequential pathway. For shake-up channels, the fact that the eigenstates of the He^+ ion are degenerate in angular momentum means that the remaining shake-up electron will be in a superposition of states that depends on the angular momentum of the ejected electron. Therefore, there is non-vanishing angular correlation between the electrons even when the (average) time delay between the ejections becomes very large. Consequently, the mutual information is expected to approach a stable non-zero value in the limit $T \rightarrow \infty$. For the longest pulses we used ($T = 9$ fs), the dominant contribution to the mutual information still comes from nonsequential

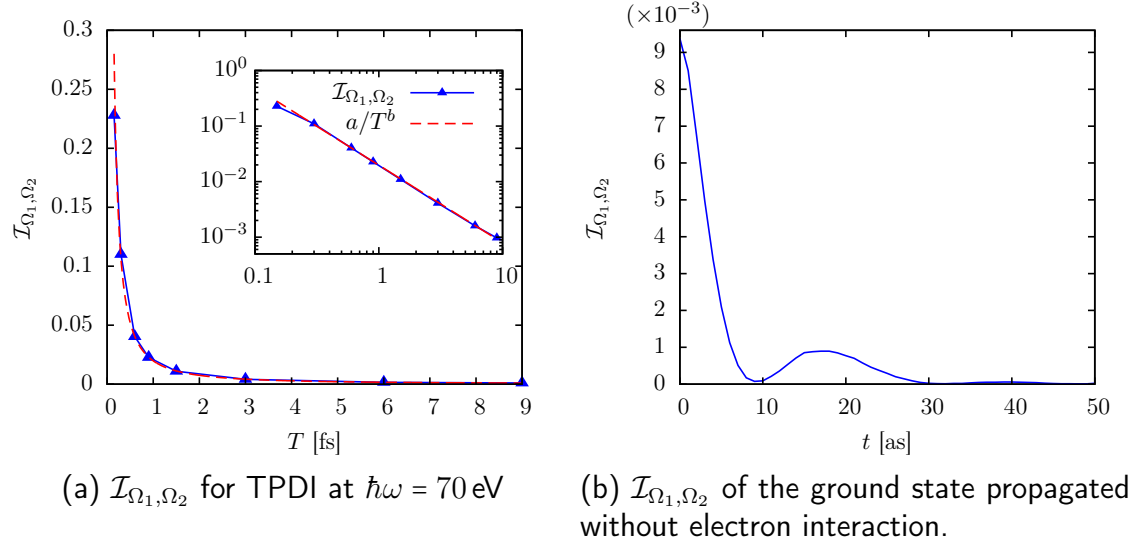


Figure 12.8: Mutual information $\mathcal{I}_{\Omega_1, \Omega_2}$. (a) shows $\mathcal{I}_{\Omega_1, \Omega_2}$ for TPDI at $\hbar\omega = 70$ eV, for \sin^2 pulses of different total duration T . The inset shows the same data using a log-log scale. The fit shows that the mutual information follows a power law dependence, with $b \approx 1.40$. (b) shows $\mathcal{I}_{\Omega_1, \Omega_2}$ for time propagation of the helium ground state without electron interaction. The system is prepared in the ground state of the full Hamiltonian, and then propagated without interaction between the electrons. This leads to a quick relaxation and decay of the angular correlations within a few attoseconds.

processes, such that the expected limiting behavior is not yet observed.

It is now instructive to inquire into the origin of the strong angular correlations observed for short pulses. Three different sources can be distinguished:

(i) Correlations in the helium ground state. Due to Coulomb repulsion, the electrons in the ground state are not independent of each other. For ultrashort pulses, TPDI can thus be interpreted as a probe that maps out the initial-state correlations.

(ii) Induced dipole polarization in the intermediate state. When the first electron leaves the core, its electric field induces polarization of the remaining ion, leading to an asymmetric probability distribution of the second electron. The second photon then probes the dynamics in this bound-free complex, such that TPDI can be interpreted as a pump-probe setup.

(iii) Final-state electron-electron interaction in the continuum. After the second electron has been released within the short time interval T as well, their mutual repulsion may redirect the electrons.

While the dividing line between those mechanisms is far from sharp, the present time-dependent wave packet propagation can shed light on their relative importance since they occur on different timescales. The pulse parameters (energy and

duration) determine the relative influence of these mechanisms on the observed angular correlations. Note that these are different timescales than for energy correlations (e.g. [86]) since angular momentum, not energy, is exchanged between the electrons. The correlations are therefore not determined by the shape function \mathcal{G} , and system-specific dynamics can be observed.

Relaxation of the ground-state angular correlations (i) is expected to occur on the timescale of the orbital period of the residual electron. As the remaining one-electron wave function is mostly in the $n=1$ and $n=2$ shells, the timescale for this relaxation can be estimated as $t_{(i)} \approx \hbar/(E_2 - E_1) \approx 16$ as, where E_n is the binding energy in the n -th shell of the He^+ ion. We have verified this timescale by starting a simulation in the ground state of the He atom and then suddenly switching off electron interaction. In the ground state, the electrons are correlated because of their mutual Coulomb repulsion. In the coupled angular momentum basis, the correlation is present because of the admixture of partial waves with non-zero single electron angular momenta l_1, l_2 . After the electron-electron interaction has been turned off, the angular correlations quickly decay. Fig. 12.8b shows this decay by plotting the mutual information in the angular distribution as a function of time for the helium ground state propagated without electron-electron interaction. The correlations disappear within a few attoseconds. Therefore, ground-state correlations can become visible only for pulses with durations much shorter than those investigated here.

The timescale for induced dipole polarization (ii) can be estimated by the time the first electron takes to escape to a distance where it does not influence the remaining bound electron strongly. We choose a distance of 10 a.u., for which the polarization of the He^+ ground state by a classical electron at that distance is negligible. The time necessary for the first electron to reach this distance after absorbing a 70 eV photon is about 120 as and thus of the order of the pulse lengths T considered. For higher photon energies, the first electron escapes more quickly, decreasing the importance of this effect. In order to verify this energy dependence, we have performed calculations at various photon energies for $T=75$ as. Fig. 12.9 demonstrates that for higher energies the asymmetry of the joint angular distribution is indeed strongly reduced.

Long-range Coulomb interactions in the continuum (iii) extend over much longer timescales, which strongly depend on the relative emission angles and energies of the electrons, i.e. $|\mathbf{k}_1 - \mathbf{k}_2|$. For example, for two electrons ejected in the same direction and with similar energies, the interaction will last much longer than for ejection in opposite directions. This can be verified by using an ultrashort pulse to start a two-electron wave packet in the continuum and observing the evolution of the joint angular distribution after the laser pulse is switched off (Fig. 12.10). Directly after the pulse, the distribution of the electrons shows a decreased probability for ejection on the same side of the nucleus (primarily because of (ii)), but the lobes in forward and backward direction still mostly retain the shape expected from a

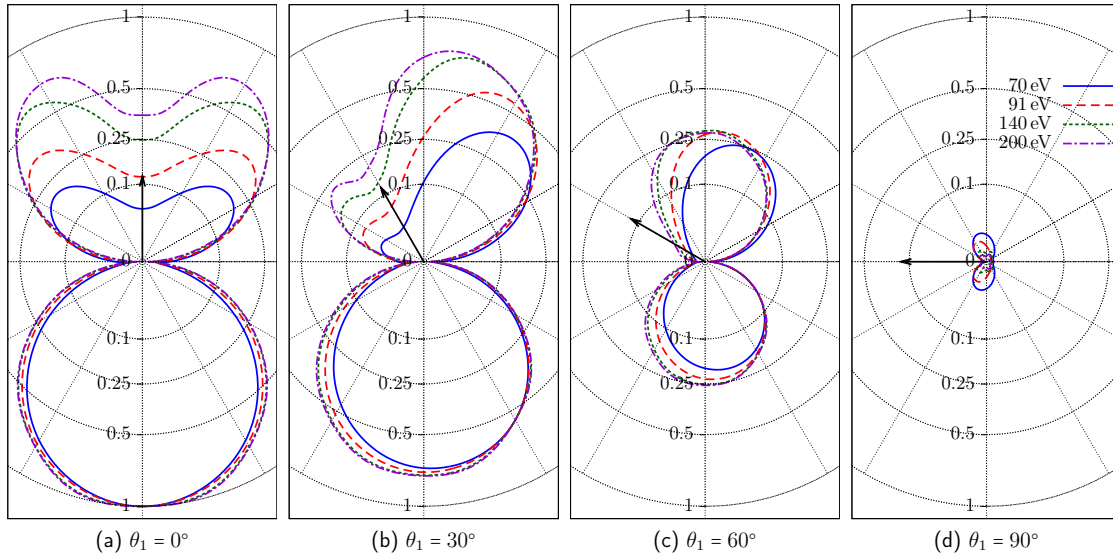


Figure 12.9: Joint angular distribution $P^{DI}(\theta_1, \theta_2)$ for TPDI from $T = 150$ as \sin^2 pulses at different photon energies. For each plot, θ_1 is fixed to a specific value (indicated by the black arrow), while θ_2 is scanned. The correlation between the electrons decreases with increasing photon energy. Note that the scale of the contour lines is quadratic.

dipole transition. As time passes, continuum final-state interactions (post-collision interactions) persist and the joint angular distribution develops a pronounced dip at equal ejection angle. The change at larger relative angles is almost negligible. The importance of the electron-electron interaction in the continuum is underlined by the angular mutual information $\mathcal{I}_{\Omega_1, \Omega_2}$, evaluated at different times after the end of the pulse (Fig. 12.11). $\mathcal{I}_{\Omega_1, \Omega_2}$ increases by a factor of four within the first femtosecond after the end of the pulse, after which it has almost reached its limiting value. A large part of the strong angular correlation observed in ultrashort pulses is thus shown to stem from electron-electron interaction after both electrons have been released into the continuum.

One remarkable feature of the conditional angular distribution is the persistence of the nodal plane at $\theta = 90^\circ$. While correlation effects strongly perturb the shape of the independent-particle dipolar shape, the nodal plane expected for the angular distribution of two electrons absorbing one photon each is preserved almost completely. Note that this also holds true in the nonsequential TPDI regime for energies approaching the sequential threshold (cf. Fig. 12.7). This is further evidence of the fact that also in the nonsequential regime, the dominant intermediate states are the singly ionized states without shake-up. This is in contrast to one-photon double ionization, where only one electron absorbs the photon energy and electron ejection at angles normal to the polarization axis is indeed observed [187].

We now turn to differential quantities characterizing the angle-energy correla-

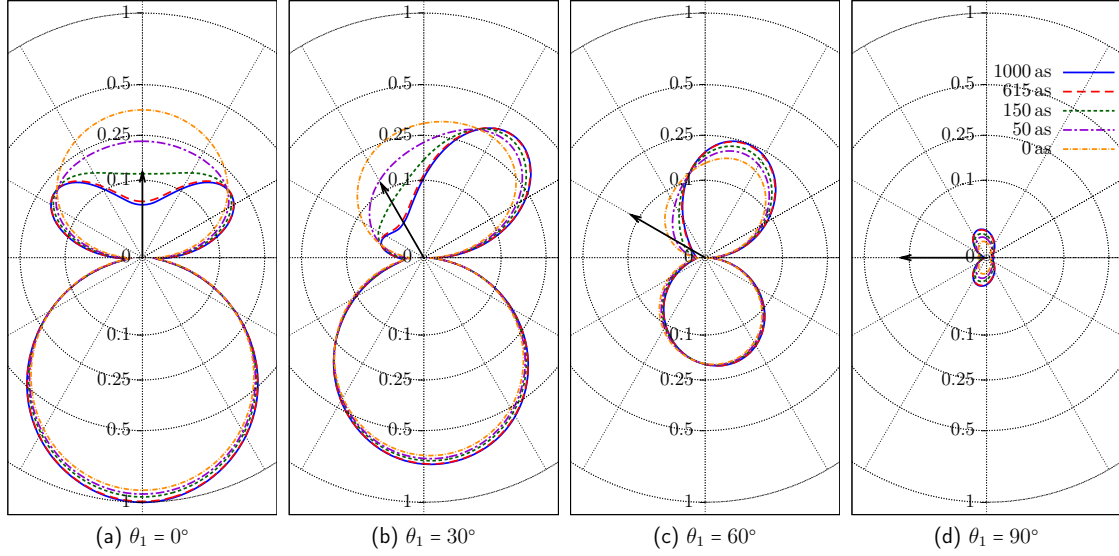


Figure 12.10: Joint angular distribution $P^{DI}(\theta_1, \theta_2)$ for different waiting times τ after the end of the pulse, for TPD from a 70 eV 150 as pulse. The projection on products of Coulomb waves is performed directly after the end of the laser pulse ($\tau = 0$ as), and then at successive intervals up to $\tau = 1000$ as after the pulse. The distribution shows a redirection of the two electrons in the continuum, due to post-collision interaction. For each plot, θ_1 is fixed to a specific value (indicated by the black arrow), while θ_2 is scanned. Note that the scale is quadratic.

tions. Fig. 12.12 shows the energy-resolved mutual angular information $\mathcal{I}_{\Omega_1, \Omega_2}(\Delta E)$. For ultrashort pulses, the correlation in the angular distribution is quite independent of the energy – if the electrons are ejected within a very short time of each other, the interaction influences the angular distribution regardless of the relative energies of the electrons. For longer pulses, a stable picture emerges: At the main sequential peaks, the electrons are emitted in independent dipolar distributions, signified by vanishing mutual information. At energies away from the shake-up satellite peaks, the mutual information converges to stable non-zero values in long pulses. At the shake-up peaks, however, the interference between nonsequential and sequential contributions produces intricate patterns depending on the pulse duration. For the photon energy used here ($\hbar\omega = 70$ eV), the correlation peaks for pulses of a few femtoseconds duration, with the highest value reached at $T = 3$ fs out of the pulses considered here. As the duration is increased and the sequential shake-up channel begins to dominate, the correlation decreases again and is expected to converge to a stable value in the limit $T \rightarrow \infty$, for which the nonsequential contribution is negligible compared to the sequential channel.

The same trends can also be seen in the forward-backward asymmetry $\mathcal{A}(\Delta E)$ (cf. Fig. 12.13). This provides additional information on the relative ejection direction

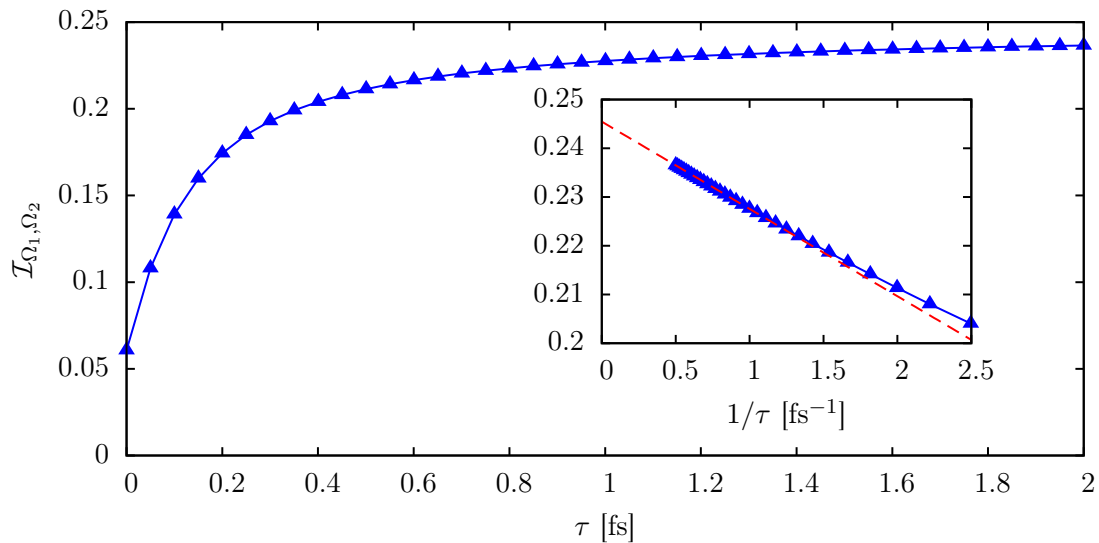


Figure 12.11: Mutual information $\mathcal{I}_{\Omega_1, \Omega_2}$ for different waiting times τ after the end of the pulse, for TPDI from a 70 eV 150 as pulse. The projection on products of Coulomb waves is performed at different times after the end of the laser pulse ($\tau = 0$ as). The inset shows the data vs. $1/\tau$. Extrapolation to $1/\tau \rightarrow 0$ using a linear fit shows a limiting value of 0.2455, only slightly larger than at $\tau = 2$ fs.

of the two electrons. For the shortest pulses, the electrons are dominantly ejected in opposite directions independent of energy, as observed previously. As the duration is increased, the asymmetry at the main sequential peaks vanishes as the electrons are essentially uncorrelated. For energies in between the two main peaks at $E_1 = \hbar\omega - I_1$ and $E_2 = \hbar\omega - I_2$, the electrons are emitted in opposite directions. This is precisely because these final state energies are reached only when the two electrons are ejected in such a configuration. This back-to-back Wannier-like emission near equal energy sharing remains pronounced even for long pulses.

For energies outside the energy interval delimited by the sequential peaks, the asymmetry is equally strong, but now positive, pointing to the same emission direction for both electrons. When the second electron is emitted in the same direction as the first one, the post-collision interaction [176–179] tends to increase the asymmetric sharing of the available energy [42]. The dividing line between the two different regimes of ejection (in opposite or in the same direction) is quite sharp and lies directly at the position of the sequential peaks. The width of the switchover between the two regimes seems to be given by the spectral width of the pulse, and not by an intrinsic property of the process. Thus, the pulses here are not yet long enough to determine whether there is a step-like behavior with vanishing width in the limit $T \rightarrow \infty$, or whether there is some intrinsic width in the switch of the angular distribution from back-to-back emission to emission in equal directions.

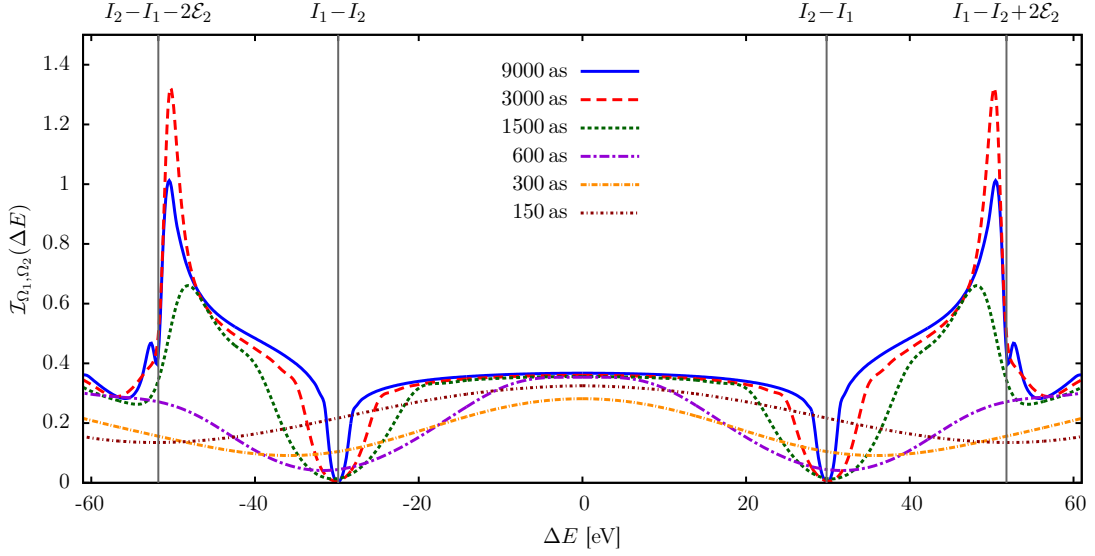


Figure 12.12: Energy-resolved mutual information $\mathcal{I}_{\Omega_1, \Omega_2}(\Delta E)$ for TPDI at $\hbar\omega = 70$ eV for different pulse durations. The vertical lines show the expected positions of the peaks for the sequential process (with and without shake-up).

A more complete representation of the two-electron energy and angular correlations is presented in Fig. 12.14 for a pulse duration of $T = 900$ as. While the height gives the joint probability $P^{DI}(E_1, E_2)$, the color represents the asymmetry distribution $\mathcal{A}(E_1, E_2)$. The borderline between positive and negative \mathcal{A} (i.e. $\mathcal{A} = 0$, white) is at the peaks associated with the sequential process. In the central region in between the main sequential peaks the emission is preferentially on opposite sides while emission into the same hemisphere prevails outside the main peaks.

Additional insights can be gained from a projection of the two-electron momentum onto the energy-angle plane,

$$P^{DI}(E_1, \theta_1, \theta_2) = \int dE_2 P^{DI}(E_1, E_2, \Omega_1, \Omega_2), \quad (12.4)$$

where we again choose coplanar geometry. This distribution is shown for various pulse durations and fixed values of θ_1 in Fig. 12.15. In order to allow comparison of the distributions, we rescale the probability distributions by T^{-3} . In the sequential regime, the total double ionization probability scales with T^2 , while the width of the main peaks in energy scales with T^{-1} . The height of the peaks therefore scales roughly with T^3 , at least as long as there are still two well-separated peaks.

While for long pulses the energy of the emitted electrons is independent of the relative emission angle, strong energy-angle correlations appear for short ($T \leq 900$ as) pulses. If the electrons are emitted in the *same* direction ($\theta_1 = \theta_2$), the slower electron is slowed down while the other one is accelerated relative to the energies

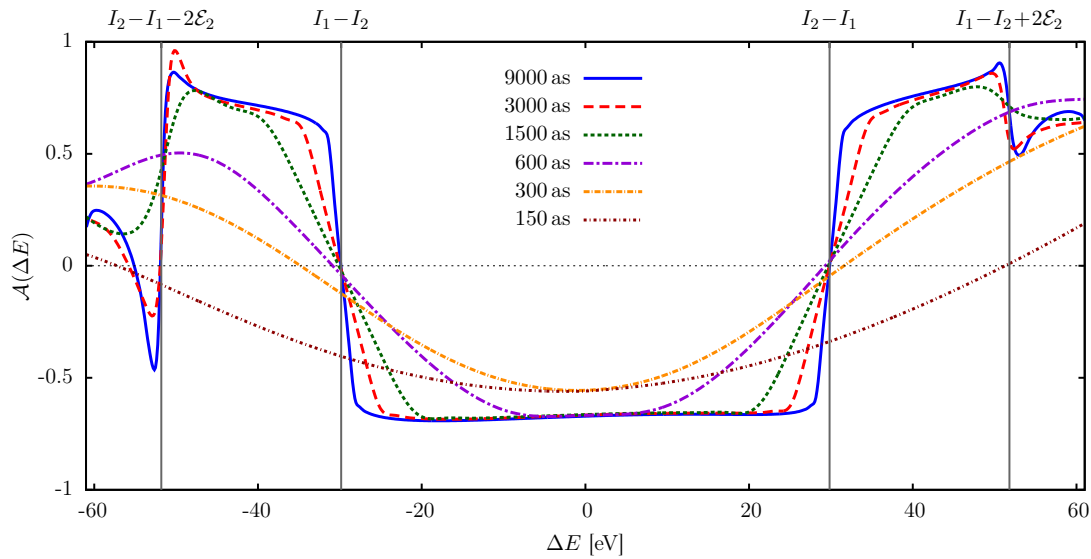


Figure 12.13: Forward-backward asymmetry $\mathcal{A}(E_1)$ for TPDI by an XUV pulse at $\hbar\omega = 70$ eV, for different pulse durations T . The gray lines show the expected positions of the peaks for the sequential process (with and without shake-up).

reached for $T \rightarrow \infty$. Hence, the slow electron “pushes” the fast electron from behind, transferring part of the energy absorbed from the photon field to the faster electron. This is the *post-collision interaction* [177–179] first observed by Barker and Berry in the decay of autoionizing states excited through ion impact [176]. Conversely, if the electrons are emitted in opposite directions ($\theta_1 = \theta_2 + 180^\circ$), their energies tend towards equal energy sharing, i.e. the slower electron is accelerated, while the faster one is slowed down. For emission in a back-to-back configuration within a short time interval, the screening of the core is reduced for the first, faster electron compared to the long-time limit, where the nucleus is perfectly screened by the remaining electron. Equivalently, the second, slower electron still feels the repulsion of the first electron and therefore gains more energy in comparison to the long-time limit, where it only feels the Coulomb attraction of the nucleus.

For ultrashort pulses ($T \leq 300$ as), the dominant channel is then back-to-back emission at equal energy sharing ($E_1 \approx 30$ eV at $\hbar\omega = 70$ eV). This can now be seen to occur due to the combination of two effects – the angular correlation only allows emission in a back-to-back configuration, which in turn shifts the energy distribution towards equal energy sharing. As noted before, the resulting configuration corresponds precisely to the Wannier ridge riding mode [181]

Another interesting feature in the angle-energy distribution occurs for $\theta_1 = 90^\circ$ for the longest pulse ($T = 9000$ as, cf. Fig. 12.15j). Here, the “main” sequential peak is strongly suppressed due to the dipolar emission pattern of the electrons, which has a node at 90° . However, this node is not present for shake-up ionization if the

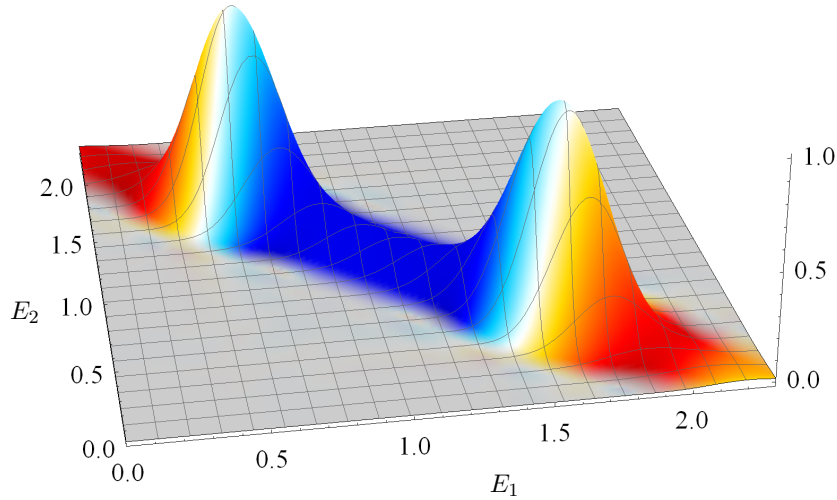


Figure 12.14: Combined double ionization probability $P^{DI}(E_1, E_2)$ and forward-backward asymmetry $\mathcal{A}(E_1, E_2)$ for TPDI by an XUV pulse at $\hbar\omega = 70$ eV with a duration of 900 as. The z -axis gives $P^{DI}(E_1, E_2)$ (in arbitrary units), while the color encodes the asymmetry, with blue signifying the largest negative values (ejection in opposite directions) and red signifying the largest positive values (ejection in the same direction). Vanishing \mathcal{A} corresponds to white. For energies where $P^{DI}(E_1, E_2)$ is negligible ($\leq 10^{-3}$ on the scale used here), the color is set to gray.

intermediate state of the He^+ ion does not have s ($l = 0$) symmetry. In that case, the free electron does not necessarily have to be in a p state. For example, for shake-up ionization via $|2p\rangle$, the free electron is in a superposition of s and d waves, which do not show the node at $\theta = 90^\circ$. Therefore, for long pulses, the dominant emission at $\theta_1 = 90^\circ$ occurs via the shake-up pathway, and the peaks at $\hbar\omega - I_1 - \mathcal{E}_2$ and $\hbar\omega - I_2 + \mathcal{E}_2$ are dominant. In addition, it can be observed that it is more likely for the slower electron to be emitted at 90° . In the shake-up channel, the slower electron is the one that is first emitted, as $\hbar\omega - I_1 - \mathcal{E}_2 < \hbar\omega - I_2 + \mathcal{E}_2$.

12.4 Nuclear recoil

We now turn to the *recoil ion momentum* probability distributions $P^{DI}(Q_x, Q_z)$ (cf. [section 6.3](#)), which can be experimentally obtained using COLTRIMS. We fix the photon energy at $\hbar\omega = 70$ eV and scan the pulse duration ([Fig. 12.16](#)). As before ([section 11.2](#)), we compare the actual distributions with distributions obtained by assuming a product of $\cos^2\theta$ angular distributions for the electrons in order to clearly see the effects of angular correlation. As the photon energy is in the sequential regime, two distinct rings can be observed in the longer pulses

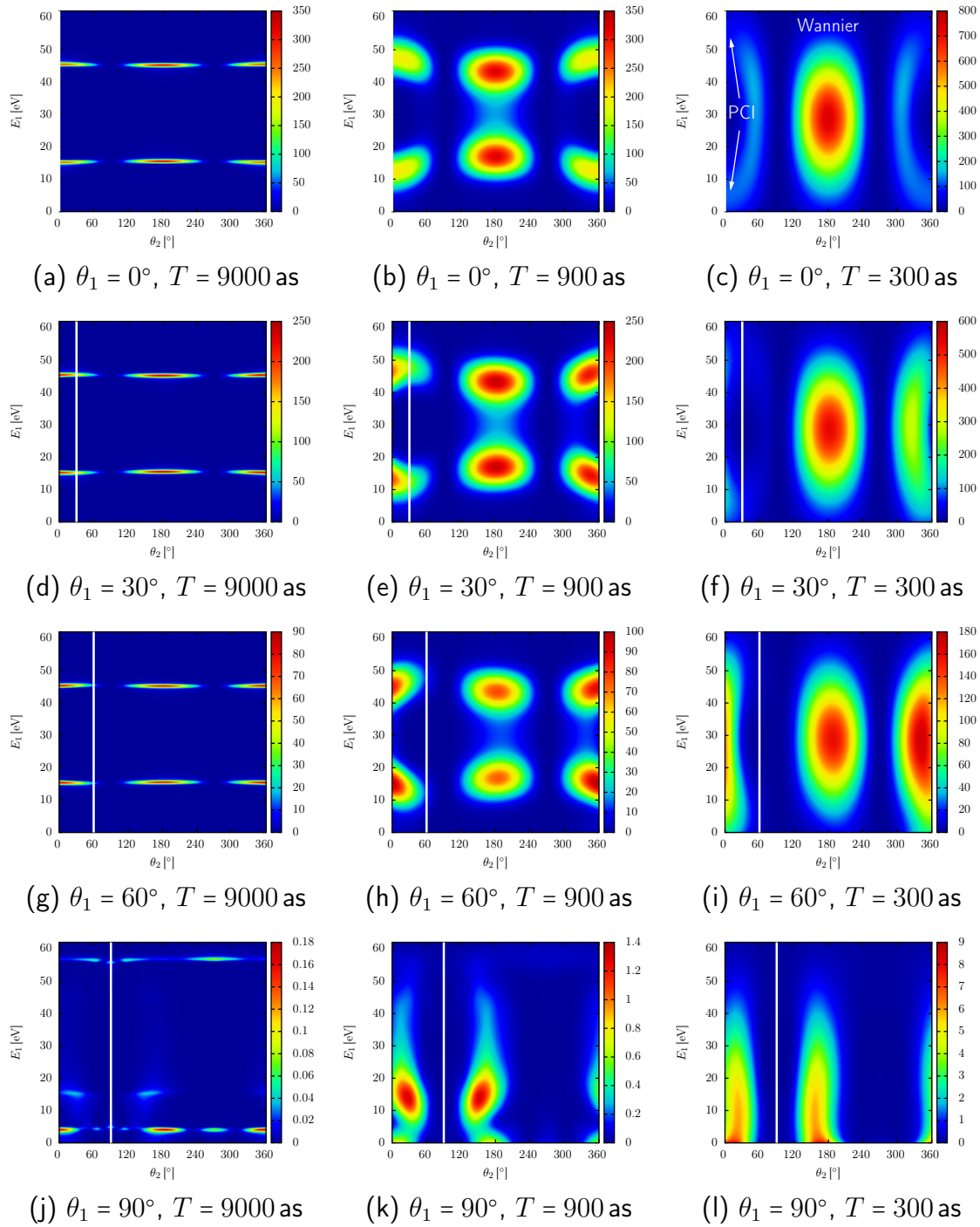


Figure 12.15: Angle-energy distributions $P(E_1, \theta_1, \theta_2)$ in coplanar geometry at 70 eV photon energy for different pulse durations ($T = 300$ as, $T = 900$ as, and $T = 9000$ as). The scale is arbitrary but identical for all distributions, with a scaling factor of $1/T^3$. The white lines indicate the emission angle θ_1 of the first electron.

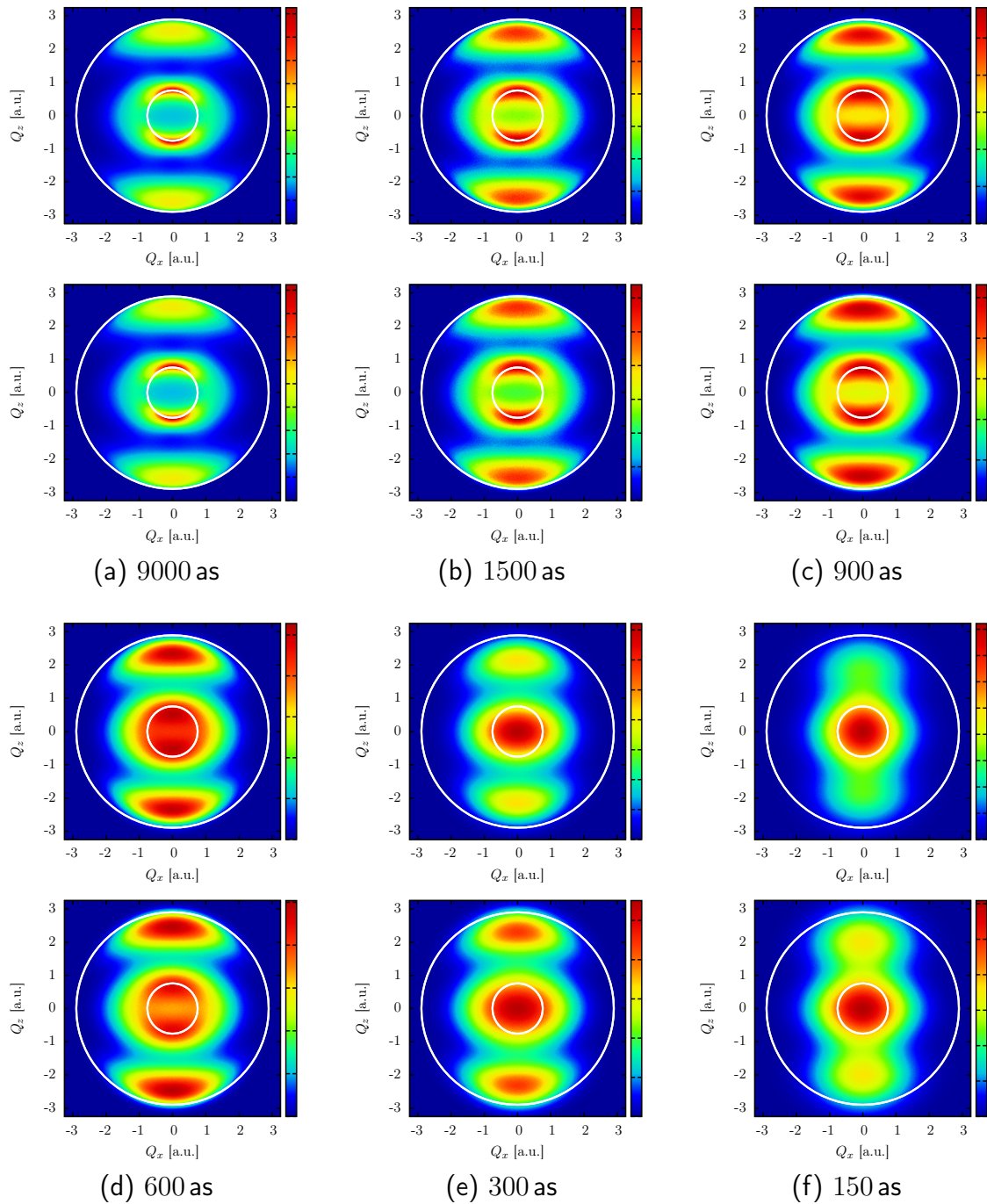


Figure 12.16: Recoil ion momentum distribution for TPDI at $\hbar\omega = 70$ eV from \sin^2 pulses of different durations. For each duration, the upper plot shows the actual distribution, while the lower plot shows the distribution obtained with a product of dipoles as the angular distribution.

($T \geq 900$ as). These stem from the fact that the electrons are either emitted with momentum $k_1 = \sqrt{2(\hbar\omega - I_1)}$ or $k_2 = \sqrt{2(\hbar\omega - I_2)}$. The angular emission pattern in the long-pulse limit is a Hertz dipole for both electrons, such that emission on the laser polarization axis is strongly favored. Consequently, the ion momentum shows peaks close to $Q = \pm(k_1 \pm k_2)$. These positions are marked by the white circles in Fig. 12.16.

For the “long” pulses, the actual distributions look very similar to the distributions obtained using the $\cos^2 \theta_1 \cos^2 \theta_2$ angular distribution, pointing towards little angular correlation. As the pulse duration is decreased, two factors influence the recoil ion momentum distribution. For one, the momentum distribution of the electrons is broadened, with the two distinct peaks merging to a single one at equal energy sharing for ultrashort pulses (cf. Fig. 12.1). This leads to the disappearance of the clear two-peak structure and the development of a single peak around zero recoil ion momentum. Secondly, the angular distributions transform from a uncorrelated product of $\cos^2 \theta$ distributions to a strongly correlated distribution favoring back-to-back emission. This leads to a suppression of the distribution for large ion momenta.

The distributions obtained with purely dipolar emission of the electrons reveal that a large part of the change in the recoil ion momentum distribution as the pulse duration is varied is due to the change of the energy distribution. As we have noted before, the energy distribution does not carry a lot of information about the dynamics of the process. The only information entering into the simple model (11.1), which reproduces the observed energy distributions very well, is the difference of the two ionization potentials I_2 and I_1 . The angular correlations, which reveal the more detailed dynamics of the two-photon double ionization process, exert some influence on the recoil ion momentum distribution, but are only important for the very shortest pulses ($T \approx 150$ as).

13 Summary

In conclusion, we have presented a detailed study of the dynamics of the two-photon double ionization process in helium, for photon energies both in the so-called “non-sequential” and “sequential” regime, and for a wide range of ultrashort pulse durations (150 as to 9 fs). We have shown how electron-electron interaction, and thereby correlation, influences the observed energy spectra and angular distributions.

In particular, we have determined well-converged results for the total and triply differential (generalized) cross sections for nonsequential TPDI. The total cross sections agree reasonably well with a number of recently published papers [55, 58, 70, 75, 80, 82, 88], but disagree with others [50, 68]. While the uncorrelated results of [62] fit well with our data, the J -matrix results that account for correlation, also presented in [62], are larger by almost an order of magnitude. In our approach, the inclusion of correlation in the final double continuum states is bypassed by waiting long enough after the end of the pulse before performing the projection onto uncorrelated final states.

We have also investigated approximate methods to extract both the triply differential and total cross sections for nonsequential two-photon double ionization directly from the wave packet in coordinate space, thereby completely avoiding projection onto (uncorrelated) final states. The excellent agreement between these complementary methods provides a measure for the reliability and accuracy of the calculated cross sections.

Additionally, we have investigated the pulse duration dependence of the extracted cross sections. In most of the previous time-dependent approaches ten-cycle pulses were employed. The resulting broad spectral width then prevents the extraction of converged cross sections. This becomes evident from our calculations with considerably longer pulses, especially at photon energies above ~ 50 eV near the threshold for sequential ionization. As the photon energy approaches the sequential threshold, the intermediate state in the two-photon transition is almost on-shell, and the total two-photon double ionization cross section strongly increases. Above the threshold, the total cross section is undefined. Our own results for ten-cycle pulses, where the threshold behavior disappears completely, agree very well with the uncorrelated data from [62] and the results from [58] and [82].

Furthermore, we have shown that the energy distributions for TPDI can be explained completely by the shape factor of second-order time-dependent perturbation theory. As long as shake-up ionization is not allowed in the first step, the only system-specific quantity that is reflected in the angle-integrated distributions is the

energy difference between the first and second ionization potentials, or “correlation energy” $E_C = I_2 - I_1$. This implies that the shape of the energy distribution is almost independent of the photon energy, which only determines the accessible final states.

The one-electron ionization rate $P^{DI}(E)/T$ converges to a stable value with increasing pulse duration for energies away from the sequential peaks ($E = \hbar\omega - I_1$ and $E = \hbar\omega - I_2$), giving rise to a well-defined (direct) differential double ionization cross section. However, near the peaks where the sequential process is allowed, $P^{DI}(E)/T$ grows with T . We have thus observed a non-uniform scaling of the double ionization probability with pulse duration.

If the photon energy is large enough to allow for shake-up ionization, i.e. ionization of He and simultaneous excitation of the remaining He^+ ion, a new kind of interference effect can be observed. Even though in this spectral range the sequential process is allowed, both the direct and sequential processes co-exist, giving rise to interferences which are induced by the short time correlation between the two emission events. This interference occurs between the nonsequential contributions of the channel without shake-up and the sequential shake-up channel, where the intermediate state after one-photon absorption is an excited state of the He^+ ion. In attosecond pulses, the nonsequential channel dominates, while in long pulses (longer than the 9 fs used here), only the sequential shake-up channel is visible. For pulse durations of a few femtoseconds, as obtained in X-ray free-electron lasers, the two channels are similarly important, such that there is strong interference. These interferences may open up the possibility to measure the duration of ultrashort XUV pulses in the femtosecond regime.

More information about the dynamics of the system is encoded in the angular distributions of the electrons. We have found that the electrons at the primary sequential peaks are essentially uncorrelated, while strong correlation is present for all other final energies. For electron energies between the sequential peaks, i.e. close to equal energy sharing, the electrons are almost exclusively emitted in a back-to-back configuration. Outside the main peaks, the situation is reversed and the electrons are emitted preferentially in the same direction. For both of these cases, the two-lobed structure of a dipole transition from an s state is still visible, most clearly in the strong suppression of emission at an ejection angle of 90° to the laser polarization axis.

In order to quantify the amount of angular correlation of the two electrons, we have compared different measures, in particular the mutual information in the angular degrees of freedom, $\mathcal{I}_{\Omega_1, \Omega_2}$, and the von Neumann entropy of the one-particle angular density matrix, S_Ω . The mutual information is a purely classical quantity, measuring the amount of information gained about the emission direction of one electron by knowing the emission direction of the other one. S_Ω , on the other hand, measures the uncertainty (or entropy) in the quantum-mechanical angular state of one electron, an uncertainty that is created because of its correlation with the

other electron. Both of these measures show the same qualitative behavior, with minima at the positions of the primary sequential peaks, and pronounced maxima at the energies where the shake-up interference dominates. The exact mechanism which leads to the strong correlation at the position of the interference is still under investigation.

The correlation in the energy-integrated angular distribution, as measured by its mutual information content, is large for photon energies in the nonsequential regime. When the photon energy is increased to above the threshold for sequential ionization, the emission pattern of the electrons is dominated by the sequential process, where there is very little angular correlation. Thus, the mutual information drops steeply as the threshold is crossed. However, by using ultrashort pulses, it is possible to again induce interaction between the electrons. The mutual information shows a simple dependence on the pulse duration, $\mathcal{I}_{\Omega_1, \Omega_2} \propto T^{-1.4}$, leading to a marked increase for ultrashort pulses of a few hundred attoseconds duration.

We have thus shown that attosecond XUV pulses can be used to probe, induce, and control electron correlation in two-photon double ionization. In such pulses, the scenario for “sequential” two-photon double ionization breaks down. Due to the small time interval between the two photoabsorption processes dynamical electron-electron correlations can be tuned by the pulse duration T . The angular and angle-energy distributions reveal the signatures of electronic correlation induced by the Coulomb interaction in the intermediate bound-free complex and in the final state with both electrons in the continuum. In ultrashort pulses, where the distinction between sequential and nonsequential processes breaks down, two well-known scenarios, the Wannier ridge riding mode and the post-collision interaction process, are simultaneously present in the two-electron emission spectrum. The favored emission channel is the Wannier ridge riding mode of back-to-back emission at equal energies.

13.1 Outlook

There are still some open questions on the topic of two-photon double ionization. For one, the simple scaling of the angular mutual information with pulse duration for photon energies in the sequential regime remains unexplained. In addition, the (joint) angular distributions of the two electrons at the position of the shake-up interference effect have not been explained yet. In particular, the strong maxima in the energy-resolved angular mutual information indicate very strong correlation. The origin of this strong angular correlation is a topic for further investigation.

A promising extension of the current results is the use of *chirped* pulses, i.e. pulses with a time-dependent frequency. In a recent publication, Lee *et al.* [90] demonstrated that the two-electron momentum distributions for TPDI strongly depend on the chirp of attosecond pulses. Such pulses can therefore be used to pro-

vide an additional “control knob” to influence the electron dynamics on ultrashort time scales. The influence of the chirp on the interference effect between sequential shake-up ionization and nonsequential ionization is particularly important with regard to the possible application of this effect as a measure for the pulse duration of XUV pulses.

Apart from TPDI from a single pulse, many other processes can be (and have been) studied using our approach for solving the time-dependent Schrödinger equation, such as *pump-probe* setups using two different pulses. One of the long-standing goals of attosecond science is to perform pump-probe measurements using two XUV pulses [72]. We have previously investigated such a setup for studies on doubly excited states of helium [38]. However, XUV-XUV pump-probe measurements are experimentally very challenging because of the need to produce two synchronized attosecond pulses with large intensities, variable time delay, and different mean photon energies.

Experimentally, it is thus favorable to perform pump-probe measurements using an XUV attosecond pulse and a synchronized IR pulse⁹, and exploiting the subcycle dynamics of the electrons in the infrared field. In a pioneering experiment, Uiberacker *et al.* [188] created a Ne⁺ ion in a superposition of excited shake-up states by XUV-photoionization. The dynamics of this shake-up wave packet are then probed by tunnel ionization in the IR pulse. The overall stepwise structure of the resulting double ionization yield as a function of delay time can be explained by incoherent tunneling of the excited shake-up states. However, sub-structures, mainly in the form of small dips superimposed on the signal, point to additional coherent effects such as population transfer between the shake-up states or quantum beats in the corresponding wave packet. The presence of the IR field also significantly affects the shake-up process itself. In addition, electron-electron interactions could play an important role as well. These effects, which are also present in the helium atom, can be studied in detail using our code, without the need to resort to approximations.

Another important application of XUV-IR pump-probe setups is *attosecond streaking* [189, 190], where the IR pulse imparts a momentum shift on the photoelectrons created by the XUV pulse. The magnitude and sign of this shift are determined by the vector potential of the infrared field at the time of release of the electron. Recently, this technique has been used to measure an apparent time delay of ~ 100 as between conduction band electrons and core electrons ejected from a Tungsten surface [191]. A current topic of research is the application of this concept to shake-up ionization, in order to determine whether there is an apparent delay between ionization of helium with and without shake-up of the ion. A conceptually interesting question here is whether an observed delay in the streaking curves corresponds to a “real” time delay or is caused by the combined influence of the IR and XUV pulses.

By choosing the parameters of the XUV and IR field correctly, the photoelectron

⁹ typically the IR pulse that was used to generate the XUV pulse by high harmonic generation

created by the XUV pulse can be scattered back against its parent ion. This approach offers a possible route to extract information about the structure of the ion from a fully coherent scattering process. First investigations in this direction are described in [39].

Part III
Appendix

A Orthogonal polynomials and quadratures

In the following we will very briefly summarize the use of orthogonal polynomials for numerical integration (*quadrature*) which is exploited by DVR methods. For a detailed treatment of the subject and rigorous proofs of the following statements refer to [110, 116, 192, 193].

A.1 Orthogonal polynomials

Polynomials $p_n(x)$ of degree n which are defined over a range $[a, b]$ and obey the relation

$$\int_a^b w(x)p_m(x)p_n(x)dx = \delta_{mn}c_n, \quad (\text{A.1})$$

with a weighting function $w(x)$, are called orthogonal with respect to the inner product defined by the integral (A.1) and orthonormal if $c_n = 1$.¹⁰

The according orthogonal polynomials for any given weight function (and interval) can be obtained by Gram-Schmidt orthogonalization of the *monom basis*

$$m_i(x) = x^i. \quad (\text{A.2})$$

In doing so one can obtain a *three-term recurrence relation*

$$p_0(x) := 1 \quad (\text{A.3})$$

$$p_1(x) = x - \beta_0 \quad (\text{A.4})$$

$$p_{n+1}(x) = (x - \beta_n)p_n(x) - \gamma_n^2 p_{n-1}(x) \quad (\text{A.5})$$

which uniquely defines the orthogonal polynomials. The coefficients β_n and γ_n are given by

$$\beta_n = \frac{\int_a^b w(x)p_n(x)xp_n(x)dx}{\int_a^b w(x)p_n(x)p_n(x)dx} \quad (\text{A.6})$$

¹⁰ Thereby, we restrict ourselves to real polynomials and inner products.

and

$$\gamma_n = \sqrt{\frac{\int_a^b w(x)p_n(x)p_n(x)dx}{\int_a^b w(x)p_{n-1}(x)p_{n-1}(x)dx}}. \quad (\text{A.7})$$

Table A.1 shows the most important orthogonal polynomials and the corresponding intervals $[a, b]$, weights $w(x)$, and normalization constants c_n .

Polynomial	$[a, b]$	$w(x)$	c_n
Legendre	$[-1, 1]$	1	$\frac{2}{2n+1}$
Laguerre	$[0, \infty)$	e^{-x}	1
Generalized Laguerre	$[0, \infty)$	$x^k e^{-x}$	$\frac{(n+k)!}{n!}$
Hermite	$(-\infty, \infty)$	e^{-x^2}	$\sqrt{\pi} 2^n n!$
Gegenbauer	$[-1, 1]$	$(1-x^2)^{\alpha-1/2}$	$\begin{cases} \frac{2^{1-2\alpha} \pi \Gamma(n+2\alpha)}{n!(n+\alpha)\Gamma(\alpha)^2} & \alpha \neq 0 \\ \frac{2\pi}{n^2} & \alpha = 0 \end{cases}$
Chebyshev 1st kind	$[-1, 1]$	$(1-x^2)^{-1/2}$	$\begin{cases} \pi & n = 0 \\ \frac{\pi}{2} & \text{otherwise} \end{cases}$
Chebyshev 2nd kind	$[-1, 1]$	$\sqrt{(1-x^2)}$	$\frac{\pi}{2}$
Jacobi	$(-1, 1)$	$(1-x)^\alpha (1+x)^\beta$	$\frac{2^{\alpha+\beta+1}}{2n+\alpha+\beta+1} \frac{\Gamma(n+\alpha+1)\Gamma(n+\beta+1)}{n!\Gamma(n+\alpha+\beta+1)}$

Table A.1: Classical orthogonal polynomials and their according intervals $[a, b]$, weight functions $w(x)$, and normalization constants c_n . [192]

A.2 Gauss quadratures

A very attractive feature of orthogonal polynomials is that for all of them there exists a quadrature formula, i.e. a discrete approximation of an integral, in the form

$$\int_a^b w(x)f(x)dx = \sum_{k=1}^n w_k f(x_k) + E_n^{(2n)} \simeq \sum_{k=1}^n w_k f(x_k) \quad (\text{A.8})$$

which is *exact* for polynomial functions $f(x)$ up to a maximal degree of $(2n-1)$.¹¹ This can be seen from the error term

$$E_n^{(2n)} \propto \frac{f^{(2n)}(\xi)}{(2n)!}, \quad (\text{A.9})$$

¹¹ Consequently, integrals of arbitrary functions are approximated with high accuracy when they are well represented by a polynomial of degree $(2n-1)$.

where $f^{(2n)}(\xi)$ denotes the $2n$ -th derivative of f at an interim value $\xi \in [a, b]$. Consequently $E_n^{(2n)}$ is zero for polynomials of maximal degree $(2n - 1)$.¹²

The definite integral of a function $f(x)$ is thus approximated by a weighted sum of n function values $f(x_k)$. The *nodes* x_k are given by the zeros of the n -th polynomial $p_n(x)$ and are

- real,
- (pairwise) distinct,
- interlacing (i.e. the roots of each polynomial lie between the roots of the next higher one)
- and lie *within* the interval (a, b) .

The (positive) *quadrature weights* w_k are related to the Lagrange interpolation polynomials by

$$w_k = \int_a^b L_k(x)w(x)dx = \int_a^b L_k^2(x)w(x)dx \tag{A.10}$$

with

$$L_i(x) = \prod_{j \neq i} \frac{x - x_j}{x_i - x_j}, \quad L_i(x_j) = \delta_{ij}. \tag{A.11}$$

For practical purposes it is often necessary to transform the intervals $[a, b]$ which are related to classical orthogonal polynomials to custom intervals $[a', b']$. This can be easily done by introducing a coordinate transformation¹³ in the integral (A.8) with the restriction that the transformation has to be *affine* if the accuracy of the quadrature is to be preserved.¹⁴ [194]

A.3 Gauss-Legendre quadrature

A Gauss quadrature over the interval $[-1, 1]$ with a weight function $w(x) = 1$ is called Gauss-Legendre quadrature and the corresponding orthogonal polynomials are the Legendre polynomials.

The quadrature weights are given by

$$w_i = \frac{2}{(1 - x_i^2) \left[\frac{\partial P_n}{\partial x}(x_i) \right]^2} = \frac{2(1 - x_i^2)}{(n + 1)^2 [P_{n+1}(x_i)]^2} \tag{A.12}$$

¹² Note that for *arbitrary* nodes only polynomials of degree $(n - 1)$ can be integrated exactly by interpolating quadrature.

¹³ sometimes called “mapping function”

¹⁴ Affine transformations map general polynomials on polynomials of the same degree.

and the integration error reads

$$E_n^{(2n)} = \frac{2^{2n+1}(n!)^4}{(2n+1)[(2n)!]^3} f^{(2n)}(\xi), \quad \xi \in [a, b]. \quad (\text{A.13})$$

A.4 Gauss-Lobatto quadrature

General Gaussian quadratures do not allow to specify the endpoint of the integration interval since the roots of the corresponding orthogonal polynomials strictly lie within the interval. However, by giving up some accuracy the formula can be modified to include the endpoints of the interval. This is particularly important for physical applications where it is often necessary to impose certain boundary conditions (and/or continuity conditions as in the case of FEDVR).

A Gauss-Legendre quadrature which also includes the endpoints -1 and 1 is called Gauss-Lobatto quadrature.¹⁵

The quadrature formula then reads

$$\begin{aligned} \int_{-1}^1 w(x)f(x)dx &= w_1f(-1) + w_n f(1) + \sum_{k=2}^{n-1} w_k f(x_k) + E_n^{(2n-2)} \\ &\simeq w_1f(-1) + w_n f(1) + \sum_{k=2}^{n-1} w_k f(x_k) \end{aligned} \quad (\text{A.14})$$

with $(n-2)$ free abscissa x_k which are now given by the roots of the polynomial $\frac{\partial P_{n-1}}{\partial x}$. In contrast to the Gauss-Legendre quadrature the Gauss-Lobatto is only *exact* for polynomials of degree $2n-3$ which can be seen from the error term

$$E_n^{(2n-2)} = -\frac{n(n-1)^3 2^{2n+1} [(n-2)!]^4}{(2n-1)[(2n-2)!]^3} f^{(2n-2)}(\xi), \quad \xi \in [a, b]. \quad (\text{A.15})$$

The corresponding quadrature weights for the inner points read

$$w_i = -\frac{2n}{(1-x_i^2) \frac{\partial^2 P_{n-1}}{\partial x^2}(x_i) \frac{\partial P_n}{\partial x}(x_i)} = \frac{2}{n(n-1) [P_{n-1}(x_i)]^2} \quad (\text{A.16})$$

and for the endpoints

$$w_{1,n} = \frac{2}{n(n-1)}. \quad (\text{A.17})$$

¹⁵ In a similar way the so called *Gauss-Radau* quadratures specify only one endpoint of the integration interval [192].

B Angular momentum algebra

For two angular momentum operators $\hat{\mathbf{L}}_1, \hat{\mathbf{L}}_2$ one can form two sets of mutually commuting operators, the *uncoupled representation*

$$\hat{\mathbf{L}}_1^2, \hat{\mathbf{L}}_2^2, L_{1,z}, L_{2,z} \quad (\text{B.1})$$

and the *coupled representation*

$$\hat{\mathbf{L}}_1^2, \hat{\mathbf{L}}_2^2, \hat{\mathbf{L}}^2, L_z, \quad (\text{B.2})$$

where

$$\hat{\mathbf{L}} = \hat{\mathbf{L}}_1 + \hat{\mathbf{L}}_2, L_z = L_{1,z} + L_{2,z}. \quad (\text{B.3})$$

The according eigenfunctions $|l_1 l_2 m_1 m_2\rangle$ and $|l_1 l_2 LM\rangle$ are connected by the unitary transformations

$$|l_1 l_2 LM\rangle = \sum_{\substack{m_1, \\ m_2}} \langle l_1 l_2 m_1 m_2 | l_1 l_2 LM \rangle |l_1 l_2 m_1 m_2\rangle \quad (\text{B.4})$$

and

$$|l_1 l_2 m_1 m_2\rangle = \sum_{L, M} \langle l_1 l_2 LM | l_1 l_2 m_1 m_2 \rangle |l_1 l_2 LM\rangle. \quad (\text{B.5})$$

B.1 Clebsch-Gordan coefficients

The expansion coefficients in (B.4) and (B.5) are called *Clebsch-Gordan (CG) coefficients* and the standard phase convention is to make them real,

$$\langle l_1 l_2 m_1 m_2 | l_1 l_2 LM \rangle = \langle l_1 l_2 LM | l_1 l_2 m_1 m_2 \rangle =: \begin{bmatrix} l_1 & l_2 & L \\ m_1 & m_2 & M \end{bmatrix}. \quad (\text{B.6})$$

The CG coefficients vanish if the conditions (selection rules)

$$\Delta(l_1 l_2 L) : |l_1 - l_2| \leq L \leq |l_1 + l_2| \quad (\text{B.7})$$

$$-L \leq M \leq L, -l_1 \leq m_1 \leq l_1, -l_2 \leq m_2 \leq l_2 \quad (\text{B.8})$$

$$m_1 + m_2 = M \quad (\text{B.9})$$

$$l_1 + l_2 + L \in \mathbb{N} \quad (\text{B.10})$$

are not fulfilled. Note that because of (B.9) the sum over m_2 (or m_1) in (B.4) is redundant since it can always be expressed by $m_2 = M - m_1$ (or vice versa).

The orthonormality relations of the CG coefficients are given by

$$\sum_{m_1, m_2} \begin{bmatrix} l_1 & l_2 & L \\ m_1 & m_2 & M \end{bmatrix} \begin{bmatrix} l_1 & l_2 & L' \\ m_1 & m_2 & M' \end{bmatrix} = \delta_{LL'} \delta_{MM'} \quad (\text{B.11})$$

and

$$\sum_{L, M} \begin{bmatrix} l_1 & l_2 & L \\ m_1 & m_2 & M \end{bmatrix} \begin{bmatrix} l_1 & l_2 & L \\ m'_1 & m'_2 & M \end{bmatrix} = \delta_{m_1 m'_1} \delta_{m_2 m'_2}. \quad (\text{B.12})$$

Some important symmetry relations under the permutation of any two columns or the sign reversal of the projection quantum numbers are

$$\begin{bmatrix} l_1 & l_2 & L \\ m_1 & m_2 & M \end{bmatrix} = (-1)^{l_1+l_2-L} \begin{bmatrix} l_1 & l_2 & L \\ -m_1 & -m_2 & -M \end{bmatrix} \quad (\text{B.13})$$

$$= (-1)^{l_1+l_2-L} \begin{bmatrix} l_2 & l_1 & L \\ m_2 & m_1 & M \end{bmatrix} \quad (\text{B.14})$$

$$= (-1)^{l_2+m_2} \frac{\sqrt{2L+1}}{\sqrt{2l_2+1}} \begin{bmatrix} l_1 & L & l_2 \\ m_1 & -M & -m_2 \end{bmatrix} \quad (\text{B.15})$$

$$= (-1)^{l_2+m_2} \frac{\sqrt{2L+1}}{\sqrt{2l_1+1}} \begin{bmatrix} L & l_2 & l_1 \\ -M & m_2 & -m_1 \end{bmatrix}. \quad (\text{B.16})$$

A special case of (B.13) for integer l_1, l_2, L is

$$\begin{bmatrix} l_1 & l_2 & L \\ 0 & 0 & 0 \end{bmatrix} = (-1)^{l_1+l_2-L} \begin{bmatrix} l_1 & l_2 & L \\ 0 & 0 & 0 \end{bmatrix} \quad (\text{B.17})$$

and as a consequence the so called *parity CG coefficient* vanishes

$$\begin{bmatrix} l_1 & l_2 & L \\ 0 & 0 & 0 \end{bmatrix} = 0 \quad (\text{B.18})$$

for odd $l_1 + l_2 - L$ (and if the triangle relation $\Delta(l_1 l_2 L)$ is not fulfilled).

B.2 The Wigner 3j-symbol

The Wigner 3j-symbols are closely related to the CG coefficients,

$$\begin{pmatrix} l_1 & l_2 & L \\ m_1 & m_2 & M \end{pmatrix} := \frac{(-1)^{l_1-l_2-M}}{\sqrt{2L+1}} \begin{bmatrix} l_1 & l_2 & L \\ m_1 & m_2 & -M \end{bmatrix}, \quad (\text{B.19})$$

but have higher symmetry because they remain unchanged under an even permutation of the columns,

$$\begin{pmatrix} l_1 & l_2 & L \\ m_1 & m_2 & M \end{pmatrix} = \begin{pmatrix} l_2 & L & l_1 \\ m_2 & M & m_1 \end{pmatrix} \quad (\text{B.20})$$

$$= \begin{pmatrix} L & l_1 & l_2 \\ M & m_1 & m_2 \end{pmatrix}. \quad (\text{B.21})$$

An odd permutation brings in the phase factor $(-1)^{l_1+l_2+L}$,

$$\begin{pmatrix} l_1 & l_2 & L \\ m_1 & m_2 & M \end{pmatrix} = (-1)^{l_1+l_2+L} \begin{pmatrix} l_2 & l_1 & L \\ m_2 & m_1 & M \end{pmatrix} \quad (\text{B.22})$$

$$= (-1)^{l_1+l_2+L} \begin{pmatrix} l_1 & L & l_2 \\ m_1 & M & m_2 \end{pmatrix} \quad (\text{B.23})$$

$$= (-1)^{l_1+l_2+L} \begin{pmatrix} L & l_2 & l_1 \\ M & m_2 & m_1 \end{pmatrix}, \quad (\text{B.24})$$

and reversing the sign of the projection quantum numbers gives

$$\begin{pmatrix} l_1 & l_2 & L \\ m_1 & m_2 & M \end{pmatrix} = (-1)^{l_1+l_2+L} \begin{pmatrix} l_1 & l_2 & L \\ -m_1 & -m_2 & -M \end{pmatrix}. \quad (\text{B.25})$$

Clearly, the 3j-symbols fulfill the same selection rules (B.7)-(B.10) as the CG coefficients since they differ only by a phase. In analogy to (B.11) and (B.12) the orthonormality relations of the Wigner 3j-symbols are

$$\sum_{\substack{m_1, \\ m_2}} (2L+1) \begin{pmatrix} l_1 & l_2 & L \\ m_1 & m_2 & M \end{pmatrix} \begin{pmatrix} l_1 & l_2 & L' \\ m_1 & m_2 & M' \end{pmatrix} = \delta_{LL'} \delta_{MM'} \quad (\text{B.26})$$

and

$$\sum_{L,M} (2L+1) \begin{pmatrix} l_1 & l_2 & L \\ m_1 & m_2 & M \end{pmatrix} \begin{pmatrix} l_1 & l_2 & L \\ m'_1 & m'_2 & M \end{pmatrix} = \delta_{m_1 m'_1} \delta_{m_2 m'_2}. \quad (\text{B.27})$$

B.3 The Wigner 6j-symbol

The Wigner 6j-symbols are a generalization of 3j-symbols (or CG coefficients respectively) and arise in the coupling of three angular momenta or in the evaluation of matrix elements of scalar products of tensor operators in the coupled basis of two angular momenta,

$$\begin{aligned} \langle l'_1 l'_2 L' M' | T^{(k)}(1) \cdot W^{(k)}(2) | l_1 l_2 L M \rangle &= \langle l'_1 l'_2 L' M' | \sum_{q=-k}^k (-1)^q T_{-q}^{(k)}(1) W_q^{(k)}(2) | l_1 l_2 L M \rangle = \\ &= (-1)^{L+l_1+l'_2} \langle l'_1 || T^{(k)}(1) || l_1 \rangle \langle l'_2 || W^{(k)}(2) || l_2 \rangle \left\{ \begin{matrix} L & l'_2 & l'_1 \\ k & l_1 & l_2 \end{matrix} \right\} \delta_{LL'} \delta_{MM'}. \quad (\text{B.28}) \end{aligned}$$

They are related to the Wigner 3j-symbols by

$$\begin{aligned} \left\{ \begin{matrix} j_1 & j_2 & j_3 \\ l_1 & l_2 & l_3 \end{matrix} \right\} &= (2j_3 + 1) \sum_{\substack{m_1, m_2, \\ n_1, n_2, n_3}} (-1)^{l_1 + l_2 + l_3 + n_1 + n_2 + n_3} \\ &\times \begin{pmatrix} j_1 & j_2 & j_3 \\ m_1 & m_2 & m_3 \end{pmatrix} \begin{pmatrix} j_1 & l_2 & l_3 \\ m_1 & n_2 & -n_3 \end{pmatrix} \begin{pmatrix} l_1 & j_2 & l_3 \\ -n_1 & m_2 & n_3 \end{pmatrix} \begin{pmatrix} l_1 & l_2 & j_3 \\ n_1 & -n_2 & m_3 \end{pmatrix} \end{aligned} \quad (\text{B.29})$$

and vanish if the triangle relations

$$\Delta(j_1 j_2 j_3), \Delta(j_1 l_2 l_3), \Delta(l_1 j_2 l_3), \Delta(l_1 l_2 j_3) \quad (\text{B.30})$$

are not fulfilled, or if the sums

$$(j_1 + j_2 + j_3), (j_1 + l_2 + l_3), (l_1 + j_2 + l_3), (l_1 + l_2 + j_3) \quad (\text{B.31})$$

are not integer.

The 6j symbols are invariant under permutation of their columns, e.g.

$$\left\{ \begin{matrix} j_1 & j_2 & j_3 \\ l_1 & l_2 & l_3 \end{matrix} \right\} = \left\{ \begin{matrix} j_2 & j_1 & j_3 \\ l_2 & l_1 & l_3 \end{matrix} \right\} = \left\{ \begin{matrix} j_3 & j_2 & j_1 \\ l_3 & l_2 & l_1 \end{matrix} \right\} = \dots \quad (\text{B.32})$$

and under exchange of *two pairs* of corresponding elements between their rows, e.g.

$$\left\{ \begin{matrix} j_1 & j_2 & j_3 \\ l_1 & l_2 & l_3 \end{matrix} \right\} = \left\{ \begin{matrix} l_1 & j_2 & l_3 \\ j_1 & l_2 & j_3 \end{matrix} \right\} = \left\{ \begin{matrix} l_1 & l_2 & j_3 \\ j_1 & j_2 & l_3 \end{matrix} \right\} = \dots \quad (\text{B.33})$$

A more complete list of symmetry properties and orthogonality relations can be found in [99, 195, 196].

Another important identity for calculating matrix elements of tensor operators in the coupled representation is [196]

$$\begin{aligned} \sum_{l_2} \begin{bmatrix} j_1 & j_2 & j_{12} \\ l_1 & l_2 & l_{12} \end{bmatrix} \begin{bmatrix} j_{12} & j_3 & j \\ l_{12} & l_3 & m \end{bmatrix} \begin{bmatrix} j_2 & j_3 & j_{23} \\ l_2 & l_3 & l_{23} \end{bmatrix} = \\ (-1)^{j_1 + j_2 + j_3 + j} \sqrt{(2j_{12} + 1)(2j_{23} + 1)} \left\{ \begin{matrix} j_1 & j_2 & j_{12} \\ j_3 & j & j_{23} \end{matrix} \right\} \begin{bmatrix} j_1 & j_{23} & j \\ l_1 & l_{23} & m \end{bmatrix}. \end{aligned} \quad (\text{B.34})$$

The Wigner 6j-symbol is related to the commonly used U coefficients and Racah W coefficients as

$$\left\{ \begin{matrix} j_1 & j_2 & j_3 \\ l_1 & l_2 & l_3 \end{matrix} \right\} = (-1)^{j_1 + j_2 + l_2 + l_1} W(j_1 j_2 l_2 l_1; j_3 l_3) \quad (\text{B.35})$$

$$= \frac{(-1)^{j_1 + j_2 + l_2 + l_1}}{\sqrt{(2j_3 + 1)(2l_3 + 1)}} U(j_1 j_2 l_2 l_1; j_3 l_3). \quad (\text{B.36})$$

B.4 The Wigner-Eckart theorem

The Wigner-Eckart Theorem states that in a space that is spanned by a set of angular momentum basis functions $|lm\rangle$ the matrix element of an irreducible tensor operator $T_q^{(k)}$ can be written as¹⁶

$$\langle lm|T_q^{(k)}|l'm'\rangle = \begin{bmatrix} l' & k & l \\ m' & q & m \end{bmatrix} \frac{\langle l||T^{(k)}||l'\rangle}{\sqrt{2l+1}} \quad (\text{B.37})$$

$$= (-1)^{l'-k-m} \begin{pmatrix} l' & k & l \\ m' & q & -m \end{pmatrix} \langle l||T^{(k)}||l'\rangle, \quad (\text{B.38})$$

thus factoring out the dependence on the magnetic quantum numbers as a CG coefficient (or 3j-symbol respectively). The physical nature of the operator $T_q^{(k)}$ is then contained entirely in the *reduced matrix element* $\langle l||T^{(k)}||l'\rangle$ whereas the CG coefficient includes its geometry and symmetry properties.

An important example is the reduced matrix element for the *renormalized spherical harmonics (Racah tensors)*

$$C_q^{(k)}(\theta, \varphi) = \sqrt{\frac{4\pi}{2k+1}} Y_q^k(\theta, \varphi) \quad (\text{B.39})$$

which is given by

$$\langle l||C^{(k)}||l'\rangle = (-1)^l \sqrt{(2l+1)(2l'+1)} \begin{pmatrix} l & k & l' \\ 0 & 0 & 0 \end{pmatrix} \quad (\text{B.40})$$

$$= (-1)^k \sqrt{2l+1} \begin{bmatrix} l & k & l' \\ 0 & 0 & 0 \end{bmatrix} \quad (\text{B.41})$$

and contains the parity CG coefficient.

¹⁶ Note that we use the phase and normalization convention introduced by Racah. [99, 197]

C Derivation of angular asymmetry parameters

In the following we give a detailed derivation of the angular asymmetry parameters (section 6.2.3). We obtain the angular asymmetry parameters from the angular probability distribution with respect to the laser polarization axis z ,

$$P^{DI}(E_1, E_2, \theta_1) = 2 \int_{\Omega_2} \int_0^{2\pi} |\psi_{DI}(E_1, E_2, \Omega_1, \Omega_2)|^2 d\Omega_2 d\varphi_1. \quad (\text{C.1})$$

The doubly ionized wave function $\Psi_{DI}(E_1, E_2, \Omega_1, \Omega_2)$ (6.34) reads

$$\begin{aligned} \Psi_{DI}(E_1, E_2, \Omega_1, \Omega_2) &= \sum_L \sum_{l_1, l_2}^{\infty} D_{l_1, l_2}^L(E_1, E_2) \mathcal{Y}_{l_1, l_2}^{L0}(\Omega_1, \Omega_2) = \\ &= \sum_{\substack{L, l_1, l_2 \\ m_1, m_2}} D_{l_1, l_2}^L(E_1, E_2) \begin{bmatrix} l_1 & l_2 & L \\ m_1 & m_2 & 0 \end{bmatrix} Y_{m_1}^{l_1}(\Omega_1) Y_{m_2}^{l_2}(\Omega_2), \end{aligned} \quad (\text{C.2})$$

with $D_{l_1, l_2}^L(E_1, E_2)$ given by equation (6.33). Inserting $\Psi_{DI}(E_1, E_2, \Omega_1, \Omega_2)$ into (C.1) leads to

$$\begin{aligned} P(E_1, E_2, \theta_1) &= 2 \int_{\Omega_2} \int_0^{2\pi} dE_2 d\Omega_2 d\varphi_1 \sum_{\substack{L', l'_1, l'_2 \\ L, l_1, l_2}} \left(D_{l'_1, l'_2}^{L'} \right)^*(E_1, E_2) D_{l_1, l_2}^L(E_1, E_2) \\ &\times \sum_{\substack{m'_1, m'_2 \\ m_1, m_2}} \begin{bmatrix} l'_1 & l'_2 & L' \\ m'_1 & m'_2 & 0 \end{bmatrix} \begin{bmatrix} l_1 & l_2 & L \\ m_1 & m_2 & 0 \end{bmatrix} Y_{m'_1}^{l'_1}(\Omega_1) Y_{m'_2}^{l'_2}(\Omega_2) Y_{m_1}^{l_1}(\Omega_1) Y_{m_2}^{l_2}(\Omega_2). \end{aligned} \quad (\text{C.3})$$

Note that due to the conservation of L_z and the selection rule (B.9) the sums over m'_2 and m_2 are redundant. For brevity we will skip the dependence on E_1 and E_2 in the following equations, as they do not affect the angular momentum calculations.

Performing the integral over Ω_2 , using the orthonormality relation of the spherical harmonics

$$\int Y_{m'}^{l'} Y_m^l d\Omega = \int_0^{2\pi} \int_0^\pi Y_{m'}^{l'}(\theta', \varphi') Y_m^l(\theta, \varphi) \sin\theta d\theta d\varphi = \delta_{mm'} \delta_{ll'} \quad (\text{C.4})$$

gives

$$P(\theta_1) = \sum_{m_1} \sum_{\substack{L', l'_1 \\ L, l_1, l_2}} \begin{bmatrix} l'_1 & l_2 & L' \\ m_1 & -m_1 & 0 \end{bmatrix} \begin{bmatrix} l_1 & l_2 & L \\ m_1 & -m_1 & 0 \end{bmatrix} \\ \times \int_0^{2\pi} d\varphi_1 Y_{m_1}^{l'_1 *}(\Omega_1) Y_{m_1}^{l_1}(\Omega_1) \left(D_{l'_1, l_2}^{L'} \right)^* D_{l_1, l_2}^L. \quad (\text{C.5})$$

Note that there is only one sum over magnetic quantum numbers left.

It is convenient to rewrite the remaining spherical harmonics with the help of

$$Y_m^l = (-1)^m Y_{-m}^l \quad (\text{C.6})$$

and using the product of two *renormalized spherical harmonics* (*Racah tensors*) (B.39) of the same angles can be written as a sum over one renormalized spherical harmonic and 3j-symbols

$$C_{m_1}^{(l_1)}(\theta, \varphi) C_{m_2}^{(l_2)}(\theta, \varphi) = \sum_j C_m^{(j)}(\theta, \varphi) (2j+1) (-1)^m \begin{pmatrix} l_1 & l_2 & j \\ m_1 & m_2 & -m \end{pmatrix} \begin{pmatrix} l_1 & l_2 & j \\ 0 & 0 & 0 \end{pmatrix}. \quad (\text{C.7})$$

This results in

$$Y_{m_1}^{l'_1 *}(\Omega_1) Y_{m_1}^{l_1}(\Omega_1) = \frac{\sqrt{(2l_1+1)(2l'_1+1)}}{4\pi} (-1)^{m_1} C_{m_1}^{(l_1)} C_{-m_1}^{(l'_1)} = \\ \frac{\sqrt{(2l_1+1)(2l'_1+1)}}{4\pi} (-1)^{m_1} \sum_j C_m^{(j)} (2j+1) (-1)^m \begin{pmatrix} l_1 & l'_1 & j \\ m_1 & -m_1 & -m \end{pmatrix} \begin{pmatrix} l_1 & l'_1 & j \\ 0 & 0 & 0 \end{pmatrix}. \quad (\text{C.8})$$

The dependence on Ω_1 is omitted for brevity.

Using

$$\begin{pmatrix} l_1 & l'_1 & j \\ m_1 & -m_1 & 0 \end{pmatrix} = \begin{pmatrix} j & l_1 & l'_1 \\ 0 & m_1 & -m_1 \end{pmatrix} = \frac{(-1)^{j-l_1+m_1}}{\sqrt{2l'_1+1}} \begin{bmatrix} j & l_1 & l'_1 \\ 0 & m_1 & m_1 \end{bmatrix}, \quad (\text{C.9})$$

inserting it back into equation C.5 and performing the sum over m_1 , using equation B.34, leads to

$$P(\theta_1) = 2 \sum_{\substack{L', l'_1 \\ L, l_1, l_2}} \frac{\sqrt{(2l_1+1)(2l'_1+1)}}{4\pi} \sum_j (2j+1) \int_0^{2\pi} C_0^{(j)} d\varphi_1 \frac{(-1)^{j-l_1}}{\sqrt{2l'_1+1}} \begin{pmatrix} l_1 & l'_1 & j \\ 0 & 0 & 0 \end{pmatrix} \\ (-1)^{j+l_1+l_2+L'} \sqrt{(2l'_1+1)(2L+1)} \begin{Bmatrix} j & l_1 & l'_1 \\ l_2 & L' & L \end{Bmatrix} \begin{bmatrix} j & L & L' \\ 0 & 0 & 0 \end{bmatrix} \left(D_{l'_1, l_2}^{L'} \right)^* D_{l_1, l_2}^L. \quad (\text{C.10})$$

Since the renormalized spherical harmonic $C_0^{(j)}$ does not depend on φ_1 anymore, the integral over φ_1 leads to a factor 2π . In addition, the renormalized spherical harmonic can be rewritten to a Legendre polynomial ($C_0^{(j)}(\theta) = P_j(\cos\theta)$) and the CG coefficient into a 3-j symbol, which leads to the final form of

$$P(\theta_1) = 2 \sum_j \sum_{\substack{L', l'_1 \\ L, l_1, l_2}} (-1)^{j-L-L'-l_2} \sqrt{(2l_1+1)(2l'_1+1)(2L+1)(2L'+1)(2j+1)} \\ \begin{pmatrix} l_1 & l'_1 & j \\ 0 & 0 & 0 \end{pmatrix} \begin{pmatrix} j & L & L' \\ 0 & 0 & 0 \end{pmatrix} \left\{ \begin{matrix} j & l_1 & l'_1 \\ & l_2 & L' & L \end{matrix} \right\} (D_{l'_1, l_2}^{L'})^* D_{l_1, l_2}^L P_j(\cos\theta_1). \quad (\text{C.11})$$

The asymmetry parameters β_j read

$$\beta_j = 2 \sum_{\substack{L', l'_1 \\ L, l_1, l_2}} (-1)^{j-L-L'-l_2} \sqrt{(2l_1+1)(2l'_1+1)(2L+1)(2L'+1)(2j+1)} \\ \begin{pmatrix} l_1 & l'_1 & j \\ 0 & 0 & 0 \end{pmatrix} \begin{pmatrix} j & L & L' \\ 0 & 0 & 0 \end{pmatrix} \left\{ \begin{matrix} j & l_1 & l'_1 \\ & l_2 & L' & L \end{matrix} \right\} (D_{l'_1, l_2}^{L'})^* D_{l_1, l_2}^L. \quad (\text{C.12})$$

D Stability of computational speed on different machines

In order to gain more insight into the behavior of the program on the different clusters, the most important routines were benchmarked separately. In addition, the runtimes of each routine were recorded separately on each process. This benchmarking is done without communication between the processes, ensuring that speed differences are clearly visible. Ideally, each process should take the same amount of time to complete a given subroutine. In that case, none of the processes has to wait for the others when they need to synchronize. [Fig. D.1](#), [Fig. D.2](#), [Fig. D.3](#), and [Fig. D.4](#) show the times needed for calculating the single electron Hamiltonians $\hat{H}_1 + \hat{H}_2$, the electron-electron interaction operator \hat{H}_{12} , and the electron-laser interaction operators in velocity gauge $\hat{H}_{1,em}^v + \hat{H}_{2,em}^v$ and in length gauge $\hat{H}_{1,em}^l + \hat{H}_{2,em}^l$. In order to again factor out the different problem sizes for each process depending on the total number of processes, the runtimes are multiplied by the number of processes used. The scales for the figures are chosen equal for each machine, such that the plots also allow for direct comparison between them.

It is not necessary to look at each line separately, as we are more interested in the general behavior of the machines. Flat lines would indicate that the processes are equally fast and do not have to wait for each other. This is reasonably well fulfilled for Abe and Ranger, as well as run 2 for Lobo. Run 1 on Lobo, on the other hand, shows a relatively flat distribution for most processes, but has significant outliers – some processes are slower by factors of 3 or more! Detailed inspection reveals that the large spikes consist of groups of 16 processes, corresponding to one node with 4 quad-core CPUs on Lobo. As the whole run has to wait for the slowest processes in the “real” program, where communication is not disabled, this means that such spikes can cause the whole run to be slowed down by a factor of 3 or more! We do not currently have a good explanation for this behavior, although one possible reason is that some other processes were running on the nodes at the same time. The second run on Lobo did not show these large spikes.

Coyote always shows relatively large fluctuations of the speed of the different routines on different processors, but does not have very strong outliers.

Lonestar shows very surprising behavior – in general, the runtimes are relatively stable across processors. However, there are some processes (in particular for the electron-electron interaction) which are much *faster* than the others. While it seems reasonable that some processors might be slowed down sometimes because of other

things going on, it is surprising that a few processors should be faster than the others, especially by a factor of two or three. One possible explanation is that one of the cores sharing access to the same memory is sometimes given priority, such that it always gets the full memory bandwidth, while the others share the remainder.

Detailed inspection of the curves for Ranger shows that in each block of 16 cores belonging to one node, there are two faster and two slightly slower blocks, each containing 8 cores, i.e. 2 CPUs. As each node should have the same memory bandwidth for its four CPUs (16 cores), this is somewhat surprising. However, the differences are relatively small, so that it does not pose a large problem.

The electron-electron interaction operator (Fig. D.2), which is most strongly limited by memory bandwidth, nicely shows the effects of different wave function block sizes on caching behavior: On most machines, the lines occur in groups. These groups are probably caused by the blocks fitting into different levels of the cache hierarchy.

D.1 Summary

The conclusions we have drawn are given in the following. They are only valid for our specific code, which heavily depends on memory bandwidth.

- Of the currently available TeraGrid machines, Kraken, Lonestar and Ranger are best suited for our code, with Kraken being the fastest per core. The two machines at LANL (Coyote and Lobo) also both work very well, with Coyote being the fastest overall, and Lobo behaving almost exactly like Ranger. Queen Bee and Abe are significantly slower than the other machines.
- Understanding the caching behavior better and trying to optimize for it might yield significant advantages, especially for the electron-electron interaction, which is also the most expensive operation in most cases.
- Some of the machines show somewhat unexpected behavior, where some nodes or processes are significantly slower or faster than the others for some runs. This is probably outside our control, which is unfortunate as a single slow node slows down the whole run.

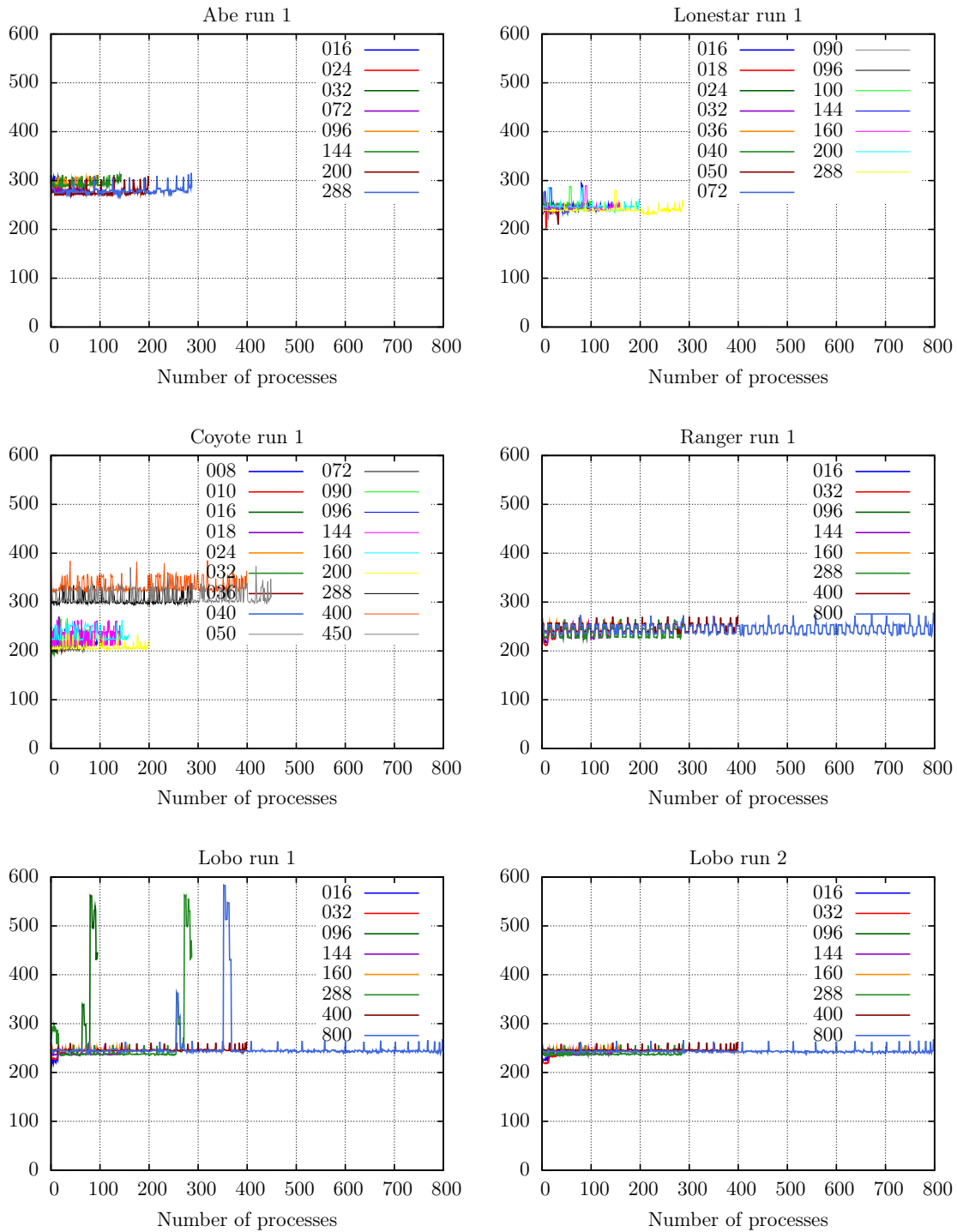


Figure D.1: Runtimes in seconds for the single electron Hamilton operator.

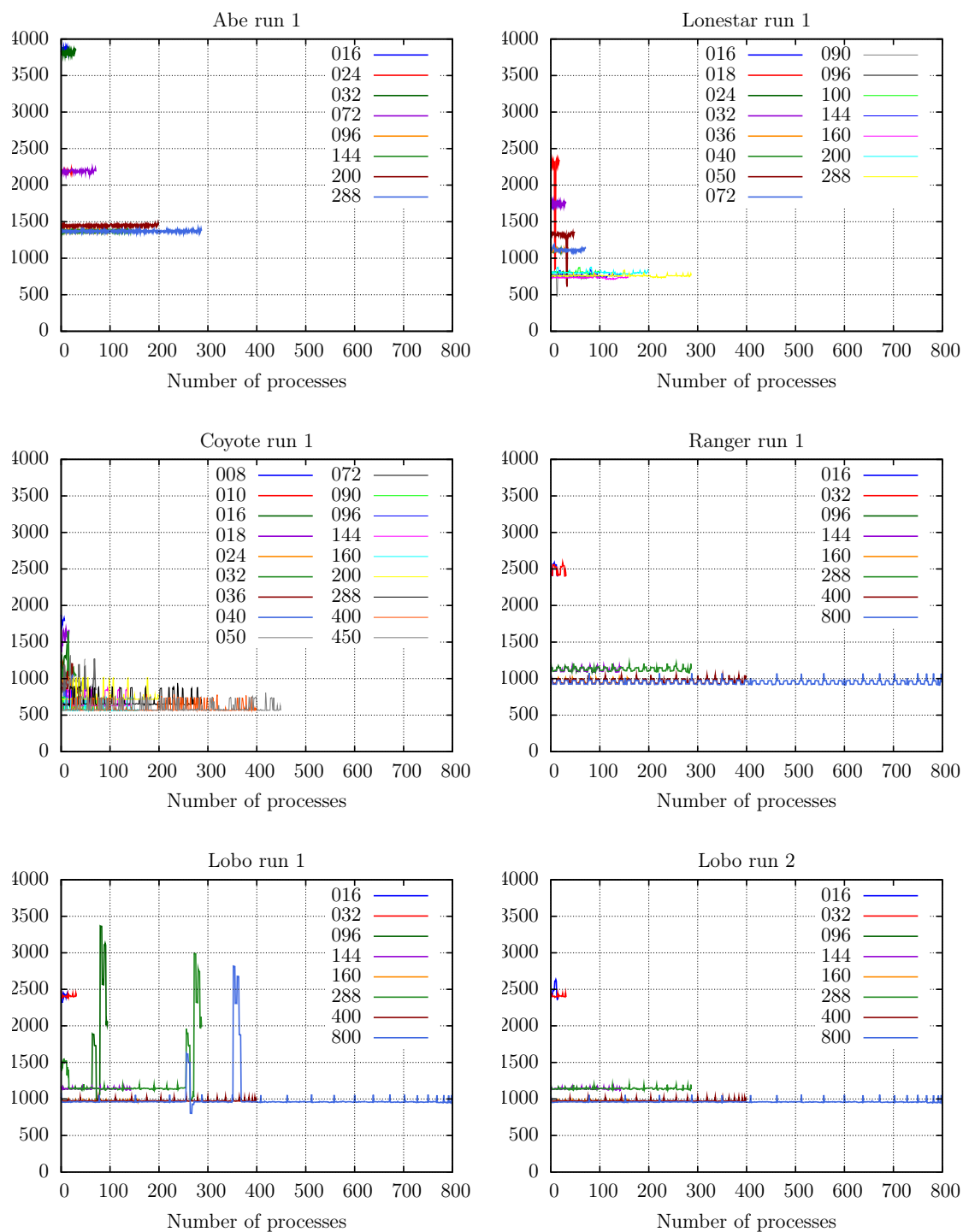


Figure D.2: Runtimes in seconds for the electron-electron interaction operator.

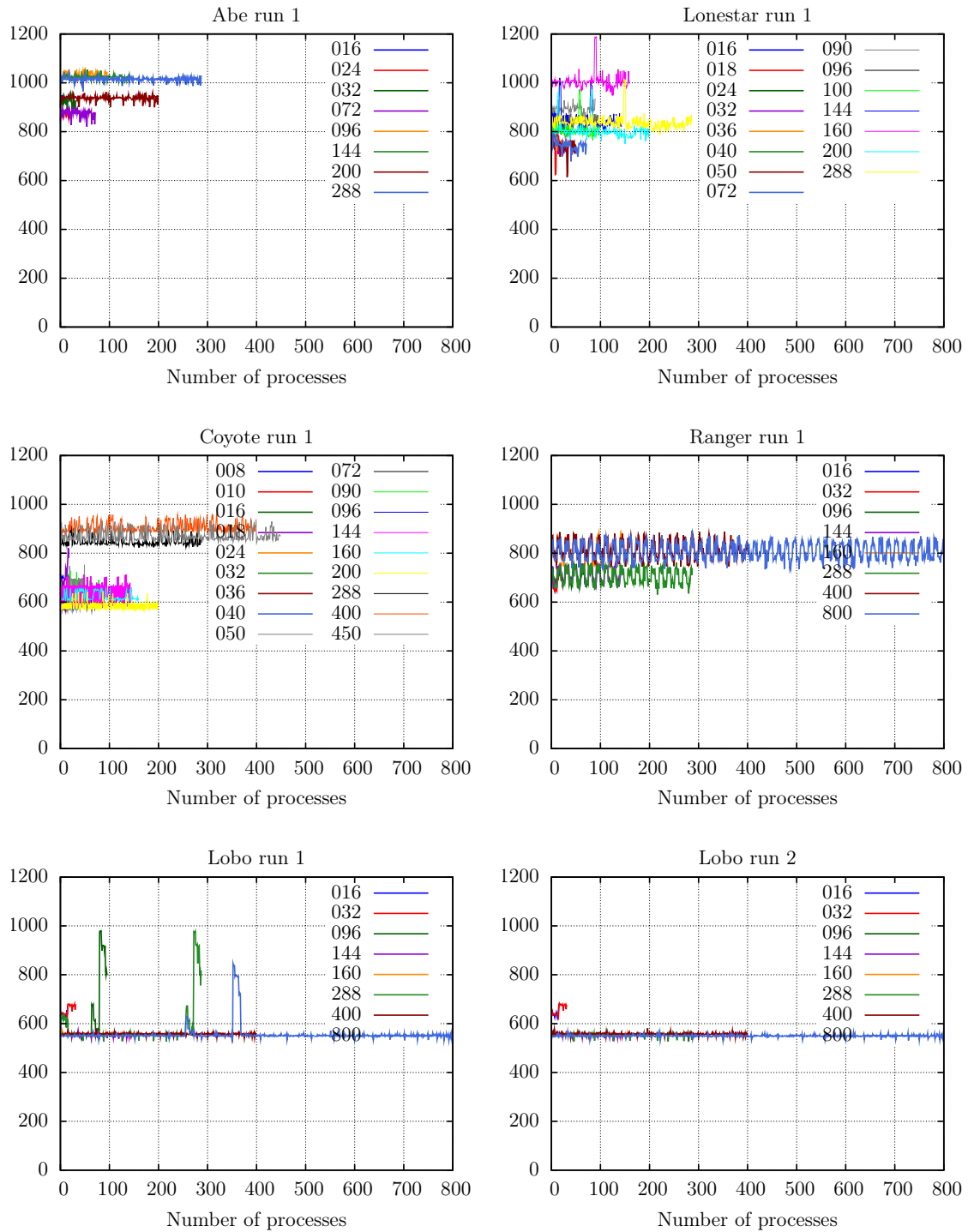


Figure D.3: Runtimes in seconds for the electron-laser interaction in velocity gauge.

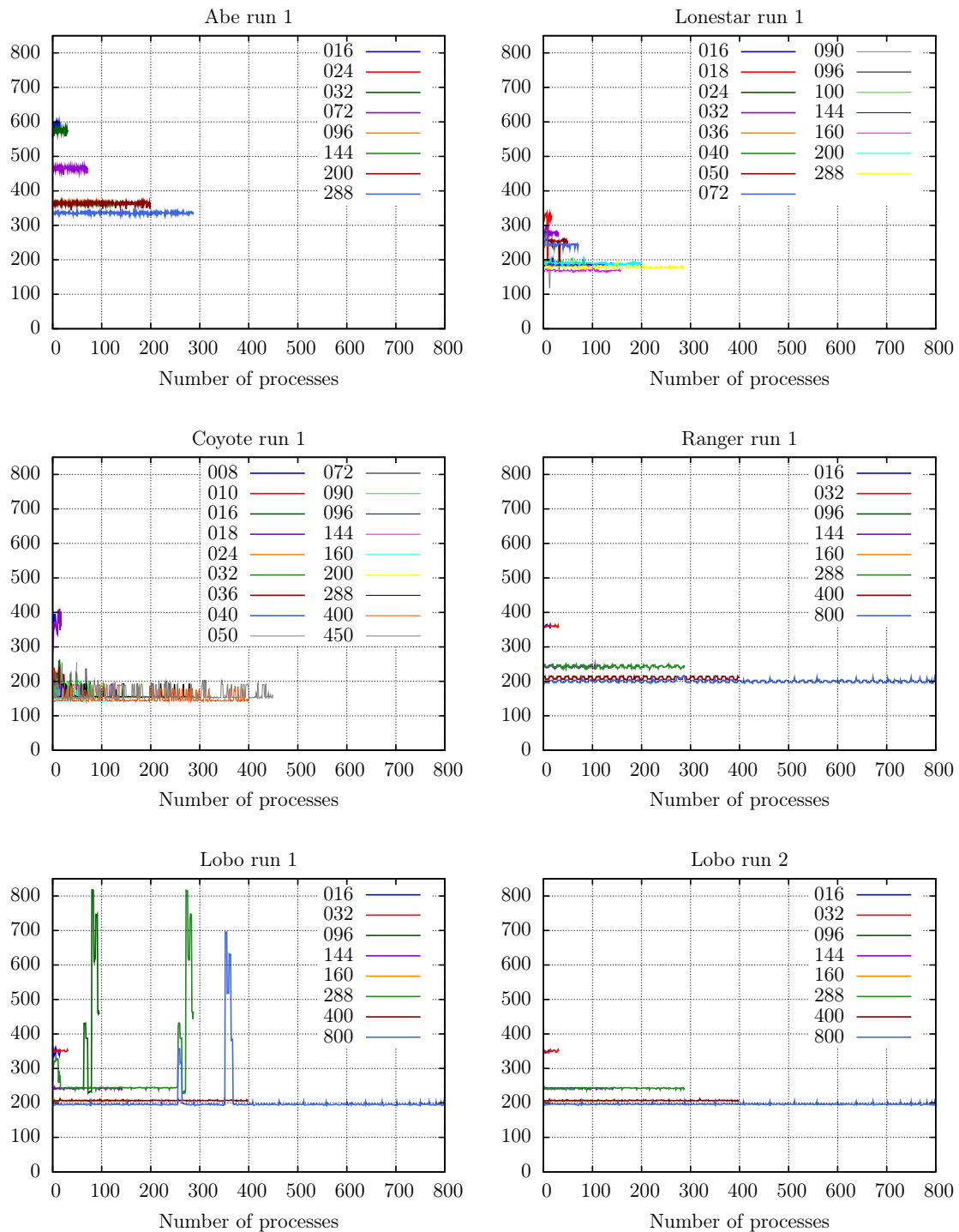


Figure D.4: Runtimes in seconds for the electron-laser interaction in length gauge.

List of Figures

Figure 2.1	Level scheme for the S , P , and D bound states of helium for $S = 0$ and $S = 1$	8
Figure 4.1	Schematic diagram of the kinetic matrix in a FEDVR basis	30
Figure 4.2	Mesh points of a typical FEDVR grid	31
Figure 4.3	Eigenvalues of the <i>discrete</i> FEDVR Laplace operator	33
Figure 5.1	Maximal eigenenergy of the discrete Laplace operator . . .	42
Figure 5.2	Sketch of the split of the radial (r_1, r_2) space for MPI . . .	47
Figure 5.3	Synchronization procedure for parts of the wave function using MPI.	48
Figure 5.4	Total CPU hours used for the benchmark run on different LANL and TeraGrid clusters.	51
Figure 7.1	Radial probability distributions of doubly excited states. . .	67
Figure 8.1	Pulse-dependent shape function $ \mathcal{G}_{\sin^2} $ in two-photon transitions	76
Figure 9.1	Energy distribution $P^{DI}(E_1, E_2)$ after nonsequential two-photon double ionization	83
Figure 9.2	Total energy distribution $P^{DI}(E_{\text{tot}})$ and Fourier spectra for 1 fs, 4 fs and 9 fs \sin^2 laser pulses.	83
Figure 9.3	Singly differential cross section $d\sigma_2/dE_1$ for 1 fs, 4 fs and 9 fs \sin^2 laser pulses at $\hbar\omega = 42$ eV and $\hbar\omega = 70$ eV.	86
Figure 9.4	Convergence of the total cross section with propagation time τ	88
Figure 9.5	Convergence of the singly differential cross section with propagation time τ	89
Figure 9.6	Convergence of the triply differential cross section with propagation time τ	90
Figure 9.7	Radial density for various times τ after the end of the pulse.	92
Figure 9.8	Comparison of different methods for extracting the triply differential cross sections.	93

Figure 9.9	Convergence of the total cross section with the size of the angular momentum expansion.	95
Figure 9.10	Convergence of the triply differential cross section with the size of the angular momentum expansion.	96
Figure 10.1	Different pulse shapes used for extracting cross sections for nsTPDI.	100
Figure 10.2	Total two-photon double ionization cross sections obtained using different pulses	101
Figure 10.3	Comparison of the total two-photon double ionization cross sections	102
Figure 10.4	Comparison of triply differential cross sections at 42 eV photon energy.	105
Figure 11.1	$P^{DI}(\Delta E)$ for different photon energies in 9 fs \sin^2 pulses.	108
Figure 11.2	Energy distribution $P^{DI}(E_1, E_2)$ for sequential two-photon double ionization	109
Figure 11.3	Joint angular distribution $P^{DI}(\theta_1, \theta_2)$ for TPDI.	111
Figure 11.4	Joint energy-angle distribution $P^{DI}(\Delta E, \theta_1, \theta_2)$ for TPDI.	112
Figure 11.5	Mutual information $\mathcal{I}_{\Omega_1, \Omega_2}$ for TPDI vs $\hbar\omega$	114
Figure 11.6	Energy-resolved mutual information $\mathcal{I}_{\Omega_1, \Omega_2}(\Delta E)$ for TPDI.	114
Figure 11.7	Energy-resolved angular von Neumann entropy $S_{\Omega}(\Delta E)$ for TPDI.	116
Figure 11.8	Forward-backward asymmetry for TPDI.	117
Figure 11.9	Recoil ion momentum distribution for TPDI.	119
Figure 11.10	Angular asymmetry parameters $\beta_2(E_1), \beta_4(E_1)$ for TPDI.	121
Figure 11.11	One-electron angular distribution $P^{DI}(E, \theta)$ for TPDI.	122
Figure 12.1	Energy distributions for TPDI with different pulse lengths.	127
Figure 12.2	Double ionization rate $P^{DI}(\Delta E)/T$ for TPDI at $\hbar\omega = 70$ eV, for different pulse durations T	128
Figure 12.3	Scaling of TPDI yields with pulse duration at $\hbar\omega = 70$ eV.	130
Figure 12.4	Fano parameters of the first shake-up peak for TPDI at $\hbar\omega = 70$ eV.	132
Figure 12.5	Double ionization rate $P^{DI}(\Delta E)/T$ for TPDI at $\hbar\omega = 91$ eV, for different pulse durations T	134
Figure 12.6	Joint angular distribution $P^{DI}(\theta_1, \theta_2)$ for TPDI at $\hbar\omega = 70$ eV.	135
Figure 12.7	Joint angular distribution $P^{DI}(\theta_1, \theta_2)$ for TPDI for ultra-short sequential and long nonsequential pulses.	136
Figure 12.8	Mutual information $\mathcal{I}_{\Omega_1, \Omega_2}$ for TPDI at $\hbar\omega = 70$ eV and for time propagation of the ground state without electron interaction.	137

Figure 12.9	Joint angular distribution $P^{DI}(\theta_1, \theta_2)$ for TPDI from 150 as pulses.	139
Figure 12.10	Joint angular distribution $P^{DI}(\theta_1, \theta_2)$ for different waiting times τ for TPDI from a 70 eV 150 as pulse.	140
Figure 12.11	Mutual information $\mathcal{I}_{\Omega_1, \Omega_2}$ for different waiting times τ for TPDI from a 70 eV 150 as pulse.	141
Figure 12.12	Energy-resolved mutual information $\mathcal{I}_{\Omega_1, \Omega_2}(\Delta E)$ for TPDI at $\hbar\omega = 70$ eV.	142
Figure 12.13	Forward-backward asymmetry $\mathcal{A}(\Delta E)$ for TPDI by an XUV pulse at $\hbar\omega = 70$ eV.	143
Figure 12.14	Combined double ionization probability $P^{DI}(E_1, E_2)$ and forward-backward asymmetry $\mathcal{A}(E_1, E_2)$ for TPDI by an XUV pulse at $\hbar\omega = 70$ eV with a duration of 900 as.	144
Figure 12.15	Angle-energy distributions for TPDI at $\hbar\omega = 70$ eV.	145
Figure 12.16	Recoil ion momentum distribution for TPDI.	146
Figure D.1	Runtimes in seconds for the single electron Hamilton operator.	173
Figure D.2	Runtimes in seconds for the electron-electron interaction operator.	174
Figure D.3	Runtimes in seconds for the electron-laser interaction in velocity gauge.	175
Figure D.4	Runtimes in seconds for the electron-laser interaction in length gauge.	176

Bibliography

- [1] F. W. Byron and C. J. Joachain. *Multiple Ionization Processes in Helium*. Phys. Rev. **164**, 1 (1967).
- [2] T. Åberg. *Asymptotic Double-Photoexcitation Cross Sections of the Helium Atom*. Phys. Rev. A **2**, 1726 (1970).
- [3] A. Dalgarno and H. R. Sadeghpour. *Double photoionization of atomic helium and its isoelectronic partners at x-ray energies*. Phys. Rev. A **46**, R3591 (1992).
- [4] L. R. Andersson and J. Burgdörfer. *Excitation ionization and double ionization of helium by high-energy photon impact*. Phys. Rev. Lett. **71**, 50 (1993).
- [5] D. Proulx and R. Shakeshaft. *Double ionization of helium by a single photon with energy 89-140 eV*. Phys. Rev. A **48**, R875 (1993).
- [6] M. Pont and R. Shakeshaft. *Absolute triply differential cross sections for double photoionization of helium at 10, 20, and 52.9 eV above threshold*. Phys. Rev. A **51**, R2676 (1995).
- [7] M. S. Pindzola and F. Robicheaux. *Time-dependent close-coupling calculations of correlated photoionization processes in helium*. Phys. Rev. A **57**, 318 (1998).
- [8] Y. Qiu, J. Z. Tang, J. Burgdörfer, and J. Wang. *Double photoionization of helium from threshold to high energies*. Phys. Rev. A **57**, R1489 (1998).
- [9] D. Dundas, K. T. Taylor, J. S. Parker, and E. S. Smyth. *Double-ionization dynamics of laser-driven helium*. J. Phys. B **32**, L231 (1999).
- [10] A. Becker and F. H. M. Faisal. *Interplay of electron correlation and intense field dynamics in the double ionization of helium*. Phys. Rev. A **59**, R1742 (1999).
- [11] M. Lein, E. K. U. Gross, and V. Engel. *Intense-Field Double Ionization of Helium: Identifying the Mechanism*. Phys. Rev. Lett. **85**, 4707 (2000).

- [12] J. S. Parker, L. R. Moore, K. J. Meharg, D. Dundas, and K. T. Taylor. *Double-electron above threshold ionization of helium*. J. Phys. B **34**, L69 (2001).
- [13] A. M. Kondratenko and E. L. Saldin. *Generation of coherent radiation by a relativistic electron beam in an undulator*. Particle Accelerators **10**, 207 (1980).
- [14] Y. Derbenev, A. Kondratenko, and E. Saldin. *On the possibility of using a free electron laser for polarization of electrons in storage rings*. Nuclear Instruments and Methods in Physics Research **193**, 415 (1982).
- [15] R. Bonifacio, C. Pellegrini, and L. M. Narducci. *Collective instabilities and high-gain regime in a free electron laser*. Optics Communications **50**, 373 (1984).
- [16] J. B. Murphy and C. Pellegrini. *Free electron lasers for the XUV spectral region*. Nuclear Instruments and Methods in Physics Research Section A: Accelerators, Spectrometers, Detectors and Associated Equipment **237**, 159 (1985).
- [17] M. J. Hogan, C. Pellegrini, J. Rosenzweig, S. Anderson, P. Frigola, A. Tremaine, C. Fortgang, D. C. Nguyen, R. L. Sheffield, J. K. Wright, A. Varfolomeev, A. A. Varfolomeev, S. Tolmachev, and R. Carr. *Measurements of Gain Larger than 10^5 at $12\mu\text{m}$ in a Self-Amplified Spontaneous-Emission Free-Electron Laser*. Phys. Rev. Lett. **81**, 4867 (1998).
- [18] S. V. Milton, E. Gluskin, N. D. Arnold, C. Benson, W. Berg, S. G. Biedron, M. Borland, Y. C. Chae, R. J. Dejus, P. K. Den Hartog, B. Deriy, M. Erdmann, Y. I. Eidelman, M. W. Hahne, Z. Huang, K. J. Kim, J. W. Lewellen, Y. Li, A. H. Lumpkin, O. Makarov *et al.* *Exponential Gain and Saturation of a Self-Amplified Spontaneous Emission Free-Electron Laser*. Science **292**, 2037 (2001).
- [19] V. Ayvazyan, N. Baboi, I. Bohnet, R. Brinkmann, M. Castellano, P. Castro, L. Catani, S. Choroba, A. Cianchi, M. Dohlus, H. T. Edwards, B. Faatz, A. A. Fateev, J. Feldhaus, K. Flöttmann, A. Gamp, T. Garvey, H. Genz, Ch. V. Gretchko *et al.* *Generation of GW Radiation Pulses from a VUV Free-Electron Laser Operating in the Femtosecond Regime*. Phys. Rev. Lett. **88**, 104802 (2002).
- [20] V. Ayvazyan, N. Baboi, J. Bähr, V. Balandin, B. Beutner, A. Brandt, I. Bohnet, A. Bolzmann, R. Brinkmann, O. I. Brovko, J. P. Carneiro, S. Casalbuoni, M. Castellano, P. Castro, L. Catani, E. Chiadroni, S. Choroba,

- A. Cianchi, H. Delsim-Hashemi, G. Di Pirro *et al.* *First operation of a free-electron laser generating GW power radiation at 32 nm wavelength.* Eur. Phys. J. D **37**, 297 (2006).
- [21] W. Ackermann, G. Asova, V. Ayvazyan, A. Azima, N. Baboi, J. Bähr, V. Balandin, B. Beutner, A. Brandt, A. Bolzmann, R. Brinkmann, O. I. Brovko, M. Castellano, P. Castro, L. Catani, E. Chiadroni, S. Choroba, A. Cianchi, J. T. Costello, D. Cubaynes *et al.* *Operation of a free-electron laser from the extreme ultraviolet to the water window.* Nat. Photonics **1**, 336 (2007).
- [22] M. Nagasono, E. Suljoti, A. Pietzsch, F. Hennies, M. Wellhöfer, J. T. Hoefft, M. Martins, W. Wurth, R. Treusch, J. Feldhaus, J. R. Schneider, and A. Föhlich. *Resonant two-photon absorption of extreme-ultraviolet free-electron-laser radiation in helium.* Phys. Rev. A **75**, 051406(R) (2007).
- [23] M. Lewenstein, P. Balcou, Ivanov, A. L'Huillier, and P. B. Corkum. *Theory of high-harmonic generation by low-frequency laser fields.* Phys. Rev. A **49**, 2117 (1994).
- [24] M. Y. Ivanov, T. Brabec, and N. Burnett. *Coulomb corrections and polarization effects in high-intensity high-harmonic emission.* Phys. Rev. A **54**, 742 (1996).
- [25] K. J. Schafer and K. C. Kulander. *High Harmonic Generation from Ultrafast Pump Lasers.* Phys. Rev. Lett. **78**, 638 (1997).
- [26] W. Becker, A. Lohr, M. Kleber, and M. Lewenstein. *A unified theory of high-harmonic generation: Application to polarization properties of the harmonics.* Phys. Rev. A **56**, 645 (1997).
- [27] I. P. Christov, M. M. Murnane, and H. C. Kapteyn. *High-Harmonic Generation of Attosecond Pulses in the "Single-Cycle" Regime.* Phys. Rev. Lett. **78**, 1251 (1997).
- [28] M. Drescher, M. Hentschel, R. Kienberger, G. Tempea, C. Spielmann, G. A. Reider, P. B. Corkum, and F. Krausz. *X-ray Pulses Approaching the Attosecond Frontier.* Science **291**, 1923 (2001).
- [29] P. Agostini and L. F. Dimauro. *The physics of attosecond light pulses.* Rep. Prog. Phys. **67**, 813 (2004).
- [30] G. Sansone, E. Benedetti, F. Calegari, C. Vozzi, L. Avaldi, R. Flammini, L. Poletto, P. Villoresi, C. Altucci, R. Velotta, S. Stagira, S. De Silvestri, and M. Nisoli. *Isolated Single-Cycle Attosecond Pulses.* Science **314**, 443 (2006).

-
- [31] E. Goulielmakis, M. Schultze, M. Hofstetter, V. S. Yakovlev, J. Gagnon, M. Uiberacker, A. L. Aquila, E. M. Gullikson, D. T. Attwood, R. Kienberger, F. Krausz, and U. Kleineberg. *Single-Cycle Nonlinear Optics*. *Science* **320**, 1614 (2008).
- [32] M. B. Gaarde, J. L. Tate, and K. J. Schafer. *Macroscopic aspects of attosecond pulse generation*. *J. Phys. B* **41**, 132001 (2008).
- [33] A. Scrinzi, M. Y. Ivanov, R. Kienberger, and D. M. Villeneuve. *Attosecond physics*. *J. Phys. B* **39**, R1 (2006).
- [34] P. B. Corkum and F. Krausz. *Attosecond science*. *Nat. Phys.* **3**, 381 (2007).
- [35] M. F. Kling and M. J. J. Vrakking. *Attosecond Electron Dynamics*. *Annual Review of Physical Chemistry* **59**, 463 (2008).
- [36] P. B. Corkum and Z. Chang. *The Attosecond Revolution*. *Opt. Photon. News* **19**, 24 (2008).
- [37] F. Krausz and M. Ivanov. *Attosecond physics*. *Rev. Mod. Phys* **81**, 163 (2009).
- [38] S. Nagele. *Interaction of helium with intense ultrashort laser pulses*. Master's thesis, TU Wien (2007).
- [39] R. Pazourek. *Electronic correlation effects in helium on the attosecond time scale*. Master's thesis, TU Wien (2008).
- [40] J. Feist, S. Nagele, R. Pazourek, E. Persson, B. I. Schneider, L. A. Collins, and J. Burgdörfer. *Nonsequential two-photon double ionization of helium*. *Phys. Rev. A* **77**, 043420 (2008).
- [41] J. Feist, R. Pazourek, S. Nagele, E. Persson, B. I. Schneider, L. A. Collins, and J. Burgdörfer. *Electron correlation in two-photon double ionization of helium from attosecond to XFEL pulses*. *J. Phys. B* **42**, 134014 (2009).
- [42] J. Feist, S. Nagele, R. Pazourek, E. Persson, B. I. Schneider, L. A. Collins, and J. Burgdörfer. *Probing Electron Correlation via Attosecond xuv Pulses in the Two-Photon Double Ionization of Helium*. *Phys. Rev. Lett.* **103**, 063002 (2009).
- [43] E. S. Smyth, J. S. Parker, and K. T. Taylor. *Numerical integration of the time-dependent Schrodinger equation for laser-driven helium*. *Comput. Phys. Commun.* **114**, 1 (1998).

- [44] M. S. Pindzola, F. Robicheaux, S. D. Loch, J. C. Berengut, T. Topcu, J. Colgan, M. Foster, D. C. Griffin, C. P. Ballance, D. R. Schultz, T. Minami, N. R. Badnell, M. C. Witthoef, D. R. Plante, D. M. Mitnik, J. A. Ludlow, and U. Kleiman. *The time-dependent close-coupling method for atomic and molecular collision processes*. J. Phys. B **40**, R39 (2007).
- [45] M. S. Pindzola and F. Robicheaux. *Two-photon double ionization of He and H⁻*. J. Phys. B **31**, L823 (1998).
- [46] M. A. Kornberg and P. Lambropoulos. *Photoelectron energy spectrum in ‘direct’ two-photon double ionization of helium*. J. Phys. B **32**, L603 (1999).
- [47] M. G. Makris, L. A. A. Nikolopoulos, and P. Lambropoulos. *Electron angular distributions in two-photon double ionization of helium*. Europhys. Lett. **54**, 722 (2001).
- [48] T. Mercouris, C. Haritos, and C. A. Nicolaides. *Theory and computation of the rate of multiphoton two-electron ionization via the direct mechanism*. J. Phys. B **34**, 3789 (2001).
- [49] J. Colgan, M. S. Pindzola, and F. Robicheaux. *Fully quantal ($\gamma, 2e$) calculations for absolute differential cross sections of helium*. J. Phys. B **34**, L457 (2001).
- [50] L. A. A. Nikolopoulos and P. Lambropoulos. *Multichannel theory of two-photon single and double ionization of helium*. J. Phys. B **34**, 545 (2001).
- [51] J. Colgan and M. S. Pindzola. *Core-Excited Resonance Enhancement in the Two-Photon Complete Fragmentation of Helium*. Phys. Rev. Lett. **88**, 173002 (2002).
- [52] T. Nakajima and L. A. A. Nikolopoulos. *Use of helium double ionization for autocorrelation of an xuv pulse*. Phys. Rev. A **66**, 041402 (2002).
- [53] B. Piraux, J. Bauer, S. Laulan, and H. Bachau. *Probing electron-electron correlation with attosecond pulses*. Eur. Phys. J. D **26**, 7 (2003).
- [54] S. Laulan and H. Bachau. *Correlation effects in two-photon single and double ionization of helium*. Phys. Rev. A **68**, 013409 (2003).
- [55] L. Feng and H. W. van der Hart. *Two-photon double ionization of He*. J. Phys. B **36**, L1 (2003).
- [56] S. Laulan and H. Bachau. *One- and two-photon double ionization of beryllium with ultrashort ultraviolet laser fields*. Phys. Rev. A **69**, 033408 (2004).

-
- [57] K. L. Ishikawa and K. Midorikawa. *Above-threshold double ionization of helium with attosecond intense soft x-ray pulses*. Phys. Rev. A **72**, 013407 (2005).
- [58] S. X. Hu, J. Colgan, and L. A. Collins. *Triple-differential cross-sections for two-photon double ionization of He near threshold*. J. Phys. B **38**, L35 (2005).
- [59] A. S. Kheifets and I. A. Ivanov. *Convergent close-coupling calculations of two-photon double ionization of helium*. J. Phys. B **39**, 1731 (2006).
- [60] A. Y. Istomin, E. A. Pronin, N. L. Manakov, S. I. Marmo, and A. F. Starace. *Elliptic and Circular Dichroism Effects in Two-Photon Double Ionization of Atoms*. Phys. Rev. Lett. **97**, 123002 (2006).
- [61] I. F. Barna, J. Wang, and J. Burgdörfer. *Angular distribution in two-photon double ionization of helium by intense attosecond soft-x-ray pulses*. Phys. Rev. A **73**, 023402 (2006).
- [62] E. Fomouo, G. Lagmago Kamta, G. Edah, and B. Piraux. *Theory of multiphoton single and double ionization of two-electron atomic systems driven by short-wavelength electric fields: An ab initio treatment*. Phys. Rev. A **74**, 063409 (2006).
- [63] E. Fomouo, Piraux, S. Laulan, and H. Bachau. *Dynamics of two-photon double-ionization of helium at the attosecond scale*. J. Phys. B **39**, S427 (2006).
- [64] L. A. A. Nikolopoulos and P. Lambropoulos. *Helium double ionization signals under soft-x-ray coherent radiation*. J. Phys. B **39**, 883 (2006).
- [65] E. A. Pronin, N. L. Manakov, S. I. Marmo, and A. F. Starace. *Polarization control of direct (non-sequential) two-photon double ionization of He*. J. Phys. B **40**, 3115 (2007).
- [66] R. Shakeshaft. *Two-photon single and double ionization of helium*. Phys. Rev. A **76**, 063405 (2007).
- [67] A. S. Kheifets, A. I. Ivanov, and I. Bray. *Different escape modes in two-photon double ionization of helium*. Phys. Rev. A **75**, 024702 (2007).
- [68] L. A. A. Nikolopoulos and P. Lambropoulos. *Time-dependent theory of double ionization of helium under XUV radiation*. J. Phys. B **40**, 1347 (2007).
- [69] T. Morishita, S. Watanabe, and C. D. Lin. *Attosecond Light Pulses for Probing Two-Electron Dynamics of Helium in the Time Domain*. Phys. Rev. Lett. **98**, 083003 (2007).

- [70] I. A. Ivanov and A. S. Kheifets. *Two-photon double ionization of helium in the region of photon energies 42–50 eV*. Phys. Rev. A **75**, 033411 (2007).
- [71] S. X. Hu and L. A. Collins. *Time-dependent study of photon-induced autoionization decay*. Phys. Rev. A **71**, 062707 (2005).
- [72] S. X. Hu and L. A. Collins. *Attosecond Pump Probe: Exploring Ultrafast Electron Motion inside an Atom*. Phys. Rev. Lett. **96**, 073004 (2006).
- [73] S. X. Hu and L. A. Collins. *Probing ultrafast electron correlation with double attosecond pulses*. J. Mod. Opt. **54**, 943 (2007).
- [74] A. S. Kheifets, I. A. Ivanov, and I. Bray. *Angular anisotropy parameters and recoil-ion momentum distribution in two-photon double ionization of helium*. Phys. Rev. A **76**, 025402 (2007).
- [75] D. A. Horner, F. Morales, T. N. Rescigno, F. Martín, and C. W. McCurdy. *Two-photon double ionization of helium above and below the threshold for sequential ionization*. Phys. Rev. A **76**, 030701(R) (2007).
- [76] S. Fritzsche, A. N. Grum-Grzhimailo, E. V. Gryzlova, and N. M. Kabachnik. *Angular distributions and angular correlations in sequential two-photon double ionization of atoms*. J. Phys. B **41**, 165601 (2008).
- [77] T. Sekikawa, T. Okamoto, E. Haraguchi, M. Yamashita, and T. Nakajima. *Two-photon resonant excitation of a doubly excited state in He atoms by high-harmonic pulses*. Opt. Express **16**, 21922 (2008).
- [78] B. Piraux, E. Fomouo, P. Antoine, and H. Bachau. *Dynamics of the direct double ionization of helium by two XUV photons*. Journal of Physics: Conference Series **141**, 012013 (2008).
- [79] P. Lambropoulos, L. A. A. Nikolopoulos, M. G. Makris, and A. Mihelic. *Direct versus sequential double ionization in atomic systems*. Phys. Rev. A **78**, 055402 (2008).
- [80] D. A. Horner, C. W. McCurdy, and T. N. Rescigno. *Triple differential cross sections and nuclear recoil in two-photon double ionization of helium*. Phys. Rev. A **78**, 043416 (2008).
- [81] P. Antoine, E. Fomouo, B. Piraux, T. Shimizu, H. Hasegawa, Y. Nabekawa, and K. Midorikawa. *Two-photon double ionization of helium: An experimental lower bound of the total cross section*. Phys. Rev. A **78**, 023415 (2008).

- [82] X. Guan, K. Bartschat, and B. I. Schneider. *Dynamics of two-photon double ionization of helium in short intense xuv laser pulses*. Phys. Rev. A **77**, 043421 (2008).
- [83] D. A. Horner, T. N. Rescigno, and C. W. McCurdy. *Decoding sequential versus nonsequential two-photon double ionization of helium using nuclear recoil*. Phys. Rev. A **77**, 030703(R) (2008).
- [84] A. Palacios, T. N. Rescigno, and C. W. McCurdy. *Cross sections for short-pulse single and double ionization of helium*. Phys. Rev. A **77**, 032716 (2008).
- [85] P. Lambropoulos and L. A. A. Nikolopoulos. *Angular distributions in double ionization of helium under XUV sub-femtosecond radiation*. New J. Phys. **10**, 025012 (2008).
- [86] E. Fomouo, P. Antoine, H. Bachau, and B. Piraux. *Attosecond timescale analysis of the dynamics of two-photon double ionization of helium*. New J. Phys. **10**, 025017 (2008).
- [87] E. Fomouo, P. Antoine, B. Piraux, L. Malegat, H. Bachau, and R. Shake-shaft. *Evidence for highly correlated electron dynamics in two-photon double ionization of helium*. J. Phys. B **41**, 051001 (2008).
- [88] A. Palacios, T. N. Rescigno, and C. W. McCurdy. *Time-dependent treatment of two-photon resonant single and double ionization of helium by ultrashort laser pulses*. Phys. Rev. A **79**, 033402 (2009).
- [89] I. A. Ivanov and A. S. Kheifets. *Angular anisotropy parameters for sequential two-photon double ionization of helium*. Phys. Rev. A **79**, 023409 (2009).
- [90] T. G. Lee, M. S. Pindzola, and F. Robicheaux. *Energy and angular differential probabilities for photoionization of He using chirped attosecond soft-x-ray pulses*. Phys. Rev. A **79**, 053420 (2009).
- [91] Y. Nabekawa, H. Hasegawa, E. J. Takahashi, and K. Midorikawa. *Production of Doubly Charged Helium Ions by Two-Photon Absorption of an Intense Sub-10-fs Soft X-Ray Pulse at 42 eV Photon Energy*. Phys. Rev. Lett. **94**, 043001 (2005).
- [92] H. Hasegawa, E. J. Takahashi, Y. Nabekawa, K. L. Ishikawa, and K. Midorikawa. *Multiphoton ionization of He by using intense high-order harmonics in the soft-x-ray region*. Phys. Rev. A **71**, 023407 (2005).
- [93] A. A. Sorokin, M. Wellhofer, S. V. Bobashev, K. Tiedtke, and M. Richter. *X-ray-laser interaction with matter and the role of multiphoton ionization:*

- Free-electron-laser studies on neon and helium.* Phys. Rev. A **75**, 051402(R) (2007).
- [94] A. Rudenko, L. Foucar, M. Kurka, Th. K. U. Kühnel, Y. H. Jiang, A. Voitkiv, B. Najjari, A. Kheifets, S. Lüdemann, T. Havermeier, M. Smolarski, S. Schössler, K. Cole, M. Schöffler, R. Dörner, S. Düsterer, W. Li, B. Keitel, R. Treusch *et al.* *Recoil-Ion Momentum Distributions for Two-Photon Double Ionization of He and Ne by 44 eV Free-Electron Laser Radiation.* Phys. Rev. Lett. **101**, 073003 (2008).
- [95] H. S. Friedrich. *Theoretical Atomic Physics.* Springer, Berlin (2005).
- [96] B. H. Bransden and C. J. Joachain. *Physics of atoms and molecules.* Longman New York (1983).
- [97] B. F. Davis and K. T. Chung. *Mass-polarization effect and oscillator strengths for S,P,D states of helium.* Phys. Rev. A **25**, 1328 (1982).
- [98] H. A. Bethe and E. E. Salpeter. *Quantum Mechanics of One-and Two-Electron Systems.* Handbuch der Physik **35**, 88 (1957).
- [99] R. D. Cowan. *The Theory of Atomic Structure and Spectra.* University of California Press (1981).
- [100] G. Tanner, K. Richter, and J. M. Rost. *The theory of two-electron atoms: between ground state and complete fragmentation.* Rev. Mod. Phys **72**, 497 (2000).
- [101] C. F. Fischer. *The Hartree-Fock method for atoms.* Wiley (1977).
- [102] M. Klaiber, K. Z. Hatsagortsyan, and C. H. Keitel. *Above-threshold ionization beyond the dipole approximation.* Phys. Rev. A **71**, 033408 (2005).
- [103] K. J. Meharg, J. S. Parker, and K. T. Taylor. *Beyond the dipole approximation for helium and hydrogen in intense laser fields.* J. Phys. B **38**, 237 (2005).
- [104] F. H. M. Faisal. *Theory of Multiphoton Processes.* Springer (1987).
- [105] M. Göppert-Mayer. *Über Elementarakte mit zwei Quantensprüngen.* Ann. Phys. **401**, 273 (1931).
- [106] C. C. Tannoudji, J. D. Roc, and G. Grynberg. *Photons and Atoms. Introduction to Quantum Electrodynamics.* Wiley-Interscience, New York (1987).
- [107] E. Cormier and P. Lambropoulos. *Optimal gauge and gauge invariance in non-perturbative time-dependent calculation of above-threshold ionization.* J. Phys. B **29**, 1667 (1996).

-
- [108] B. N. Taylor and P. J. Mohr. *Fundamental Physical Constants - Non-SI units*. <http://physics.nist.gov/constants> (2006).
- [109] R. L. R. Mohan. *Finite Element and Boundary Element Applications in Quantum Mechanics*. Oxford University Press (2002).
- [110] W. Schweizer. *Numerical Quantum Dynamics*. Springer (2001).
- [111] J. C. Light, I. P. Hamilton, and J. V. Lill. *Generalized discrete variable approximation in quantum mechanics*. J. Chem. Phys. **82**, 1400 (1985).
- [112] J. V. Lill, G. A. Parker, and J. C. Light. *The discrete variable-finite basis approach to quantum scattering*. J. Chem. Phys. **85**, 900 (1986).
- [113] J. V. Lill, G. A. Parker, and J. C. Light. *Discrete variable representations and sudden models in quantum scattering theory*. Chem. Phys. Lett. **89**, 483 (1982).
- [114] G. C. Corey and J. W. Tromp. *Variational discrete variable representation*. J. Chem. Phys. **103**, 1812 (1995).
- [115] A. S. Dickinson and P. R. Certain. *Calculation of Matrix Elements for One-Dimensional Quantum-Mechanical Problems*. J. Chem. Phys. **49**, 4209 (1968).
- [116] G. Szegő. *Orthogonal Polynomials*. American Mathematical Society (1975).
- [117] D. Baye and P. H. Heenen. *Generalised meshes for quantum mechanical problems*. J. Phys. A **19**, 2041 (1986).
- [118] D. Baye, M. Hesse, and M. Vincke. *The unexplained accuracy of the Lagrange-mesh method*. Phys. Rev. E **65**, 026701 (2002).
- [119] D. Baye. *Lagrange-mesh method for quantum-mechanical problems*. Phys. Status. Solidi B **243**, 1095 (2006).
- [120] J. C. Light and T. Carrington. *Discrete-Variable Representations and Their Utilization*. Adv. Chem. Phys **114**, 263 (2000).
- [121] B. I. Schneider and L. A. Collins. *The discrete variable method for the solution of the time-dependent Schrodinger equation*. J. Non-Cryst. Solids **351**, 1551 (2005).
- [122] B. I. Schneider, L. A. Collins, and S. X. Hu. *Parallel solver for the time-dependent linear and nonlinear Schrödinger equation*. Phys. Rev. E **73**, 036708 (2006).

-
- [123] T. N. Rescigno and C. W. McCurdy. *Numerical grid methods for quantum-mechanical scattering problems*. Phys. Rev. A **62**, 032706 (2000).
- [124] C. W. McCurdy, D. A. Horner, and T. N. Rescigno. *Practical calculation of amplitudes for electron-impact ionization*. Phys. Rev. A **63**, 022711 (2001).
- [125] A. Scrinzi and N. Elander. *A finite element implementation of exterior complex scaling for the accurate determination of resonance energies*. J. Chem. Phys. **98**, 3866 (1993).
- [126] C. Leforestier, R. H. Bisseling, C. Cerjan, M. D. Feit, R. Friesner, A. Guldberg, A. Hammerich, G. Jolicard, W. Karrlein, H.-D. Meyer, N. Lipkin, O. Roncero, and R. Kosloff. *A comparison of different propagation schemes for the time dependent Schrodinger equation*. J. Comp. Phys. **94**, 59 (1991).
- [127] C. Lanczos. *An iteration method for the solution of the eigenvalue problem of linear differential and integral operators*. Journal of Research of the National Bureau of Standards **45**, 255 (1950).
- [128] W. E. Arnoldi. *The principle of minimized iterations in the solution of the matrix eigenvalue problem*. Q. Appl. Math. **9**, 17 (1951).
- [129] T. J. Park and J. C. Light. *Unitary quantum time evolution by iterative Lanczos reduction*. J. Chem. Phys. **85**, 5870 (1986).
- [130] A. I. Kuleff, J. Breidbach, and L. S. Cederbaum. *Multielectron wave-packet propagation: General theory and application*. J. Chem. Phys. **123**, 044111 (2005).
- [131] C. W. McCurdy, M. Baertschy, and T. N. Rescigno. *Solving the three-body Coulomb breakup problem using exterior complex scaling*. J. Phys. B **37**, R137 (2004).
- [132] S. E. Koonin and D. C. Meredith. *Computational Physics: Fortran Version*. Addison-Wesley Redwood City, Calif (1990).
- [133] F. He, C. Ruiz, and A. Becker. *Absorbing boundaries in numerical solutions of the time-dependent Schroedinger equation* (2007). Physics/0701265v1.
- [134] U. V. Riss and H.-D. Meyer. *Reflection-free complex absorbing potentials*. J. Phys. B **28**, 1475 (1995).
- [135] *MPI Forum*. <http://www.mpi-forum.org>.
- [136] G. Breit and H. A. Bethe. *Ingoing Waves in Final State of Scattering Problems*. Phys. Rev. **93**, 888 (1954).

-
- [137] S. Altshuler. *Ingoing waves in the final state of ionization problems*. Il Nuovo Cimento (1955-1965) **3**, 246 (1956).
- [138] R. Szmytkowski and M. Gruchowski. *Ingoing and outgoing waves in the non-relativistic theory of photoionization*. J. Quant. Spectrosc. Radiat. Transfer **94**, 127 (2005).
- [139] J. Berakdar and J. S. Briggs. *Three-body Coulomb continuum problem*. Phys. Rev. Lett. **72**, 3799 (1994).
- [140] F. Maulbetsch and J. S. Briggs. *Angular distribution of electrons following double photoionization*. J. Phys. B **26**, 1679 (1993).
- [141] C. W. McCurdy and F. Martín. *Implementation of exterior complex scaling in B-splines to solve atomic and molecular collision problems*. J. Phys. B **37**, 917 (2004).
- [142] P. L. Bartlett. *A complete numerical approach to electron-hydrogen collisions*. J. Phys. B **39**, R379 (2006).
- [143] G. F. Gribakin, V. K. Ivanov, A. V. Korol, and Y. M. Kuchiev. *Two-photon detachment of electrons from halogen negative ions*. J. Phys. B **32**, 5463 (1999).
- [144] J. Ullrich, R. Moshhammer, R. Dörner, O. Jagutzki, V. Mergel, H. Schmidt-Böcking, and L. Spielberger. *Recoil-ion momentum spectroscopy*. J. Phys. B **30**, 2917 (1997).
- [145] M. A. Abdallah, A. Landers, M. Singh, W. Wolff, H. E. Wolf, E. Y. Kamber, M. Stockli, and C. L. Cocke. *Capture and ionization processes studied with COLTRIMS*. Nuclear Instruments and Methods in Physics Research Section B: Beam Interactions with Materials and Atoms **154**, 73 (1999).
- [146] J. Ullrich, R. Moshhammer, A. Dorn, R. Dörner, L. P. H. Schmidt, and H. Schmidt-Böcking. *Recoil-ion and electron momentum spectroscopy: reaction-microscopes*. Rep. Prog. Phys. **66**, 1463 (2003).
- [147] M. Pont and R. Shakeshaft. *Asymmetry parameter and momentum distribution of the nucleus in double photoionization of helium*. Phys. Rev. A **54**, 1448 (1996).
- [148] R. H. Landau and M. J. Páez. *Computational Physics: Problem Solving with Computers*. Wiley-Interscience, har/dsk/co edn. (1997).

-
- [149] M. Matsumoto and T. Nishimura. *Mersenne twister: a 623-dimensionally equidistributed uniform pseudo-random number generator*. ACM Trans. Model. Comput. Simul. **8**, 3 (1998).
- [150] ARPACK. <http://www.caam.rice.edu/software/ARPACK>.
- [151] K. Maschhoff and D. Sorensen. *P_ARPACK: An efficient portable large scale eigenvalue package for distributed memory parallel architectures*. Applied Parallel Computing Industrial Computation and Optimization pp. 478–486 (1996).
- [152] F. T. Newman. *A very accurate grid method for the solution of Schrödinger equations: The helium ground state*. Int. J. Quantum Chem. **63**, 1065 (1997).
- [153] G. W. F. Drake. *Long range Casimir forces: Theory and recent experiments on atomic systems*. In F. S. Levin and D. A. Micha (editors), *Long range Casimir forces: Theory and recent experiments on atomic systems*, p. 146. Plenum Press, New York (1993).
- [154] S. D. Bergeson, A. Balakrishnan, K. G. H. Baldwin, T. B. Lucatorto, J. P. Marangos, T. J. McIlrath, T. R. O'Brian, S. L. Rolston, C. J. Sansonetti, J. Wen, N. Westbrook, C. H. Cheng, and E. E. Eyler. *Measurement of the He Ground State Lamb Shift*. Phys. Rev. Lett. **80**, 3475 (1998).
- [155] A. Scrinzi and B. Piraux. *Two-electron atoms in short intense laser pulses*. Phys. Rev. A **58**, 1310 (1998).
- [156] N. Elander and E. Yarevsky. *Exterior complex scaling method applied to doubly excited states of helium*. Phys. Rev. A **57**, 3119 (1998).
- [157] A. Bürgers, D. Wintgen, and J. M. Rost. *Highly doubly excited S states of the helium atom*. J. Phys. B **28**, 3163 (1995).
- [158] H. Beutler. *Über Absorptionsserien von Argon, Krypton und Xenon zu Termen zwischen den beiden Ionisierungsgrenzen $2P_{3/2}/0$ und $2P_{1/2}/0$* . Zeitschrift für Physik A Hadrons and Nuclei **93**, 177 (1935).
- [159] U. Fano. *Effects of Configuration Interaction on Intensities and Phase Shifts*. Phys. Rev. **124**, 1866 (1961).
- [160] J. J. Boyle and M. S. Pindzola. *Many-Body Atomic Physics: lectures on the application of many-body theory to atomic physics*. Cambridge University Press (1998).

- [161] E. L. Saldin, E. A. Schneidmiller, and M. V. Yurkov. *A new technique to generate 100 GW-level attosecond X-ray pulses from the X-ray SASE FELs*. Optics Communications **239**, 161 (2004).
- [162] A. A. Zholents and W. M. Fawley. *Proposal for Intense Attosecond Radiation from an X-Ray Free-Electron Laser*. Phys. Rev. Lett. **92**, 224801 (2004).
- [163] A. A. Zholents and G. Penn. *Obtaining attosecond x-ray pulses using a self-amplified spontaneous emission free electron laser*. Phys. Rev. ST Accel. Beams **8**, 050704 (2005).
- [164] E. L. Saldin, E. A. Schneidmiller, and M. V. Yurkov. *Self-amplified spontaneous emission FEL with energy-chirped electron beam and its application for generation of attosecond x-ray pulses*. Phys. Rev. ST Accel. Beams **9**, 050702 (2006).
- [165] N. R. Thompson and B. W. J. Mcneil. *Mode Locking in a Free-Electron Laser Amplifier*. Phys. Rev. Lett. **100**, 203901 (2008).
- [166] G. Lambert, T. Hara, D. Garzella, T. Tanikawa, M. Labat, B. Carre, H. Kitamura, T. Shintake, M. Bougeard, S. Inoue, Y. Tanaka, P. Salieres, H. Merdji, O. Chubar, O. Gobert, K. Tahara, and M. E. Couprie. *Injection of harmonics generated in gas in a free-electron laser providing intense and coherent extreme-ultraviolet light*. Nat. Phys. **4**, 296 (2008).
- [167] E. A. Gibson, A. Paul, N. Wagner, R. Tobey, D. Gaudiosi, S. Backus, I. P. Christov, A. Aquila, E. M. Gullikson, D. T. Attwood, M. M. Murnane, and H. C. Kapteyn. *Coherent Soft X-ray Generation in the Water Window with Quasi-Phase Matching*. Science **302**, 95 (2003).
- [168] J. Seres, V. S. Yakovlev, E. Seres, C. Strelis, P. Wobrauschek, C. Spielmann, and F. Krausz. *Coherent superposition of laser-driven soft-X-ray harmonics from successive sources*. Nat. Phys. **3**, 878 (2007).
- [169] X. Zhang, A. L. Lytle, T. Popmintchev, X. Zhou, H. C. Kapteyn, M. M. Murnane, and O. Cohen. *Quasi-phase-matching and quantum-path control of high-harmonic generation using counterpropagating light*. Nat. Phys. **3**, 270 (2007).
- [170] N. M. Naumova, J. A. Nees, I. V. Sokolov, B. Hou, and G. A. Mourou. *Relativistic Generation of Isolated Attosecond Pulses in a λ [sup 3] Focal Volume*. Phys. Rev. Lett. **92**, 063902 (2004).
- [171] B. Dromey, M. Zepf, A. Gopal, K. Lancaster, M. S. Wei, K. Krushelnick, M. Tatarakis, N. Vakakis, S. Moustazis, R. Kodama, M. Tampo, C. Stoeckl,

- R. Clarke, H. Habara, D. Neely, S. Karsch, and P. Norreys. *High harmonic generation in the relativistic limit*. Nat. Phys. **2**, 456 (2006).
- [172] G. D. Tsakiris, K. Eidmann, J. Meyer-Ter-Vehn, and F. Krausz. *Route to intense single attosecond pulses*. New J. Phys. **8**, 19 (2006).
- [173] Y. Nomura, R. Horlein, P. Tzallas, B. Dromey, S. Rykovanov, Z. Major, J. Osterhoff, S. Karsch, L. Veisz, M. Zepf, D. Charalambidis, F. Krausz, and G. D. Tsakiris. *Attosecond phase locking of harmonics emitted from laser-produced plasmas*. Nat. Phys. **5**, 124 (2009).
- [174] T. A. Carlson. *Double Electron Ejection Resulting from Photo-Ionization in the Outermost Shell of He, Ne, and Ar, and Its Relationship to Electron Correlation*. Phys. Rev. **156**, 142 (1967).
- [175] X. Guan, O. Zatsarinny, C. J. Noble, K. Bartschat, and B. I. Schneider. *A time-dependent B-spline R-matrix approach to double ionization of atoms by XUV laser pulses*. J. Phys. B **42**, 134015 (2009).
- [176] R. B. Barker and H. W. Berry. *Electron Energy Distributions from Ionizing Collisions of Helium and Neon Ions with Helium*. Phys. Rev. **151**, 14 (1966).
- [177] G. Gerber, R. Morgenstern, and A. Niehaus. *Ionization processes in slow collisions of heavy particles. I. He and Ne+ on Ne, Ar, Kr, and Xe*. J. Phys. B **5**, 1396 (1972).
- [178] A. Russek and W. Mehlhorn. *Post-collision interaction and the Auger line-shape*. J. Phys. B **19**, 911 (1986).
- [179] G. B. Armen, J. Tulkki, T. Åberg, and B. Crasemann. *Quantum theory of post-collision interaction in inner-shell photoionization: Final-state interaction between two continuum electrons*. Phys. Rev. A **36**, 5606 (1987).
- [180] R. M. Gray. *Entropy and Information Theory*. Springer, 1 edn. (1990).
- [181] G. H. Wannier. *The Threshold Law for Single Ionization of Atoms or Ions by Electrons*. Phys. Rev. **90**, 817 (1953).
- [182] S. Cvejanovic and F. H. Read. *Studies of the threshold electron impact ionization of helium*. J. Phys. B **7**, 1841 (1974).
- [183] L. Végh and J. H. Macek. *Coherences in the decay of autoionizing states in photoionization. I. Exchange effect between photo- and Auger electrons*. Phys. Rev. A **50**, 4031 (1994).

- [184] F. H. Read. *The analysis of post-collision interactions in ejected-electron spectra*. J. Phys. B **10**, L207 (1977).
- [185] J. A. de Gouw, J. van Eck, A. C. Peters, J. van der Weg, and H. G. M. Heideman. *Coherence between the photoionization of different inner-shell vacancy states of argon*. Phys. Rev. Lett. **71**, 2875 (1993).
- [186] B. Rouvellou, S. Rioual, L. Avaldi, R. Camilloni, G. Stefani, and G. Turri. *Angle-dependent postcollisional interaction and interference effects in resonant double photoionization of neon*. Phys. Rev. A **67**, 012706 (2003).
- [187] H. Bräuning, R. Dörner, C. L. Cocke, M. H. Prior, B. Krässig, A. S. Kheifets, I. Bray, A. Bräuning-Demian, K. Carnes, S. Dreuil, V. Mergel, P. Richard, J. Ullrich, and H. Schmidt-Böcking. *Absolute triple differential cross sections for photo-double ionization of helium - experiment and theory*. J. Phys. B **31**, 5149 (1998).
- [188] M. Uiberacker, T. Uphues, M. Schultze, A. J. Verhoef, V. Yakovlev, M. F. Kling, J. Rauschenberger, N. M. Kabachnik, H. Schröder, M. Lezius, K. L. Kompa, H. G. Muller, M. J. J. Vrakking, S. Hendel, U. Kleineberg, U. Heinzmann, M. Drescher, and F. Krausz. *Attosecond real-time observation of electron tunnelling in atoms*. Nature **446**, 627 (2007).
- [189] J. Itatani, F. Quéré, G. L. Yudin, Ivanov, F. Krausz, and P. B. Corkum. *Attosecond Streak Camera*. Phys. Rev. Lett. **88**, 173903 (2002).
- [190] V. S. Yakovlev, F. Bammer, and A. Scrinzi. *Attosecond streaking measurements*. J. Mod. Opt. **52**, 395 (2005).
- [191] A. L. Cavalieri, N. Müller, T. Uphues, V. S. Yakovlev, A. Baltuška, B. Horvath, B. Schmidt, L. Blümel, R. Holzwarth, S. Hendel, M. Drescher, U. Kleineberg, P. M. Echenique, R. Kienberger, F. Krausz, and U. Heinzmann. *Attosecond spectroscopy in condensed matter*. Nature **449**, 1029 (2007).
- [192] P. J. Davis and P. Rabinowitz. *Methods of Numerical Integration*. New York (1984).
- [193] M. Abramowitz and I. A. Stegun. *Handbook of Mathematical Functions*, vol. 55. National Bureau of Standards (1965).
- [194] A. R. Krommer and C. W. Überhuber. *Numerical integration on advanced computer systems*. Springer, Berlin (1994).
- [195] A. Messiah. *Quantenmechanik II*. Walter de Gruyter (1990).

-
- [196] V. Devanathan. *Angular momentum techniques in quantum mechanics*. Kluwer Academic Publishers Boston (1999).
- [197] A. Edmonds. *Angular Momentum in Quantum Mechanics*. Princeton University Press (1974).

Acknowledgments

I would like to take this opportunity to thank the many people without whose support and encouragement this thesis would not have been possible, and the time spent working on it not as enjoyable. First of all, I would like to thank my advisor, Joachim Burgdörfer, who convinced me to stay in Vienna for my PhD studies, a decision I have never regretted. He not only helped in countless discussions through his great physical insight, but also provided support and guidance throughout the last years, as well as ensuring a constant supply of chocolate for the whole group.

I am very grateful to Matthias Kling for reviewing and evaluating this thesis and for being the second examiner for my thesis defense.

I am deeply indebted to Barry Schneider, who was a huge help in the development of our program and who has been an endless source of enthusiasm and ideas. I am equally thankful to Lee Collins for providing insight and perspective and for making it possible for us to access the supercomputers at Los Alamos National Laboratory, without which many of the results presented could not have been obtained. Kenichi Ishikawa shared his code for the solution of the two-electron Schrödinger equation with us, which was a great basis for the development of our code and ensured that I always had a running program that any new developments could be tested against.

It would be hard to thank Stefan Nagele and Renate Pazourek too much, both of whom I have had the pleasure to collaborate with for their diploma and PhD theses. A lot of the work presented here would not exist without them. In addition, I was able to build on the description of our method from their diploma theses for putting together **Part I** of this thesis. Furthermore, they have become great friends in the past few years.

I thank Emil Persson for many helpful discussions in which he shared his experience in laser-atom interactions, and who helped improve the presentation of our results.

I would also like to thank Matthias Liertzer and Andreas Kaltenbäck, who did student research projects with us and solved all the problems we threw at them with ease.

At the beginning of my studies, I was fortunate enough to spend two months at NIST in Gaithersburg, Maryland, starting the collaboration with Barry Schneider and Lee Collins. This was possible through the financial support provided by Charles Clark, which I am grateful for. I also thank Károly Tókési for hosting two visits at the ATOMKI in Debrecen, Hungary, and for coordinating our mutual collaboration with Sándor Borbély.

All the people in our group have made the last years enjoyable and created a great working atmosphere. In particular, I would like to thank Klaus Schiessl, with whom I had the great pleasure to share an office. Our compatible musical tastes made working long hours much more bearable. In addition to the people mentioned above, the other members of our group, Florian Aigner, Iva Březinová, Cornelia Deiss, Stefanie Gräfe, Christoph Lemell, Florian Libisch, Stefan Rotter, Beate Solleder, Paul Tiwald and Georg Wachter, as well as “honorary” member Katharina Igenbergs, have not only made the lunch breaks enjoyable, but have also been great partners for such diverse activities as beach volleyball, poker, hiking and dancing.

I would also like to express my gratitude to Heike Höller, Roswitha Uden, and Elfriede Mössmer for managing the administration of the institute and always being helpful and resourceful in resolving any problems, and to Monika Wild for managing the administration of the International Max-Planck Research School on Advanced Photon Science and ensuring that we were well fed on our visits to Munich.

Last, but certainly not least, I want to thank my family and friends. My parents have always supported me, and have looked out for me when I was preoccupied with other things. My brother Alexander has been a great flatmate and is always able to make me laugh, even after a hard day at work. I thank my grandparents for their support and enthusiasm, and all my family members for many enjoyable times. Finally, I thank all my friends for being there for me and for all the fun, and apologize for not listing you by name. You know who you are.